BCCT family:

Dynamics in stress-regulated betaine transport and role of pathogen-relevant choline transport

Dissertation
zur Erlangung des Doktorgrades
der Naturwissenschaften

vorgelegt beim Fachbereich Biochemie, Chemie und Pharmazie
der Johann Wolfgang Goethe – Universität
in Frankfurt am Main

von
Izabela Jadwiga Waclawska-Krzeminski
aus Pila/Polen

Frankfurt am Main, 2015

(D 30)

Die Arbeit wurde in der Abteilung Strukturbiologie des Max-Planck-Institutes für Biophysik in Frankfurt am Main unter der Betreuung von Prof. Dr. Christine Ziegler durchgeführt und vom Fachbereich Biochemie, Chemie und Pharmazie der Johann Wolfgang Goethe – Universität als Dissertation angenommen.

Dekan : Prof. Dr. Michael Karas

1. Gutachter : Prof. Dr. Clemens Glaubitz
2. Gutachter : Prof. Dr. Christine Ziegler

Datum der Disputation: 19.04.2016

Parts of this thesis have been published, are in revision or in preparation for publication in the following articles:

Sand, M., Stahl, J., **Waclawska, I.**, Ziegler, C., and Averhoff, B. 2014. Identification of an osmo-dependent and an osmo-independent choline transporter in *Acinetobacter baylyi*: implications in osmostress protection and metabolic adaption. *Environ Microbiol.* 16:1490-502

Waclawska, I., and Ziegler, C. 2015. Regulatory role of charged clusters in the N-terminal domain of BetP from *Corynebacterium glutamicum*. *Biol. Chem.* 396: 1117-1126

Spindler, P.E., **Waclawska, I.**, Endeward, B., Plackmeyer, J., Ziegler, C., and Prisner, T. 2015. Carr-Purcell Pulsed Electron Double Resonance with shaped inversion pulses. *J Phys Chem Lett*. 6:4331-5

Waclawska, I., Endeward, B., Haeri, H.H., Prisner, T., and, Ziegler, C. Conformational dynamics of the trimeric betaine transporter BetP (in preparation).

Other article contributions cited in this thesis:

Ge, L., Perez, C., **Waclawska, I.**, Ziegler, C. and Muller, D. J. 2011. Locating an extracellular K^+-dependent interaction site that modulates betaine-binding of the Na^+-coupled betaine symporter BetP. *Proc. Natl. Acad. Sci. U.S.A.* 108:E890-8

Table of Contents

List of symbols and abbreviations

2D	two-dimensional
3D	three-dimensional
Å	Angstrom(s)
aa	amino acids
A. baylyi	*Acinetobacter baylyi*
A. baumannii	*Acinetobacter baumannii*
A.b.BetT1	*Acinetobacter baylyi* osmo-independent choline transporter
A.b.BetT2	*Acinetobacter baylyi* osmo-dependent choline transporter
ABC	ATP-binding cassette
AdiC	Arginine/amantine antiporter
APC	amino acids, polyamines and organic cation transporters
ApcT	proton-coupled amino acid transporter
APS	ammonium persulfate
BCCT	betaine-choline-carnitine transporter
BetP	betaine permease
B. subtilis	*Bacillus subtilis*
BetT	choline transporter
bp	base pairs
BSA	bovine serum albumin
BN-PAGE	blue native-polyacrylamide gel electrophoresis
°C	degrees Celsius
Cα	Alpha carbon
CaiT	carnitine/γ-butyrobetaine antiporter
CCCP	carbonyl cyanid m-chlorophenyl hydrazone
C. glutamicum	*Corynebacterium glutamicum*
CL	cardiolipin
cpm	counts per minute
CuPh	copper-o-phenanthroline
CV	column volume(s)
cw	continuous wave
Cymal-5	5-cyclohexyl-1-pentyl-β-D-maltoside
Da	Dalton

DDM	n-dodecyl-β-D-maltoside
DEER	double electron-electron resonance
DMSO	Dimethyl sulfoxide
DNA	deoxyribonucleic acid
dNTP	deoxyribonucleotide triphosphate
DOPC	1,2 dioleoyl-s*n*-glycero-3-phosphocholine
DOPG	1,2 dioleoyl-s*n*-glycero-3-phosphoglycerol
DTT	dithiothreitol
dw	dry weight
D_2O	Deuterium oxide
E.c.BetT1	*E. coli* choline transporter
E. coli	*Escherichia coli*
EctT	ectoine transporter
EDTA	ethylenediaminetetraacetic acid
EPL	*E. coli* polar lipids
EPR	electron paramagnetic resonance
et al.	et alia
FRET	Fluorescence resonance energy transfer
g	acceleration of gravity or gram(s)
Glt_{Ph}	sodium-coupled aspartate transporter from *Pyrococcus horikoshii*
h	hour(s)
HEPES	2-(4-(2-hydroxyethyl)-1-piperazinyl)-ethansulfonacid
HiLiDe	high lipid/detergent
His6	hexa-histidine tag
H_2O_{dd}	double distilled water
IEX	ion-exchange chromatography
IMAC	immobilized metal ion affinity chromatography
k	kilo
K	Kelvin
Km	Michaelis-Menten constant
l	liter
LacY	Lactose permease
LB	Luria Bertani media
LcoP	low capacity osmoregulated permease
LeuT	sodium-dependent leucine/alanine transporter
LPR	lipid-to-protein ratio

µ	micro
M	moles per liter
m	milli
MD	Molecular dynamics
MFS	major facilitator superfamily
Mhp1	benzyl-hydantoin transporter
min	minute(s)
MW	molecular weight
MMTSL	methyl methanethiosulfonate
MTSL	methanothiosulfonate
NCS1	nucleobase/cation symporter-1
NiEDDA	nickel(II)-ethylenediamine diacetate
NMR	Nuclear magnetic resonance
NSS	neurotransmitter sodium transporters
o-PDM	o-phenylenediamalrimide
P.a.BetT1	*Pseudomonas aeruginosa* choline transporter
P.a.BetT2	*Pseudomonas aeruginosa* betaine transporter
P.a.BetT3	*Pseudomonas aeruginosa* choline transporter
PAGE	Polyacrylamide gel electrophoresis
PC	phosphatidylcholine
PCR	polymerase chain reaction
PDB	protein data base
PE	phosphatidylethanolamine
PG	phosphatidylglycerol
PEG	polyethylenglycol
PELDOR	pulsed electron-electron double resonance
POPG	1-Palmitoyl-2-oleoyl-s*n*-glycero-3- phosphatidylglycerol
Pfu	*Pyrococcus furiosus*
PG	phosphatidylglycerol
pI	isoelectric point
r.m.s.d.	root mean square deviation
rpm	rotations per minute
RT	room temperature
S.D.	standard deviation
SDS	sodium dodecyl sulfate
SDSL	site-directed spin labeling
SEC	size exclusion chromatography

sec, s	second(s)
S.E.M	standard error of the mean
SERp	Surface entropy reduction prediction
SLS	Swiss light source
SSS	solute sodium symporters
T	temperature
t	time
Taq	*Thermus aquaticus*
TCEP	Tris(2-carboxyethyl)phosphine
TM	transmembrane
Tris	2-amino-2-hydroxymethyl-propane-1,3-dio
TSS	transformation and storage solution
V_{max}	maximum velocity
vSGLT	*Vibrio parahaemolyticus* sodium/galactose transporter
v/v	volume per volume
w/v	weight per volume
w/w	weight per weight
WT	wild type

Amino acid	One-letter code	Three-letter code
alanine	A	Ala
cysteine	C	Cys
glutamic acid	E	Glu
phenylalanine	F	Phe
glycine	G	Gly
histidine	H	His
isoleucine	I	Ile
lysine	K	Lys
leucine	L	Leu
methionine	M	Met
asparagine	N	Asn
proline	P	Pro
glutamine	Q	Gln
arginine	R	Arg
serine	S	Ser
threonine	T	Thr
valine	V	Val
tryptophan	W	Trp
tyrosine	Y	Tyr
variable	X	-

List of Figures

List of Tables

Zusammenfassung

Transportprozesse durch die Membran sind essentiell um das Überleben jeder lebenden Zelle zu gewährleisten. Daher wird der Austausch Membran-undurchlässiger Moleküle durch spezifische Transportproteine, die innerhalb der Lipid-Doppelschicht eingebettet vorliegen, ermöglicht. Eine wichtige Klasse dabei sind die sekundär aktiven Transporter, die den Transport des ersten Substrates entgegen das Konzentrationsgefälle sehr effizient an den Transport eines weiteren Substrates in Richtung Konzentrationsgefälle koppeln. Diese Transporter sind in allen Reichen des Lebens weit verbreitet, da sie äußerst wichtige Funktionen ausführen. Eine Funktion ist es, dem schädlichen Effekt von hyperosmotischen Stress in Bakterien entgegenzuwirken. Mehrere Mitglieder der BCCT (Betain-Cholin-Carnitin-Transport)-Familie von sekundären Transportern schützen vor osmotischem Stress durch die Akkumulation von dem kompatiblem Solut Betain oder dessen Vorstufe, dem Cholin (Lamark *et al.*, 1991; Peter *et al.*, 1996; Ziegler *et al.*, 2010). Abgesehen von osmotisch abhängigen Natrium- und Proton-gekoppelten Symportern, gehören auch einige wenige osmotisch unabhängige Transporter, wie der Substrat:Endprodukt Antiporter CaiT von *E. coli*, zu der BCCT-Familie (Jung *et al.*, 2002; Ziegler *et al.*, 2010).

Das bestcharakterisierte Mitglied der BCCT-Familie ist der Natrium-gekoppelte Betain-Transporter BetP von *Corynebacterium glutamicum*. BetP zählt zusammen mit dem ABC-Transporter OpuA und dem H^+-Solut Symporter ProP als Paradigma für osmotisch regulierten Osmolyt-Transport. Obwohl alle drei Transporter ausgiebig untersucht worden sind, ist der generelle Mechanismus der Osmoregulation noch weitgehend unverstanden. Demnach war eine Aufgabe, die Aufklärung weiterer regulatorischen Eigenschaften von BetP.

BetP wird unter hyperosmotischem Stress aktiviert und erhöht mit steigender externer Osmolalität seine basale Betain-Aufnahmeaktivität innerhalb einer Sekunde (Peter *et al.*, 1998a). Der osmotische Stress wird mittels zweier Reize von BetP wahrgenommen, der eine ist die Erhöhung der internen K^+-Konzentration über den Grenzwert von 220 mM (Rübenhagen *et al.*, 2001) und der zweite bezieht sich auf eine Veränderung des physikalischen Zustandes der

Membran (Maximov *et al.*, 2014). Bisher konnten die gelösten Kristallstrukturen in Kombination mit funktionellen und Computer-gestützten Analysen Einblick in den Kopplungsmechanismus von Betain mit dem Co-Substrat Natrium vermitteln (Khafizov *et al.*, 2012; Perez *et al.*, 2012). Trotz umfangreicher Daten ist der genaue Regulationsmechanismus des BetP-Trimers noch immer unklar.

Die Beteiligung der N- und C-terminalen Domäne an den osmoregulatorischen Eigenschaften wurde zuvor bereits umfassend untersucht. Die hauptsächlich positiv geladenen C-terminale Domäne wurde als Schlüsselkomponente in der Regulation identifiziert und dient der Wahrnehmung der internen K^+-Konzentration (Schiller *et al.*, 2004). Im Gegensatz dazu ist die funktionelle Rolle der einzigartigen negativ geladenen N-terminalen Domäne unbekannt. Die gelösten Strukturen erbrachten keine weiteren Information, da nur Kristallstrukturen der N-terminal verkürzten BetP Variante (BetPΔ29EEE44/45/46AAA) existieren (Ressl *et al.*, 2009). Funktionelle Analysen der N-terminal verkürzten BetP Mutante in *C. glutamicum,* dessen Membran ausschließlich nur anionische Lipide beinhaltet, zeigten eine verminderte osmotische Sensitivität durch die Verschiebung des Aktivitätsoptimums zu höheren Osmolalitäten im Vergleich zum Wildtyp (Peter *et al.*, 1998a). Zudem führte die Kürzung der N-terminalen Domäne von BetP, das heterolog in *E. coli* (30 % negative geladenen Lipide) exprimiert wurde, zu einem Verlust der osmoregulatorischen Eigenschaften (Ott *et al.*, 2008). Demzufolge wurde den umgebenden Lipiden eine besondere Rolle zugesprochen. Im Rahmen dieser Arbeit wurde die regulatorische Rolle der negativ geladenen *Cluster* in der N-terminalen Domäne untersucht. Die Alanin-Substitutionen der drei *Cluster*, E13/D14, E24/E25 und E44/E45/E46 sowie Sequenz-basierte sekundäre Struktur-Vorhersagen ergaben geringe Veränderungen in der α-helikalen Faltung des N-terminalen Teils im Bereich des zweiten und dritten *Clusters*. Funktionelle Analysen der Substitutionsmutanten identifizierten das *Cluster* E24/E25 als unerlässlich für die Osmoregulation im heterologen Wirt *E. coli*. Da in vorhergegangenen Studien große Mengen an negative geladenen Lipiden die Abwesenheit der N-terminalen Domäne kompensierten (Ott *et al.*, 2008) wurde angenommen, dass die N-terminale Domäne und die Lipide um die gleiche Interaktionsstelle konkurrieren. Aufgrund der Position der C-terminalen Domäne in der Kristallstruktur (Ressl *et*

al., 2009) sowohl als auch deren hauptsächlich positiven Ladung und der Lipidmembran-Bindekapazität (Ott *et al.*, 2008), wurde die C-terminale Domäne als Interaktionspartner in Betracht gezogen. Um dies zu prüfen wurden Disulfid-Crosslinking-Studien zwischen dem N-terminalen *Cluster* und entsprechender positiv geladener Residuen innerhalb der C-terminalen Domäne mittels Cystein-Substitutionen durchgeführt. Trimere Oligomerisierungszustände in nicht-reduzierten SDS-PAGE deuteten auf eine Interaktion zwischen den N- und C-terminalen Domänen von benachbarten Protomeren. Zusätzlich wurde die Aktivierung des Transports von in *E. coli* Liposomen rekonstituierten N- und sowohl C-terminal substituierten Mutanten in BetP durch Cross-linking moduliert. Basierend auf den Daten dieser Arbeit, konnte ein Regulationsmechanismus vorgeschlagen werden, in dem die C-terminale Domäne zwischen einer Interaktion mit der N-terminalen Domäne des eigenen Protomers zur N-terminalen Domäne des benachbarten Protomers wechselt.

BetP liegt als stabiles Trimer innerhalb der Membran und in Detergenz vor (Ressl *et al.*, 2009; Ziegler *et al.*, 2004). Artifizielle Monomerisierung von BetP wies darauf hin, dass das Trimer die Grundvoraussetzung für die Regulation sei (Perez *et al.*, 2011a). Darüber hinaus wurde in strukturellen Daten aus der 2D- und 3D-Kristallisation gezeigt, dass BetP konformativ asymmetrische Trimere bildet, in dem jedes Protomer eine andere Konformation annimmt (Perez *et al.*, 2012; Tsai *et al.*, 2011). Die strukturelle Asymmetrie in Kombination mit zusätzlichen inter-protomeren Interaktionen deutet auf einen Kommunikation zwischen den Protomeren eines Trimers hin. Weitere gelöste Kristallstrukturen von entweder symmetrischen als auch asymmetrischen Trimeren lieferten sequenzielle kristallographische Schnappschüsse von unterschiedlichen Transporter-zuständen, die als verschiedene Konformationen des *alternating access mechanismus* interpretiert wurden (Perez *et al.*, 2014; Perez *et al.*, 2012; Ressl *et al.*, 2009). Laut Jardetzky (1966) beschreibt der *alternating acces cycle* eine Abfolge von Konformationsänderungen, die benötigt werden, um die Substrat-Bindestelle abwechselnd zu beiden Seiten der Membran zu öffnen, um die Bindung und die Freisetzung des Substrates zu ermöglichen. Um weitere Einsichten in den funktionellen Zustand des BetP Trimers zu liefern, wurden Konformationsänderung innerhalb des Trimers mittels PELDOR (*pulsed electron-*

electron double resonance) in Kombination mit *site-directed spin labeling* in einer nativeren Umgebung als in 3D-Kristallen durchgeführt. Demnach wurden intra-trimere Distanzen zwischen Spinlabeln in verschiedenen Bedingungen gemessen, um Betain- und K^+-abhängige Konformationsänderungen aufzuklären. Die erste Labelingstrategie von BetP als Drei-Spin-System, erwies sich als ungeeignet um die Asymmetrie von BetP zu untersuchen, da sich die sehr langen intra-trimeren Distanzen an der Höchstgrenze des Standard 4-Puls PELDOR befanden. Daher wurden Optimierungen der Methode in der Gruppe von Prof. Dr. Prisner (Goethe Universität, Frankfurt) durchgeführt, um die Distanzlimitierung zu überwinden.
Die Kristallstrukturen deuteten auf einen Transportmechanismus von BetP bestehend aus einer Mischung von *rigid body* Bewegungen und *individual flexing* von symmetrie-bezogenen Helices (Perez *et al.*, 2012). Im Vergleich zu anderen Transporten, die eine LeuT-ähnliche Faltung aufweisen, wies BetP eine grundlegend geringer ausgeprägte konformationelle Änderung auf. Demzufolge wurde eine alternative Labelingstrategie entwickelt, um die in den Kristallstrukturen beobachteten kurzen Distanzbewegungen von maximal 6 Å zu verfolgen. Aufgrund dessen wurden kürzere intra-protomere Distanzen zwischen zwei Spinlabeln innerhalb eines Protomers gemessen, das in einem innovativem Multi-Spin-System von sechs Spinlabeln in einem Trimer resultierte. Die Ergebnisse dieses Teils der Arbeit zeigten Verschiebungen in der Abstandsverteilung, die Konformationsänderungen widerspiegelten. In den Messungen auf der cytoplasmatischen Seite von BetP konnten Konformationsänderungen beobachtet werden, die mit der *gating-like* Bewegung von TM12 zur Schließung des Substratweges nach der Substratbindung übereinstimmen (Perez *et al.*, 2012). Für die gegenüberliegende Seite des Proteins, konnten Distanzverschiebungen detektiert werden, die der *hinge-like* Bewegung von TM3 zur Öffnung des cytoplasmatischen Substratweges (Perez *et al.*, 2012), entsprechen. Bemerkenswerterweise blieben die Distanz-verschiebungen in Transport-defizienten Mutanten aus, das die Relevanz der Distanzveränderungen in den Messungen betont. Überdies konnten vergleichbare Muster der Abstandsverteilungen für spin-gelabeltes BetP, das in Liposomen rekonstituiert vorlag, beobachtet werden, wobei die cytoplasmatischen Varianten eine Verschiebung zu längeren Distanzen zeigten. Die Konformationsänderungen, von denen in dieser Arbeit berichtet wird, repräsentieren ein dynamischeres Bild

von BetP verglichen zu den Kristallstrukturen. Jedoch konnte gezeigt werden, dass die Konformationsänderungen, die bisher nur in Kristallstrukturen von BetP beobachtet wurden, mit den durch PELDOR gemessenen Distanzen, übereinstimmen.

Basierend auf der langjährigen Erfahrung unserer Gruppe im Bezug zu dem BCCT BetP, war ein weiterer Aspekt dieser Arbeit die Charakterisierung neuer BCC-Transporter. Aufgrund der hohen klinischen Relevanz und der stetig steigenden Multi-Antibiotika-Resistenz von pathogenen *Acinetobacter* Spezien, wurde der Modelorganismus *Acinetobacter baylyi* ADP1 als Ziel gewählt. Die Fähigkeit von *Acinetobacter* jede Oberfläche zu kolonisieren und dabei Trockenheit und Feuchtigkeit zu überleben (Doughari *et al.*, 2011; Vallenet *et al.*, 2008), deutete auf einen starken Osmostress-Mechanismus, welcher möglicherweise zur Virulenz dieses Bakteriums beiträgt. In der Tat wurden bei der Prüfung des Genoms von *A. baylyi* potentielle BCC-Transporter entdeckt. Vorangegangene Studien zeigten, dass erste Aussagen über die Substrat-Spezifizität schon anhand der Sequenz des sogenannten Glycin-reichen Motives, das für Transporter der gleichen Substrat-Spezifizität konserviert vorliegt, gemacht werden können (Perez *et al.*, 2011b; Ziegler *et al.*, 2010). Vorläufige funktionelle Studien des Transporters BetT2 mit dem Glycin-Motiv Ala-Gly-Ile-Gly-Ile-Asp bestätigten die Einstufung als Proton-gekoppelten Cholin-Symporter, der dem hyperosmotischen Stress entgegen wirkt. Im Vergleich zu BetT2, konnte ein Alanin anstelle des Aspartats am Ende des Glycin-Motives des anderen BCCT BetT1 von *A. baylyi* gefunden werden. Unsere funktionellen Analysen identifizierten BetT1 als Transporter mit hoher Affinität, jedoch geringer Kapazität, der sehr wahrscheinlich eher in der Cholin-Aufnahme für den Katabolismus als zur osmotischen Stress-Antwort beteiligt ist. Des Weiteren zeigt BetT1 alle Charakteristika eines außergewöhnlichen Uniporters in der BCCT-Familie, der die positive Ladung des Cholins zu Konformationsänderungen ausnutzt. Erste 3D-Kristallisationsversuche erzielten Kristalle mit einer Beugung bis 8 Å. Die Kristallisation muss weiter optimiert werden um strukturelle Informationen zur Aufklärung des molekularen Mechanismus des Cholin-Uniports, welcher ausschließlich durch das Membranpotential angetrieben wird, zu erhalten. In der Zwischenzeit wurde BetP von *C. glutamicum* als Modelsystem für BetT1 verwendet. Die Umwandlung von BetP in

einen Transporter mit einer erweiterten Substrat-Spezifität war in vorherigen Versuchen erfolgreich und wird durch etablierte Aufreinigungs- und Kristallisationsprotokolle begünstigt (Gärtner, 2014; Perez *et al.*, 2011b). Hierzu wurde das Glycin-Motiv von BetP, Ala-Gly-Met-Gly-Ile-Gly, hinsichtlich der BetT1 Sequenz mutiert und die Fähigkeit Cholin zu transportieren wurde überprüft, um als alternatives Kristallisationsziel in der Zukunft zu dienen. Die Ergebnisse dieser Arbeit in Kollaboration mit der Gruppe von Prof. Dr. Averhoff (Goethe Universität, Frankfurt) gewährten Aufschluss in die physiologische Rolle und der Regulation von pathogen-relevanten Cholin-Transport in *Acinetobacter*.

Abstract

Transport processes across the membrane are essential to ensure survival of every living cell. Therefore, the exchange of membrane impermeable molecules is mediated by specific transport proteins, which are embedded in the lipid bilayer. One important class comprises secondary active transporters, which couple very efficiently the uphill transport of the main substrate against its concentration gradient to the downhill transport of an additional substrate. These transporters are widely distributed among all kingdoms of life and accomplish many crucial functions. One function is to counteract the deleterious effect of hyperosmotic stress in bacteria. Several members of the BCCT (betaine-choline-carnitine-transport) family of secondary transporters mediate osmostress protection by the accumulation of the compatible solute betaine or its precursor choline (Lamark *et al.*, 1991; Peter *et al.*, 1996; Ziegler *et al.*, 2010). Besides osmo-dependent sodium or proton-coupled symporters, the BCCT family includes few rare representatives of osmo-independent transporters such as the substrate:product antiporter CaiT from *E. coli* (Jung *et al.*, 2002; Ziegler *et al.*, 2010).

The best-characterized member of the BCCT family is the sodium-coupled betaine transporter BetP from *Corynebacterium glutamicum*. BetP together with the ABC-transporter OpuA and the H^+-solute symporter ProP, became a paradigm for osmoregulated osmolyte transport. Although, all three transporters were extensively studied, the general mechanism of osmoregulation is still far from being understood. Thus, one task of this thesis was to elucidate further the regulatory properties of BetP.

BetP is tightly regulated by osmotic stress and is able to increase its basal betaine uptake activity dramatically upon elevated osmolalities within one second (Peter *et al.*, 1998a). The osmotic stress is sensed by BetP via two stimuli, one is the increase of the internal K^+ concentration above a threshold of 220 mM (Rübenhagen *et al.*, 2001), the second is related to a change in the physical state of the membrane (Maximov *et al.*, 2014). So far, several solved crystal structures in combination with functional and computational analysis provided insights into the coupling mechanism of betaine and its co-substrate sodium (Khafizov *et al.*,

2012; Perez *et al.*, 2012). Despite the wealth of data, the precise regulatory mechanism of trimeric BetP is still unclear.

The contribution of the N- and C-terminal domain to osmoregulatory properties of BetP was already extensively studied. The mostly positively charged C-terminal domain was identified as key player in regulation by sensing the internal K^+ concentration (Schiller *et al.*, 2004). In contrast, the functional role of the unique negatively charged N-terminal domain is unknown. The solved structures could not provide any information, because only crystal structures of an N-terminally truncated BetP variant (BetPΔ29EEE44/45/46AAA) exist (Ressl *et al.*, 2009). Functional analysis of N-terminally truncated BetP mutants in *C. glutamicum,* which comprise only anionic lipids in the membrane, showed to be less osmo-sensitive by shifting the activation optimum to higher osmolalities when compared to the wild type (Peter *et al.*, 1998a). Moreover, truncation of the N-terminal domain of BetP heterologously expressed in *E. coli* (30 % negatively charged lipids) lead to the lost of the osmoregulatory properties (Ott *et al.*, 2008). Thus, an important role for the surrounding lipids in BetP was assumed. Because the functional impact of the N-terminal domain is still unclear, the regulatory role of the negatively charged clusters in the N-terminal domain was investigated in this part of the thesis. Alanine substitution of three clusters, namely E13/D14, E24/E25 and E44/E45/E46 as well as sequence based secondary structure predictions revealed slight changes in the α-helical fold of the N-terminal parts around the second and third cluster. Functional analysis of the substitution mutants evaluated the role of the clusters and identified the cluster E24/E25 to be crucial for osmoregulation in the heterologous host *E. coli*.

Because high amounts of negatively charged lipids seemed to compensate for the absence of the N-terminal domain in previous studies (Ott *et al.*, 2008), it was assumed that the N-terminal domain and lipids might compete for the same interaction site. Due to the orientation of the C-terminal extension in the crystal structure (Ressl *et al.*, 2009), the positive charge and its lipid membrane binding capacity (Ott *et al.*, 2008), the C-terminal domain was considered as a potential interaction partner. To investigate this, disulfide cross-linking studies between the N-terminal cluster and appropriate positively charged residues of the C-terminal domain were performed by cysteine substitution. Trimeric states in non-reducing

SDS-PAGE analysis indicated interactions between the N- and C-terminal domains of adjacent protomers. In addition, transport activation for the N- and C-terminal cysteine substituted mutants in BetP reconstituted in *E. coli* polar lipid liposomes was modulated by cross-linking. Based on the data of this work, a regulation mechanism can be proposed in which the C-terminal domain switches between interactions of the N-terminal domain of its own protomer to the N-terminal domain of an adjacent protomer.

BetP is a stable trimer in membranes and in detergent (Ressl *et al.*, 2009; Ziegler *et al.*, 2004). Artificial monomerization of BetP suggested that the trimer is the prerequisite for regulation (Perez *et al.*, 2011a). Moreover, in structural data obtained by 2D and 3D crystallization, BetP forms conformational asymmetric trimers in which each protomer adopts a distinct conformation (Perez *et al.*, 2012; Tsai *et al.*, 2011). This structural asymmetry in combination with additional interprotomeric interactions suggests a crosstalk between the protomers within one trimer. Additional solved crystal structures either of symmetric or asymmetric trimers provided sequential crystallographic snapshots of different transporter states, which were interpreted as different conformations of the alternating access cycle (Perez *et al.*, 2014; Perez *et al.*, 2012; Ressl *et al.*, 2009). According to Jardetzky (1966), the alternating access mechanism is described by a series of conformational changes, which are required to alternately open the substrate-binding site to either sides of the membrane to enable binding and release of the substrate.

In order to provide further insights into the functional state of trimeric BetP, conformational changes within the trimer were probed by PELDOR (pulsed electron-electron double resonance) in combination with site-directed spin labeling in a more native environment than provided within a 3D crystal. Thus, intratrimeric distances between spin labeled positions were measured at different conditions to elucidate betaine and K^+ dependent conformational changes. The first label strategy of BetP including a three-spin system turned out to be inadequate to address the asymmetry of BetP due to very long intratrimeric distances at the limit of standard 4-pulse PELDOR. Consequently, optimizations of the method to overcome the distance limitation were performed by the group of Prof. Dr. Prisner (Goethe University, Frankfurt).

Crystal structures suggest the transport mechanism of BetP as a hybrid of rigid body movements and individual flexing of symmetry-related helices (Perez *et al.*, 2012; Tsai *et al.*, 2011). In comparison to the structures of other LeuT-fold transporters, BetP has substantially less pronounced conformational re-arrangements. Therefore, an alternative labeling strategy was designed to trap this short distance movements of maximum ~6 Å observed in the crystal structures. Subsequently, shorter intraprotomeric distances were measured between two spin labeled positions in each protomer that result in an innovative multi-spin system of six spin labels in a trimer. The results of this part of the thesis indicated shifts in distance distributions reflecting conformational changes at the periplasmic as well as cytoplasmic side of BetP. The measurements for the periplasmic side of BetP are consistent with the gating-like movement of TM12, which is required to close the periplasmic substrate pathway after substrate binding (Perez *et al.*, 2012). On the opposite side of the protein, distance shifts can be related to the cytoplasmic hinge-like movement of TM3, which is needed for the release of the substrate (Perez *et al.*, 2012). Remarkably, betaine transport impaired mutants did not show this distance shifts upon activation in detergent, which emphasizes the relevance of the distance changes observed in these measurements. Moreover, comparable patterns of distance distributions were even observed for spin labeled BetP variants reconstituted into liposomes, although cytoplasmic variants showed in general a shift to longer distances. The conformational changes reported in this work present a more dynamic picture of BetP compared to the diverse crystal structures. Even thought the protein was not trapped due crystal contacts, the application of PELDOR additionally verified the conformational rearrangements, which were captured in the diverse crystal structures of BetP.

Based on the longstanding experience in our group on the BCCT BetP, another aspect of this thesis was to characterize novel BCC transporters. Due to the high clinical relevance and increasing multidrug resistance of pathogenic *Acinetobacter* species, the model organism *Acinetobacter baylyi* ADP1 was selected as target. The ability of *Acinetobacter* to colonize almost any surface persisting desiccation and moisture (Doughari *et al.*, 2011; Vallenet *et al.*, 2008) points towards a strong osmostress mechanism, which might contribute to the

virulence of these bacteria. Indeed, the inspection of the genome of *A. baylyi* revealed several potential BCC transporters. Preceding studies of BCCTs showed, that first substrate specificity predictions could be performed already on the basis of the sequence of the so-called glycine motif, which is highly conserved for transporters with the same substrate specificity (Perez *et al.*, 2011b; Ziegler *et al.*, 2010). Preliminary functional studies of the transporter BetT2 with the glycine motif Ala-Gly-Ile-Gly-Ile-Asp confirmed the assignment as proton-coupled choline symporter, responsible to counteract hyperosmotic stress. In contrast to BetT2, an exceptional unpolar alanine is found instead of the aspartate at the end of the glycine motif for the other *A. baylyi* BCCT BetT1. Our functional analysis of BetT1 identified a high affinity, but low capacity choline transporter most likely involved in choline uptake for catabolism than in osmotic stress response. Furthermore, BetT1 seems to show all characteristics of an exceptional uniporter in the BCCT family exploiting the positive charge of choline to trigger conformational changes. Initial 3D crystallization trials yielded crystals diffracting to 8 Å. Crystallization has to be optimized to obtain any structural information, which could provide insights into the molecular mechanism of choline uniport driven entirely by the membrane potential. Meanwhile, the model system BetP from *C. glutamicum* was used as a blue print for BetT1. Transforming BetP into a transporter with different substrate specificity was already successful in former approaches, which benefited from the well-established purification and crystallization protocol (Gärtner, 2014; Perez *et al.*, 2011b). Therefore, the glycine motif of BetP Ala-Gly-Met-Gly-Ile-Gly was mutated in respect to the sequence of BetT1 and examined for the ability to transport choline in order to serve as alternative crystallization target in the future. The results of this work in collaboration with the group of Prof. Dr. Averhoff (Goethe University, Frankfurt) helped to shed light into the physiological role and regulation of pathogen-relevant choline transport in *Acinetobacter*.

1 Introduction

1.1 Secondary active transporters

Living cells are surrounded by a lipid bilayer, the membrane, which serves as a physical barrier. Gas, hydrophobic as well as small polar molecules like water can diffuse though the lipid bilayer, while larger polar or charged molecules have to be transported across the membrane. The exchange of biological molecules plays an important role in a diversity of vital physiological processes like signal transduction, metabolism, maintenance of cellular homeostasis, drug extrusion and much more. One key element of life is the transport of molecules, namely amino acids, sugars, ions, lipids etc., which is facilitated by membrane-spanning proteins categorized mainly in channels and transporters. Whereas channels in the open state act as pores allowing the molecules to pass the membrane along the concentration gradient, transporters translocate their substrates through a series of conformational changes. Consequently, the turnover rate for a transporter with 10^1 to 10^3 substrate molecules per second is lower than a channel, which has not to undergo prominent conformational changes to reach up to 10^8 molecules per second (Giacomini and Sugiyama, 2011). Membrane transporters are classified further. Transporters, which facilitate the movement of one substrate along the concentration gradient, are called uniporters (Figure 1.1). Transporters translocating molecules against their gradient can be divided into primary and secondary active transporters. While primary transporters drive their transport by energy from chemical reactions like ATP hydrolysis, secondary active transporters couple the uphill transport of one substrate to the downhill transport of a second substrate, commonly ions like for example H^+ or Na^+. The driving forces involved in active ion-coupled substrate transport are named after the movement of the respective ions, e.g., proton motive force (pmf) and sodium motif force (smf), respectively. Different substrates can be co-transported in symporters or counter-transported in antiporters (Figure 1.1). It was shown that the early description of the basic principle of transport by Jardetzky (Jardetzky, 1966), in particular known as alternating access model, is valid for secondary active transporters (Forrest *et al.*, 2011).

Secondary transporters are widely distributed in all kingdoms of life and a comprehensive classification system is accessible in the Transporter Classification Database (http://www.tcdb.org) (Saier *et al.*, 2009). Because secondary active transporters can be found in almost every living cell and their crucial involvement in essential life processes, these transporters are subject of diverse biochemical, biophysical and theoretical approaches.

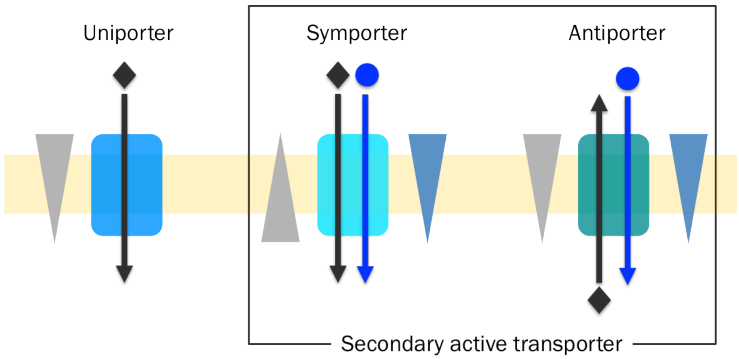

Figure 1.1: Three types of transporters.
Uniporters translocate a single molecule down its concentration gradient. Secondary active transporters, namely symporters and antiporters, couple the uphill transport of one substrate to the downhill transport of a second molecule, either in the same or opposite direction, respectively.

1.2 Spectroscopic applications on secondary active transporters

The mechanistic description of biological function on a molecular level is one main topic in biochemical and biophysical research. In the past, many techniques contributed to the membrane protein structure determination. The availability of structures obtained by 2D and 3D crystallization has improved the mechanistic understanding of secondary active transport. However, the challenging crystallization process of especially membrane proteins is a limiting factor. Furthermore, also high-resolution structures give only static pictures of a protein in non-native conditions trapped by crystal contacts. Consequently, the dynamic process of transport cannot be understood solely by crystallographic snapshots (Forrest *et al.*, 2011). Thus, spectroscopic methods gained importance to investigate the molecular function of secondary active transporters (Figure 1.2). Nuclear magnetic resonance (NMR) can be used to study the membrane protein structure, protein dynamics, substrate binding and interaction between different

proteins and other interacting partners (Hellmich and Glaubitz, 2009). Although the application of NMR to solve protein structures is restricted to proteins with a size below 50 kDa, it is a very suitable tool to investigate dynamics when the structure is already known. NMR requires large amounts of the sample in a µM to mM concentration range (Hellmich and Glaubitz, 2009). In contrast, Fluorescence resonance energy transfer (FRET) (Förster, 1948) is a method that does not require excessive amounts of proteins and overcomes the size restriction of proteins. Interaction between different partners as well as dynamical and structural information can be gained by measuring distances between corresponding donor and acceptor chromophores attached to the protein (Truong and Ikura, 2001). As complementary method, pulsed EPR (electron paramagnetic resonance) spectroscopy in combination with site-directed spin labeling has emerged as powerful tool to elucidate the structure as well as structural changes of transporters in more native environment. Beside various diverse applications of EPR, PELDOR (pulsed electron-electron double resonance or double electron-electron resonance (DEER)) (Milov *et al.*, 1984) is used to measure inter- and intramolecular distances between spin labels, which were introduced into the protein of interest.

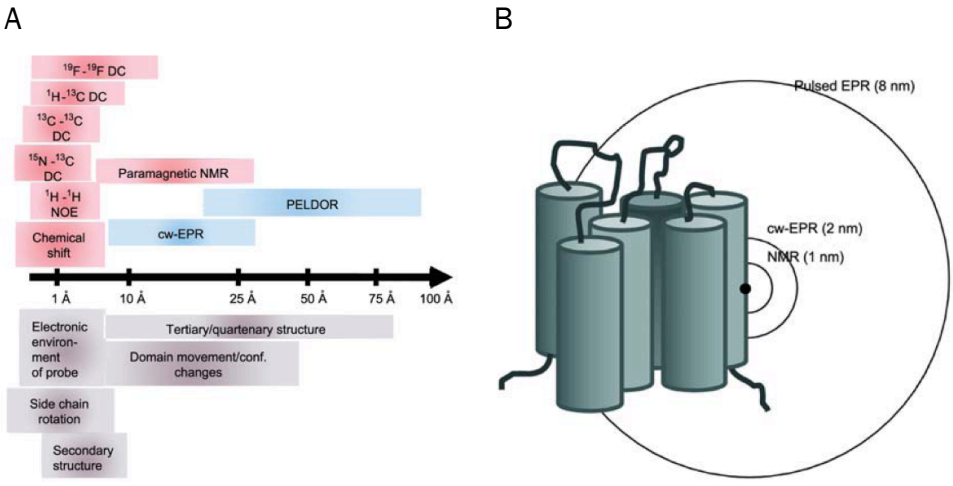

Figure 1.2: Comparison of spectroscopic methods.
A) The distance scale displays with which method, which range of structural information can be obtained. B) Schematic representation of a protein and the corresponding distances, which can be covered by NMR and EPR methods. The position of the spin label (paramagnetic center for EPR, NMR-active nucleus for NMR) is depicted as black sphere (Hellmich and Glaubitz, 2009).

PELDOR was already applied successfully for secondary transporters like LacY from *E. coli.* LacY belongs to the major facilitator superfamily (MFS) and is the most extensively studied secondary active transporter. The X-ray structure of the monomeric galactoside/H^+ symporter was solved in the inward open conformation (Abramson *et al.*, 2003). PELDOR was used to determine interspin distances between nitroxide-labeled paired Cys-replacements at the cytoplasmic as well as periplasmic side of the transporter for the WT and the conformationally restricted variant C154G in the presence of galactosidic and non-galactosidic sugars (Smirnova *et al.*, 2007). Upon binding of the galactosidic sugar to the LacY WT protein, the distances at the cytoplasmic side decreased in the range of 4 – 21 Å indicating the closure of the cytoplasmic site. Simultaneously, the interspin distances between the periplasmic labeled double Cys pairs increased about 4 - 14 Å implying the opening of the periplasmic side of WT LacY. Interestingly, periplasmic conformational changes were almost not observed for LacY C154G. Moreover, the obtained distances for the WT were in good agreement with distances, which were proposed for a LacY model in the outward open conformation. Further PELDOR experiments confirmed an apo-intermediate state of LacY, a modeled conformer with the sugar-binding site inaccessible of both sides of the transporter, devoid of sugar (Figure 1.3) (Madej *et al.*, 2012). Also here the model was evaluated by the comparison of experimental distances between the spin labeled double Cys variants with modeled interhelical distances. Incidentally, data indicated also a second fully occluded conformation of LacY, in contrast with bound sugar. Application of PELDOR in conjunction with molecular modeling based on the X-ray structure provided strong evidence for the alternating access cycle for LacY (Madej *et al.*, 2012).

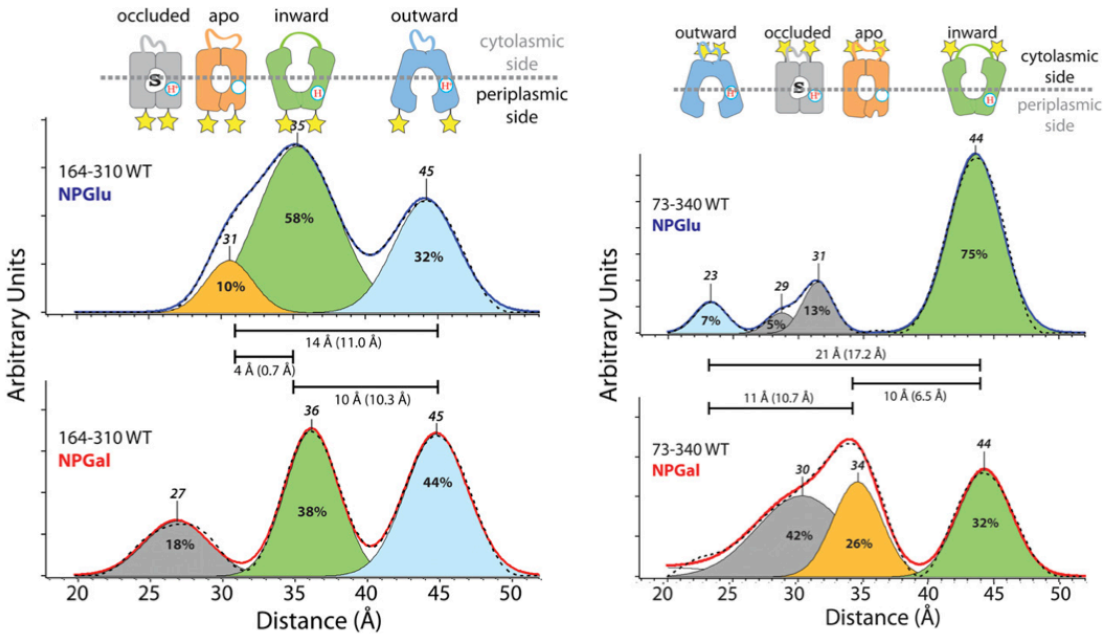

Figure 1.3: PELDOR measurements of LacY.
Interspin distance distribution detected for nitroxide-labeled periplasmic Cys pair 164/310 (left) and cytoplasmic Cys pair 73/340 (right) of LacY. Distance distributions were obtained by Tikhonov regularization of dipolar spectra in absence and in presence of bound sugar, NPGlu (blue solid line) and NPGal (red solid line). Relative distributions of conformational populations were obtained by multi-Gaussian deconvolution as described previously (Smirnova *et al.*, 2007). The interspin distance is indicated on top of the Gaussian peaks and attributed to the corresponding conformation. The relative area of the Gaussian peaks in % is representing the fraction of each conformer population within the multi-Gaussian fit (dashed black line). The horizontal bars represent the distance differences between the peak centers in different conformers. The Cα – Cα distance differences between the different conformers in the structure models are indicated in parenthesis (Madej *et al.*, 2012).

In another more elaborated case, PELDOR was applied to probe the structure and conformational composition of the sodium-coupled aspartate transporter Glt_{Ph} from *Pyrococcus horikoshii* (Georgieva *et al.*, 2013; Hänelt *et al.*, 2013). Glt_{Ph} is a bacterial homolog of the mammalian glutamate transporters, also known as excitatory amino acid transporters (EAATs), involved in synaptic transmission. The crystal structure of homotrimeric Glt_{Ph} was solved, in which each protomer consists of a central trimerization domain mediating intersubunit contacts and a peripheral transporter domain (Yernool *et al.*, 2004). In structures of conformationally symmetric trimers, all protomers adopt either the outward facing conformation or the inward facing conformation obtained by cross-linking of a conformationally constrained mutant (Reyes *et al.*, 2009; Yernool *et al.*,

2004). Additionally, the structure of an asymmetric trimer was solved with two protomers in the inward facing state and one protomer in an intermediate conformation (Verdon and Boudker, 2012). According to these structures, during transport a conformational change involving a large-scale movement of the transport domain across the membrane to expose the binding site alternatingly to both sides of the membrane cycle was suggested. The determination of interspin distances by PELDOR confirmed the rigid structure of the trimerization domain of Glt_{Ph}. Furthermore, a broad distance distribution was identified between the spin labels in the transporter domains, which sample multiple conformations (Georgieva *et al.*, 2013; Hänelt *et al.*, 2013). Outward and inward facing states are populated independently from each other, although the binding of Na^+ ions and aspartate shifted the distribution mainly to longer distances for Cys-replacements at the extracellular side and to shorter one at the intracellular side, corresponding to the outward facing conformation (Figure 1.4) (Georgieva *et al.*, 2013). In general, the broad distributions between nitroxide-labeled protein in detergent and reconstituted into proteoliposomes varied only modestly confirming the conformational heterogeneity. But some exceptions in which unique conformations were more stabilized than others were observed (Georgieva *et al.*, 2013; Hänelt *et al.*, 2013).

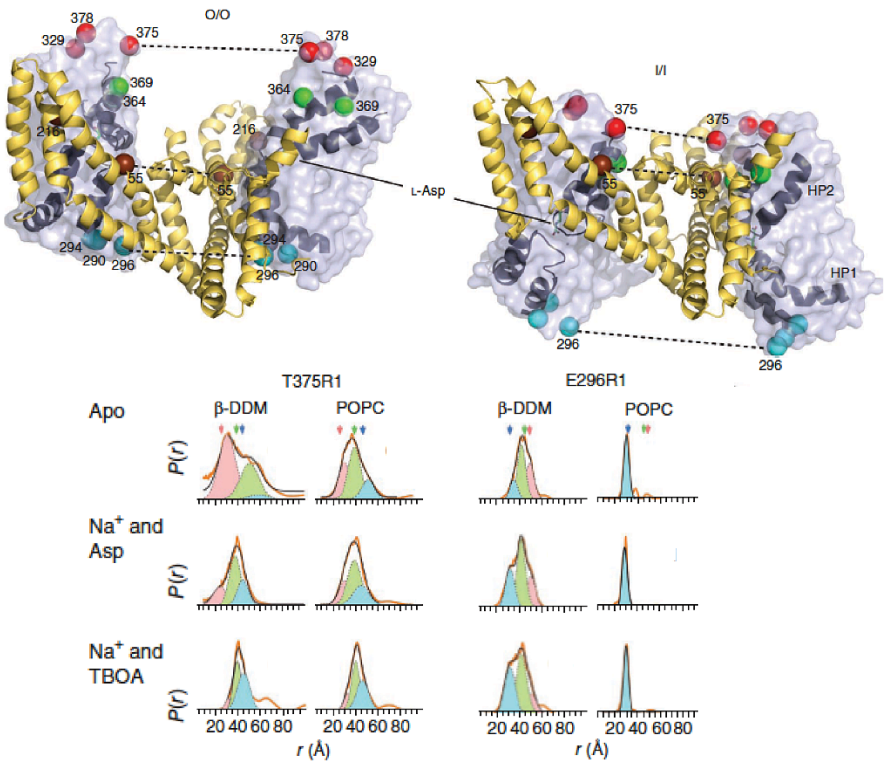

Figure 1.4: PELDOR measurements of Glt_{Ph}.
Pairs of spin labels in Glt_{Ph} in the outward facing (O/O) and the inward facing (I/I) state (top). The trimerization and transport domains are shown as cartoon (yellow) and transparent surface (blue), respectively. The third protomer is removed for clarity. The Cβ-atoms of the native residues mutated to cysteines are depicted as spheres. Distance distributions in DDM and POPC bilayers measured for T375R1 and E296R1 in the transport domain at the extracellular and intracellular side, respectively. The experimental data (orange) and the envelope of the fitted Gaussians (black) are shown. The three Gaussians are representing distances from the symmetric outward facing (blue), mixed (green) and symmetric inward facing (red). Arrows mark the Cβ – Cβ distances expected from the crystal structures with the similar color code for the corresponding conformation (adapted from Georgieva *et al*., 2013).

These were just two examples of secondary active transporters among many other transporters, which were already studied by PELDOR in combination with site-directed spin labeling. The determination of interspin distances turned out to be useful to evaluate given crystal structures and models as well as to gain insights into the conformational dynamics of membrane proteins in more native environment.

1.3 Secondary active transporters of the BCCT family

The members of the prokaryotic betaine-choline-carnitine-transporter (BCCT) family are secondary active transporters, which serve as uptake systems for substrates with mainly quaternary ammonium groups [R – $N^+(CH_3)_3$] as common feature. As the name of the family already implies, the main substrates are betaine, choline and carnitine although in the last years additional substrates were found. As new substrates are counting compounds with fully methylated sulphonium headgroups like dimethylsulphoniopropionate (DMSP) and dimethylsulphonioacetate (DMSA) as well as ectoine and hydroxyectoine, which do not fit to the general chemical scheme (Figure 1.5) (Ziegler *et al.*, 2010). However, the BCCT family was classified as a sub-family of the APC (amino acid polyamine cation) superfamily in the Transporter Classification (TC) system (www.tcdb.org/superfamily.php) (Saier *et al.*, 2009).

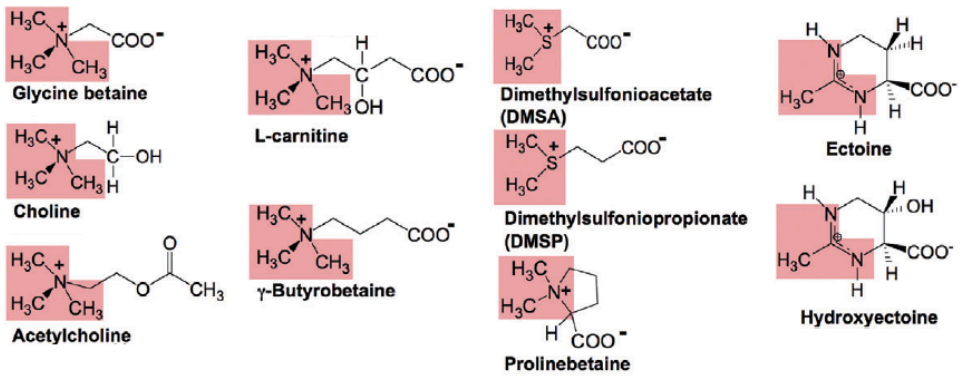

Figure 1.5: Substrates of the BCCT family.
The positively nitrogen or sulphur headgroups as well as the delocalized positive charge in ectoine and hydroxyectoine are highlighted in red (Ziegler *et al.*, 2010).

Among the functionally characterized members of the BCCT family, mainly proton- as well sodium-coupled symporters involved in the osmostress response of bacteria can be found (Ziegler *et al.*, 2010). According to this, the first characterized BCC transporter was discovered during genetic analysis of the osmoregulatory choline-glycine betaine pathway of *E. coli* (Lamark *et al.*, 1991). The gene for the BCC transporter BetT is organized together with the so-called *Bet* regulon including the genes coding for the Bet enzymes: BetI, BetB and BetA (Figure 1.6). BetT is a proton-driven high affinity uptake system for choline and involved to counteract hyperosmotic stress (Tondervik and Strom, 2007), although choline serves only as precursor for the compatible solute glycine betaine, also referred to as betaine. The oxidation of choline to betaine is performed by the corresponding Bet enzymes (Lamark *et al.*, 1991).

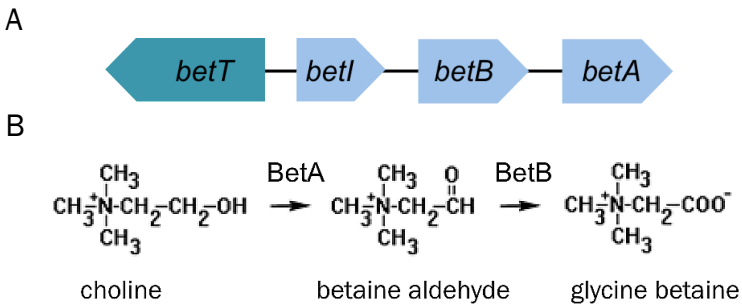

Figure 1.6: *Bet* regulon organization and choline oxidation.
A) The *bet* operon of *E. coli* consists of *betA* (choline dehydrogenase), *betB* (betaine aldehyde dehydrogenase), *betI* (repressor protein) and is located downstream of *betT* coding for a high affinity choline uptake system belonging to the BCCT family (Lamark *et al.*, 1991). B) Choline conversion. The enzymes catalyze the oxidation of choline over betaine aldehyde in two-step reaction to glycine betaine, which functions as compatible solute (Kempf and Bremer, 1998).

Also betaine specific BCC transporters involved in the osmostress response like OpuD from *Bacillus subtilis* (Kappes *et al.*, 1996) as well as BetP from *C. glutamicum* were identified. As an exception, CaiT from *E. coli* and *P. mirabilis* functions as substrate:product antiporter (Jung *et al.*, 2002) exchanging L-carnitine against the metabolized product γ-butyrobetaine under anaerobic growth conditions. Based on the trimethylammonium compounds serving as substrates for these transporters, a new transporter sub-family was proposed (Kappes *et al.*, 1996; Saier, 2000). Beside the substrate specificity for classification of a BCC transporter, the highly conserved signature motif consisting of tryptophans in TM8 is used as reference (Figure 1.7). For the most BCCTs, 12 TM helices are predicted with N- and C-termini facing the cytoplasm. The length and the amino acid sequence of the termini are among the members of the BCCT family highly variable. The contribution of these terminal extensions to the transport and osmoregulatory properties were first identified for BetP (Peter *et al.*, 1998a) and subsequently also for other BCCTs like BetT from *E. coli* (Tondervik and Strom, 2007). However, the involvement of BCCTs in response to chill as well as to in heat stress was demonstrated for EctT from *Virgibacillus pantothenticus* (Kuhlmann *et al.*, 2011) and OpuD from *B. subtilis* (Holtmann and Bremer, 2004), respectively.

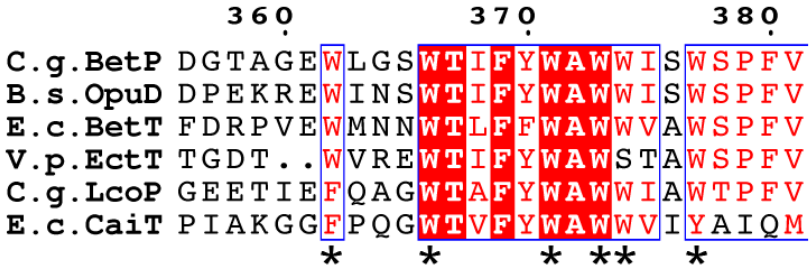

Figure 1.7: Sequence alignment of the tryptophan box of selected BCCT family members.

The amino acid sequence of BetP from *C. glutamicum* is aligned against OpuD from *B. subtilis*, BetT from *E. coli*, EctT from *V. pantothenticus*, LcoP from *C. glutamicum* and CaiT from *E. coli*. Numbering corresponds to BetP. The (*) marked residues are highly conserved in the BCCT family (Ziegler *et al.*, 2010).

Table 1.1: Functionally characterized members of the BCCT family

BCCT (Ref.)	Organism	Substrate	Driving force/ Direction	Total No. (aa)	N-term No. (aa)	C-term No. (aa)
BetP (Peter *et al.*, 1996)	*Corynebacterium glutamicum*	GB	smf/sym	595	58	50
OpuD (Kappes *et al.*, 1996)	*Bacillus subtilis*	GB	smf/sym	512	4	24
BetL (Sleator *et al.*, 1999)	*Listeria monocytogenes*	GB	smf/sym	507	3	20
BetH (Lu *et al.*, 2004)	*Halobacillus trueperi*	GB	smf/sym	505	3	18
BetM (Vermeulen and Kunte, 2004)	*Marinococcus halophilus*	GB	smf/sym	493	3	7
BetT3 (Sand *et al.*, 2011)	*Acinetobater baylyi*	GB	smf/sym	660	11*	164*
ButA (Baliarda *et al.*, 2003)	*Tetragenococcus halophila*	GB	smf/sym	539	34	15
OpuD (Naughton *et al.*, 2009)	*Vibrio cholera*	GB	smf/sym	539	34	15
BetT (Laloknam *et al.*, 2006)	*Aphanothece halophytica*	GB	smf/sym	564	36	38
BetP (Naughton *et al.*, 2009)	*Vibrio parahaemolyticus*	GB	smf/sym	523	41	14
BetU (Ly *et al.*, 2003)	*Escherichia coli*	GB	smf/sym	667	17	162
BetT (Fan *et al.*, 2003)	*Haemophilus influenzae*	Cho	sym	669	6*	174*
BetT3 (Malek *et al.*, 2011)	*Pseudomonas aeruginosa*	Cho	pmf/sym	661	12*	168*
BetT1 (Malek *et al.*, 2011)	*Pseudomonas aeruginosa*	Cho	pmf/sym	516	1*	28*
CudT (Rosenstein *et al.*, 1999)	*Staphylococcus xylosus*	Cho	pmf/sym	540	7	36
BetT (Lamark *et al.*, 1991)	*Escherichia coli*	Cho	pmf/sym	667	14	175
EctT (Kuhlmann *et al.*, 2011)	*Virgibacillus pantothenticus*	E/HE	smf/sym	501	7	14
EctM (Vermeulen and Kunte, 2004)	*Marinococcus halophilus*	E/HE	smf/sym	439	10	25
CaiT (Eichler *et al.*, 1994)	*Escherichia coli*	C/γ-BB	anti	504	10	5
PmCaiT (Schulze *et al.*, 2010)	*Proteus mirabilis*	C/γ-BB	anti	514	15	10
BetT (Chen and Beattie, 2008)	*Pseudomonas syringae*	Cho/Ac	pmf/sym	667	14	160
LcoP (Steger *et al.*, 2004)	*Corynebacterium glutamicum*	E/GB	smf/sym	630	43	96
BetS (Boscari *et al.*, 2002)	*Sinorhizobium meliloti*	GB/PB	smf/sym	706	52	167
DddT (Todd *et al.*, 2010)	*Psychrobacter sp.*	GB/DMSP	smf/sym	550	25	17
EctP (Weinand *et al.*, 2007)	*Corynebacterium glutamicum*	E/P/GB	smf/sym	615	21	102

Ac: acetylcholine; C: carnitine; Cho: choline; DMPS: dimethylsulphoniopropiate; E: ectoine; γ-BB: γ-butyrobetaine; GB: glycine betaine; HE: hydroxyectoine; P: proline; PB: proline betaine; smf: sodium motive force; pmf: proton motive force; sym: symport; anti: substrate:product antiport
*length of the N-terminal and C-terminal domains were predicted by TMHMM (www.cbs.dtu.dk/services/TMHMM-2.0/).

1.4 BetP: a paradigm for BCC transporters

The betaine permease BetP is one of three BCC transporters in *Corynebacterium glutamicum*, a bacterium used for industrial glutamate/lysine production. During fermentation as well as in its environment, the gram-positive soil bacterium *C. glutamicum* has to cope with diverse stress conditions like osmotic stress (Figure 1.8). Thus, the Na^+-coupled transporter BetP counteracts hyperosmotic stress by the accumulation of the compatible solute betaine. The uptake of compatible solutes is preferred over *de novo* synthesis due to energetic reasons (Oren, 1999). Compatible solutes can be accumulated to high concentrations without disturbing cellular metabolism and prevent the lost of water of the cell. The osmolyte betaine is excluded by the hydration shell of proteins promoting proper protein folding and can be found as osmoprotectant in all kingdoms (Arakawa and Timasheff, 1985; Brown, 1976; Kempf and Bremer, 1998). An adequate uptake of betaine is ensured by BetP, which the most characterized BCC transporter in terms of transport and regulation. Furthermore, BetP encompasses three functions:

1. Transport catalysis of exclusively betaine coupled to 2 Na^+ ions
2. Activity regulation by adapting the catalytic activity in dependence of the hyperosmotic stress
3. Sensing of the osmotic stress and further signal transduction

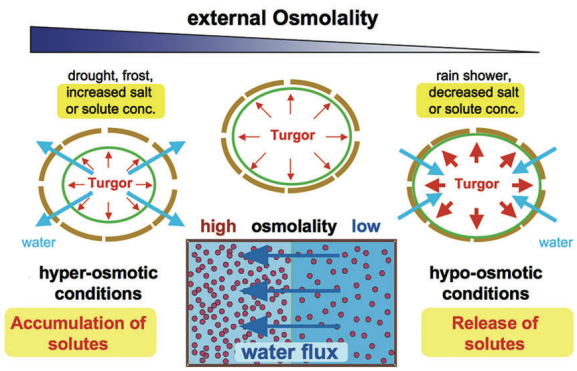

Figure 1.8: Types of osmotic stress.
Osmotically driven water fluxes the cytoplasmic membrane of a microbial cell. Upon hyperosmotic stress the efflux of water is counteracted by the accumulation of solutes, whereas upon hypoosmotic the water influx is counterbalanced by the release of solutes (Ziegler *et al.*, 2010).

1.4.1 Transport properties of BetP

A steady-state betaine accumulation of 4 x 10^6 was observed for the osmoregulated transporter BetP of *C. glutamicum* (Farwick *et al.*, 1995). Further kinetic analysis revealed a high affinity uptake system for betaine with an apparent K_m of 8.6 ± 0.4 µM and a V_{max} of 110 nmol/min*mg dw. Additionally, as driving force for the betaine uptake, the electrochemical potential of sodium with a stoichiometry of two ions to one betaine molecule was identified. For the co-substrate sodium an apparent K_m of 4.1 ± 0.4 mM was determined (Farwick *et al.*, 1995). Heterologous expression in *E. coli* MKH13 cells, which are deficient in transporters for compatible solutes and are unable to synthetize betaine from its precursor choline (Haardt *et al.*, 1995), revealed with an apparent K_m of 12.8 ± 1.2 µM for betaine and 6.1 ± 1.2 mM for sodium comparable kinetic parameters (Peter *et al.*, 1996). A chill stress activation of BetP as it was observed in *C. glutamicum* (Özcan *et al.*, 2005) is missing in *E. coli*.
The successful reconstitution of purified protein in *E. coli* polar liposomes demonstrated the osmosensing and osmoregulatory properties of BetP. In contrast, the betaine uptake is very fast in proteoliposomes with apparent K_m values of 3.6 ± 0.5 µM for betaine and 15.0 ± 1.5 mM for the co-substrate (Peter *et al.*, 1996). Moreover, it was reported that the maximum betaine uptake is achieved in the presence of a Na^+ gradient and electrical potential (Rübenhagen *et al.*, 2000).

1.4.2 Transport activity regulation of BetP

The activity of BetP mediating betaine uptake is regulated by the external osmolality. Until a threshold of an external osmolality of 0.3 osmol/kg (~150 mM NaCl), BetP has only a low activity in *C. glutamicum*. Increasing external osmolalities up-regulate the transporter, which is reaching the maximum activity

at approximately 1.25 osmol/kg (~625 mM NaCl). The transition from inactive to fully activated BetP occurs in less than 1 s by exposure to external high osmolalities (Peter *et al.*, 1998a). After stress compensation by betaine accumulation, the activity of BetP is reduced to prevent an excess of betaine within the cell (Morbach and Krämer, 2005). The ability to regulate the activity is retained for heterologously expressed BetP in *E. coli*, although the maximal activity is reached at lower osmolalities (Figure 1.9) (Peter *et al.*, 1996). The shift of the activation optimum in *E. coli* was attributed to a different membrane lipid composition and a higher cell turgor of the gram-positive bacterium *C. glutamicum* (Peter *et al.*, 1996; Rübenhagen *et al.*, 2000). Whereas the membrane of the *C. glutamicum* consists of negatively charged lipids, namely phosphatidylglycerol (PG), phosphatidylinositol (PI) and cardiolipin (CL) (Hoischen and Krämer, 1990; Özcan *et al.*, 2007; Schiller *et al.*, 2006), *E. coli* comprises beside PG and CL to ~70 % phosphatidylethanolamine (PE) (Prasad, 1996). BetP reconstituted into *E. coli* polar lipid liposomes shows activation profiles comparable to *E. coli* cells. Variation of the membrane composition of the proteoliposomes demonstrated that the major factor for regulation of BetP activity is the nature of the phospholipid surrounding (Rübenhagen *et al*., 2000). Furthermore, studies with reconstituted BetP indicated, that the increase of internal K^+ (or related cations such as Rb^+ or Cs^+) is one activation stimulus of BetP. The observed K^+ specificity argues for K^+-binding sites. However, the internal increase of the internal K^+ concentration upon hyperosmotic stress as first response for bacteria like *E. coli* (Dinnbier *et al.*, 1988) as well as *C. glutamicum* (Wolf *et al.*, 2003) supports strongly the contribution of K^+ for BetP activation (Morbach and Krämer, 2005). More precisely, the half-maximal activation of BetP is reached at a K^+ concentration threshold of 221 ± 23 mM (Rübenhagen *et al.*, 2001). Recent studies indicated that a second stimulus from the surrounding membrane, yet not identified, is required for full activation of BetP (Maximov *et al.*, 2014).

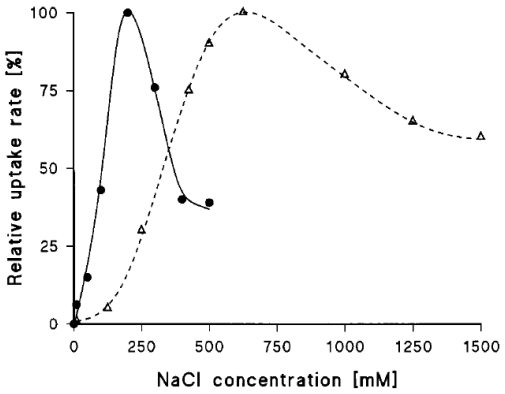

Figure 1.9: Betaine uptake by BetP in different host cells.
The relative betaine uptake rate is compared for BetP expressed either in *C. glutamicum* (Δ) or *E. coli* MKH13 (•) cells at different external NaCl concentrations (Peter *et al.*, 1996).

1.4.3 X-ray structure of BetP

The three-dimensional structure of BetP was solved at 3.35 Å for a N-terminally truncated and surface-engineered BetP mutant forming a homotrimer (Figure 1.10) (Ressl *et al.*, 2009). The trimeric nature of BetP was already confirmed for the solubilized protein in a detergent micelle by analytical centrifugation (Ziegler *et al.*, 2004), BN-PAGE (Tsai and Ziegler, 2005) as well as by first structural data obtained in 2D crystallization (Ziegler *et al.*, 2004). Each cylindrical shaped protomer consists of 12 TM helices of which 10 TMs form the transporter core and an additional helix h7 running parallel to the plane of the membrane. The substrate-binding site for betaine was found in in the center of the transporter core, halfway across the membrane, between TM4, TM8 and the unwound region of TM3 (Figure 1.11). The side chains of Trp189, Trp194, Tyr197 (TM4) and Trp374 (TM8) are involved in the coordination of the trimethylammonium group of betaine in an aromatic box by cation-π and Van der Waals interactions. Further crystal structures in different conformations displayed the contribution of Trp373 and Trp377 to the coordination of the substrate (Perez *et al.*, 2012). Later the existence of a potential second regulatory binding site at the periplasmic side of BetP was proposed. The formation was shown to be K^+ dependent, because cooperativity of betaine was observed under high K^+ concentrations (Ge *et al.*, 2011).

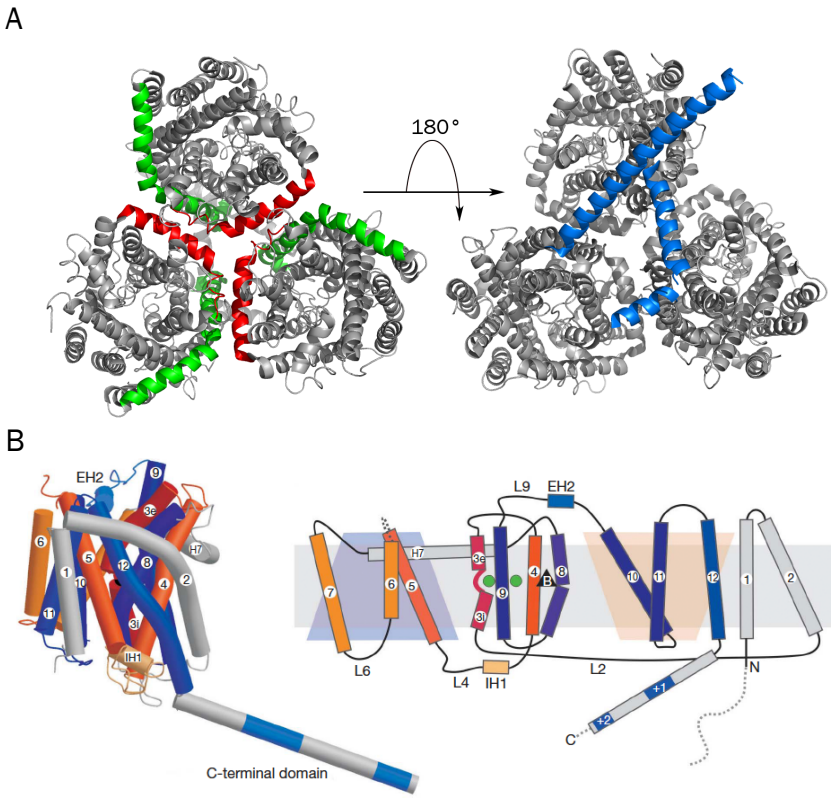

Figure 1.10: Structure of the N-terminally truncated, surface-engineered BetP mutant.
A) BetP trimer as seen from the periplasmic (left) and cytoplasmic (right) side of the membrane. The amphipathic helix 7 (h7) is colored in red, TM2 in green and the C-terminal domains in blue. B) Side view (left) and inverted repeat topology (right) of the BetP monomer. Helices are depicted as cylinders and repeat 1 (TM3-TM7) is colored orange, whereas the topologically related repeat 2 (TM8-TM12) is colored blue. Positively charged clusters are indicated within the C-terminal domain in blue. The substrate is represented as a black triangle and the sodium ions are green. Unresolved residues are indicated by dotted lines (adapted from Ressl *et al.*, 2009).

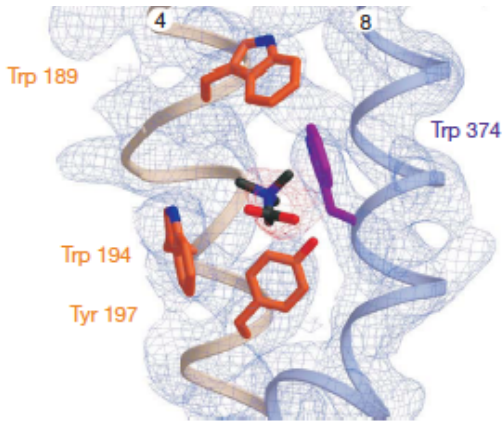

Figure 1.11: Betaine-binding site in BetP.
$2F_o - F_c$ map, contoured at 1σ, showing density for betaine (red) and the densities for TM4 (beige) and TM8 (blue). The tryptophan box of the betaine-binding motif is defined by the side chains of Trp189, Trp194, (Tyr197) and Trp374 (Ressl *et al.*, 2009).

All three protomers are related by a non-crystallographic symmetry (NCS) running perpendicular to the membrane (Ressl *et al.*, 2009). The periplasmic side of the trimer is negatively charged, whereas the cytoplasmic surface is positively charged. Between the protomers is a central cavity, which was found to be filled with PG lipids crucially involved in transport regulation (Figure 1.12) (Koshy *et al.*, 2013). Intratrimeric interactions between the protomers are mediated by h7 with TM2, TM3, TM9 and h7 of the adjacent protomer. Moreover, the long α-helical C-terminal domain interacts with loop 2 and the C-terminus of the adjacent chain. The different orientations of the three C-terminal domains, which are resolved in different extents, are leading to a break in the NCS symmetry.

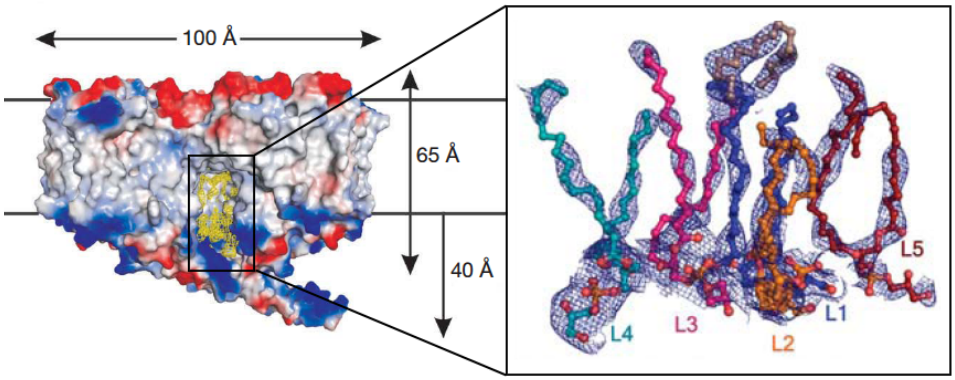

Figure 1.12: Central lipids of BetP.
BetP trimer in surface representation within the membrane depicted by lines indicating the boundaries of the lipid bilayer. The electrostatic is colored red (negative) and blue (positive). The F_o – F_c non-protein density (2σ contour level) in the hydrophobic cavity between the trimer is shown in yellow. The inset indicated five completely resolved POPG lipids (L1 - L5) in stick representation. The final $2F_o$ – F_c maps for the lipids are contoured at 0.8σ (adapted from Ressl *et al.*, 2009; Koshy *et al.*, 2013).

1.4.4 Functional features of the N- and C-terminal domain of BetP

Besides the 12 TM segments and the aliphatic helix h7, BetP possesses long terminal hydrophilic extensions facing the cytoplasm (Peter *et al.*, 1998a; Ressl *et al.*, 2009). Although the C-terminal domain was found to be a common feature of choline and betaine transporting BCCTs, the length and sequence of both terminal domains are not conserved throughout the family. Interestingly, N- and C-terminal domains of BetP are highly charged. The ~50 amino acid long C-terminal domain carries clusters of positively charged residues, whereas 15

negatively and only 2 positively charged residues are found within the unique ~60 amino acid long N-terminal domain. Due to the special charged feature of these extensions, the function of these domains was extensively studied with respect to their osmosensing properties. Peter *et al*. (1998a) demonstrated that partial truncations of the C-terminal domain led to deregulated constitutively active BetP in *C. glutamicum* cells. Mutations of charged residues or residues affecting the helical conformation of the C-terminal domain can severely alter the regulation, e. g. the substitution Ala564Pro maintained BetP at full activity (Becker *et al.*, 2014). In fact, the C-terminal domain was identified as key player in K^+ sensing and regulation (Peter *et al.*, 1998a; Schiller *et al.*, 2004). However, the role of the N-terminal domain is not conclusive. N-terminal truncated variants were less osmosensitive and an increased osmotic upshift was required for activation. Consequently, the maximum activity for the wild type at 1.3 osmol/kg was shifted to 2.6 osmol/kg for N-terminally truncated BetP in *C. glutamicum* (Figure 1.13), although the activation profile remained unaltered (Peter *et al.*, 1998a).

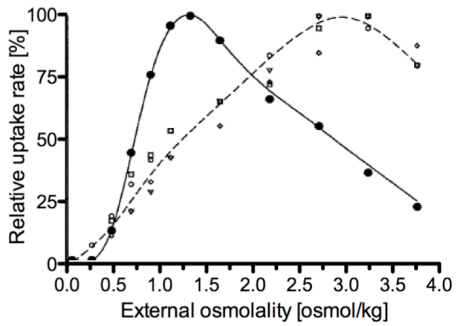

Figure 1.13: Glycine betaine uptake of N-terminally truncated BetP variants in *C. glutamicum*.
Glycine betaine uptake was measured in *C. glutamicum* strain DHP1/pGTG corresponding to the wild type (•) and DHP1 strains producing BetP with N-terminal truncations of 20 – 60 residues (o,△,□). Maximum uptake at optimum conditions of external osmolality was set to 100 % for better comparison (adapted from Peter *et al*., 1998a).

Interestingly, this effect resembles the shift in the activation optimum observed when BetP is surrounded by an increasing amount of negatively charged lipids *in vitro* and *in vivo* (Peter *et al.*, 1996; Rübenhagen *et al.*, 2000). In *C. glutamicum* comprising only negatively charged lipids, the maximum activity is reached at 1.3 osmol/kg (Peter *et al.*, 1998a), while in *E. coli* with less than 30 % negatively

charged lipids, the maximum activity was already found at 0.6 osmol/kg (Figure 1.14).

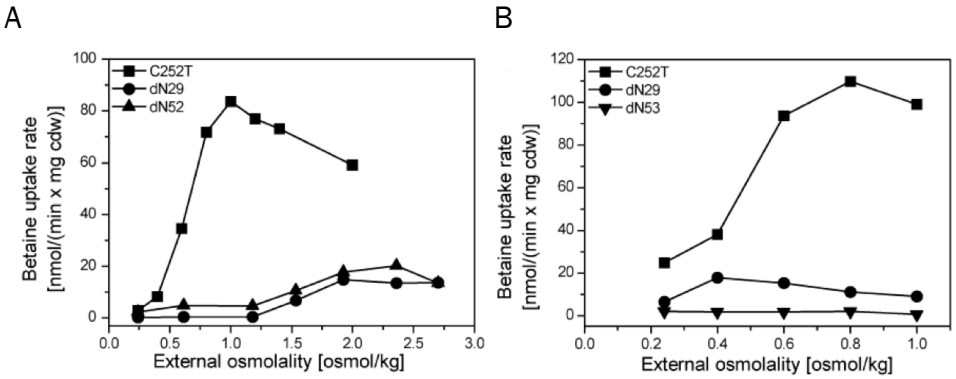

Figure 1.14: Comparison of osmo-dependent regulation of N-terminally truncated variants in different host organisms.
Regulation of the activity in dependence of the external osmolality is shown for BetP C252T and BetP variants with N-terminal truncations of either 29 (dN29) or 53/52 (dN53/52) residues, produced in *C. glutamicum* DHPF cells (A) and *E. coli* MKH13 cells (B) (Ott *et al*., 2008).

In addition, osmoregulation was lost in the N-terminally truncated BetP mutant in *E. coli,* which again was indicating the significance of lipids (Figure 1.14 B). The data suggest that negative charges either from lipids (scenario in *C. glutamicum*) or the N-terminal domain (scenario in *E. coli*) are absolutely essential for regulation.

It seems that negatively charged lipids can compensate for the lack of the N-terminal domain, however, higher amounts of stress are required for activation in *C. glutamicum*. In absence of a high content of negatively charged lipids as in *E. coli*, the N-terminal domain is a prerequisite for regulation. In consequence, the N-terminal domain and negatively charged lipids are assumed to compete for the same interaction site.

Diverse studies contributed to the idea of an interaction between the negatively charged N-terminal domain and/or lipids with the positively charged C-terminal domain. For instance, an interaction of both terminal domains was observed in a peptide array (Ott *et al.*, 2008). Additionally, competition experiments with BetP reconstituted into liposomes revealed an affected osmo-dependent activation of BetP, if proteoliposomes were preloaded with N-terminal peptides (Ott *et al.*, 2008). Furthermore, the binding of the C-terminal domain to lipid membranes in

surface plasmon resonance spectroscopy was reduced by the addition of N-terminal peptides, whereas the N-terminus itself showed no binding to lipid surfaces (Ott *et al.*, 2008). Based on these findings, the ''switch model'' was proposed for the mechanism of BetP activation, depending on electrostatic interactions (Figure 1.15). According to this model, the membrane bound state of the C-terminal domain was suggested to represent the inactive state of BetP. Upon increasing internal K^+ concentrations, a reorientation of the C-terminal domain would switch the interaction to cytoplasmic loops and the N-terminal domain.

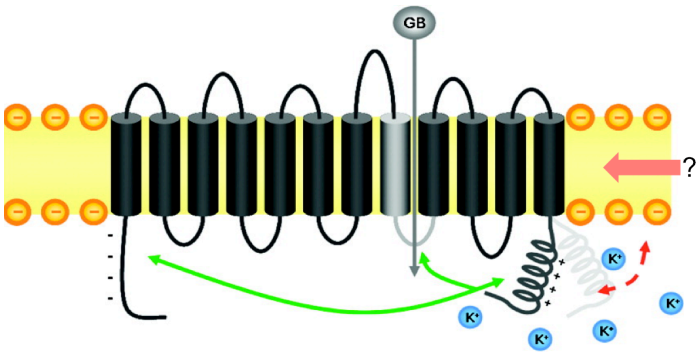

Figure 1.15: Switch model of the C-terminal mediated activation mechanism in BetP. In the absence of stress, the positively charged C-terminal domain of BetP is bound to the negatively charged lipids in the membrane (protein-lipid interaction, red dashed arrow) inactivating BetP. In the presence of hyperosmotic stress, increase of the cytoplasmic K^+ concentration in addition to an unknown membrane stimulus induces the reorientation of the C-terminal domain leading to the interaction with cytoplasmic loops and the N-terminal domain (protein-protein interaction, green arrow). The protein-bound state represents active BetP transporting betaine (GB) (modified after Ott *et al.*, 2008).

The X-ray structure of BetP solved in 2009 (Ressl *et al.*, 2009; PDB: 2WIT) shed light to the asymmetric orientation of the helical C-terminal domains of the BetP trimer interacting partly with cytoplasmic loops and the C-terminus of the adjacent protomer. Unfortunately, this structure could not provide further information about the unique N-terminal domain, because an N-terminally truncated, surface-engineered BetP variant (BetPΔ29EEE44/45/46AAA) was crystallized. The last resolved amino acids of the C-terminal helix are interacting via crystal contacts (Arg575 and Arg584) with the periplasmic side of the adjacent trimer, indicating a possible non-physiological orientation due to crystal contact restriction (Krämer and Ziegler, 2009). However, based on the

structurally suggested high flexibility of the C-terminal domains the switch model was adapted to the trimeric state (Figure 1.16).

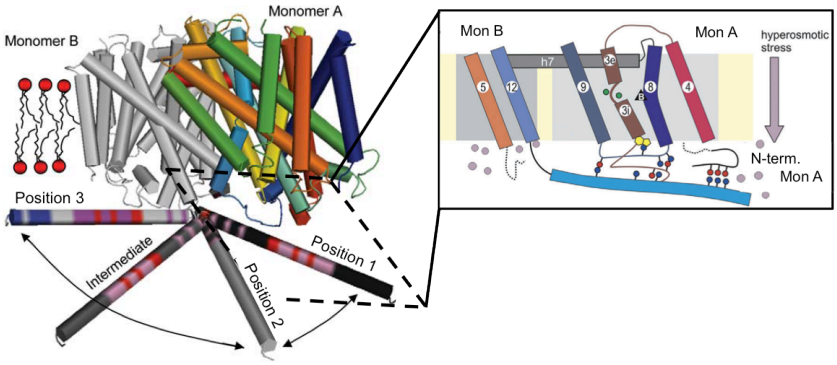

Figure 1.16: Putative orientations of the C-terminal domain of monomer B within the BetP trimer.

Position 1 illustrates the orientation of the C-terminus of monomer A in the crystal structure (Ressl *et al*., 2009) corresponding to the protein bound state. Position 2 shows a protein and lipid unbound state (C-terminus monomer B) and position 3 is the proposed lipid bound position of the C-terminal domain via positively charged clusters (blue) (Krämer and Ziegler, 2009). The inset displays a schematic representation of potential interactions of the C-terminal domain of one monomer with cytoplasmic loops and the N-terminal domain of the adjacent monomer. Positively charged residues within the C-terminal domain are interacting with negatively charged residues of the cytoplasmic loop 2 and indirectly with loop 8 connecting TM3 and TM8 (Ressl *et al*., 2009), which gate the substrate pathway. Moreover, an interaction with negatively charged residues in N-terminal domain could be suspected in this position (adapted from Ziegler *et al*., 2010).

A recently published BetP structure exhibit at least a part of the N-terminal domain resolved from residue 41 in chain A of PDB: 4AIN (Perez *et al.*, 2012) forming an α–helical structure (Figure 1.17). Although, many structures of BetP in different conformations were solved, the impact of the N-terminus in possible protein interactions regarding the C-terminal domain is still far from understood since only a partly N-terminally truncated mutant was used in all crystallization studies.

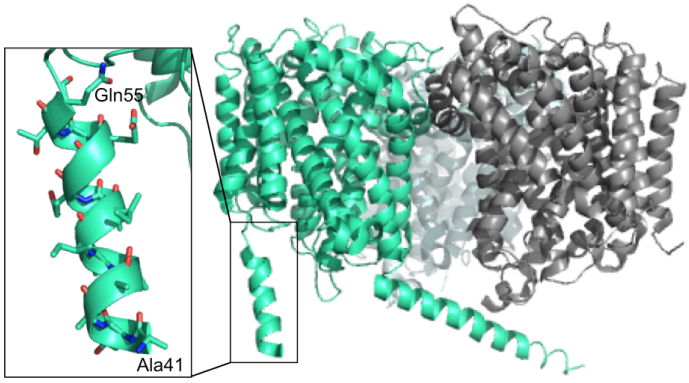

Figure 1.17: Partially resolved N-terminal domain of BetP.
The N-terminal domain is resolved for monomer A (green) of the X-ray structure of BetP (Perez *et al.*, 2012, PDB 4AIN). The α-helical structure of the N-terminal domain begins with residue Gln55 and is resolved until Ala41 (Inset).

1.4.5 Structure relation between different transporter families

The X-ray structure of BetP revealed that the 10 C-terminal TM helices share the five transmembrane helix inverted-topology repeat, LeuT-like (FIRL) fold, which is also commonly known as LeuT-fold. In the FIRL-fold, an internal two-fold pseudo-symmetry, with an axis running parallel to the membrane through the transporter center, relating the first set of five TM helices (TM3 – TM7) to the second set of five helices (TM8 – TM12), such that their TM topologies are inverted with respect to one another (Figure 1.18) (Yamashita *et al.*, 2005). The elements of the fold can be further divided: the first two helices in each repeat (TM3/TM4 and TM8/TM9) form the 4-helix bundle and the remaining three TM helices of each repeat are forming a so-called scaffold (Figure 1.19). Within the scaffold a smaller element, the hash domain, is build by TM5/TM6 and TM10/TM11 (Forrest *et al.*, 2008; Ressl *et al.*, 2009). The FIRL-fold is additionally characterized by a prominent feature of discontinuous TM helices (Figure 1.18 B), for instance TM3 in BetP, which is involved in substrate coordination. Besides the BCCT and NSS family, the fold was also identified for members of amino acid polyamine organocation (APC) family like AdiC and ApcT (Fang *et al.*, 2009; Shaffer *et al.*, 2009), in Mhp1 from the nucleobase cation symporter-1 (NCS1) family (Shimamura *et al.*, 2010; Weyand *et al.*, 2008) and in vSGLT from the solute sodium symporter (SSS) transporter family (Faham *et al.*, 2008). Although these transporters do not share any sequence identity, they are characterized by the same structure topology.

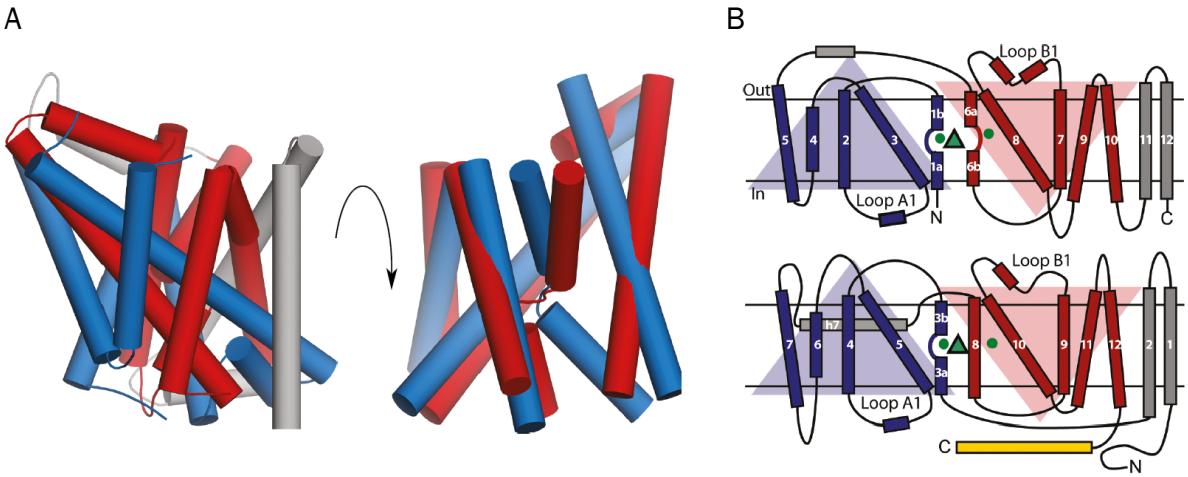

Figure 1.18: The LeuT-fold.
A) Side view of the X-ray structure of LeuT (left). Both 5 TM repeats of LeuT were superimposed by two-fold inversion (right). Inverted repeat 1 in blue, repeat 2 in red and peripheral helices in gray. B) Inverted repeat topology of LeuT (top) and BetP (below). Coloring as described before. In addition, the amphipathic helix h7 of BetP is colored gray, whereas the C-terminal domain is colored yellow. Substrates and ions are indicated by green triangles and circles, respectively (Khafizov *et al.*, 2010).

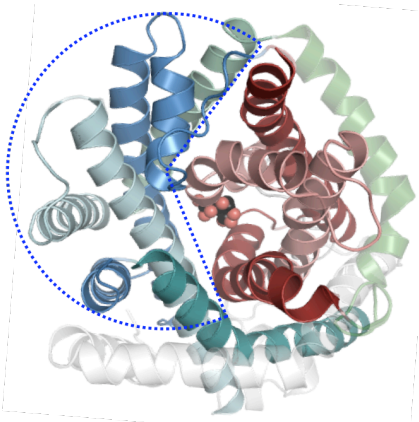

Figure 1.19: 4-helix bundle and scaffold of BetP.
Periplasmic view of a BetP protomer. The 4-helix bundle consisting of the first two helices of the first and second inverted repeat (TM3/TM4 and TM8/TM9) are colored light and dark red, respectively. The substrate-binding site is located within the 4-helix bundle. The remaining helices forming the scaffold are colored for the first repeat in shades of blue (TM5/TM6/TM7) and the helices of repeat 2 in shades of green (TM10/TM11/TM12). The amphipathic helix h7 is depicted in green while peripheral helices (TM1/TM2) are gray.

1.4.6 Conformational asymmetry in BetP

Oligomerization of membrane proteins is often observed, in particular for stabilizing effects (Van Dort *et al.*, 2001). To investigate the role of the trimer,

BetP was monomerized by mutations of intratrimeric interaction sites in the amphipathic helix h7, which is located between the protomers. Subsequent analysis of transport and regulation revealed that the monomer is the functional unit able to transport betaine, although regulation occurs only in the trimeric form of BetP (Figure 1.20) (Perez *et al.*, 2011a).

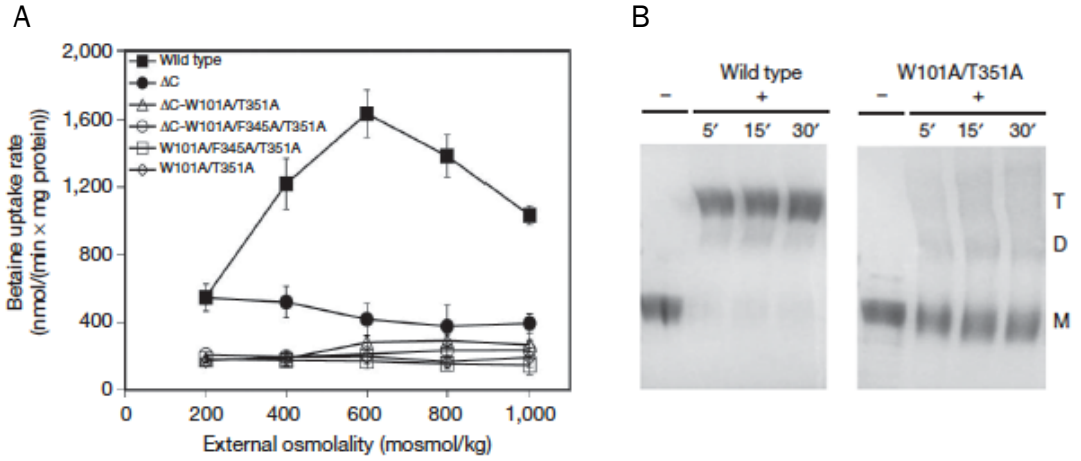

Figure 1.20: The role of trimerization of BetP.

A) Measurements of [^{14}C]-betaine uptake rates for BetP WT, -ΔC, -ΔC-W101A/T351A, -ΔC-W101A/F345A/T351A, -W101A/F345A/T351A and -W101A/T351A reconstituted into proteoliposomes. B) Glutaraldehyde cross-linking of detergent solubilized BetP WT and monomerized BetP W101A/T351A shown in a Coomassie-stained SDS-PAGE (10 %). Samples were incubated without (-) and with 0.13 % glutaraldehyde (+) for the indicated time points in min (Perez *et al*., 2011a).

Remarkably, structural data obtained by 3D and 2D crystallization indicated BetP forming conformational asymmetric trimers, in which each protomer can adopt a distinct conformation. More precisely, already in the 2D projection map at 8 Å of C-terminally truncated BetP, different conformation can be distinguished. At least one protomer was suggested to adopt the outward open and the other protomers an inward open conformation (Tsai *et al.*, 2011). Although the first X-ray structure was solved as symmetrical trimer, more recent asymmetrical structures of trimeric BetP were obtained (Figure 1.21) (Perez *et al.*, 2014; Perez *et al.*, 2012). Interestingly, in each asymmetric trimer at least one protomer, namely protomer C, is in the inward facing state, presumably forced by crystal contacts at the periplasmic side with the C-terminal domain of protomer A of a symmetry related trimer. Surprisingly, the involvement in crystal contacts have no consequence on the conformation of protomer A, it can adopt every state. Since crystal contacts

significantly differ between 2D and 3D crystals, the appearance of asymmetric trimers could not be just explained by restrictive consequences of the crystal contacts. Moreover, the observed structural asymmetry in the BetP trimers suggests a crosstalk between the protomers. Conformational coupling may reduce the energetic barrier to one or more rate limiting steps in the transport cycle and could facilitate the conversion between the states (Tsai *et al.*, 2011). Currently, it remains unclear if BetP forms either symmetric or asymmetric trimers due to the synchronization, random or consecutive cycling through the states in more native environment.

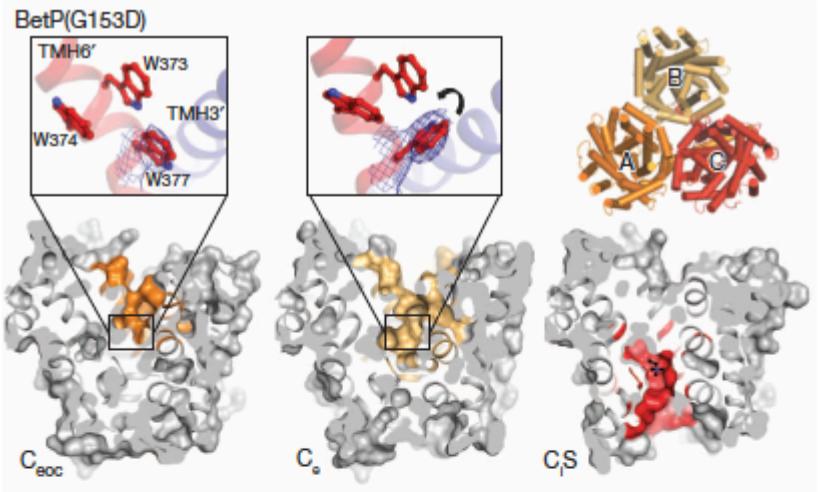

Figure 1.21: Conformationally asymmetric BetP trimer.
3D crystal structure of BetP G153D (PDB 4DOJ) consisting of protomers in different conformations; A: $C_{eo}c$ (outward occluded apo); B: C_e (outward open) and C: C_iS (inward open substrate bound). Insets show the $2F_o - F_c$ map of Trp 377 in the C_e and C_{eoc} state presented at 1.4σ level (Perez *et al.*, 2012).

However, with six obtained trimeric crystal structures eight different conformational states of BetP could be captured providing a molecular description of the local and global conformational changes in the transport mechanism of BetP (Figure 1.22). Based on the three major conformers (outward open, fully occluded and inward open), the alternating access mechanism of BetP can be described as a hybrid of rigid body movement and individual flexing of symmetry related helices (Perez *et al.*, 2012).

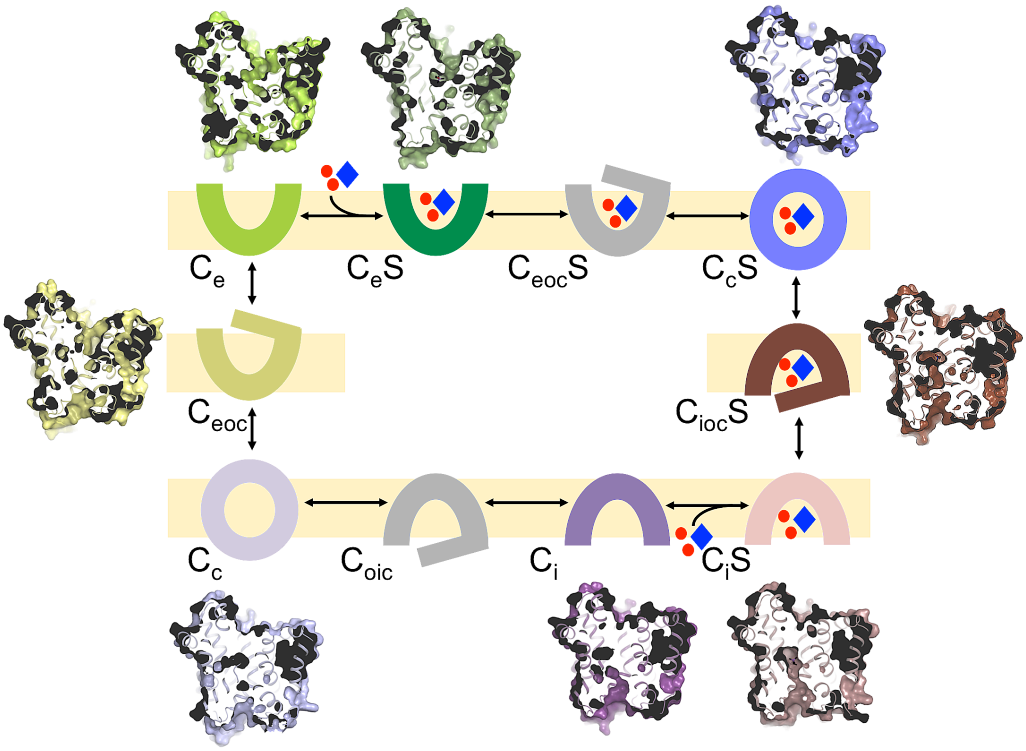

Figure 1.22: Alternating access cycle of BetP.
BetP crystal structures in different conformations: C_e (outward open apo; PDB 4DOJ), C_eS (substrate-bound outward open, PDB 4LLH), C_cS (substrate-bound closed, PDB 4AIN), $C_{ioc}S$ (substrate-bound inward occluded; PDB 2WIT), C_iS (substrate-bound inward open, PDB 3P03, 4DOJ, 4AIN, 4LLH), C_i (inward open apo, PDB 4C7R), C_c (closed apo, PDB 4AIN) and C_{eoc} (outward occluded apo; PDB 4DOJ). No crystal structures are available for $C_{eoc}S$ (substrate-bound outward occluded) and C_{oic} (inward occluded apo). Sodium and betaine are depicted as red circles and blue rhombus, respectively.

The rigid body movement is performed by TM5/TM6 of the first repeat and TM10/TM11 of the second repeat tilting relative to the 4-helix bundle. As gating mechanism to open adequately the pathway, a spring-like movement of TM3 to open the cytoplasmic gate and a less pronounced movement of TM8 to close the periplasmic gate was observed. Additionally, gating-like movements of TM7 and TM12 were identified. Furthermore, it was shown that all structural elements of BetP, which are involved in the transition from the outward to the inward open conformation of BetP, are either directly or indirectly forming the sodium-binding sites (Perez *et al.*, 2012). MD simulations, functional as well as structural investigations identified one sodium-binding site, Na2, between TM3 (A147, M150) and TM10 (F646, T467, S468) (Khafizov *et al.*, 2012; Perez *et al.*, 2012). Based on the pseudosymmetry of the FIRL-fold, computational and biochemical studies located the second sodium-binding site, Na1, between TM5 (T246,

T250), TM8 (F380) and TM11 (T499) (Khafizov *et al.*, 2012). According to this, the following sequence of sodium and substrate binding was proposed: The residues of the Na2 site allow binding and coordination of the first Na^+ ion in the outward open conformation. This event is followed by the binding of the substrate betaine and the second Na^+ ion. Subsequent conformational changes lead to the closure of the periplasmic pathway, because only in the closed state a proper coordination of the Na^+ ion in the Na1 site occurs, whereas in the outward and inward open state TM5 and TM8 are too distant for coordination. Driven by the sodium motive force, the Na2 site is destabilized and a spring-like movement of the cytoplasmic part of TM3 is opening the cytoplasmic pathway to release the substrates from the corresponding binding sites (Khafizov *et al.*, 2012; Perez *et al.*, 2012).

1.4.7 Impact of the glycine stretch in substrate specificity

The solved X-ray structures of BetP and CaiT demonstrated the coordination of the trimethylammonium group of the common BCCT substrates betaine and carnitine by the tryptophan box of TM4 and TM8 (Ressl *et al.*, 2009; Schulze *et al.*, 2010; Tang *et al.*, 2010). However, besides the highly conserved signature motif also residues in the unwound stretch of TM3 were found to be involved in substrate coordination (Ressl *et al*., 2009). An alignment of this glycine-rich motif with other BCCTs showed conservation among transporters with similar substrate specificity. The glycine stretch with the sequence Ala-Gly-Met-Gly-Ile-Gly was indicated for betaine specific transporters like BetP from *C. glutamicum*, OpuD from *B. subtilis* and other representatives (Figure 1.23). In comparison, the last glycine within the stretch is replaced by an aspartate for the highly choline-specific BCC transporter BetT from *E. coli*. In order to elucidate the role of this residue in substrate specificity, the last glycine was exchanged in BetP against an aspartate creating the mutant BetP G153D (Perez *et al.*, 2011b). Subsequently, betaine and choline transport was examined for BetP G153D reconstituted into liposomes. This single mutation was sufficient to convert BetP in a choline transporter, although betaine transport was still possible. Remarkably, choline transport in this BetP mutant was energized by smf as well as pmf. Crystallization of BetP G153D confirmed the coordination of the trimethylammonium group by

the tryptophans, whereas the carboxyl group of the introduced Asp153 coordinates the hydroxyl group of choline (Perez *et al.*, 2011b). Thus, it was demonstrated, that a single residue in TM3 is determining the substrate and co-substrate specificity.

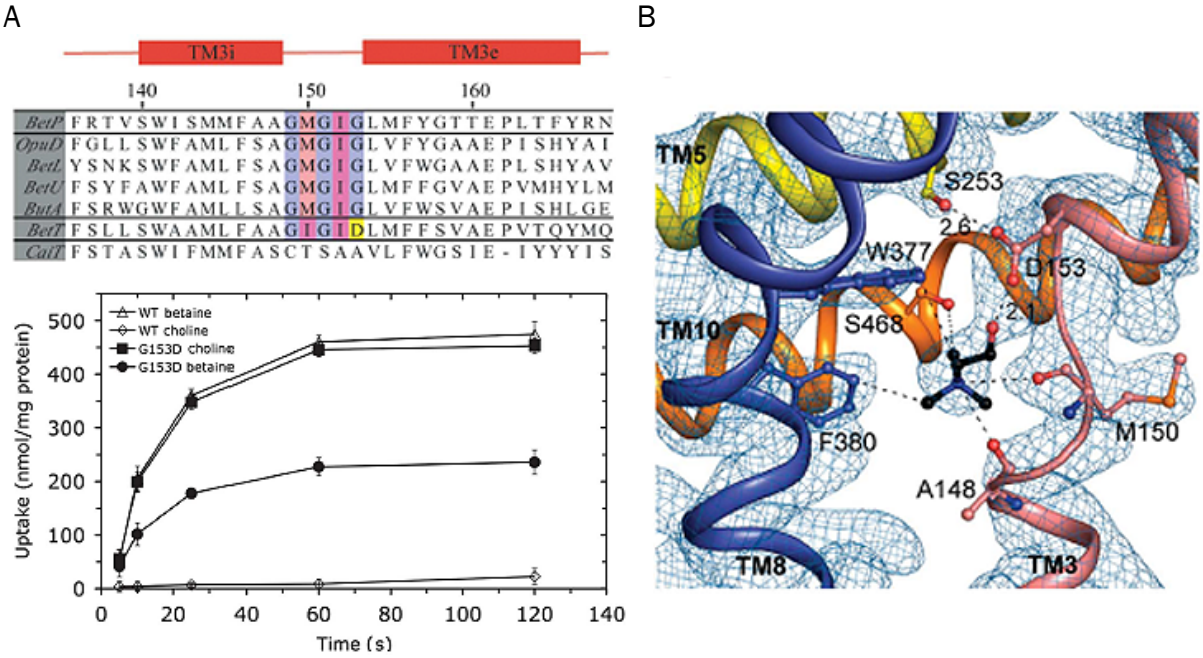

Figure 1.23: Choline transport in BetP G153D.

A) Amino acid sequence alignment of TM3 of BetP from *C. glutamicum* with *B. subtilis* OpuD, *L. monocytogenes* BetL, *P. mirabilis* BetU, *T. halophile* ButA, *E. coli* BetT and CaiT (top). Residues within the unwound stretch of TM3 are colored; α-helical segments of TM3 are depicted as red bars on top of the alignment. Na^+-coupled transport of either [^{14}C]-betaine or [^{14}C]-choline was measured for BetP WT and G153D, reconstituted in *E. coli* lipid liposomes (below). Uptake was started by the addition of saturating concentrations of [^{14}C]-betaine (15 µM for WT; 400 µM for G153D) and [^{14}C]-choline (400 µM for WT and G153D) at 0.6 osmol/kg adjusted with proline. Each value represents three independent measurements ± S.D.. B) The $2F_o$-F_c map (blue) of the choline-binding site contoured at 1.4σ is shown with choline (black) in stick representation. TM3, TM5, TM8 and TM10 are colored salmon, yellow, dark blue and orange, respectively. For clarity, TM10 is displayed without density. Hydrogen bonds and Van der Waals interactions are depicted as dashed lines (Perez *et al*., 2011b).

1.5 The role of BCCTs in pathogens

Pathogenic bacteria, which cause food- and waterborne diseases, have to cope with changing environments during production, preparation and storage of feed, food and water as well as defenses of the immune system within their human or

animal hosts for successful infection (Abee and Wouters, 1999). Beside known virulence factors, bacterial stress tolerance mechanisms are assumed to enhance bacterial virulence (Sleator and Hill, 2001). According to this, also BCC transporters involved in the bacterial osmotic stress response may play a role of adaption of specific pathogens to hostile environments. For instance, an outbreak of listeric septicemia was linked to the consumption of salted mushrooms stored at low temperatures (Junttila and Brander, 1989). The ability of *Listeria monocytogenes* to survive high salt concentrations and low temperatures was related to the accumulation of betaine and indeed, a BCC transporter BetL, highly specific for betaine, was identified for this organism (Sleator and Hill, 2001). For the halophilic facultative pathogen *Vibrio cholerae*, which inhabit marine and estuarine environments, OpuD belonging to the BCCT family was found. Although *V. cholerae* is devoid of the *bet* genes, betaine is accumulated by OpuD to counteract hyperosmotic stress. Furthermore, it was demonstrated that betaine excreted by other microorganisms leads to the surface attachment of *V. cholerae* and seems to facilitate survival of osmotic stress by the formation of microbial communities such as biofilms (Kapfhammer *et al.*, 2005). In contrast, *V. parahaemolyticus* containing the *betABI* genes and several BCCTs showed a growth advantage over *V. cholerae* at high salinity and low temperature (Naughton *et al.*, 2009). The nosocomial pathogen *Pseudomonas aeruginosa* comprises one betaine specific and two choline specific BCC transporters BetT2, BetT1 and BetT3, respectively (Malek *et al.*, 2011). Either betaine can be directly accumulated from the environment or the Bet enzymes convert choline into betaine. Choline can be derived in potential infection sites of the lungs, urinary tract, skin or eyes from abundant host molecules such as phosphatidylcholine, acetylcholine or phosphorylcholine (Magoon *et al.*, 1982; Malek *et al.*, 2011; Pesin and Candia, 1982). Moreover, a study demonstrated that the choline transporter and *betIBA* genes are among the most highly expressed genes in cystic fibrosis patients (Son *et al.*, 2007). Choline seems to be actively acquired during lung infections and these transporters may have an impact in colonization of the lungs (Malek *et al.*, 2011).

1.5.1 The genus of *Acinetobacter*

Bacteria belonging to the genus *Acinetobacter* are strictly aerobic, gram-negative coccobacillary rods, which are non-motile, catalase positive and oxidase negative. These γ-proteobacteria were classified into the family of *Moraxellaceae* and are ubiquitous and widely distributed in the environment due to their high nutritional versatility. *Acinetobacter* can be found in soil, water and sewage but also on small-size organisms like body lice as well as on human skin (Berlau *et al.*, 1999; La Scola and Raoult, 2004; Peleg *et al.*, 2008) and include both, non-pathogenic and pathogenic species. In the past decades, especially *Acinetobacter baumannii* emerged as source for nosocomial infections in humans and obtained high clinical relevance due to its increasing multi-drug resistance. These human opportunistic pathogens show resistances against β-lactams, broad-spectrum cephalosporins, aminoglycosides and quinolones (Peleg *et al.*, 2008). More recently, the increasing resistance against the last-line antibiotic Carbapenem was reported, which is further limiting the options for therapeutic treatments (Kempf and Rolain, 2012). *A. baumannii* strains are isolated up to 1 % of nosocomial infections mostly from immunosuppressed patients at intensive care units and are associated with high rates of morbidity and mortality due to pulmonary, urinary tract, bloodstream and surgical wound infections (Vallenet *et al.*, 2008; Yamada *et al.*, 2012). However, other *Acinetobacter* species like the as non-pathogenic referred *A. baylyi* strain ADP1 gained biotechnical importance because of its high competence in natural transformation (Elliot and Janik, 1969). Due to the robust physiological properties and simple genetic manipulation, the complete genome of *A. baylyi* ADP1 was sequenced (Barbe *et al.*, 2004; de Berardinis *et al.*, 2009). The genome analysis revealed that about 20 % of the genes in strain ADP1 are involved in catabolic function, which is allowing the transformation of a large variety of compounds during metabolic pathways turning *A. baylyi* into a model for metabolic system biology (Barbe *et al.*, 2004; de Berardinis *et al.*, 2009). However, the comparison to the genome of the human pathogenic representative *A. baumannii* AYE revealed that the latter has even higher catabolic capacities than *A. baylyi* (Vallenet *et al.*, 2008). In contrast, *A. baylyi* genome includes very few characteristics that are associated with pathogenesis, there were also reports of *A. baylyi* being isolated from clinical samples in hospitals (Chen *et al.*, 2008). In addition, the genome of stain ADP1

comprises 10 % genes associated with transport functions, which is consistent with the metabolic versatility, but also play a role in the ability to adapt to changing environments. This is not only relevant for the soil bacterium but also for pathogenic representatives, which are able to survive prolonged periods also throughout hospital environments. The ability to colonize almost any surface persisting desiccation and moisture (Doughari *et al.*, 2011; Vallenet *et al.*, 2008) indicates tolerance of osmotic stress. Indeed, studies demonstrated, that *A. baylyi* is able to cope with different salinities tolerating concentrations up to 900 mM NaCl (Sand *et al.*, 2011). In order to counteract hyperosmotic stress, *A. baylyi* is able to synthetize the compatible solutes mannitol and glutamate *de novo* (Sand *et al.*, 2013). However, in the presence of the compatible solute glycine betaine, the uptake of this quaternary ammonium compound is favored due to energetically reasons. Inspection of the genome revealed two genes encoding potential secondary betaine transporters, ACIAD2280 and ACIAD3460, belonging to the MFS and BCCT family, respectively (Sand *et al.*, 2011). Deletion experiments identified the BCC transporter, later renamed into BetT3, as essential for betaine transport upon hyperosmotic stress in *A. baylyi*. Sequence analysis indicated similarities to the most prominent BCC transporter BetP from *C. glutamicum*. The sequence similarity suggests a sodium-coupled betaine uptake system for BetT3, even though the N-terminal domain is shorter and the C-terminal domain is almost three times longer as in BetP. Although it is not much known about the accumulation of compatible solutes of pathogenic *Acinetobacter* strains, BCC transporters were also found in *A. baumannii* suggesting an impact in the adaption of the opportunistic pathogens to osmotic stress conditions contributing to the virulence of these bacteria (Sand *et al.*, 2011).

1.6 Aim of the work

The mechanism of transport regulation in the trimeric transporter BetP to counteract hyperosmotic stress in *Corynebacterium glutamicum* is still not described on a molecular level. The function of the terminal domains was already studied with respect to their osmoregulatory properties (Ott *et al.*, 2008; Peter *et al.*, 1998a). While the C-terminal domain was identified as a key player sensing the increase of the internal K^+ concentration (Schiller *et al.*, 2004), functional data investigating the role of the negatively charged N-terminal domain were less conclusive. Hence, one aim of this thesis was to shed light on the regulatory role of the negatively charged clusters of the N-terminal domain by mutagenesis and functional studies. In addition, potential interactions between the N-terminal and the C-terminal domains were investigated by cross-linking studies (Chapter 4).

Previous functional studies suggest the trimeric architecture of BetP as a prerequisite for regulation (Perez *et al.*, 2011a). Structural data obtained by 2D and 3D crystallization shows BetP as an asymmetric trimer with each protomer adopting a distinct transporter state (Perez *et al.*, 2012; Tsai *et al.*, 2011). These transporter states were interpreted as different conformations underlying the alternating access mechanism. The rather unusual conformational asymmetry suggests a regulatory crosstalk between the protomers within the trimer. However, the question arises if the occurrence of asymmetric trimers represents a physiologically relevant state with cooperatively working individual protomers in the BetP trimer. This would suggest that a fixed order of the different states detected in all crystal structures is pointing toward a consecutive cycling as it was observed in the multidrug efflux pump AcrB (Murakami *et al.*, 2006; Seeger *et al.*, 2006). A biophysical approach to probe conformational changes was found in the PELDOR method that in combination with site-directed spin labeling allowed to study conformational cycling in a more native-like environment (Chapter 5).

Another aspect of this thesis was to characterize novel betaine-choline-carnitine transporters. Due to the increasing clinical relevance of the pathogenic *Acinetobacter* species and the high gene orthology, the non-pathogenic representative *Acinetobacter baylyi* was selected as the subject for investigation.

The characterization of BCCTs has a strong impact on our understanding of the mechanism of persistence of pathogenic *Acinetobacter*. So far, only one of the three BCC transporters existing in *A. baylyi* was identified as an osmo-dependent betaine transporter (Sand *et al.*, 2011). Thus, the aim was to express the other two transporters BetT1 and BetT2 heterologously in *E. coli* to enable functional characterization and to obtain first structural information on these transporters (Chapter 3).

2 Material and Methods

2.1 Materials

2.1.1 Instruments

Äkta Explorer (GE Healthcare)

Cary 50 UV-Vis Spectrometer (Varian)

EPR Spectrometer EleXsys E580 (Bruker)

Freeze fracture set-up: BAF 060 machine (Bal-Tec)

Mosquito™ pipetting robot (TTP Labtech)

NanoDrop 1000 (Peqlab)

TPersonal Thermocycler (Biometra)

Trans-Blot SD (Bio-Rad)

TRI-CARB 1500 scintillation counter (Canberra-Packard)

2.1.2 Chemicals

Unless otherwise indicated, chemicals used in this work were purchased from Anatrace, Avanti, Bio-Rad, Glycon, Merck, Movarek Biochemicals Inc., New England Biolabs, Roth, Roche, Sigma-Aldrich® and Thermo Scientific Molecular Biology.

2.1.3 Reagent kits

PCR Purification Kit (Qiagen)

QuikChange II® Site-Directed Mutagenesis Kit (Stratagene)

QiaQuick Gel Extraction Kit (Qiagen)

QIAprep Spin Miniprep Kit (Qiagen)

2.1.4 Column materials

Superose 6 10/300 GL (GE Healthcare)

Strep-Tactin® Macro-Prep resin (IBA GmbH)

SP-Sepharose (GE Healthcare)

Q-Sepharose (GE Healthcare)

Ni-NTA Agarose (Qiagen)

2.1.5 Media and Antibiotics

2.1.5.1 LB medium

Bacto-tryptone	10 g/l
Bacto-yeast extract	5 g/l
NaCl	10 g/l

2.1.5.2 SOC medium

Bacto-tryptone	20 g/l
Bacto-yeast extract	5 g/l
NaCl	10 mM
KCl	2.5 mM
$MgCl_2$	10 mM
$MgSO_4$	10 mM
Glucose	20 mM

2.1.5.3 Antibiotics

Carbenicillin	50 mg/ml

2.1.6 *E. coli* strains and vectors

Table 2.1: *E. coli* strains

E. coli strain	Genotype	Reference
DH5α™-T1^R	F- φ80*lac*ZΔM15 Δ(*lac*ZYA-*arg*F)U169 *rec*A1 *end*A1 *hsd*R17(r_{k^-}, m_{k^+}) *pho*A *sup*E44 *thi*-1 *gyr*A96 *rel*A1 *ton*A (confers resistance to phage T1)	(Killmann *et al.*, 1996)
MKH13	*araD39 (argF-lac) U169 relA51 rps150 flbB5301 deoC ptsF25* Δ(putPA)101 Δ(proP)2 Δ(proU)	(Haardt *et al.*, 1995)
XL-1 Blue	*recA1 endA1 gyrA96 thi-1 hsdR17 supE44 relA1 lac [F' proAB lacI^{q}ZΔM15 Tn10 (Tet^r)]*	Stratagene
TOP10	F– *mcr*A Δ(*mrr-hsd*RMS-*mcr*BC) Φ80*lac*ZΔM15 Δ*lac*X74 *rec*A1 *ara*D139 Δ(*ara- leu*) 7697 *gal*U *gal*K *rps*L (Str^R) *end*A1 *nup*G	Invitrogen

Table 2.2: Vectors

Vector	Resistance	Properties	Reference
pASK-IBA5*betP*	Amp^R	pASK-IBA5 with *betP* cloned over BsaI and HindIII restriction site; N-terminal Strep-tagII	(Rübenhagen *et al.*, 2000)
pASK-IBA7*betA* ΔN29EEE44/45/46AAA	Amp^R	pASK-IBA7 with *betP* ΔN29EEE44/45/46AAA cloned over BsaI and HindIII restriction site; N-terminal Strep-tagII	(Ressl *et al.*, 2009)
pBAD/HisA	Amp^R	*ara*BAD promotor ; N-terminal His_6-tag; *ara*C gen	Invitrogen
pBAD/HisA_AClAD1011	Amp^R	pBAD/HisA with *betT1* cloned over XhoI and PstI, N-terminal His_6-tag	M. Sand, Goethe University, Frankfurt
pBAD/HisA_AClAD1012	Amp^R	pBAD/HisA with *betT2* cloned over SacI and EcoRI, N-terminal His_6-tag	This study

2.1.7 Oligonucleotide primers

To mutate the *betP* sequence, primer sequences with exchanged nucleotides in the corresponding codons were designed.

Table 2.3: Primers for BetP constructs investigated in PELDOR studies

Primer	Sequence (5' to 3')
S140C$_s$	CCAGAGTTTCGCACGGTGTGCTGGATTTCCATGATG
S140C$_{as}$	CATCATGGAAATCCAGCACACCGTGCGAAACTCTGG
C140S$_s$	GAGTTTCGCACGGTGTCATGGATTTCCATGATG
C140S$_{as}$	CATCATGGAAATCCATGACACCGTGCGAAACTC
G450C$_s$	CTTCATGCACTTCCAGGTTGCCAAATCATGGGC
G450C$_{as}$	GCCCATGATTTGGCAACCTGGAAGTGCATGAAG
N488C$_s$	GGCCAGCTGGAAGCCTGCAAGTGGGTGACAGCTGCC
N488C$_{as}$	GGCAGCTGTCACCCACTTGCAGGCTTCCAGCTGGCC
K489C$_s$	CAGCTGGAAGCCAACTGCTGGGTGACAGCTGCC
K489C$_{as}$	GGCAGCTGTCACCCAGCAGTTGGCTTCCAGCTG
W490C$_s$	CTGGAAGCCAACAAGTGCGTGACAGCTGCCTGG
W490C$_{as}$	CCAGGCAGCTGTCACGCACTTGTTGGCTTCCAG
A514C$_s$	CTTTCTGGTGGTGACAATTGCTTGAGCAACTTGC
A514C$_{as}$	GCAAGTTGCTCAAGCAATTGTCACCACCAGAAAG
L515C$_s$	TCTGGTGGTGACAATGCCTGCAGCAACTTGCAAAAC
L515C$_{as}$	GTTTTGCAAGTTGCTGCAGGCATTGTCACCACCAGA
S516C$_s$	GGTGACAATGCCTTGTGCAACTTGCAAAACGTCACC
S516$_{as}$	GGTGACGTTTTGCAAGTTGCACAAGGCATTGTCACC

Exchanged codons are underlined. Sense ($_s$) and antisense ($_{as}$) are listed.

Table 2.4: Primers for N- and C-terminal BetP constructs

Primer	Sequence (5' to 3')
ED13/14AA$_s$	CCGATAGTGGCGGCTGCTCAGCCACAG
ED13/14AA$_{as}$	CTGTGGCTGAGCAGCCGCCACTATCGG
E24C$_s$	GAGCAAATTACCGCAACCTGCGAACTGGCGGGCTTG
E24C$_{as}$	CAAGCCCGCCAGTTCGCAGGTTGCGGTAATTTGCTC
EE24/25AA$_s$	ACCGCAACCGCAGCACTGGCGGGCTTG
EE24/25AA$_{as}$	CAAGCCCGCCAGTGCTGCGGTTGCGGT
E25C$_a$	ACCGCAACCGAATGCCTGGCGGGCTTGCTTGAG
E25C$_{as}$	CTCAAGCAAGCCCGCCAGGCATTCGGTTGCGGT
EEE45/46/47AAA$_s$	CTGGCCGACGCCGCAGCAGCAATTATCCTCGAA
EEE45/46/47AAA$_{as}$	TTCGAGGATAATTGCTGCTGCGGCGTCGGCCAG
R576C$_s$	CACAATGAACACCGCAAGTGTGAACTGGCTGCAAAG
R576C$_{as}$	CTTTGCAGCCAGTTCACACTTGCGGTGTTCATTGTG
R583C$_s$	CTGGCTGCAAAGCGATGCAGGGAGCGTAAGGCG
R583C$_{as}$	CGCCTTACGCTCCCTGCATCGCTTTGCAGCCAG

Exchanged codons are underlined. Sense ($_s$) and antisense ($_{as}$) are listed.

Table 2.5: Primers for BetP constructs mimicking the glycine motif in BetT1

Primer	Sequence (5' to 3')
M150I$_s$	ATGTTTGCTGCAGGTATAGGTATTGGTTTG
M150I$_{as}$	CAAACCAATACCTATACCTGCAGCAAACAT
G153A$_s$	GCAGGTATGGGTATTGCGTTGATGTTCTACGGAACC
G153A$_{as}$	GGTTCCGTAGAACATCAACGCAATACCCATACCTGC
M150I/G153A$_s$	TCCATGATGTTTGCTGCAGGTATCGGTATTGCGTTGATGTTCTAC
M150I/G153A$_{as}$	GTAGAACATCAACGCAATACCGATACCTGCAGCAAACATCATGGA

Exchanged codons are underlined. Sense ($_s$) and antisense ($_{as}$) are listed.

In order to clone the *betT2* gen into the pBAD/HisA vector, primers with the respective restriction sites were designed.

Table 2.6: Primers for BetT2 constructs

Primer	Sequence (5' to 3')	Description
BetT2_SacI$_s$	ACTGCAGCCCTTGAGCTCTGTATGGA CAGATAATCCAAG	Sense primer with SacI restriction site
BetT2_EcoRI$_{as}$	ATTAGGATCGAATTCCCTAGGCTTTAG TCTGGAAATAGGCGG	Antisense primer with EcoRI restriction site

2.1.8 Crystallization screens

MemGold™ HT-96 Green Screen (Molecular Dimensions)

JBScreen Classic 5-8 (Jena Bioscience)

JBScreen Membrane 1-3 (Jena Bioscience)

MbClass Suite™ (Qiagen)

MbClass Suite II™ (Qiagen)

2.2 Molecular biological methods

2.2.1 Polymerase chain reaction (PCR)

The polymerase chain reaction is a technique to amplify template DNA *in vitro* (Mullis and Faloona, 1987) with synthetic DNA oligonucleotides (primer), which are complementary to the ends of the desired DNA fragment. PCR is a cyclic repetitive three-step reaction with denaturation of the DNA strand, annealing of the primers to the single-stranded DNA and elongation of the DNA primers at the 3'-OH end by a thermo-stable DNA polymerase to synthetize a new complementary DNA strand.

The PfuUltra™ DNA polymerase (Stratagene) was used to perform all PCRs to mutate the *betP* gene while for preparative PCR, Phusion DNA polymerase (Fermentas) was used. Pfu and Phusion DNA polymerase possess a 3' – 5' exonuclease proofreading activity to correct mutations produced during amplification.

Table 2.7: PCR mixture (Stratagene)

Component	Volume (µl)
DNA template (5 - 15 ng)	5
Primer sense (125 ng)	1.25
Primer antisense (125 ng)	1.25
PfuUltra polymerase reaction buffer (10x)	5
dNTP mix (25 mM)	1
H_2O_{dd}	35.5
Pfu Ultra DNA Polymerase (2.5 U/µl)	1

Table 2.8: Standard PCR program (Stratagene)

Step	Cycles	Temperature	Time
Denaturation	1	95°C	30 sec
Denaturation	18	95°C	30 sec
Hybridization	18	55°C	1 min
Elongation	18	68°C	4 min
	1	4°C	∞

Table 2.9: PCR mixture (Fermentas)

Component	Volume (µl)
DNA template (10 ng)	1
Primer sense (125 ng)	2.5
Primer antisense (125 ng)	2.5
Phusion HF reaction buffer (5x)	10
dNTP mix (10 mM)	1
DMSO (100 %)	1.5
H_2O_{dd}	31
Phusion DNA Polymerase (2 U/µl)	0.5

Table 2.10: Touchdown PCR program (Fermentas)

Step	Cycles	Temperature	Time
Denaturation	1	98°C	30 sec
Denaturation	30	98°C	10 sec
Hybridization	30	55°C + 1°C/cycle	30 sec
Elongation	30	72°C	1 min
Elongation	1	72°C	10 min
	1	4°C	∞

2.2.2 Site-directed mutagenesis

Site-directed mutagenesis was performed with the QuickChange Site-directed Mutagenesis Kit II (Stratagen) according to the manufacturer's instructions by using the corresponding PfuUltra DNA Polymerase described in Section 2.2.1. All obtained constructs were verified by nucleotide sequencing.

2.2.3 DNA cleavage by restriction endonucleases

Hydrolytic cleavage of vectors (Table 2.2) and DNA inserts for cloning were performed by using restriction endonucleases from New England Biolabs (NEB). The reaction was incubated for 1.5 – 2 h at 37 °C.

Table 2.11: Restriction set-up

Component	Volume (µl)
DNA (1000 ng)	10
NEB buffer (10x)	5
Enzyme 1 (10 U)	0.5 - 1
Enzyme 2 (10 U)	0.5 - 1
BSA (100x)	0.5
H_2O_{dd}	33.5 – 32.5
DNA (1000 ng)	10

Cleaved vector and insert were purified according to the manufacturer's instructions with PCR Purification Kit (Qiagen) or QiaQuick Gel Extraction Kit (Qiagen), respectively.

2.2.4 Agarose gel electrophoresis

Amplified DNA or cleaved vectors were analyzed by separation on an agarose gel. Therefore, DNA samples were mixed with 6x DNA sample buffer prior loading on a 1 % agarose gel in TAE-buffer (Table 2.12). The electrophoresis was performed 1 h at 100 V. To visualize DNA, Ethidium bromide (0.5 µg/ml) was added to the agarose gel. Ethidium bromide intercalates as an organic fluorescent dye with aromatic rings with the nucleotides of the DNA and can be illuminated at the excitation wavelength of λ = 312 nm.

Table 2.12: TAE-buffer

Component	Concentration
Tris-acetate, pH 8.0	40 mM
Na_2EDTA	1 mM
Acetic acid	40 mM

2.2.5 DNA concentration determination

Determination of the dsDNA concentration and purity was performed photometrical using the NanoDrop 1000. To calculate the DNA concentration, the optical density (OD) at the absorption maximum of 260 nm (OD_{260}) was measured. For a pure dsDNA solution of 50 µg/ml, the reference value of OD_{260}=1 have to be reached. Because tyrosine and tryptophan residues in co-purified proteins absorb at 280 nm, the ratio of OD_{260} and OD_{280} (Warburg and Christian, 1942) estimates the purity of the DNA sample. A pure DNA sample without protein contaminations shows a reference value of OD_{260}/OD_{280}= 1.8 – 2.0.

2.2.6 Ligation of DNA fragments

Prior to ligation vector and DNA insert have been cleaved by the corresponding restriction endonucleases to generate compatible ends. For ligation, 50 – 100 ng purified vector is incubated with a 5-fold molar excess of insert DNA and T4-Ligase (200 U) in 10x T4-ligase buffer (Thermo Scientific Molecular Biology) for 1 h at room temperature. Afterwards, the ligation reaction was transformed into competent *E. coli* XL-1 Blue cells.

Test cleavage and nucleotide sequencing were performed to verify the correct insertion of the DNA fragment into the vector.

2.2.7 Preparation and transformation of competent cells

Chemically competent *E. coli* cells were produced by the method described by Chung (Chung *et al.*, 1989) using TSS medium.

An *E. coli* strain was grown in LB medium overnight (37°C, 180 rpm). The following day, the overnight culture was used to inoculate fresh LB media in a ratio of 1:100 and the culture was cultured to an early exponential phase (OD_{600} 0.3 – 0.4). Cells were transferred onto ice, splitted into 1 ml aliquots and harvested at 4500 rpm for 10 min at 4°C. Each cell pellet was resuspended in 100 µl TSS medium and directly shock frozen in liquid nitrogen. The aliquots were stored at –80°C till use.

Table 2.13: TSS-Medium

Component	Concentration
LB medium	-
PEG 8000	10 % (w/v)
DMSO	5 % (v/v)
$MgCl_2$	50 mM
Glycerol	15 % (v/v)

Sterilized by filtration

For transformation, one aliquot of *E. coli* competent cells were thawed on ice, mixed with 100 ng of vector DNA and incubated for 30 min on ice. A heat shock at 42°C for 45 sec was performed to increase the transformation rate. After an incubation of the cells on ice for 2 min, 0.9 ml SOC medium was added and cells were further incubated at 37°C for 1 h shaking. This step allows the expression of the antibiotic-resistance gene located on the transformed vector and positive clones were selected by plating cells on a LB agar plate including the corresponding antibiotic as selection marker. The plate was incubated at 37°C overnight.

2.2.8 Isolation of vector DNA

Transformed *E. coli* cells were grown at 37°C overnight in 5 ml LB medium including the appropriate selection marker (50 µg/ml carbenicillin). After 16 h, cells were harvested at 4200 rpm for 10 min at 20°C. Vector DNA was isolated using the QIAprep Spin Miniprep Kit according to the manufacturer's instructions.

2.3 Biochemical methods

2.3.1 Protein production of BetP WT and mutants

Cell culture and protein purification was performed as described previously (Rübenhagen *et al.*, 2000). *E. coli* One Shot®Invitrogen DH5α™-T1 cells (Killmann *et al.*, 1996) were transformed with pASK-IBA5*betP* WT and mutants according to manufacturer's instructions and used for the heterologous expression of *strep-betP*. Transformed cells were used to inoculate LB medium supplemented wit carbenicillin (50 µg/ml) and grown at 37°C and 180 rpm

overnight. At the following day 6 flasks of 1 – 2 l fresh LB medium (50 µg/ml carbenicillin) were inoculated with an OD_{600} of 0.15. Cells were grown at 37 °C at 120 rpm to an OD_{600} of 1.5 for an induction with 200 µg/l anhydrotetracycline. After reaching the stationary phase cells were harvested at 4200 rpm and 4 °C for 15 min by centrifugation. Cell pellets were resuspended in $Cellbreakbuffer_{BetP}$.

Table 2.14: $Cellbreakbuffer_{BetP}$

Component	Concentration
Tris-HCl, pH 7.5	100 mM
Pefabloc	1 mM

2.3.2 Protein production BetT1

The pBAD/HisA vector containing the gene assigned by the locus tag ACIAD1011 (pBAD/HisA_ACIAD1011) cloned over XhoI and PstI restriction sites was kindly provided by Miriam Sand (Group Prof. Dr. Beate Averhoff, Goethe University, Frankfurt). The corresponding gene product is referred to as BetT1. For heterologous expression the vector pBAD/HisA_ACIAD1011 was transformed into *E. coli* One Shot®TOP10 cells according to manufacturer's instructions. Transformed cells were grown in LB medium supplemented with 50 µg/ml carbenicillin at 37 °C and 180 rpm overnight. The following day, 6 flasks of 1 – 2 l LB medium (50 µg/ml carbenicillin) were inoculated with a OD_{600} of 0.2 and incubated at 37 °C at 120 rpm to OD_{600} of 0.6 – 0.8 to initiate the induction with 0.02 % arabinose. Cells were further cultured for 2 h. Cells were harvested by centrifugation at 4200 rpm for 15 min at 4 °C and cell pellets were resuspended in $Cellbreakbuffer_{BetT1}$.

Table 2.15: $Cellbreakbuffer_{BetT1}$

Component	Concentration
Tris-HCl, pH 7.5	20 mM
NaCl	50 mM
Glycerol	10 %

2.3.3 Cell disruption

2.3.3.1 Cell disruption using the microfluidizer

Smaller cell volumes up to 50 ml were disrupted by the microfluidizer (Model M-110L, Microfluidics Corp.). The cells are pressed at a pressure of 7 kbar through a narrow nozzle (0.5 mm in diameter) and lysed due to the high pressure leading to shearing forces by leaving the nozzle. During cell disruption an increase of temperature is avoided by precooling the microfluidizer with ice.

2.3.3.2 Cell disruption using the cell disrupter

Disruption of cell volumes more than 100 ml was performed with the cell disrupter (Constant systems), which operates like a French Press and microfluidizer in combination. The cells are pressed at a high pressure of 1.8 kbar through a needle valve and clash with a high velocity on a sloped plate.

2.3.4 Protein purification

2.3.4.1 Membrane preparation

For *E. coli* membrane isolation, broken cells were centrifuged by low spin centrifugation at 12500 rpm for 35 min at 4°C to remove cell fragments. As second step, membranes were isolated by ultracentrifugation for 1 h at 45000 rpm at 4°C. The membrane pellet was resuspended in Solubilizationbuffer to a total protein concentration of 10 mg/ml and were frozen in liquid nitrogen before storage at -80°C.

Table 2.16: Solubilizationbuffer

Component	Concentration
Tris-HCl, pH 7.5	50 mM
Glycerol	17.2 %

2.3.4.2 Solubilization

To isolate the membrane protein of interest for further purification steps, membranes were solubilized with detergents.

Membranes containing BetP (10 mg/ml) were thawed and the same volume Solubilizationbuffer including 2 % DDM were dropwise added to the membranes incubated on ice constantly stirred. After 20 – 30 min, 200 mM NaCl is additionally added and followed by further incubation for 30 min at room temperature. To remove the unsolubilized fraction, the solubilisate was centrifuged at 45000 rpm for 35 min at 4 °C.

Solubilization of BetT1 was performed by adding 2 % DDM directly to the membranes (10 mg/ml). Membranes were incubated for 1 h on ice under constantly stirring before the addition of 200 mM NaCl. After 1 h further incubation, the solubilisate was ultracentrifuged at 45000 rpm for 35 min at 4 °C.

2.3.4.3 StrepTactin®-affinity chromatography

Recombinantly expressed BetP WT and mutants harbor a N-terminal Strep-tag®II (WSHPQFEK, IBA (Schmidt *et al.*, 1996)) which allow protein isolation by a column packed with StrepTactin®. The Strep-tag®II including the protein of interest is able to bind exclusively to the StrepTactin® resin while other proteins not. D-Desthiobiotin, which counteracts with a higher affinity the binding of the Strep-tag®II to the StrepTactin® is applied to elute the Strep-tag®II fusion protein. To regenerate the StrepTactin®, HABA is loaded on the column and the removal of d-Desthiobiotin is indicated by a color change to deep orange.

Solubilized membranes containing BetP were loaded on a preequilibrated 3 ml StrepTactin® column with a flow rate of 1 drop/5 sec overnight. Prior to loading, 1 mM DTT was added to the solubilisate for PELDOR application. The next day, 3 washings steps with first 20 column volumes (CV) buffer A with 0.05 % DDM, followed by 20 ml high salt buffer B with 0.6 % Cymal-5 and again 20 ml buffer A

with 1.2 % Cymal-5 for detergent exchange were applied, if protein was used for crystallization. Protein for PELDOR and reconstitution was washed once with 40 CV of buffer A with 0.1 % DDM. The protein was eluted with buffer A with 5 mM d-Desthiobiotin containing either 1.2 % Cymal-5 or 0.1 % DDM for crystallization or PELDOR application, respectively. Fractions from 1 ml to 200 µl were collected, checked for protein content by Bradford assay (Bradford, 1976) and fractions with high protein concentration were pooled. All purification steps were performed at 4 °C.

Table 2.17: StrepTactin®-affinity chromatography buffers

Buffer	Component	Concentration
A	Tris-HCl, pH 7.5	50 mM
	NaCl	200 mM
	Glycerol	8.6 %
B	Tris-HCl, pH 7.5	50 mM
	NaCl	500 mM
	Glycerol	8.6 %

2.3.4.4 Immobilized Metal Ion Affinity Chromatography (IMAC)

For isolation of the recombinantly expressed BetT1 fused N-terminally to a hexa-histidine tag (His_6-tag), Ni^{2+}-conjugated agarose beads (Qiagen) packed into a column were used. The desired protein binds by formation of a chelate complex between the Ni^{2+} ions and two histidine residues within the His_6-tag. This coordination can be displaced by elution with imidazole.

The supernatant of the solubilized membranes containing BetT1 was loaded on a preequilibrated 5 ml Ni^{2+} agarose column with a flow rate of 1 drop/5 sec. Two washing steps were applied with first 10 CV IMAC buffer with 0.1 % DDM followed by 10 CV IMAC buffer with 0.1 % DDM and 5 mM imidazole to remove unspecific bound proteins. Protein was eluted with a stepwise increase of imidazole from 5 mM to 150 mM per 2 CV in IMAC buffer with 0.1 % DDM. Fractions were collected and tested for protein content via Bradford assay. Fractions were checked additionally for contaminations by SDS-PAGE (Section 2.3.7.1) and aliquots with minor contaminations were pooled.

Table 2.18: IMAC buffer

Component	Concentration
Tris-HCl, pH 7.5	25 mM
NaCl	200 mM
Glycerol	10 %

2.3.4.5 Ion-exchange chromatography (IEX)

As a further purification step for proteins, ion-exchange chromatography can be performed. In this method, proteins are separated according to their net surface charge by binding to the column matrix with the opposite charge. The net charge of the protein is depending on the condition of the mobile phase. To elute the bound protein, the condition of the mobile phase is changed, most frequently by increasing the ionic strength (salt concentration). Consequently, salt ions will compete with the bound protein. Alternatively, conditions can be chosen to maximize the binding of contaminants, whereas the protein of interest passes through the column.

For further purification of BetT1 after IMAC, a cation-exchanger and an anion-exchanger, SP-Sepharose and Q-Sepharose, respectively, were tested. After equilibration of the respective columns with IEX buffer with 0.1 % DDM, the protein sample was loaded 2 – 3 times on the column. One washing steps was applied with 10 CV IEX buffer with 0.1 % DDM. Subsequent elution of the protein was performed by the stepwise increase of the NaCl concentration from 25 – 125 mM per 2 CV in IEX buffer with 0.1 % DDM. Flow trough and elution fractions were analyzed for protein content via the Bradford assay as well as by SDS-PAGE (Section 2.3.7.1). Fractions containing BetT1 were pooled.

Table 2.19: IEX buffer

Component	Concentration
Tris-HCl, pH 7.5	25 mM
NaCl	25 mM
Glycerol	10 %

2.3.4.6 Size-exclusion chromatography (SEC)

As further purification step for BetP crystallization, but also to remove imidazole after IMAC in case of BetT1, or to remove unbound spin label for PELDOR studies, preparative SEC was performed. For each application a Superose 6 10/300 column connected to a Äkta system was preequilibrated with the appropriate degassed Gelfiltration buffer (Table 2.20). 500 µl protein solution was loaded with a maximum concentration of 10 mg/ml onto the column and the flow rate was set to 0.3 - 0.4 ml/min. To detect the elution of the protein, the absorption at 280 nm was monitored while fractions of 300 – 400 µl were collected. Fractions with high protein content from the corresponding monodisperse peak were pooled.

Table 2.20: Gelfiltration buffers

Protein	Application	Component	Concentration
BetP	Crystallization	Tris-HCl, pH 7.5	25 mM
		NaCl	200 mM
		Cymal-5	0.6 %
BetP/	PELDOR/	Tris-HCl, pH 7.5	25 mM
BetT1	Crystallization	NaCl	200 mM
		DDM	0.1 %

2.3.5 Protein concentration

Protein was concentrated by centrifugation at 4°C using Vivaspin (Sartorius, MW cut-off 50 kDa) and Amicon Ultra (Millipore, MW cut-off 30 kDa) concentrator tubes according to manufacturer's instructions.

2.3.6 Determination of protein concentration

2.3.6.1 Bradford assay

The Bradford assay (Bradford, 1976) was applied for determination of the total protein concentration of a membrane or purified protein solution. As a component of the Bradford reagent (Sigma), the Coomassie Brilliant Blue G250 dye binds to basic amino acids (Arg, His, Lys) and interacts with hydrophobic amino acids (Phe, Tyr, Trp). As a result, the anionic form of the dye is stabilized

which is leading to a bathochromic shift of the absorption from 465 nm without bound protein to 595 nm with bound protein. The intensity of the blue coloration is directly proportional to the protein concentration. Diluted BSA with known concentration was used to prepare a standard curve, which allows the calculation of the unknown concentration of a protein sample by measuring the absorption at 595 and 465 nm.

2.3.6.2 Amido Black assay

To estimate the concentration of protein, reconstituted into liposomes, the Amido black assay (Schaffner and Weissmann, 1973) was applied. The total protein concentration down to 0.75 µg/ml can be measured with this colorimetric method. The qualitatively precipitated protein by trichloroacetic acid (TCA) is collected on membrane filters and stained with Amido black.

A 5 µl proteoliposome sample, diluted to the final volume of 225 µl with water, was mixed with denaturating buffer. Protein was precipitated by adding 90 % TCA (v/v). After mixing, the sample is incubated at room temperature for maximum 5 min. A filter (Millipore, HAWP02500, Ø 0.45 µm) was marked with circles for sample application and rinsed with water while suction was applied via a connected vacuum pump. 200 µl sample was loaded on each circle and directly washed with the same volume of 6 % (v/v) TCA. After all samples were applied the filter was rinsed completely with 1 – 2 ml of 6 % (v/v) TCA. The filter was stained for 2 – 3 min in Amido black solution, rinsed with water and then washed 2 – 3 min with destaining solution. The blue appearing spots containing protein were cut out and incubated with 1 ml of elution solution in a test tube at room temperature shaking for 10 min. The ODs of these samples as well as the prepared BSA standard curve (concentration range of 0 µg to 10 µg) were measured at 630 nm to calculate the protein concentration.

Table 2.21: Amido black buffers

Solution	Component	Concentration
Denaturating	Tris-HCl, pH 7.4	1 M
	SDS	2 % (w/v)
Amido black	Amido black	0.25 % (w/v)
	Methanol	45 % (v/v)
	Glacial acetic acid	10 % (v/v)
Destaining	Methanol	90 % (v/v)
	Glacial acetic acid	2 % (v/v)
Elution	NaOH	25 mM
	Na_2EDTA	50 µM
	Ethanol	50 % (v/v)

2.3.7 Polyacrylamide gel electrophoresis (PAGE)

2.3.7.1 Denaturing SDS-PAGE

Discontinuous SDS-PAGE under denaturing conditions was used to analyze the purity of a protein sample or production levels of protein of whole cell extracts according to Laemmli (Laemmli, 1970). Either 10 % or 12.5 % separating gels with 4 % stacking gels were prepared and stored until use at 4°C.

Table 2.22: SDS-PAGE gel mixture for 5 gels

Component	4 % Stacking gel	10/12.5 % Separating gel
0.5 M Tris-HCl, pH 6.8	5 ml	-
1.5 M Tris-HCl, pH 8.8	-	7.5 ml
40 % Acrylamide	2 ml	7.5/9.4 ml
10 % SDS	200 µl	300 µl
H_2O_{dd}	10 ml	14.7/12.7 ml
TEMED	20 µl	25 µl
10 % APS	100 µl	100 µl

The samples were mixed prior to electrophoresis with 4x sample buffer containing the anionic detergent SDS that denatures, linearizes and charges the proteins. For non-reducing SDS-PAGE, the sample was mixed with 4x sample buffer lacking the reducing reagent DTT. For electrophoresis, 80 V was applied until the sample enters the stacking gel, afterwards the voltage was increased to 120 V for approximately 1.5 h. Gels were used either for Western Blot or stained with Coomassie according to Studier (Studier, 2005). Therefore, the gel was boiled up in Solution I. After 10 min incubation under shaking at room temperature, Solution I was exchanged against Solution II with Coomassie

brilliant blue R250 solution. After the second heating, the stained protein bands appeared within some minutes and washing with water stopped staining.

Table 2.23: SDS-PAGE buffers

Buffer	Component	Concentration
Running	Tris-HCl, pH 7	25 mM
	Glycine	200 mM
	SDS	0.1 % (w/v)
4x Sample	Tris-HCl, pH 8	100 mM
	SDS	10 % (w/v)
	Glycerol	10 % (v/v)
	Bromphenol blue	1.6 % (w/v)
	± DTT	0.64 M

Table 2.24: Coomassie staining solutions

Solution	Component	Concentration
I	Ethanol	50 % (v/v)
	Acetic acid	10 % (v/v)
II	Ethanol	5 % (v/v)
	Acetic acid	7.5 % (v/v)
Coomassie stock	Ethanol	95 % (v/v)
	Coomassie brilliant blue R250	0.25 % (w/v)

2.3.7.2 Blue-Native-PAGE

To analyze undenatured proteins after purification, discontinuous Blue-Native (BN)-PAGE (Schägger and von Jagow, 1991) was performed using Coomassie blue G250, which induces a charge shift on the protein.

Before loading, the sample was mixed with loading dye and 4 – 16 % polyacrylamide Tris glycine gels (Invitrogen) were used. The electrophoresis was performed for 1 h at 100 V and 3 h at 200 V.

Table 2.25: BN-PAGE buffers

Buffer	Component	Concentration
Anode	Bis Tris, pH 7	50 mM
Cathode	Tricine	50 mM
	Bis Tris, pH 7	15 mM
	Coomassie Blue G250	0.02 % (w/v)
Loading dye	Coomassie Blue G250	5 % (w/v)
	Glycerin	10 % (v/v)
	Bis Tris, pH 7	100 mM

2.3.8 Western blot analysis

Western blot analysis was performed for immuno-detection of proteins separated by SDS-PAGE. Therefore, proteins from an SDS gel were transferred to a PVDF membrane (Millipore) via the ''semi-dry'' method (Kyhse-Andersen, 1984). Afterwards the target protein can be detected with specific antibodies.

The methanol-activated PVDF membrane and SDS gel were arranged between transfer buffer soaked 3MM filter paper (Whatman). Blotting was carried out in a Western Blot machine for 30 min at 15 V. Afterwards, the PVDF membrane was incubated for 1 h at room temperature in blocking buffer to prevent unspecific antibody binding. For immuno-detection, the PVDF membrane was washed 3 times with TBS buffer and incubated with the first antibody for 1.5 h at room temperature or overnight at 4°C. For BetP, in mouse produced anti-Strep-tagII IgG1 (IBA, 1:3000 dilution in TBS buffer) and for BetT1 in mouse produced monoclonal anti-polyHistidine antibody (Sigma, 1:2500 dilution in TBS buffer) was applied. Prior to the exchange against the second antibody, the membrane was washed 3 times with TBS buffer. The Anti-mouse IgG alkaline phosphatase conjugated antibody (Sigma, 1:5000 dilution in TBS buffer) produced in rabbit was used as second antibody and additionally incubated for 1 h at room temperature. After the PVDF membrane was washed subsequently with TBS buffer, one tablet SigmaFast™ BCIP/NBT (Sigma) dissolved in 10 ml water was added until the specific protein bands were visualized. The PVDF membrane was washed with water to stop the reaction.

Table 2.26: Western blot buffers

Buffer	Component	Concentration
Transfer	Tris-HCl, pH 8	25 mM
	Glycine	10 mM
	Methanol	10 % (v/v)
	DTT	0.25 mM
TBS	Tris-HCl, pH 7.5	5 % (v/v)
	NaCl	7.5 % (v/v)
Blocking	TBS buffer	1 x
	BSA/milk powder	3/5 % (w/v)

2.3.9 Protein reconstitution

2.3.9.1 Protein reconstitution for transport measurement

Functional reconstitution of BetP WT and mutants as well as BetT1 were performed as described by Rigaud and Rübenhagen (Rigaud *et al.*, 1995; Rübenhagen *et al.*, 2000) using *E. coli* polar lipid extract (Avanti). Therefore, an *E. coli* polar lipids aliquot in chloroform:methanol was dried under a nitrogen stream and subsequently resuspended in the corresponding lipid buffer to a concentration of 20 mg/ml. Aliquots of 800 µl were frozen in liquid nitrogen and stored at -80°C until use.

After thawing, one aliquot *E. coli* polar lipids were prepared by extrusion through a filter (polycarbonate membrane, pore size Ø 400 nm, Avestin) and diluted 1:4 with lipid buffer. In case of crosslinking studies, lipid buffer without the reducing agent was used. The solution was further titrated with 10 % (w/v) Triton-X-100 to the start of solubilization while measuring the absorbance at 540 nm. Afterwards, purified BetP or BetT1 was added to the lipid solution in a lipid to protein ratio (LPR) of 30:1. Prior to the addition of BioBeads® SM-2 (Bio-Rad) at ratios (w/w) of 5 (BioBeads/Triton X-100) and 10 (BioBeads/DDM), the lipid protein mixture was incubated for 30 min at room temperature. The BioBeads were added in 5 steps to remove detergent, whereas the last step was performed overnight at 4°C. At the next day, the proteoliposomes were washed twice with lipid buffer by centrifugation at 70000 rpm at 20°C for 20 min. Finally, the proteoliposomes were resuspended in lipid buffer to a concentration of 60 mg/ml before freezing in liquid nitrogen. Aliquots of proteoliposomes were stored at -80°

Table 2.27: Lipid buffers for reconstitution for transport measurements

Protein	Component	Concentration
BetP	KP_i, pH 7.5	100 mM
	TCEP	2 mM
BetT1	KP_i, pH 7.5	100 mM

2.3.9.2 Protein reconstitution for PELDOR

For PELDOR application, *E. coli* polar lipids were dried under a nitrogen steam and resuspended subsequently in the corresponding lipid buffer to the final

concentration of 20 mg/ml. Lipids were split in 800 µl aliquots and frozen in nitrogen for storage at -80°C until use.

For reconstitution of spin labeled BetP mutants, several aliquots of *E. coli* polar lipids were thawed, extruded through a polycarbonate membrane filter (pore size Ø 400 nm, Avestin), diluted and titrated to the onset of solubilization by adding 10 % (w/v) Triton X-100. Spin labeled protein was added to the lipid solution with a LPR of 20:1 and incubated for 30 min at room temperature. Afterwards, the lipid protein solution was transferred into a dialysis membrane (MW cut-off 12 – 14 kDa, Spectrumlabs). BioBeads® SM-2 (Bio-Rad) at ratios (w/w) of 5 (BioBeads/Triton X-100) and 10 (BioBeads/DDM) were added to the dialysis buffer in 4 steps. The last step was performed overnight at 4°C. The following day, the proteoliposomes were centrifuged for 20 min at 75000 rpm and 20°C. One half was resuspended before extrusion in Tris_inactive, the other part in Tris_active$_{in}$ buffer. After the next centrifugation (100000 rpm, 20°C, 20 min), the proteoliposomes were resuspended accordingly in Tris_inactive or Tris_active$_{out}$ buffer to a maximum volume of 75 µl. The samples were used to determine the spin label concentration by cw-EPR, prior to the investigation by PELDOR.

Table 2.28: Reconstitution buffers for PELDOR

Buffer	Component	Concentration
Lipid	Tris-HCl, pH 7.5	200 mM
Tris_inactive	Tris-HCl, pH 7.5	200 mM
(in D_2O)	NaCl	500 mM
Tris_active$_{in}$	Tris-HCl, pH 7.5	200 mM
(in D_2O)	KCl	300 mM
Tris_active$_{out}$	Tris-HCl, pH 7.5	200 mM
(in D_2O)	NaCl	300 mM
	Proline	350 mM
	Betaine	5 mM
	Valinomycin	1 mM

2.3.10 Transport measurements

2.3.10.1 Transport measurements in *E. coli* MKH13 cells

Uptake measurements of [^{14}C]-labeled substrates in *E. coli* MKH13 cells lacking endogenous transporter for compatible solutes were performed as described previously (Ott *et al.*, 2008). *E. coli* MKH13 were first transformed with the

according vector DNA for expression of strep-*betP* variants, His-*betT1* and His-*betT2*. The transformed *E. coli* MKH13 were cultivated in LB supplemented with 50 µg/ml carbenicillin. Protein production of BetP variants were induced through the addition of 200 µg/l AHT at an OD_{600} of 0.5 and cells were harvested after 2 h. Cells were washed in buffer Ax and finally resuspended in buffer Ax containing 20 mM glucose to an OD_{600} of 2. Protein production of BetT1 as well as BetT2 was induced at OD_{600} 0.6 - 0.8 by adding 0.02 % arabinose and cells were further cultivated for 2.5 h. Next, cells were washed with buffer Ax with or without 100 mM NaCl and resuspended in the same buffer with additional added 30 mM glucose to an OD_{600} of 3. Prior to the incubation of cells for 3 min at 37°C, cells were diluted 1:1 with the corresponding buffer for uptake measurements. Uptake was started by the addition of 250 – 500 µM [^{14}C]-labeled substrates. For K_m and V_{max} determination, the concentration of the [^{14}C]-labeled substrates was varied and different external osmolalities were adjusted by the addition of KCl. At various intervals, samples were passed through glass fiber filters (Millipore), washed twice with 2.5 ml 0.6 mM KP_i buffer and the radioactivity retained on the filters were subsequently determined by a scintillation counter TRI-CARB 1500 (Canberra-Packard). For data analysis, Michaelis-Menten kinetics were applied for curve fitting of the uptake rates versus the substrate concentration with GraphPad Prism version 5.0c for Mac OS X, GraphPad Software (Motulsky, 1999).

Table 2.29: Buffers applied for *E. coli* MKH13 cell transport measurements

Buffer	Component	Concentration
KP_i, pH 7.5	K_2HPO_4	814 mM
	KH_2PO_4	186 mM
Ax	KP_i, pH 7.5	25 mM
	± NaCl	100 mM

2.3.10.2 Transport measurements in proteoliposomes

Uptake measurements of [^{14}C]-labeled glycine betaine were performed as described previously by Rübenhagen (Rübenhagen *et al.*, 2000). Therefore, proteoliposomes were extruded in internal buffer through a filter with a pore size of 400 nm (polycarbonate membrane, Avestin), collected by centrifugation (70000 rpm, 20 min, 20°C) and subsequently resuspended to a lipid

concentration of 60 mg/ml. For crosslinking studies, to prevent reduction, the standard internal buffer was used for extrusion. To reduce cysteine disulfide bonds, $internal_{red}$ buffer was applied during extrusion. Uptake measurements were initiated by diluting proteoliposomes in a ratio of 1:200 in osmotic buffer containing 15 µM [^{14}C]-labeled glycine betaine as substrate and valinomycin creating an outward driven K^+ diffusion potential. The external osmolalities of the osmotic buffer were adjusted by adding proline. At time points of 5 and 10 sec, samples were filtered through 0.22 µM nitrocellulose filters (Millipore) and washed once with 2 ml of 100 mM LiCl. Determination of [^{14}C]-glycine betaine, which was incorporated into the proteoliposomes during uptake, was performed by scintillation counting.

Table 2.30: Buffers applied for transport measurements in proteoliposomes

Buffer	Component	Concentration
internal	KP_i, pH 7.5	100 mM
$internal_{red}$	KP_i, pH 7.5	100 mM
	TCEP	2 mM

2.3.11 Crosslinking via disulfides

The effect of site-directed crosslinking on the oligomerization and regulation were investigated for N- and C-terminal BetP mutants. Therefore, the property of cysteine residues was used, which crosslink by the formation of disulfide bridges under oxidative conditions, if two residues are localized close to each other. Furthermore, the disulfide bound could be cleaved easily by the addition of a reducing agent.

Crosslinking was performed for purified protein or protein within the *E. coli* membranes. For the oxidation of the cysteine residues, 100 µg or for reconstitution 500 µg protein was mixed with 100 µM CuPh (copper-o-phenanthroline). To 150 µg membranes were added either 100 µM or 1 mM CuPh. Samples were incubated for 1 h at room temperature. By the addition of 2 mM TCEP, the reverse effect leading to the reduction of disulfide bond was obtained. Oxidized or reduced samples were mixed with non-reducing sample buffer (Table 2.23) for SDS-PAGE and could be further analyzed by immuno-

blotting against the N-terminal Strep-tag®II. Oxidized protein was then used for reconstitution into liposomes.

2.3.12 Site-directed spin labeling and detergent sample preparation

The basic requirements to study biomacromolecules with diverse EPR techniques are paramagnetic centers in form of unpaired electrons. Because the natural occurrence of these paramagnetic centers is limited, site-directed spin labeling (SDSL) provides assistance in the investigation of proteins. Therefore, amino acids at desired position within the protein sequence have to be replaced into cysteine residues by site-directed mutagenesis. During spin labeling, sulfhydryl groups of the cysteine residue react by the formation of disulfide bounds with the functional group of the spin label.

For BetP cys-mutant protein, derived from StrepTactin®-affinity chromatography, first a buffer exchange into labeling buffer was performed using a PD-10 desalting column (GE Healthcare) according to manufactur's instruction by the spin protocol. Next, protein was diluted to the concentration of 1.5 mg/ml and the 30-fold molar access of the spin label MTSL or MMTSL (Toronto Research Chemicals) dissolved in DMSO or methanol, respectively, was added. Spin labeling was conducted over night in batch at 4°C. Next day, the free spin label was removed by SEC as described in Section 2.3.4.6. After SEC, protein was either used for reconstitution of labeled protein (Section 2.3.9.2) or further prepared for measurements directly performed in detergent. Therefore, protein was split to exchange buffer via Zeba™ Spin Desalting Columns (Thermo Scientific) into Tris_active$_{DDM}$ and Tris_inactive$_{DDM}$ buffer. Protein was concentrated up to 15 mg/ml and final protein concentration was determined by Bradford assay. Prior to PELDOR measurements, room temperature cw (continuous wave) –EPR was performed to elucidate the spin label concentration.

Table 2.31: Buffer conditions for SDSL and PELDOR

Buffer	Component	Concentration
Labeling	Tris-HCl, pH 7	50 mM
	NaCl	200 mM
	DDM	0.1 % (w/v)
Tris_inactive$_{DDM}$	Tris-HCl, pH 7.5	25 mM
(in D_2O)	NaCl	500 mM
	DDM	0.1 % (w/v)
Tris_active$_{DDM}$	Tris-HCl, pH 7.5	25 mM
(in D_2O)	NaCl	200 mM
	KCl	300 mM
	Betaine	10 mM
	DDM	0.1 % (w/v)

2.4 Biophysical methods

2.4.1 Freeze fracture electron microscopy

In Freeze fracture, a frozen biological sample is fractured and by building a replica of the fractured surface using vacuum-deposition of platinum/carbon, structural details of the fractured plane could be visualized in electron microscopy.

A proteoliposome sample was pelleted by centrifugation and pipetted between two cooper plates. The sample was rapidly frozen in liquid ethane at -180°C and transferred into liquid nitrogen. The frozen sample was fractured using a BAF 060 machine (Bal-Tec) at a temperature of -130°C and a pressure of 1.5 x 10^{-7} mbar. To make the replica, the fractured planes were vaporized with platinum/carbon first and with pure carbon afterwards. As a next step, the replica was cleaned in 40 – 50 % (v/v) of chromosulfuric acid (2 – 5 % $Na_2Cr_2O_7$ in ~ 90 % H_2SO_4) for 16 h at room temperature to remove the biological material. The next day, the replicas were washed with water and investigated in an EM208S electron microscope (FEI Company, USA) at 80 kV. Images were collected on a 1K & 1K slow-scan CCD camera (Tietz Video & Image Processing Systems) with 1024 x 1024 pixel. All required steps for Freeze fracture were performed by Susann Kaltwasser at the MPI of Biophysics.

2.4.2 X-ray crystallography

X-ray crystallography is the most powerful method to obtain the three-dimensional structures of proteins at atomic resolution. A purified protein sample is crystallized and the resulting crystals are exposed to an X-ray beam generating a diffraction pattern. The diffraction pattern is a two-dimensional array of spots due to the scattered radiation by the diffraction lattice of the highly regular arranged molecules in the crystal. This pattern is processed further and the intensity of the spots are used to determine the "structure factors" to calculate the electron density map from which the molecular structure of the protein can be built.

2.4.2.1 Crystallization

The challenging task in protein structure determination by crystallography is to obtain crystals diffracting at high resolution. During the crystallization process, crystal grow from aqueous protein solution under supersaturating conditions (Chayen, 2004). The phase diagram (Figure 2.1) represents how the protein concentration is related to an adjustable parameter like the precipitant concentration (salts, organic compounds and polyethylene glycol polymers). In the unsaturated region, low protein and low precipitant concentration prevent crystal grow, because the protein is fully dissolved. In contrast, too high protein as well precipitant concentration lead to protein precipitation characterized by the precipitation zone. In the nucleation zone, adequate high concentrations of protein and precipitant induce spontaneous nucleation starting crystal formation. During crystal growth, protein concentration drops to the metastable zone. This is the best region for the growth of well-ordered and stable crystals (Chayen, 2004). The metastable zone is separated from the region of undersaturation by the solubility curve.

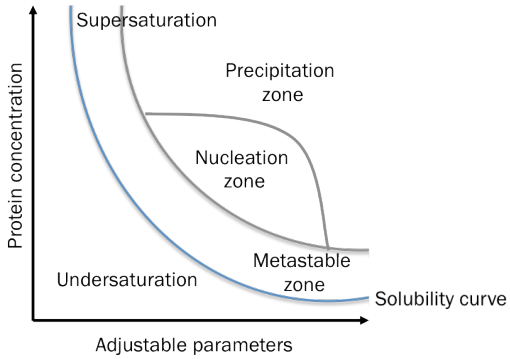

Figure 2.1: Phase diagram for protein crystal growth.
The crystallization can be illustrated as a phase diagram, which is divided in four zones representing different degrees of supersaturation. In the precipitation zone, the protein will precipitate. In the nucleation zone, spontaneous crystal nucleation occurs. In the metastable zone, crystals are formed and in the zone of undersaturation, the protein will never crystallize. As adjustable parameter can be varied the concentration of precipitant and additives, pH, temperature and other parameters versus the protein concentration (adapted from Chayen, 2004).

Protein crystallization demands a slow change of the precipitant concentration, which is ensured by the widely used method of vapor diffusion in form of sitting as well as hanging drop (Chayen and Saridakis, 2008). The latter set-up was applied in this work. Here, the protein solution in the drop is mixed with a suitable buffer and precipitant. In a closed system, the drop equilibrates against the reservoir containing the similar buffer and precipitant in higher concentration (Figure 2.2). The precipitant concentration in the droplet is initially insufficient for crystallization. Because the concentration in the bigger reservoir solution is higher, water evaporates gradually from the drop to the reservoir increasing the concentration to an optimal condition for crystallization. This optimal level in equilibrium is maintained until the crystallization process finished (McRee, 1993).

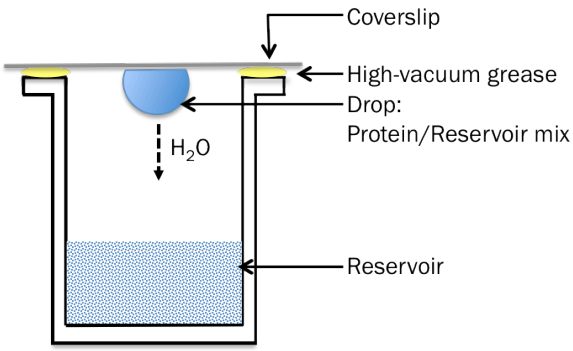

Figure 2.2: Schematic representation of the vapor diffusion method as hanging drop for crystallization.
Reservoir solution (blue pattern) contains suitable buffer and precipitant in appropriate concentration. The protein solution is mixed with the same reservoir solution comprising consequently a lower concentration. The protein/reservoir mix is placed as a drop on an inverted coverslip opposite to the reservoir. In a closed system ensured by the high-vacuum grease, water diffuses from the drop with lower compound concentration to the reservoir with higher concentration to reach equilibrium.

For crystallization of BetT1, the hanging drop vapor diffusion method was used. The initial screening for appropriate crystallization conditions were performed with commercial available screens (Section 2.1.8) in 96-well hanging drop plates. The reservoir solution of 100 µl in the 96-well plates was manually filled. The crystallization set-up of 300 nl protein (10 mg/ml) mixed with 300 nl reservoir solution as drop were carried out by the *Mosquito*™ pipetting robot.
Crystallization conditions were further optimized in 24-well plates (Hampton Research). In this case, 1 ml manually prepared and optimized crystallization condition were used as reservoir solution. The drop ratio was varied from 1 µl protein solution (10 mg/ml) plus 1 or 2 µl reservoir solution. Protein solution was incubated partially with 2.5 mM of the substrate choline for 30 min prior to crystallization. The crystallization plates were incubated at least for two weeks at 18°C.

2.4.2.2 Cryocrystallography

The technique of cryocrystallography has emerged as an indispensable tool in crystallography due to the reduction of X-ray induced radiation damage by flash-cooling of protein crystals to near 100 K, compared to room temperature. Dose-dependent primary radiation damage cause an energy lost by direct interactions

between the beam and the molecules within the crystal, which leads to heat (thermal vibration of molecules) and to bond breaking between the atoms. Secondary damage is induced by radicals formed by direct damage of the polypeptide and indirect by water destruction (H*, OH*) diffusing through the crystal at room temperature. This is causing further destruction in a time- and temperature-dependent manner. At low temperature, the reactive species is immobilized leading to no further damage to areas, which are not exposed to the beam. Therefore, crystals were frozen in liquid nitrogen and measured at cryogenic temperature (Garman, 1999).
Flash-cooling requires a crystal held by surface tension in a fiber loop in a suitable cryobuffer containing an cryoprotectant. This cryoprotectant, typically a water-soluble organic material (PEG, glycerol, sucrose), reduces the overall freezing point of the solution as well as prevents the formation of ordered ice. In contrast, the cryobuffer forms a vitreous solid, which does not disrupt the crystal order and interfere with the diffraction (Garman, 1999).

BetT1 crystals were transferred from the crystallization drop into a nylon loop (Molecular Dimensions) of appropriate size. The cryoprotection was ensured by the mother liquid already containing PEG or by immersion of the crystal in additional PEG prior to freezing in liquid nitrogen.

2.4.2.3 Basic principles of X-ray crystallography

A crystal can be described as regular array of molecules in a three-dimensional space. The molecules are packed in a periodic and repeating manner with the unit cell as the smallest repeating part forming the crystal lattice. Three vectors (a, b and c) together with the three angles α, β and γ characterize the unit cell and define the seven main crystal systems namely, triclinic, monoclinic, orthorhombic, tetragonal, hexagonal and cubic (Miller and Tanner, 2008). A number of asymmetric units referring to one or more copies of a molecule in conjunction with symmetry operations like rotations and possible translations again assemble the unit cell.
The crystal lattice is described as an infinite array of points repeated periodically in the three-dimensional space such that the surrounding points are arranged in

an identical way (Sheehan, 2009). There are fourteen types of lattices known as Bravais lattices possible by coupling one of the seven crystal systems with lattice centering operations. If lattice points lie at the vertices at the unit cell, they are referred as primitive (P). Additional lattice points at the center of the single face, all faces or center of the unit cell result in a centered (A, B or C), face-centered (F) or body-centered (I) lattice, respectively. The symmetry of the lattice can be defined by different symmetry operations leading to 32 symmetry classes also called point groups (Messerschmidt, 2007). Due to the chirality, the symmetry classes of protein crystals are reduced to 11, because only 2-fold (180°), 3-fold (120°), 4-fold (90°) and 6-fold (60°) rotational symmetry is allowed. The number n of the rotation axes and the angle ϕ are related by $\phi = (360/n)°$.
The space group is build from the combination of the Bravais lattice symmetry and the point group providing a complete description of the crystal symmetry. Of total 230 different space groups only 65 are possible for chiral protein molecules (Ilari and Savino, 2008). For example, BetP crystallizes in the orthorhombic $P2_12_12_1$ space group with two-fold screw axis (180°) along a, b and c followed by a translation of ½ of the lattice vector.

X-ray diffraction involves the coherent interference of scattered X-ray radiation. X-rays are scattered by electrons of a crystal, if the wavelength of the radiation is comparable to the interatomic distances (~ 0.15 nm). The diffraction of the X-rays can be treated as reflections from parallel planes of atoms in a crystal (Miller and Tanner, 2008). These crystal lattice planes are defined by the Miller indices hkl. Bragg´s law illustrates the relation between the scattering angel θ of the rays and the distance between the planes (Figure 2.3). According to this law, constructive interference occurs only if the path length difference between rays diffracting from the parallel planes equals an integer number of the wavelength:

$$n\lambda = 2d * sin\theta$$

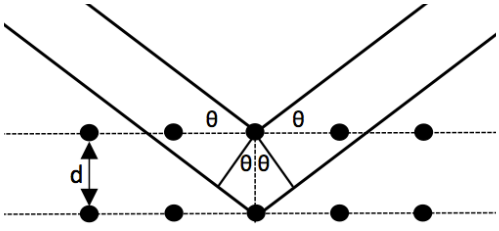

Figure 2.3: Conditions for constructive interference: Bragg's law.

The X-rays scattered by crystal planes with an angle of θ interfere constructively when the distance (d) between the rays equals an integer number (n) of the wavelength (adapted from Sheehan, 2009).

The Ewald sphere construction provides a geometrical description of Bragg´s law. The crystal is represented by a reciprocal lattice, because the distances are related reciprocally to points in the crystal lattice and accordingly to the unit cell dimensions. An Ewald sphere is constructed by a circle with the radius of 1/λ centered at the point C standing for the crystal. An incident X-ray directed toward the origin O of the reciprocal lattice diffract at the point C (Miller and Tanner, 2008; Sheehan, 2009). When a reciprocal lattice point lies at the surface of the Ewald sphere, where the reflected beam intersects the cycle, the interference condition is fulfilled (Figure 2.4) (Dauter, 1999). To bring more reflections into diffraction, the crystal has to be rotated leading as well to the rotation of the reciprocal lattice. Since all diffracted rays from the same plane form a cone, the diffraction pattern will consist of spots arranged in concentric ellipses (Dauter, 1999).

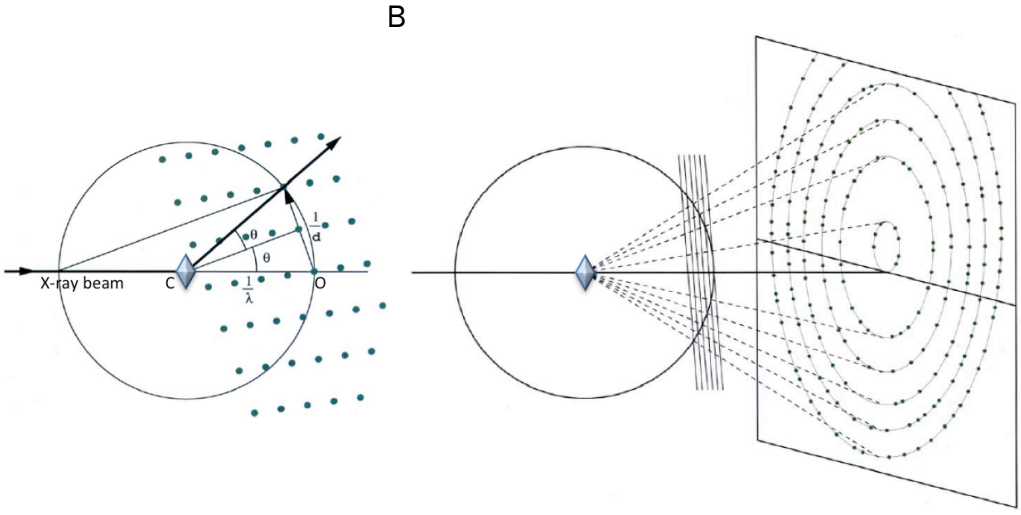

Figure 2.4: The Ewald construction and diffraction pattern.
A) The Ewald construction shows that the constructive interference occurs when a reciprocal lattice point coincides with the sphere of a radius 1/λ. The condition 1/d = (2/nλ) sinθ corresponding to the Bragg´s law nλ = 2d sinθ is fullfiled. B) In a diffraction pattern, spots are separated in ellipses as a consequence of constructive interference of X-rays diffracted by planes of the crystal (adapted from Dauter, 1999).

2.4.2.4 Data collection

Crystals of BetT1 were tested at the Max Planck Society beamline at the Swiss Light Source (SLS, Villingen, Switzerland) PXII-X10SA. The beamline is designated for high-intensity and high-energy resolution measurements over a wide range of X-ray wavelengths (0.6 – 2.1 Å). Crystal diffraction screening was performed under a steady cryo-stream and three test images were collected each 60° or 90° apart.

2.4.3 Electron Paramagnetic Resonance

Electron paramagnetic resonance (EPR) in combination with site-directed spin labeling is a widely used spectroscopic technique to study sequence-specific secondary structures, define topologies, tertiary folds and measure distances within biomolecules like proteins (Mchaourab *et al.*, 2011). In contrast to the challenging crystallization of membrane proteins for structure determination, EPR methods are suited to obtain structural information and in particular dynamic data of membrane proteins in more native-like environment. Pulsed EPR methods enable to monitor protein motions by spin labeled (membrane) proteins. In order to examine structural changes of proteins, distances between spin label pairs could be measured via magnetically dipolar coupled electrons.

2.4.3.1 Basic principles of EPR

EPR is a spectroscopic method, which is based on the absorption of electromagnetic radiation by paramagnetic species. Paramagnetic substances like triplet state and radical pair molecules in photosynthesis, transition metal ions and free radicals are characterized by an unpaired electron (Lund *et al.*, 2011), which possess a permanent magnetic dipole. The negatively charged electron is described by two movements. The electron rotates around its nucleus leading to an orbital angular momentum, whereas spinning around its own axis leads to an intrinsic (spin) angular momentum, the latter contributing primarily to the arising magnetic momentum. The magnetic momentum is directly proportional to the spin angular momentum. The orientation of the magnetic

momentum of the electron is collinear but antiparallel to the spin itself (Murphy, 2009). An electron exhibit a spin quantum number s of ½ with its magnetic component $m_s = \pm ½$ describing the orientation of magnetic momentum in a magnetic field. The electron's magnetic moment is able to align either antiparallel ($m_s = +½$) or parallel ($m_s = -½$) to an external applied magnetic field. This energy difference or Zeemann splitting in presence of a magnetic field B_0 depends on the strength of the field as well as the g value (g_e for the free electron) (Figure 2.5 A). According to the Boltzmann distribution, more spins are typically in the lower energy state. The transition between these levels could be described as absorption of energy in form of electromagnetic radiation in a certain resonance frequency, which depends on the applied magnetic field strength. It has to be noted, that on the energy scale of Q-band frequency (33.5 GHz), the difference between the levels is less than 1 percent and the typical energy absorption scheme like in the optic spectroscopy is not valid anymore.

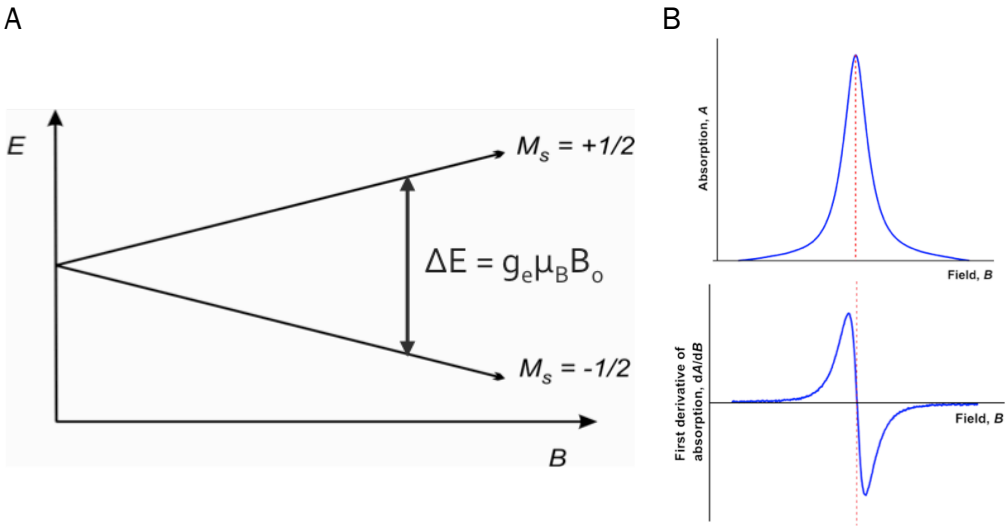

Figure 2.5: Zeeman splitting and EPR absorption spectrum.
A) The energy levels of an electron in an external applied magnetic field B_0 split according to the spin quantum number m_s and can be described as following term: $E = m_s g_e \mu_B B_0$ with μ_B being the Bohr's magneton, g_e being the so called g-factor for a free electron (g_e = 2.0023). m_s can have two values (½ or -½) resulting in two energy levels and a possible transition between them with the following transition energy: $\Delta E = g_e \mu_B B_0 = h\nu$. B) The energy, which is required for the transition between the energy levels, is measured as the first derivative of the absorption. The absorption maximum corresponds to the point where the spectrum passes through zero and is further used to determine the center of the signal (Murphy, 2009).

2.4.3.2 Cw-EPR

In this work, only two of several diverse EPR methods were applied. Conventional continuous wave (cw) -EPR was used to estimate the spin label efficiency of protein samples in detergent or reconstituted into liposomes.
In a cw-EPR experiment, the frequency of the applied microwave radiation is kept constant while the magnetic field generated by an electromagnet is changed (swept) and modulated with an additional small magnetic field (Murphy, 2009). When the magnetic field corresponds to the resonance, ''energy is absorbed''. In a cw-EPR set-up, the microwaves are provided from a microwave source and transferred through waveguides to the resonator cavity containing the sample. The cavity is designed corresponding to the wavelength of the specific applied frequency. This allows the microwave to resonate the cavity and absorption by the sample leads to reflected microwaves, which are converted by the detector in a low frequency signal to monitor the change of the microwave. This ''absorption of energy'' dependency of the magnetic field is converted into a spectrum, which is the first derivative as a result of the additional field modulation and the phase-sensitive detection (Figure 2.5 B) (Lund *et al.*, 2011).

EPR experiments are conducted at different fields and frequency like for X-band frequency at 9.5 GHz and the typical field for organic radicals of 0.34 T. In the past higher field/higher frequency EPR measurements were not commonly carried out due to technical reasons. Nowadays Q-band (34 GHz/1.2 T) and W-band (95 GHz/3.4 T) spectrometers are commercial available and lead to an easier access of better spectral resolution and higher sensitivity of high field/high frequency spectrometers, which is in particular interesting for samples of limited quantity (Murphy, 2009).

2.4.3.3 PELDOR

The main application in this thesis was the distance measurements between spin labels with the pulsed EPR method named PELDOR standing for pulsed electron-electron double resonance also known as DEER (double electron-electron resonance). Here, a sample is exposed to a series of short intense microwave

pulses (Figure 2.6 A, top sequence at frequency ν_A), which is making the instrument sensitive for changes at one (spin A) of two dipolar coupled spins. The frequency of this microwave pulse (ν_A) are referred as detection pulses while the second frequency (ν_B) is the inversion pulse (Reginsson and Schiemann, 2011a; Reginsson and Schiemann, 2011b). If the second frequency is in resonance with the second spin (spin B) of the coupled spin pair, the sensitized instruments detect a change. The change is correlated to the position of the pump pulses within the whole pulse sequence, which is the recorded PELDOR time trace. The detection pulse sequence of π/2 (90°) and first π (180°) pulse generate a Hahn echo, another π pulse leads to a refocus of the echo (Figure 2.6 C). The inversion pulse π inverts meanwhile the magnetic moments of the second spin B. If both spins are coupled via magnetic dipolar interactions, the intensity of the refocused echo will be affected (Reginsson and Schiemann, 2011a).

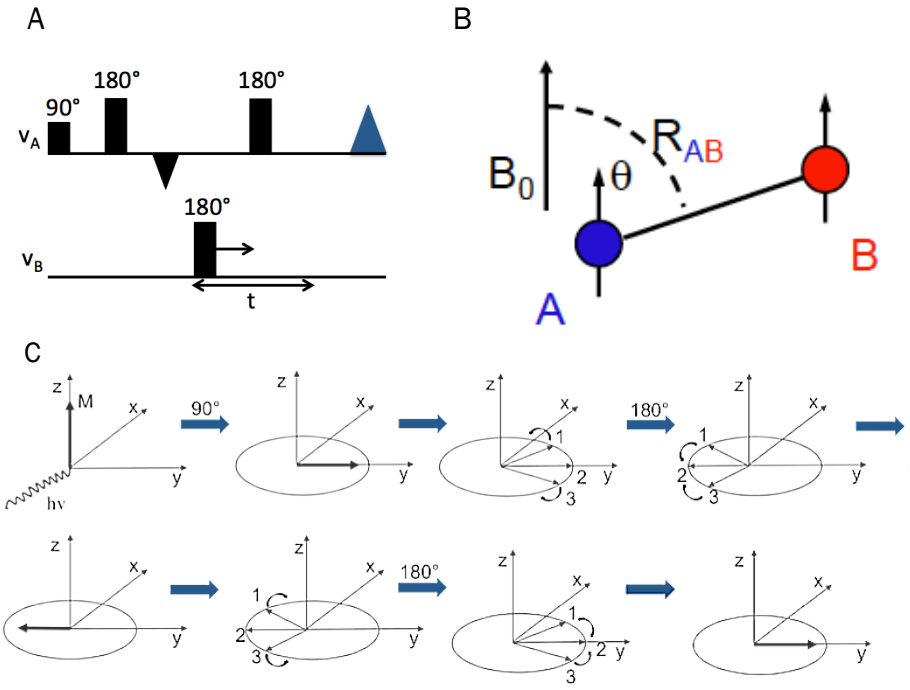

Figure 2.6: PELDOR experiment.

A) The 4-pulse PELDOR sequence consists of the three detection pulses and single inversion pulse of frequency ν_A and ν_B, respectively (adapted from Reginsson and Schiemann, 2011a). B) The dipolar coupling depends on the distance between the spins A and B (R_{AB}) and the angle θ within the magnetic field B_0. C) Vector model for the spin reorientation by the detection pulses in the rotating frame. The first detection pulse of 90° flips the spins into the xy-plane. During dephasing, the spin packages rotate around the z-axis leading to a decay of magnetization through slight different resonance frequencies. The second 180° pulse flips the spins back to the y-axis refocusing the spins, again running together, generating a magnetization in form of a spin echo.

Because the spins are dephasing after the pulse end, the third detection pulse reverses the spins to create a refocused echo, which could be affected by dipolar coupling (Reginsson and Schiemann, 2011a) (adapted from Lund *et al*., 2011).

If a biomolecule contains two unpaired electrons, the dipolar coupling ω_{dd} is described by the spin Hamiltonian

$$\widehat{H}_{dd} = \omega_{dd} = 2\pi\nu_{dd} = -\frac{\mu_0 g_A g_B \mu_B^2}{4\pi\hbar}\frac{1}{R^3}\,(3cos^2\theta - 1)$$

$$|\omega_\perp| = 2\pi|\nu_\perp| = \frac{\mu_0 g_A g_B \mu_B^2}{4\pi\hbar}\frac{1}{R^3}$$

where μ_0 is the vacuum permeability, μ_B is the Bohr's magneton, $\hbar$ is the reduced Planck constant, R is the length of the distance vector between the spins with θ being the angle between the distance vector and the magnetic field, because each molecule has a specific orientation in a frozen sample. $\nu_\perp$ is the frequency for the perpendicular ($\theta = 90°$) orientation. For nitroxides g_A =g_B=2.006 are leading to

$$|\nu_\perp|[MHz] = \frac{52.16}{R^3[nm]}$$

$$R[nm] = \sqrt[3]{\frac{52.16}{|\nu_\perp|[MHz]}}$$

In a PELDOR experiment, dipolar coupling leads to an oscillation of the amplitude V(t) of the refocused echo as a function of t (position of the inversion pulse within the pulse sequence). Considering PELDOR not being a single-molecule experiment, the signal V(t) is the product of the interaction between spins in one molecule $V(t)_{intra}$, whereas $V(t)_{inter}$ takes into account the signal decay caused by the interaction between spins in different molecules. Dividing V(t) by the background decay $V(t)_{inter}$ results in the modulated intramolecular signal $V(t)_{intra}$ (Figure 2.7 B). Fourier transformation of $V(t)_{intra}$ reveals a so called dipolar Pake pattern (Figure 2.7 C) (Schiemann *et al.*, 2007). Substitution of the frequency at

$\theta_{\perp}$=90° into the latter equation yields the distance R between the spins. Thus, the frequency of the oscillation is the dipolar coupling between the spins.

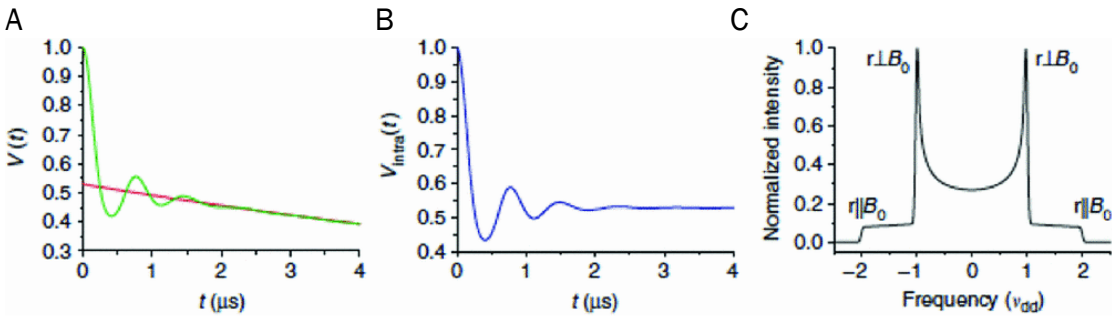

Figure 2.7: Representation of the PELDOR signal.
A) The PELDOR time trace V(t) = $V(t)_{intra}$ $V(t)_{inter}$ obtained in a PELDOR experiment in green whereas the red line represents the fitted intermolecular contribution of the background decay $V(t)_{inter}$. B) $V(t)_{intra}$ after division of V(t) by $V(t)_{inter}$. C) Pake pattern as a result of Fourier transformation if $V(t)_{intra}$ (Schiemann *et al.*, 2007).

In order to obtain the distance distribution function P(R), the PELDOR time traces are nowadays commonly analyzed with the software program DeerAnalysis from G. Jeschke, which is based on the Tikhonov-regularization instead of Fourier Transformation (Jeschke *et al.*, 2006).

In this work, PELDOR spectra were recorded on a Bruker EleXsys E580 spectrometer. The typical set-up included a pump frequency, which was set to the center transition of the nitroxide EPR spectra as well as to the center of resonator mode (typically 9.68 GHz at X-Band or 33.7 GHz at Q-Band). The detection was set to 70 MHz offset larger than the pump frequency (X-Band) or 56 MHz offset smaller than the pump frequency (Q-Band), off-center to the cavity mode. A typically pump pulse of 12 ns (X-Band) or 20 ns (Q-Band) and detection pulses of 32 ns (both bands) were applied. The 4-pulse sequence with tau averaging at a temperature of 50 K was utilized. Analysis of the PELDOR data was performed by Tikhonov-regularization derived distance distribution.

Cw-EPR and PELDOR measurements as well as the corresponding data analysis were performed in collaboration by Dr. Burkhard Endeward, Dr. Haleh Hashemi Haeri and Dr. Philipp Spindler in the group of Prof. Dr. Thomas Prisner (Goethe University, Frankfurt).

2.4.3.4 Site-directed spin labeling of proteins

Since the natural occurrence of paramagnetic centers is limited, the introduction of spin labels containing paramagnetic species became a powerful tool to probe structure and structural changes of proteins. Here, cysteine residues replace amino acids at desired positions during site-directed mutagenesis. Posttranslational spin labeling is leading to the formation of disulfide bonds between the sulfhydryl groups of the cysteines reacting with the functional group of the label. Spin labels like methanothiosulfonate (MTSL) (Figure 2.8 A) are stable nitroxyl radicals with an unpaired electron predominantly localized to the N-O bond. The generated new side chain is often referred as R1 (Klare and Steinhoff, 2009). MTSL is characterized by a high selectivity for cysteines leading to high label efficiency. The side chain of MTSL exhibits a molecular volume of a tryptophan residue and renders flexible due to rational motion around four internal bonds attaching the nitroxide ring to the protein backbone minimizing disturbances of the native fold (Klare and Steinhoff, 2009). Although due to the intrinsic mobility of the spin label, the separation between the mobility of the label and structural changes of the protein seem to be difficult (Polyhach and Jeschke, 2010). But studies of molecular dynamics (MD) simulations demonstrated that the conformational distribution of the spin label could provide the major contribution to the width of measured distance distribution. Accordingly, so-called rotamer libraries are applied in order to model the conformational distribution of the spin labels and to predict spin-to-spin distance distributions from a model for the protein structure (Polyhach and Jeschke, 2010).

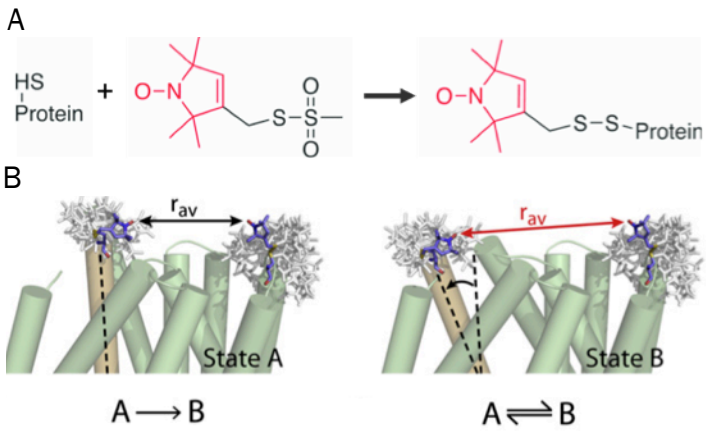

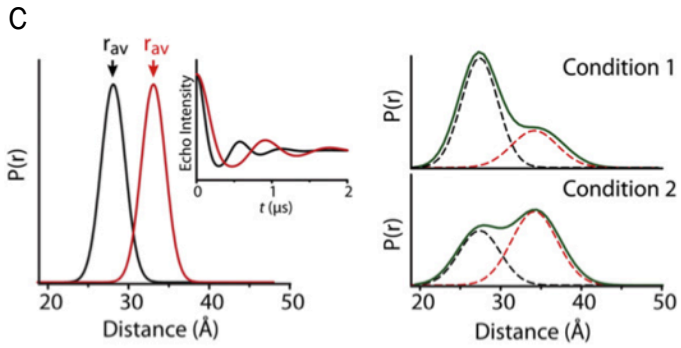

Figure 2.8: Conformational change of site-directed spin labeled protein.
A) MTSL spin label reacts with the sulfhydryl group of the protein forming a disulfide bond (Reginsson and Schiemann, 2011a). B) Hypothetical movement of a transmembrane helix (yellow) within a double labeled protein. The spin label pair (blue) and all possible rotamers (light gray) are represented as sticks. The conformational change from state A to B alters the average distance (r_{av}) between the spin labels. C) Distinct conformers represented by state A and B will shift the distance peak of r_{av} in the distance distribution (left). Accordingly, the period of the spin echo decay (inset) will change. The shape and width of the distance distribution will change if the conformations, which are present in equilibrium, will alter the contribution of each distinct conformation (dashed curve) to the distance distribution (green curve) (right) (adapted from Mchaourab *et al.*, 2011).

2.4.3.5 Multi-Spin Systems

If PELDOR experiments are performed for systems containing more than two spin labels, the resulting increased total modulation depth and in sum and difference dipolar frequency contributions give rise to additional peaks in the distance distribution (Von Hagens *et al.*, 2013). This distance peaks are not corresponding to real interspin distances and are consequently referred to as ghost contributions. According to this, a separation from the pair signal and ghost contribution is required to identify real interspin distance peaks.

The PELDOR signal with an N spin system is considered with N(N – 1)/2 pairwise distances within the sensitivity range of PELDOR experiments for a sufficiently diluted probe, in which the intramolecular distances between the single spin system is longer than the sensitivity range of PELDOR (2 – 8 nm). The PELDOR signal V(t) is obtained by summing over the signals of all N possible spins

$$V(t) = B(t)\frac{1}{N}\sum_{k=l}^{N}\prod_{l\neq k}^{N} f_{kl}(t)$$

with $f_{kl}(t)$ as dipolar evolution function of an individual spin pair (k,l), which contains the intramolecular contributions of the biomolecule. Because the background factor B(t), which is taking into account the intermolecular contributions, can be fitted and extracted during analysis, the form factor of an N spin system for a particular orientation relative to the magnetic field vector B_0 can be obtained by

$$F_N\,(t,\theta,\phi) = V(t)/\,B(t) = \frac{1}{N}\sum_{k=l}^{N}\prod_{l\neq k}^{N} f_{kl}\,(t)$$

with

$$f_{kl}(t) = 1 - \,\lambda_l(1 - cos(\omega_{kl}t))$$

where λ_l is the inversion efficiency of the pump pulse for the pumped spin l. For ω_{kl} see dipolar coupling ω_{dd} (Section 2.4.3.3, p. 79).

Taking all considerations into account, the form factor is containing the constant, unmodulated contribution that defines the modulation depth $\Delta_N = 1 - (1 - \lambda)^{N-1}$ and frequency-modulated terms that are grouped by the number of coupled spins involved and can be written as

$$F_N(t) = (1-\lambda)^{N-1} + \,\lambda(1-\lambda)^{N-2}P_N(t) + \lambda^2(1-\lambda)^{N-3}T_N(t) + \lambda^3(1-\lambda)^{N-4}Q_N(t) + \,\lambda^4(1-\lambda)^{N-5}V_N(t) + \lambda^5(1-\lambda)^{N-6}W_N(t) + \cdots$$

where $P_N(t)$ is the pair frequency contribution

$$P_N(t) = \,\frac{1}{N}\frac{1}{1!}\sum_{k=l}^{N}\sum_{k\neq l}^{N} cos\omega_{kl}t$$

for $T_N(t)$ the three-spin frequency contribution

$$T_N(t) = \,\frac{1}{N}\frac{1}{2!}\sum_{k=l}^{N}\sum_{k\neq l}^{N}\sum_{m\neq k,l}^{N} cos\omega_{kl}t cos\omega_{km}t$$

etc. for $Q_N(t)$ the four-spin frequency contribution, $V_N(t)$ the five-spin frequency contribution and $W_N(t)$ the six-spin frequency contribution (Von Hagens *et al.*, 2013).

Standard PELDOR experiments at X-band frequencies on nitroxide spin labels have inversion efficiencies λ of 0.2 – 0.6. They can be varied experimentally by the variation of the pump pulse power. The influence of the number of coupled spins for the interspin distance and inversion efficiency λ can be obtained by

simulation. In consequence, simulation of data with decreasing number of coupled spins allows the determination of ghost artifacts (Figure 2.9).

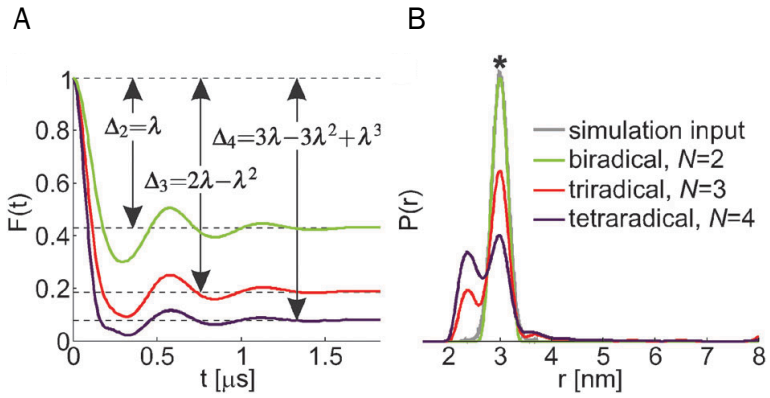

Figure 2.9: Ghost artifacts in multi-spin systems. Simulated form factors (A) and distance distributions obtained by Tikhonov regularization (B). Simulated distance distributions are shown for a two-spin (green), three-spin (red) and four-spin (violet) system. Ghost distances can be identified at shorter distances for the three- and four-spin system. The real interspin distance peak is labeled with an asterisk (Von Hagens *et al.*, 2013).

The procedure to suppress ghost contributions by manipulating the experimentally obtained form factor during analysis by a power scaling with a scaling exponent $\xi_N = 1/(1-N)$, with N being the number of coupled spins was developed and is implemented in the DeerAnalysis Software (Von Hagens *et al.*, 2013).

3 Pathogen-relevant choline transporters of *Acinetobacter baylyi*

Pathogenic *Acinetobacter* species obtained threatening clinical relevance over the past few decades. Especially, *Acinetobacter baumannii* is nowadays a very common nosocomial pathogen, because of its extraordinary multi-drug resistance.

The ability of *Acinetobacter* species to colonize almost any surface persisting desiccation and moisture (Doughari *et al.*, 2011; Vallenet *et al.*, 2008) is pointing towards a strong osmostress mechanism, which might contribute to the virulence of these bacteria. In order to counteract hyperosmotic stress, the uptake of compatible solutes is commonly performed by transporters belonging to the BCCT family (Ziegler *et al.*, 2010). *Acinetobacter baylyi* ADP1 comprises three potential BCC transporters. The characterization of those BCCTs is important to understand the mechanism of persistence of pathogenic *Acinetobacter spp*. the non-pathogen *A. baylyi* was chosen as model organism for *A. baumannii* due to their high gene orthology (Vallenet *et al.*, 2008).

3.1 Results

3.1.1 Classification of BCC transporters from *A. baylyi*

Inspection of the genome sequence of *Acinetobacter baylyi* ADP1 identified three genes encoding potential BCC transporters. The three genes, which are annotated with the locus tags ACIAD1011, ACIAD1012 and ACIAD3460 will be hereinafter referred to as *betT1, betT2* and *betT3*, respectively, as well as the corresponding gene products will be named accordingly BetT1, BetT2 and BetT3. Interestingly, the genes for BetT1 and BetT2 are organized together within the *bet* cluster (Figure 3.1), while the gene for BetT3 is located approximately 2000 kb far apart in the genome of *A. baylyi* ADP1.

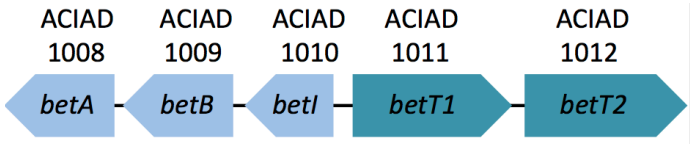

Figure 3.1: Organization of the *bet* gene cluster.
The genes are annotated with the corresponding gene locus tag. The cluster consists of *betA* (choline dehydrogenase), *betB* (betaine aldehyde dehydrogenase), *betI* (regulator protein), *betT1* and *betT2*, the latter coding for putative BCC transporters.

The substrate specificity of BCC transporters is related to the glycine motif located in the middle of TM3 responsible for the coordination of the substrate carboxyl groups (Ressl *et al.*, 2009; Schulze *et al.*, 2010). This motif is highly conserved among BCCTs with the same trimethylammonium substrate specificity (Ziegler *et al.*, 2010).

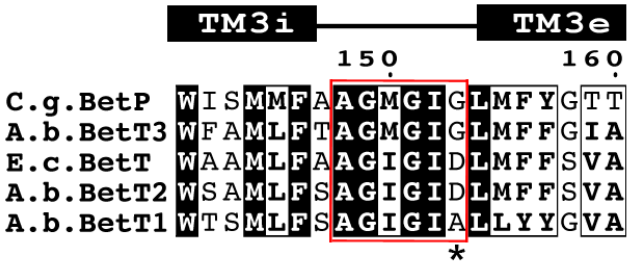

Figure 3.2: Sequence alignment of the glycine motif of BCCTs from *A. baylyi*.
Multiple amino acid sequence alignment of the glycine stretch (red) of *A. baylyi* BCCTs BetT1, BetT2 and BetT3 to BetP from *C. glutamicum* as well as BetT from *E. coli.* Numbering of the residues corresponds to BetP. In the structure of BetP, the glycine motif is located in an unwound segment between the intracellular part and extracellular part of TM3 (TM3i and TM3e) (Ressl *et al.*, 2009). The α–helical parts are depicted as black bars on the top of the alignment. The (*) marked residues were shown to be mainly responsible for substrate specificity (Perez *et al.*, 2011b).

The sequence alignment of the glycine motif identified BetT3 from *A. baylyi* with Ala-Gly-Met-Gly-Ile-Gly as Na^+-coupled betaine BetP-type transporter, whereas *A. baylyi* BetT2 was classified by Ala-Gly-Ile-Gly-Ile-Asp as H^+-coupled choline symporter corresponding to *E. coli* BetT (Figure 3.2). In contrast, a non-polar alanine is found instead of the aspartate for BetT1, which made its assignment difficult.

The role of the glycine betaine transporter BetT3 of *A. baylyi* was already studied in the past (Sand *et al*, 2011). Accordingly, the following results in this thesis will focus on the investigation of the both latter mentioned BCCTs BetT2 and BetT1 from *A. baylyi*.
Secondary structure prediction for BetT1 and BetT2 consisting of 526 and 686 amino acids, respectively, confirmed the characteristic composition of 12 TM domains for the BCCT family (Figure 3.3). Additionally, BetT2 comprises a long C-terminal domain of 178 amino acids.

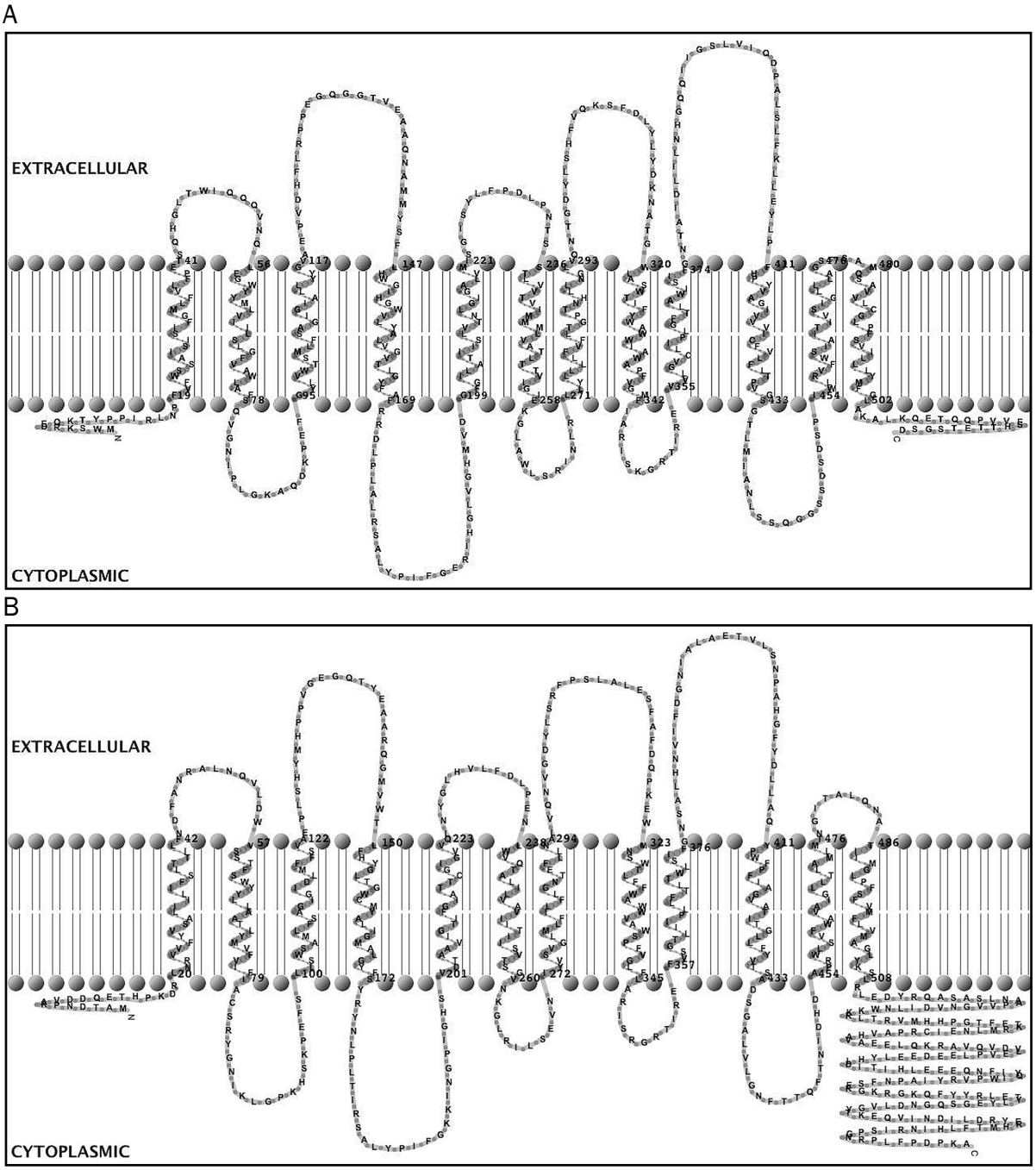

Figure 3.3: Topological models of BetT1 and BetT2 from *A. baylyi*.
For secondary structure prediction and model generation of *A. baylyi* BetT1 (A) and BetT2 (B) the TMRPres2D tool (Spyropoulos *et al.*, 2004) in combination with the prediction algorithm TMHMM (Krogh *et al.*, 2001) was used.

3.1.2 Expression and first purification trials of BetT2

For heterologous expression of BetT2 from *A. baylyi* in *E. coli*, the gene *betT2* (locus tag ACIAD1012) was cloned into the pBAD/HisA vector using the restriction endonucleases SacI and EcoRI. Success of cloning was confirmed by digestion with the corresponding

restriction endonucleases and subsequent sequencing. Plasmids containing the correctly inserted gen, referred to as pBAD/HisA_ACIAD1012, were transformed into *E. coli* TOP10 and MKH13 cells. Cells were grown in 1 l LB media either at 30 °C or 37 °C and the gene expression was induced by 0.02 % arabinose at an OD_{600} of 0.6 – 0.8. The cells were further cultured either for 3 h or 5 h before cells were harvested and membranes were prepared. The protein content of BetT2 within the membranes was analyzed by SDS-PAGE and Western blot (Figure 3.4).

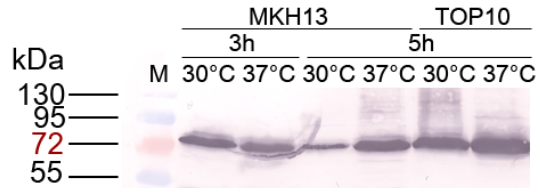

Figure 3.4: Western blot of BetT2 test expression.
BetT2 producing *E. coli* MKH13 and TOP10 cells were cultured for 3 h or 5 h at 30 °C or 37 °C in 1 l LB after gene expression induction. For each condition, cells were harvested, membranes were prepared and adjusted to the same OD_{600} of 2.5. 10 µl of the membranes were loaded onto an SDS gel (12.5 %) and subsequent used for immunoblotting against the N-terminal His_6-tag. (M) PageRuler™ Prestained Protein Ladder (Thermo Scientific Molecular Biology).

Western blot analysis revealed for all conditions a protein band slightly higher than 72 kDa corresponding to the calculated mass (Gasteiger *et al.*, 1999) of 77.6 kDa for BetT2. The expression tests showed adequate production levels of BetT2 in *E. coli* TOP10 at 37 °C for further structural investigations. For functional studies, sufficient production levels of BetT2 in *E. coli* MKH13 were obtained already 3 h after gene expression induction at 37 °C.

The first purification step for BetT2 includes the solubilization with a suitable detergent. Preliminary solubilization trials for BetT2 within *E. coli* TOP10 membranes were performed with different detergents and at different conditions. Samples were examined by SDS-PAGE and Western blot analysis (Figure 3.5).

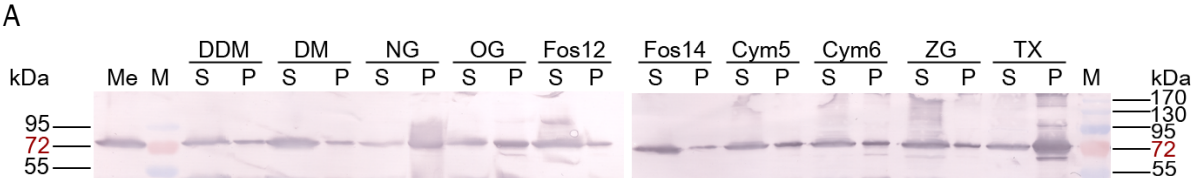

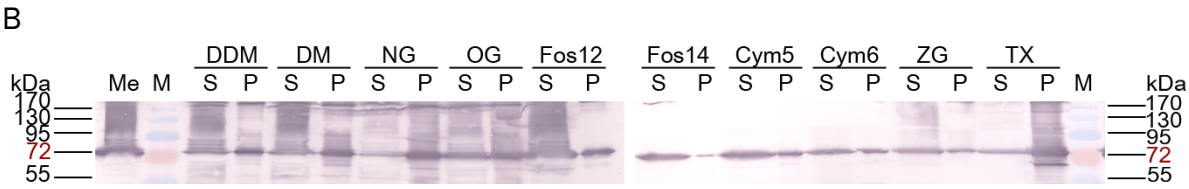

Figure 3.5: Solubilization test for BetT2.

E. coli TOP10 membranes (5 mg/ml) containing BetT2 were solubilized with 2 % DDM, DM, Nonyl-β-glucopyranoside (NG), Octyl-β-glucopyranoside (OG), Fos-Choline-12 (Fos12), Fos-Choline-14 (Fos14), Cymal-5 (Cym5), Cymal-6 (Cym6), Zwittergent (ZG) as well as Triton X-100 (TX) and incubated for 2 h at 4 °C (A) or RT (B). Samples were evaluated by applying 5 µl of the supernatant (S) and the pellet (P) dissolved in the equal set-up volume after ultracentrifugation onto an SDS gel (12.5 %) and subsequent used for immunoblotting against the N-terminal His_6-tag. Additionally, 5 µl membranes (Me) were loaded. (M) PageRuler™ Prestained Protein Ladder (Thermo Scientific Molecular Biology).

First solubilization trials identified detergents like DDM, DM, Fos-Choline-14, Cymal-5 as well as Cymal-6 as good candidates at 4 °C and partly at room temperature. Further experiments varying the detergent concentrations and screening for appropriate salts to improve the solubilization process have to be carried out.

3.1.3 Transport properties of BetT2 in *E. coli* MKH13 cells

In order to investigate the transport properties, BetT2 was produced in *E. coli* MKH13 cells lacking the transport systems BetT, PutP, ProP and ProU responsible for the uptake of compatible solutes. Based on the previous classification of BetT2, [^{14}C]-choline uptake rates were measured. According to the role of BCC transporters like BetT from *E. coli* during osmoprotection, uptake activity of BetT2 was investigated upon increasing hyperosmotic conditions at external pH 6 or 7.5.

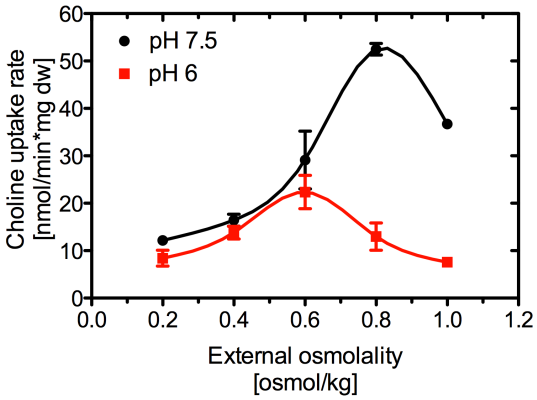

Figure 3.6: Choline uptake rates of BetT2 in *E. coli* MKH13 cells.

Uptake rates of choline in nmol per min and mg dry cell weight were measured by increasing external osmolality at pH 7.5 and 6 for BetT2 in *E. coli* MKH13 cells. Uptake was started by adding saturating concentrations of 500 µM [^{14}C]-choline. The measurements represent the mean of at least three replicates/data point. The errorbars represent ± S.E.M..

Transport measurements in *E. coli* MKH13 undoubtedly identified BetT2 as choline transporter (Figure 3.6). Moreover, increasing external osmolalities increased the choline uptake activity at pH 7.5 and also with lower extent at pH 6. The choline uptake rate for BetT2 increases 5-fold from approximately 10 nmol/min* mg dw at 0.2 osmol/kg to 50 nmol/min* mg dw reaching maximal activity at 0.8 osmol/kg at pH 7.5. In turn, BetT2 is less active at pH conditions of 6 reaching already maximum activity at 20 nmol/min* mg dw with a shifted optimum to 0.6 osmol/kg. Indeed, these results indicated BetT2 from *A. baylyi* serving as osmoregulated choline transporter. The osmoprotective properties of BetT2 by deletion mutants of *A. baylyi* were confirmed by our collaborators (Sand *et al.*, 2014).

Studies identified BetT from *E. coli* as proton-coupled choline transporter (Lamark *et al.*, 1991) and it was demonstrated that the protonation of the aspartate within the glycine motif is crucially involved in proton-coupled choline transport (Perez *et al.*, 2011b). Beside the equal composition of the glycine stretch, *E. coli* BetT and *A. baylyi* BetT2 are sharing a total sequence identity of 68 %. Thus, [^{14}C]-choline uptake of BetT2 was measured in sodium-free buffer (100 mM KP_i, pH 6 and pH 7.5) at an osmolality of 600 osmol/kg in presence and absence of the protonophore CCCP evaluating the suggested proton-coupled choline uptake properties.

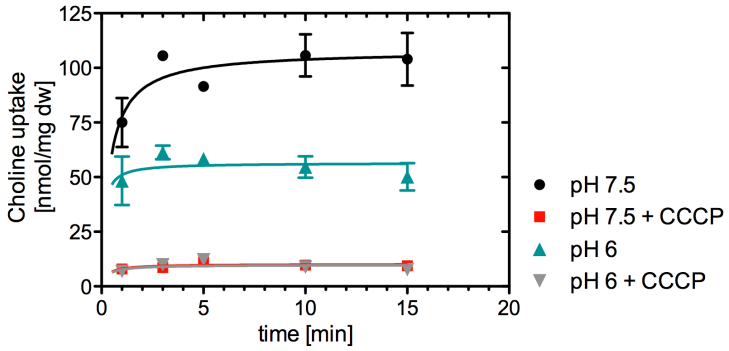

Figure 3.7: Effect of the protonophore CCCP on BetT2-mediated choline uptake in *E. coli* MKH13 cells.

Uptake of choline in nmol per mg dry cell weight was measured in sodium-free buffer (100 mM KP_i) at 600 osmol/kg for pH 7.5 and 6 in presence and absence of 50 µM CCCP for BetT2 in *E. coli* MKH13 cells. Uptake was started by adding saturating concentrations of 500 µM [^{14}C]-choline. Each value is the mean ± S.E.M of three independent measurements.

Under hyperosmotic conditions, the choline uptake activity of BetT2 decreases dramatically upon addition of the protonophore CCCP at pH 7.5 indicating the uncoupling of the choline transport (Figure 3.7). Because the transport activity is already reduced at pH 6, the reduction of the choline uptake upon CCCP addition is less pronounced. However, these results are demonstrating that the proton-motive force drives choline transport in BetT2. Further experiments have to be performed to characterize the choline uptake of BetT2 by kinetic parameters.

3.1.4 Expression and purification of BetT1

The gene *betT1* (locus tag ACIAD1011) was cloned into the pBAD/HisA vector using the restriction endonucleases XhoI and PstI. The plasmid containing the correct inserted gene, referred to as pBAD/HisA_ACIAD1011, was kindly provided by Miriam Sand (Goethe University, Frankfurt). For heterologous expression of *betT1*, the plasmid pBAD/HisA_ACIAD1011 was transformed into *E. coli* TOP10 and MKH13 cells for structural and functional investigations, respectively. Cells were cultured in 1 l LB media at 30 °C as well as 37 °C and gene expression was induced at an OD_{600} of 0.6 – 0.8 by 0.02 % arabinose. Cells were further cultured for 3 h or 5 h, subsequently harvested and membranes were prepared. In addition, samples were collected before gene expression induction and during expression each hour. The samples were adjusted to the same OD by centrifugation of an appropriate volume of the culture, subsequently cell pellets were dissolved in SDS sample buffer and heated up to 95 °C for 10 min. The protein content of BetT1 within the whole cell samples and isolated membranes was analyzed by SDS-PAGE and by Western blot (Figure 3.8).

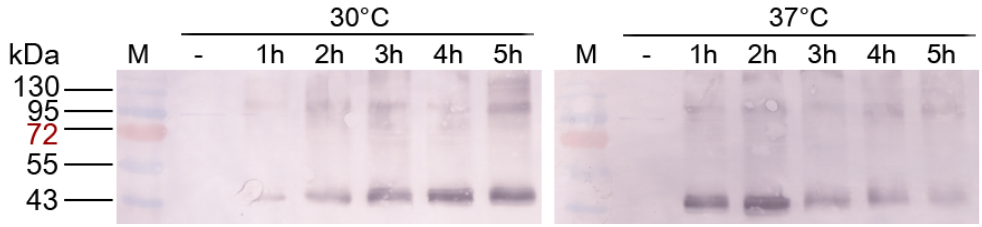

Figure 3.8: Western blot of BetT1 test expression within *E. coli* cells.
E. coli TOP10 cells were cultured for 5 h at 30 °C or 37 °C. Samples were collected before (-) and after *betT1* expression induction each hour (1 h – 5 h) and adjusted to the same OD_{600} of 5. 5 µl of each sample were loaded onto an SDS gel (12.5 %) and subsequent used for immunoblotting against the N-terminal His_6-tag. (M) PageRuler™ Prestained Protein Ladder (Thermo Scientific Molecular Biology).

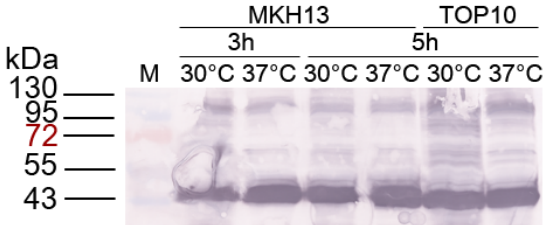

Figure 3.9: Western blot of BetT1 test expression within *E. coli* membranes.
BetT1 producing *E. coli* MKH13 and TOP10 cells were cultured for 3 h and/or 5 h at 30 °C or 37 °C in 1 l LB after gene expression induction. For each condition, cells were harvested, membranes were prepared and adjusted to the same OD_{600} of 2.5. 10 µl of the membranes were loaded onto an SDS gel (12.5 %) and subsequent used for immunoblotting against the N-terminal His_6-tag. (M) PageRuler™ Prestained Protein Ladder (Thermo Scientific Molecular Biology).

Western blot analysis of cells and membranes revealed after gen expression induction pronounced protein bands at approximately 43 kDa, which is lower than the expected molecular weight of 58.18 kDa for BetT1 (Figure 3.9). A shift in the molecular weight during SDS-PAGE is frequently observed especially for hydrophobic membrane proteins (Rath and Deber, 2013). In addition, in Figure 3.8 and Figure 3.9, a second less pronounced band at approximately 95 kDa might demonstrate a higher oligomeric state of BetT1. The expression test including whole *E. coli* TOP10 cells allows tracing the production levels of BetT1 with time. Like expected, no protein is detectable before induction of the expression at both temperature conditions. At 30 °C, the protein content increases with time. In contrast, at 37 °C the maximum protein level is reached faster even after 2 h expression. Therefore, the expression of BetT1 in *E. coli* TOP10 was hereinafter performed at 37 °C and cells were subsequently harvested 2 h after induction. An expression test with whole cells was not feasible for *E. coli* MKH13, because the Western blot membrane remained empty after several repetitions of the experiment (data not shown). To confirm the expression in *E. coli* MKH13 membranes were prepared. The Western blot shows adequate BetT1 production levels even after 3 h at 37 °C.

After succesfull expression, the next step for purification was the isolation of BetT1 from *E. coli* TOP10 membranes by solubilization for structural investigations. Isolation of BetT1 by immobilized metal affinity chromatography (IMAC, Section 2.3.4.4) was facilitated by the fusion of the N-terminus of the protein with a His_6-tag. Further purification steps included preparative size exlusion chromatography (SEC, Section

2.3.4.6) and additionally optimization of purification for BetT1 was obtained by ion exchange chromatography (IEX, Section 2.3.4.5).

Solubilization of *E. coli* TOP10 membranes containing BetT1 was performed with different detergents at 4 °C. After 1 h incubation, 200 mM NaCl was added to the solubilization mixture and was incubated further for 1 h at 4 °C prior to centrifugation. Samples were examined by SDS-PAGE and Western blot analysis (Figure 3.10). The following result includes only a selection of tested detergents.

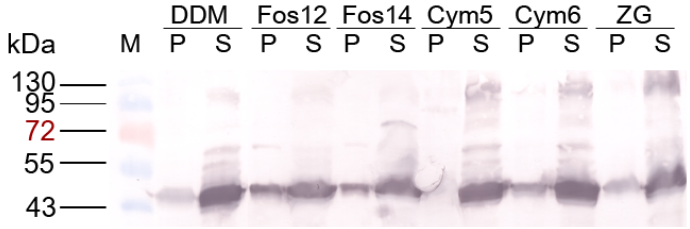

Figure 3.10: Solubilization test for BetT1.
E. coli TOP10 membranes (5 mg/ml) containing BetT1 were solubilized with 2 % DDM, Fos-Choline-12 (Fos12), Fos-Choline-14 (Fos14), Cymal-5 (Cym5), Cymal-6 (Cym6) as well as Zwittergent (ZG) and incubated at 4 °C. After 1 h incubation, 200 mM NaCl was added to each sample, which were further incubated for 1 h at 4 °C. Samples were evaluated by applying 5 µl of the supernatant (S) and the pellet (P) dissolved in the equal set-up volume after ultracentrifugation onto an SDS gel (12.5 %) and subsequently used for immunoblotting against the N-terminal His_6-tag. (M) PageRuler™ Prestained Protein Ladder (Thermo Scientific Molecular Biology).

Solubilization tests resulted in sufficient solubilization of BetT1 by the addition of 2 % DDM as well as 2 % Cymal-5 (Figure 3.10). Therefore, first purification of BetT1 was performed with Cymal-5. Solubilized membranes were loaded slowly on a Ni^{2+}-affinity column. The column was washed in absence of imidazole and with 5 mM imidazole to remove unspecific bound proteins. The detergent concentration was set to 0.6 % Cymal-5 during washing and elution steps. BetT1 was eluted by an stepwise increase of the imidazole concentration and the purity of BetT1 was analyzed by SDS-PAGE. The elution fractions were pooled and concentrated to 500 µl for preparative SEC in order to improve the purity of the protein. Protein content of the elution fractions of Ni^{2+}-affinity column and SEC were analyzed by SDS-PAGE (Figure 3.11).

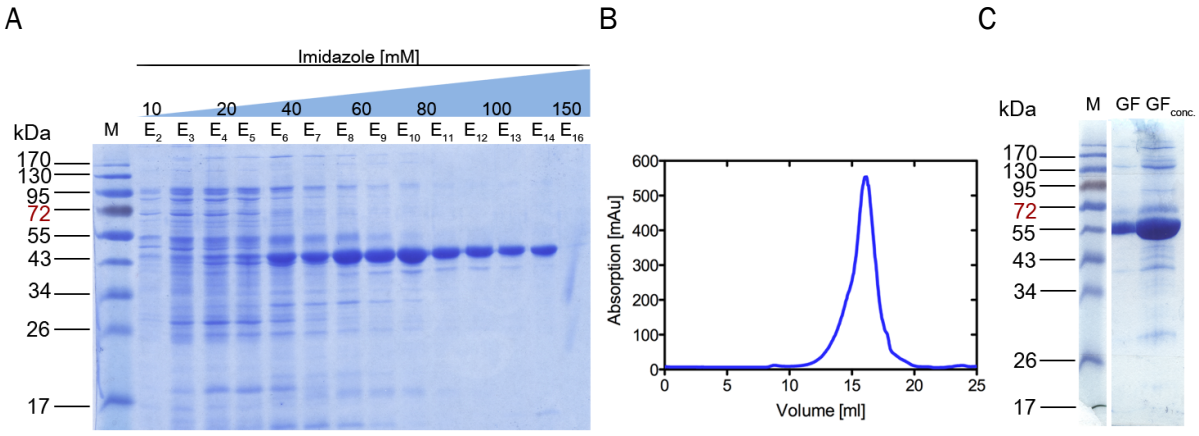

Figure 3.11: BetT1 purification with Cymal-5 as detergent.

A) Solubilized *E. coli* TOP10 membranes containing BetT1 were applied on a Ni^{2+}-affinity column, subsequently washed and protein was eluted by a stepwise increase of imidazole from 10 – 150 mM. 5 µl of each elution fraction (E_2-E_{16}) were loaded onto an SDS gel (12.5 %). B) Elution fractions E_9 – E_{14} were pooled and concentrated to 500 µl. Protein was injected on a Superose 6 10/300 column for preparative SEC. A constant flow rate of 0.3 ml/min was used and the absorption was measured at 280 nm. C) Elution fractions of SEC within the peak were pooled (GF), concentrated to 6 mg/ml ($GF_{conc.}$) and 5 µl of each sample were analyzed by SDS-PAGE (12.5 %). (M) PageRuler™ Prestained Protein Ladder (Thermo Scientific Molecular Biology) was used.

During IMAC (Figure 3.11 A), BetT1 starts to elute in combination with diverse unspecific bound inpurities very early at low imidazole concentrations of 40 mM. This is indicated by the increasing intensity of the protein band at approximately 43 kDa corresponding to BetT1. With higher imidazole concentrations, less impurities are detectable, whereas the content of BetT1 increases. Between 80 – 100 mM imidazole, one last impurity below the BetT1 protein band is present. Adequate elution fractions were subjected to SEC for further purification of the protein of interest. Although the SEC profile (Figure 3.11 C) shows a monodisperse peak, concentration of the pooled fractions within the peak to 6 mg/ml indicated bands corresponding to contaminations. However, first 3D crystallization approaches were performed with the sample derived from SEC. Unfortunately, crystallization of BetT1 failed with the protein purified in Cymal-5. In consequence, solubilization and purification was performed with DDM as detergent (Figure 3.12). The concentration of DDM was adjusted to 0.1 % during purification by IMAC and SEC.

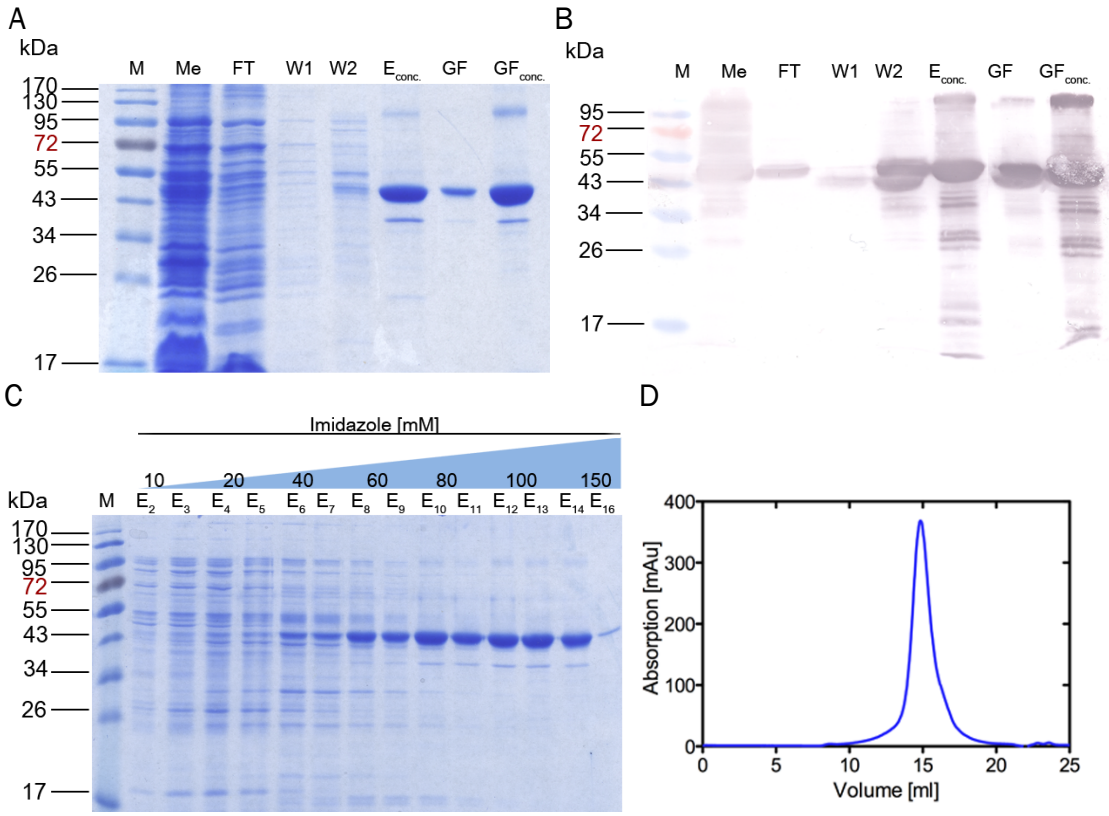

Figure 3.12: BetT1 purification with DDM as detergent.

DDM solubilized *E. coli* TOP10 membranes containing BetT1 were applied on a Ni^{2+}-affinity column, subsequently washed and protein was eluted. SDS-PAGE (A) and Western Blot (B) of BetT1 purification. 10 µl of the membranes (Me) (10 mg/ml), the flow trough of the affinity column (FT), wash 1 with 0 mM imidazole (W1), wash 2 with 5 mM imidazole (W2) as well as 1 µl of the concentrated eluat from the affinity column ($E_{conc.}$), pooled SEC fractions unconcentrated (GF) and concentrated to 10 mg/ml ($GF_{conc.}$) were loaded onto an SDS gel (12.5 %). C) 5 µl of each elution fraction (E_2-E_{16}) derived from the Ni^{2+}-affinity column eluted by a stepwise increase of imidazole from 10 – 150 mM were examined by SDS-PAGE (12.5 %). (M) PageRuler™ Prestained Protein Ladder (Thermo Scientific Molecular Biology) was used. D) For preparative SEC, Ni^{2+}-affinity column elution fractions E_9 – E_{16} were pooled and concentrated to 500 µl. Protein was injected on a Superose 6 10/300 column with a constant flow rate of 0.3 ml/min and the absorption was monitored at 280 nm.

The overview of the purification (Figure 3.12 A – B) indicated that BetT1 only moderately binds to the Ni^{2+}-affinity column and has the tendency to elute with low imidazole concentrations of 5 mM. Thus, BetT1 starts to elute together with diverse other proteins at low concentrations of imidazole (Figure 3.12 C). Comparable to the Cymal-5 purification (Figure 3.11), BetT1 content increases with higher imidazole concentrations, whereas impurities are decreasing. Further purification of pooled elution fractions by preparative SEC yielded a monodispers peak (Figure 3.12 D), although one last impurity is detected between 34 and 43 kDa (Figure 3.12 A ($GF_{conc.}$)).

Altogether, the yield of BetT1 during DDM purification was sufficient and even more efficient regarding the level of purity than with Cymal-5.

In order to improve the purification of BetT1, an additional step of ion exchange chromatography was tested (Bachelor thesis of Jessica Devant (Devant, 2014)). For this purpose, the applicability of an anion exchanger (Q-Sepharose) as well as a cation exchanger (SP-Sepharose) were examined. The concentrated elution after IMAC was applied several times on the exchanger material packed in a column, washed and eluted afterwards by a stepwise increase of the NaCl concentration from 25 - 125 mM. The efficiency of the ion exchange chromatography was evaluated by SDS-PAGE (Figure 3.13).

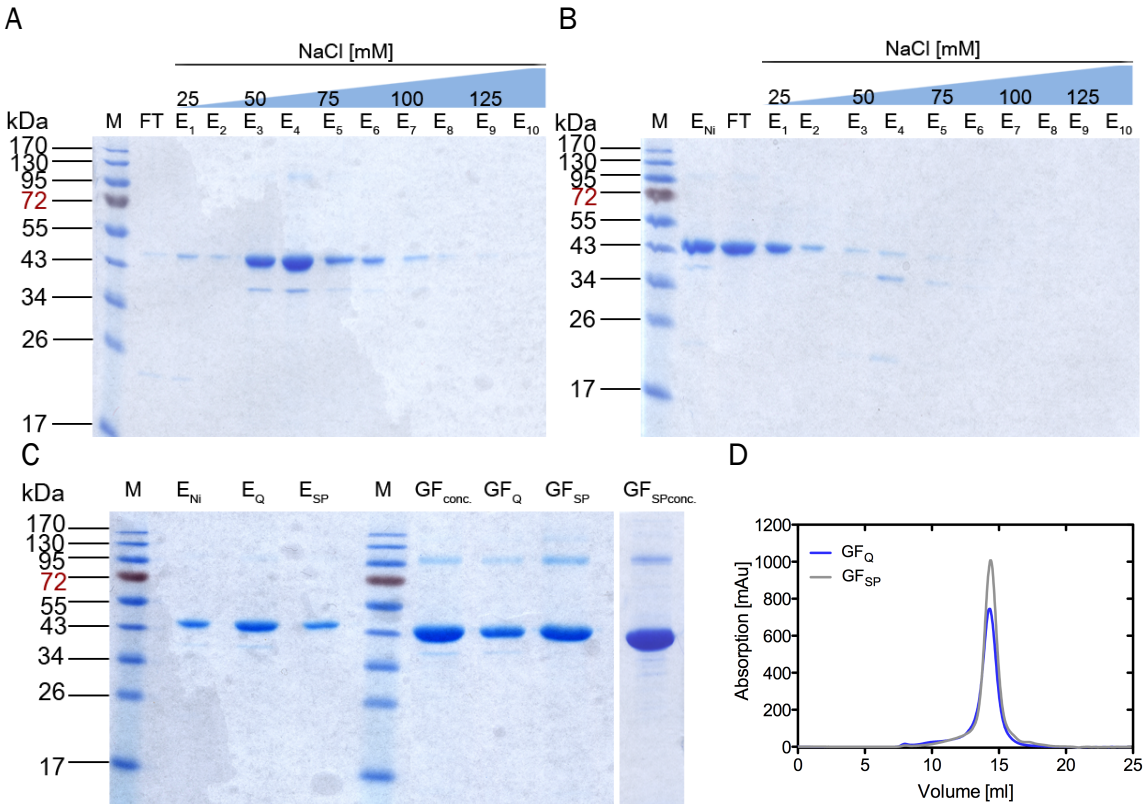

Figure 3.13: Comparison of anion and cation exchange chromatography for BetT1 purification.

Ni^{2+}-affinity column eluate (E_{Ni}) containing BeT1 protein and last impurities were applied on a Q-Sepharose (anion exchanger) (A) and SP-Sepharose (cation exchanger) (B) column and subsequently eluted by the stepwise increase of the NaCl concentration from 25 – 125 mM. Elution fractions E_1 – E_{10} as well as the flow through (FT) of the according ion exchange chromatography were analyzed by SDS-PAGE. C) Direct comparison of the pooled elution fractions from Ni^{2+}-affinity column before (E_{Ni}) and after Q-Sepharose (E_Q) and SP-Sepharose (E_{SP}) column. Preparative SEC with the corresponding pooled fractions was performed by using

a Superose 6 10/300 column. $GF_{conc.}$ beeing the concentrated protein sample after Ni^{2+}-affinity column and SEC, GF_Q and GF_{SP} beeing the samples after the corresponding ion exchange chromatography and SEC. In addition, the concentrated sample GF_{SP} ($GF_{SPconc.}$) is shown. For SDS-PAGE, in all cases 1 µl of each sample and 5 µl of the marker PageRuler™ Prestained Protein Ladder (Thermo Scientific Molecular Biology) (M) was used for 12.5 % SDS gels. Ionexchange chromatography was performed by Jessica Devant (Devant, 2014).

The application of Q-Sepharose as anion exchanger demonstrated that the matrix binds efficiently BetT1 as well as the impurity. No protein is detectable in the flow through (Figure 3.13 A). The elution of BetT1 starts already with low NaCl concentrations (E_1, E_2), although complete elution of the protein of interest together with the impurity occurs at concentrations of 50 mM NaCl (E_3, E_4). The anion exchanger did not provide the separation of BetT1 from its contamination. In contrast, ion exchange chromatography with a cation exchanger revealed that the SP-Sepharose matrix is not able to efficiently bind BetT1, which is indicated by the high protein content in the flow through (Figure 3.13 B). Small amounts of BetT1 bound to the matrix elute within the first elutions (E_1, E_2). The matrix is not able to bind BetT1, whereas a strong interaction with the impurity (band between 34 – 43 kDa) could be observed, which is missing in the flow through and elutes at 50 – 75 mM NaCl (E_3 – E_5). Indeed, SP- Sepharose as cation exchanger ensures the separation of BetT1 from the impurity. For further experiments, the flow through and first elution fractions containing only BetT1 were pooled to assure a sufficient concentration of protein. Independent from the results, pooled samples derived directly from IMAC or additionally from anion exchange (E3, E4) and cation exchange chromatography were subjected to SEC for comparison. As expected, SEC leads only after ion exchange with the SP-Sepharose as cation exchanger to a high level of purity of BetT1 ($GF_{SPconc.}$) (Figure 3.13 C) enabling further structural and functional investigations.

3.1.5 Oligomeric state of BetT1

Based on the solved trimeric structures of the BCCT family members BetP from *C. glutamicum* and CaiT from *E. coli* and *Proteus mirabilis* (Schulze *et al.*, 2010; Tang *et al.*, 2010), a trimeric state was also proposed for the BCC transporter BetT1 from *A. baylyi*. Moreover, for BetP was demonstrated that this transporter forms a stable trimer in detergent as well as in membranes (Ressl *et al.*, 2009; Ziegler *et al.*, 2004)

Therefore, the oligomeric state of BetT1 was compared to BetP by BN-PAGE (Figure 3.14).

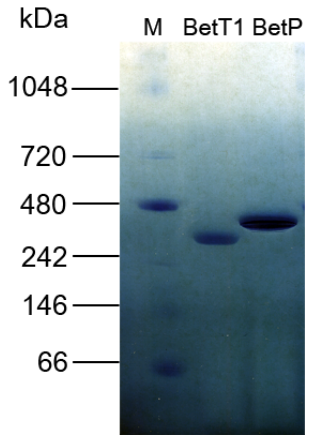

Figure 3.14: BN-PAGE of BetT1 from *A. baylyi* and BetP from *C. glutamicum*.
10 µg of purified protein, *A. baylyi* BetT1 as well as *C. glutamicum* BetP WT in 0.1 % DDM, were loaded onto a BN-PAGE gradient gel (4 – 16 %). (M) NativeMark™ Unstained Protein Standard from Invitrogen/Novex®. BN-PAGE was performed by Jessica Devant (Devant, 2014).

In Figure 3.14, for BetP a protein band slightly below 480 kDa could be detected, whereas the corresponding band for BetT1 is visible between 242 – 480 kDa. The monomer size of 64.2 kDa for BetP results in a trimer size of 192.6 kDa. The size of monomeric BetT1 is 58.2 kDa and consequently 174.6 kDa for trimeric BetT1. In BN-PAGE, the additionally mass of bound lipids and the detergent molecules within the micelle for membrane proteins have to be considered. Here, in both protein samples DDM is adjusted to 0.1 %. The result confirms the trimeric oligomerization for BetT1, which migrates based on the smaller molecular weight compared to trimeric BetP, slightly faster during BN-PAGE.

3.1.6 Crystallization of BetT1

Successful purification of *A. baylyi* BetT1 as well as high yields of pure protein allowed starting structural investigations by 3D crystallization. Protein, which was used for crystallization was purified with DDM as detergent as described previously in Section 3.1.4 including IMAC, IEX and SEC along with subsequent concentration to 10 mg/ml. Crystallization set-ups were pipetted with protein in buffer containing 25 mM Tris-HCl (pH 7.5) and 200 mM NaCl as well as with desalted protein samples. In order to find appropriate crystallization conditions for BetT1, first crystallization trials were performed in 96-well plates with the commercially available screens from Molecular

Dimensions and Qiagen by using the hanging drop method (Figure 3.15). The following results will give a brief overview of crystallization conditions in which crystal growth of BetT1 was observed. Several crystals were tested at the SLS beamline (Villigen, Switzerland). Crystallization of BetT1 was partly supported during the Bachelor thesis of Jessica Devant.

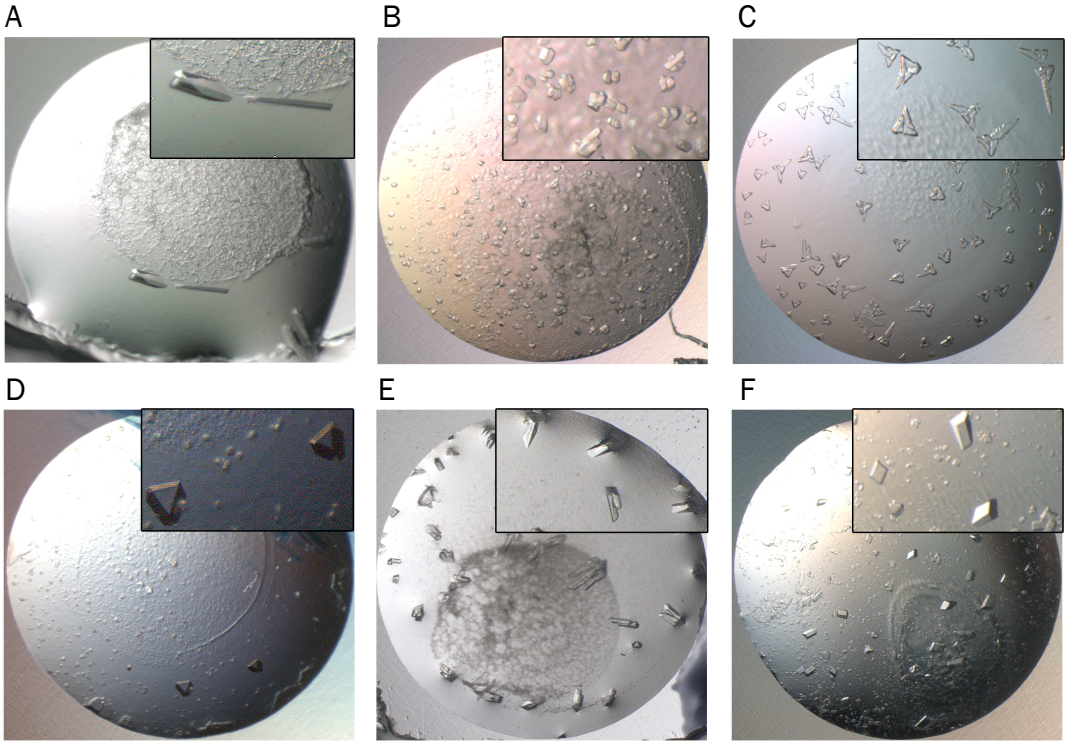

Figure 3.15: Crystals of *A. baylyi* BetT1 in commercially available screen conditions. Crystals grown in (A) 0.04 M NaCl, 0.04 M Tris pH 8, 27 % v/v PEG 350 MME; (B) 0.07 M NaCl, 0.05 M Na_3-Citrate pH 4.5, 22 % v/v PEG 400 and (C) 0.5 M NaCl, 0.05 M Tris pH 7.5, 12 % w/v PEG 2000. Crystal formation in conditions containing (D) 0.1 M NaCl, 0.1 M Bicine pH 9.0, 20 % w/v PEG 550 MME; (E) 0.02 M Bis-Tris pH 7, 15 % w/v PEG 2000 as well as (F) 0.05 M $MgAc_2$, 0.05 M NaAc pH 4.6, 25 % v/v PEG 400. For all crystal set-ups except in F, desalted protein in 25 mM Tris pH 7.5 was used.

Crystal formation for BetT1 was observed in various conditions of the commercially available screens (Figure 3.15). Furthermore, different crystal sizes and morphologies like rode shaped, rhombic, triangular and unshaped crystals could be found. However, most hits were obtained with the MemGold™ screen from Molecular Dimensions (Figure 3.15 A – C). Based on these results, the most promising conditions were varied in PEG concentration for first optimization in 96-well plates and 24-well plates (DDM Screen, Na_3-Citrate Screen; Section 7.6).

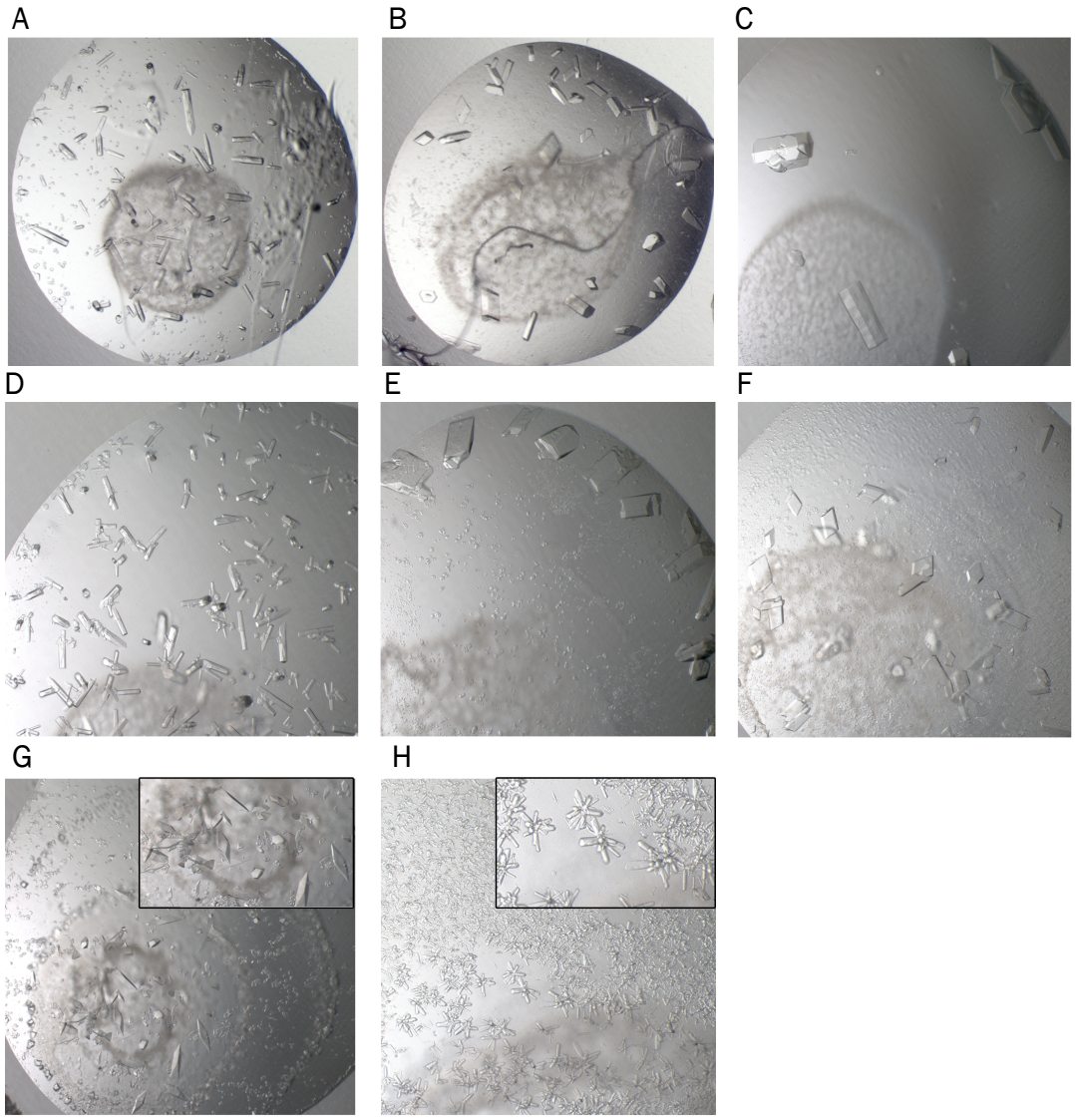

Figure 3.16: Crystals of *A. baylyi* BetT1 in optimized screen conditions.

Crystals grown in (A) 0.1 M $(NH_4)_2SO_4$, 0.1 M HEPES pH 7.5, 14 % w/v PEG 4000, 22 % Glycerol; (B) 0.1 M NaCl, 0.04 M Tris pH 8, 25.5 % v/v PEG 350 as well as (C) 0.1 M $MgCl_2$, 0.1 M Tris pH 7.5, 20 % v/v PEG 400. Crystals were observed in conditions containing (D) 0.1 M $MgCl_2$, 0.1 M Tris pH 7.5, 22 % v/v PEG 400; (E) 0.1 M NaCl, 0.04 M Tris pH 8, 25 % v/v PEG 350 and (F) 0.1 M NaCl, 0.04 M Tris pH 8, 26.5 % v/v PEG 350. Crystal formation in (G) 0.05 M $MgAc_2$, 0.05 M NaAc pH 5.4, 22 % v/v PEG 400 and (H) 0.1 M NaCl, 0.05 M Glycine pH 9.5, 31.5 % v/v PEG 300. For all set-ups, protein was crystallized with 1 mM choline in 25 mM Tris pH 7.5 was used.

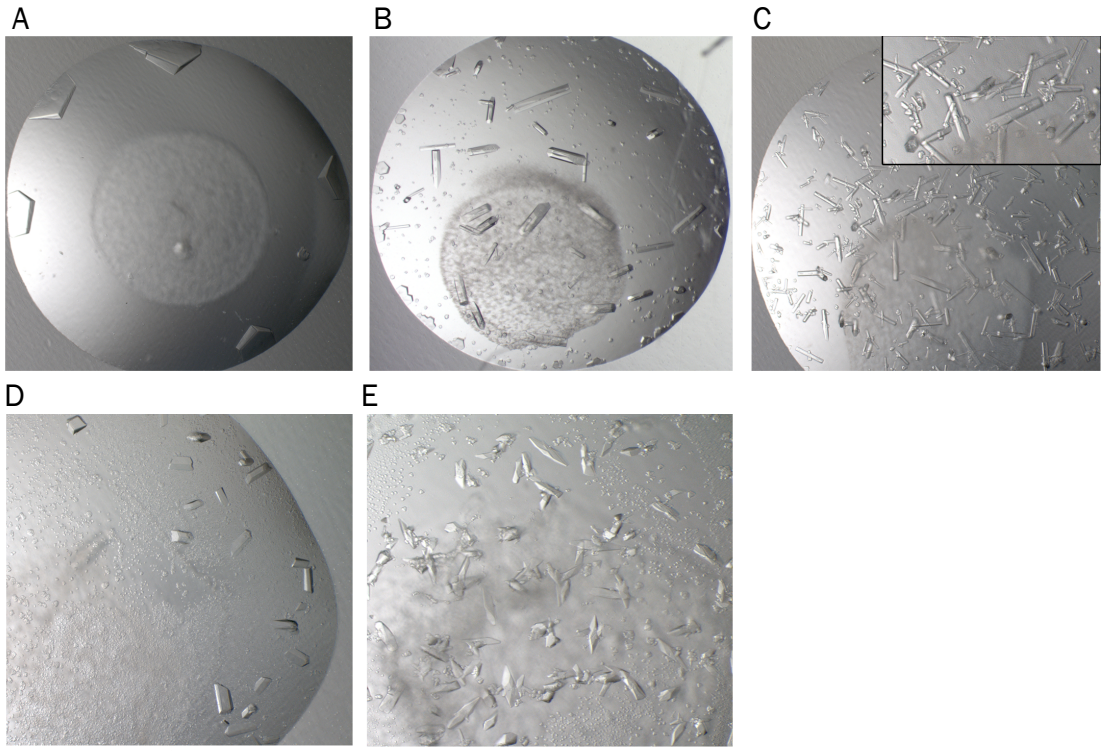

Figure 3.17: Crystals of *A. baylyi* BetT1 in optimized screen conditions with choline as additive.

Crystals grown in 0.1 M $MgCl_2$, 0.1 M Tris pH 7.5 with either 19.5 % (A), 20.5 % (B) and 21.5 % (C) v/v PEG 400. Crystal formation in conditions containing (D) 0.1 M NaCl, 0.04 M Tris pH 8, 26.5 % PEG 350 as well as (E) 0.05 M $MgAc_2$, 0.05 M NaAc pH 5.4 and 22.5 % PEG 400. For all set-ups, protein in 25 mM Tris pH 7.5 was incubated with 1 mM choline for 1 h prior to crystallization.

First optimization of the crystal conditions in 96-well plates resulted in partly bigger sized crystals (Figure 3.16). Crystals appear in various numbers and in different forms like rod shaped, rhombic as well as branched crystals. In addition, protein was also incubated with the potential substrate choline prior to crystallization revealing comparable results (Figure 3.17).

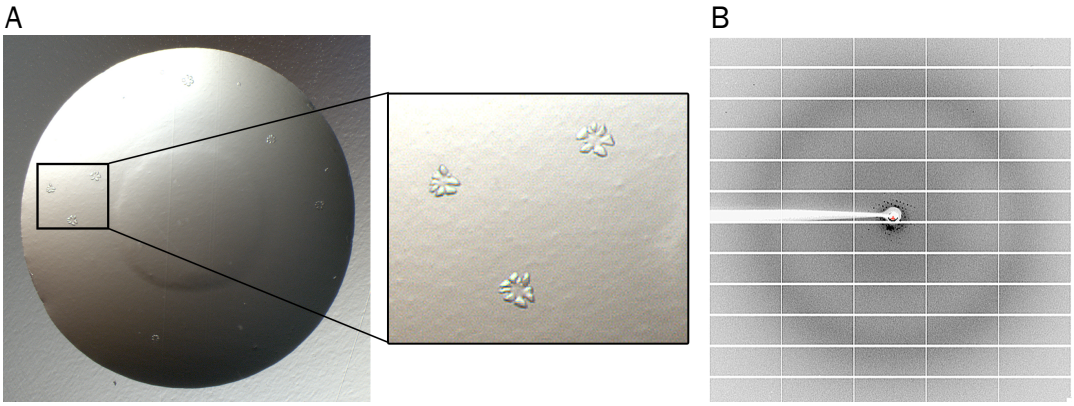

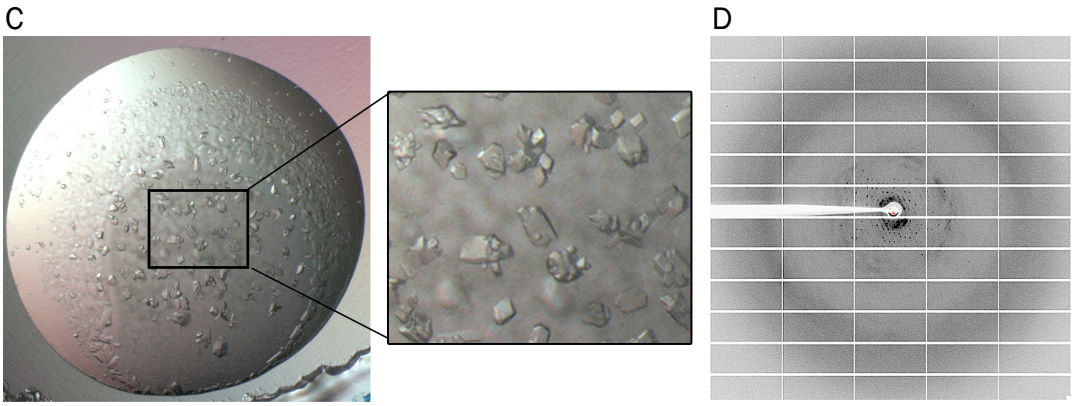

Figure 3.18: Crystals of BetT1 with corresponding diffraction pattern.
A) Crystals grown in 0.1 M $(NH_4)_2SO_4$, 0.1 M HEPES pH 7.5 and 12 % (w/v) PEG 4000 and B) shows the corresponding diffraction pattern with a resolution around 17 Å. C) Crystals grown in 0.05 M NaCl, 0.1 M Na_3-citrate pH 5.5 and 26 % (v/v) PEG 400 and D) displays the corresponding diffraction pattern with a resolution of 8 Å.

The most promising crystals were tested at the SLS beamline (Villigen, Switzerland) and resulted in a diffraction of 30 – 10 Å. An example for a crystal diffracting till 17 Å is shown in Figure 3.18. The crystals in the size of 50 – 75 µm were triangular shaped and assembled to complexes of 6 – 7 crystals. Up to now, the best diffracting crystal with a size of 100 – 200 µm diffracted to a resolution of 8 Å. This crystal was grown in 0.05 M NaCl, 0.1 M Na_3-citrate pH 5.5 and 26 % (v/v) PEG 400. Interestingly, this condition is very similar to the conditions, which are used for the crystallization of BetP from *C. glutamicum* (Ressl *et al*., 2009).

3.1.7 Reconstitution of BetT1 in *E. coli* polar lipid liposomes

In order to investigate transport properties, BetT1 was reconstituted into liposomes. Pure protein samples of BetT1 derived from the DDM purification were reconstituted into *E. coli* polar lipids according to the protocol prior established for reconstitution of BetP (Rübenhagen *et al.*, 2000). To test diverse conditions, *E. coli* polar lipids were dissolved in either 100 mM HEPES (pH 7.5), 100 mM Tris-HCl (pH 7.5) or 100 mM KP_i (pH 7.5) to a concentration of 20 mg/ml and as lipid-to-protein ratio (LPR) 1:10, 1:10 and 1:30, respectively, was used. Subsequently, freeze fracture electron microscopy was performed by Susann Kaltwasser to evaluate the reconstitution trials.

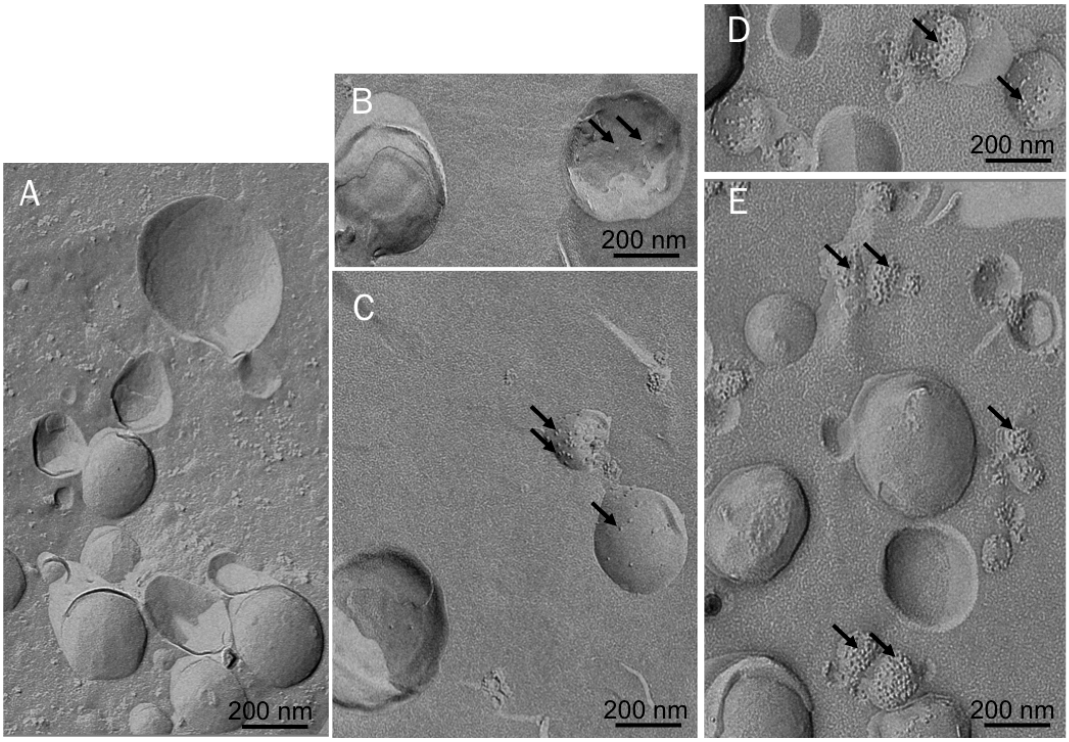

Figure 3.19: Freeze fracture images of BetT1 reconstitution into *E. coli* liposomes.
Images of freeze fracture electron microscopy of BetT1 reconstitution into *E. coli* polar liposomes in 100 mM HEPES, LPR 10:1 (A); in 100 mM Tris-HCl, LPR 10:1 (B, C) and in 100 mM KP_i, LPR 30:1 (D, F). Arrows indicate incorporated BetT1 into the liposomes. Scale bar is 200 nm. Freeze fracture was performed by Susann Kaltwasser.

Freeze fracture electron microscopy images (Figure 3.19) of the different reconstitution set-ups revealed successfully incorporated BetT1 in *E. coli* polar lipids in Tris-HCl and KP_i. In contrast, reconstitution into liposomes in HEPES buffer failed. Although in the KP_i sample, less protein with a LPR of 30:1 was used, the proteoliposomes indicated more reconstituted protein than in Tris-HCl with a LPR of 10:1. BetT1 incorporated into proteoliposomes provide a starting point for further functional measurements, for example by manipulating the conditions on each side of the membrane.

3.1.8 Transport properties of BetT1 in *E. coli* MKH13 cells

BetT1 was further investigated in *E. coli* MKH13 cells to validate the hypothesis of choline transport. [^{14}C]-choline and [^{14}C]-betaine uptake properties in different buffer conditions were determined.

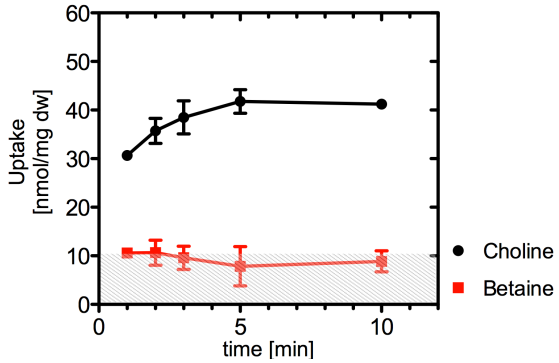

Figure 3.20: Choline vs. betaine uptake of BetT1 in *E. coli* MKH13 cells.
Uptake of choline and betaine in nmol per mg dry cell weight were measured in 100 mM KP_i and 100 mM NaCl for BetT1 in *E. coli* MKH13 cells. Uptake was started by adding saturating concentrations of 500 µM [^{14}C]-choline or betaine. The gray highlighted area resembles the background activity for [^{14}C]-choline and -betaine of MKH13 cells missing the corresponding plasmid coding for BetT1. The measurements represent the mean of at least three replicates/data point. The errorbars represent ± S.E.M..

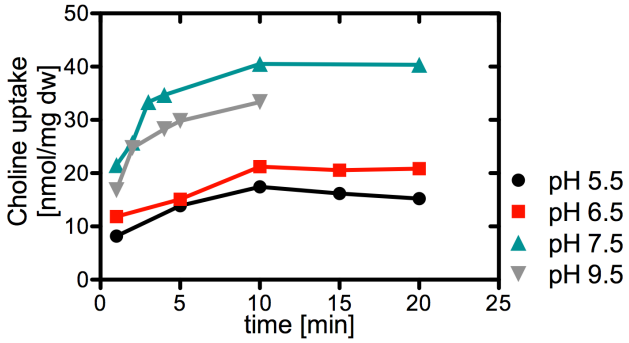

Figure 3.21: Preliminary pH dependency of BetT1 choline uptake in *E. coli* MKH13 cells.
Uptake of choline in nmol per mg dry cell weight were measured for BetT1 in *E. coli* MKH13 cells in 100 mM MES (pH 5.5), 100 mM MES pH (6.5), 100 mM HEPES (pH 7.5) and 100 mM CHES (pH 9.5). Uptake was started by adding saturating concentrations of 500 µM [^{14}C]-choline.

Transport measurements could verify BetT1 as choline specific transporter (Figure 3.20). Betaine was excluded as potential substrate with an uptake close to background activity in MKH13 *E. coli* cells. Furthermore, uptake measurements at different pH indicated optimal choline uptake activity at pH 7.5 (Figure 3.21).

Subsequently, [^{14}C]-choline uptake was explored at different external osmolalities to evaluate potential osmoregulatory properties of BetT1 (Figure 3.22). As perquisite for osmo-dependent choline transport, proton coupling was identified for the choline transporters BetT from *E. coli* and BetT2 from *A. baylyi*. In consequence, choline transport is inhibited by the protonophore CCCP, which uncouples proton and choline

transport. The influence of the ionophore CCCP on the choline uptake activity of BetT1 in sodium-free buffer was investigated (Figure 3.23). In addition, kinetic parameters were determined for BetT1 in *E. coli* MKH13 cells (Table 3.1).

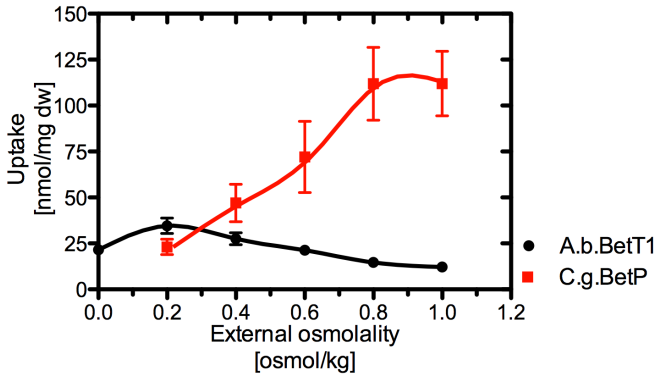

Figure 3.22: Comparison of uptake activities of BetT1 and BetP in *E. coli* MKH13 cells.
Uptake of choline for BetT1 of *A. baylyi* (A.b.BetT1) and betaine for BetP of *C. glutamicum* (C.g.BetP) in nmol per mg dry cell weight was measured in *E. coli* MKH13 cells under different external osmolalities for the time point of 1 min. Uptake was started by adding saturating concentrations of 500 µM [^{14}C]-choline or 250 µM betaine, respectively. Each value is the mean ± S.E.M. of at least three measurements.

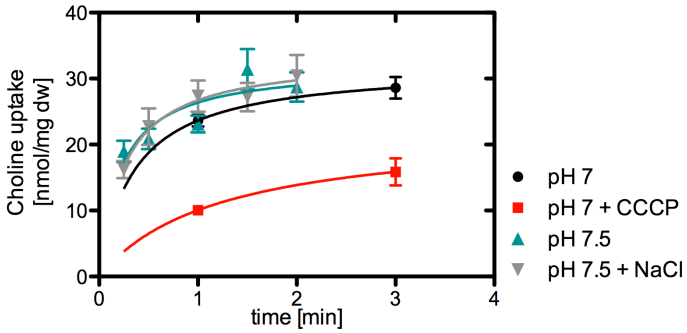

Figure 3.23: Effect of the protonophore CCCP and a sodium gradient on BetT1-mediated choline uptake in *E. coli* MKH13 cells.
Uptake of choline in nmol per mg dry cell weight was measured in sodium-free buffer (100 mM KP_i) in presence and absence of 50 µM CCCP in 100 mM KP_i buffer (pH 7) as well as in presence and absence of 100 mM NaCl in KP_i buffer (pH 7.5) for BetT1 in *E. coli* MKH13 cells. Uptake was started by adding saturating concentrations of 500 µM [^{14}C]-choline. Each value is the mean ± S.E.M of three independent measurements.

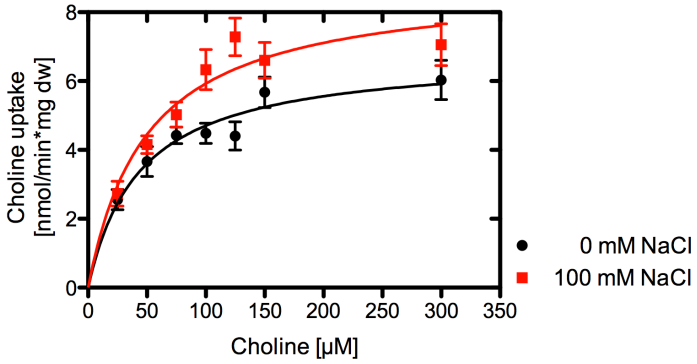

Figure 3.24: Determination of kinetic parameters of BetT1-mediated choline uptake in *E. coli* MKH13 cells.

Uptake of choline in nmol per minute and mg dry cell weight was measured in KP_i buffer in absence and presence of 100 mM NaCl for BetT1 in *E. coli* MKH13 cells. For K_m determination, the substrate concentration was varied from 25 to 300 µM [^{14}C]-choline. Each value shows the average ± S.E.M of at least six independent measurements.

Table 3.1: Kinetic parameters of BetT1-mediated choline uptake

NaCl [mM]	K_m [µM]	V_{max} [nmol/min*mg dw]	R^2
0	44.3 ± 10.6	6.8 ± 0.5	0.92
100	49.9 ± 14.3	8.9 ± 0.8	0.91

In Figure 3.22, the choline uptake activity of *A. baylyi* BetT1 is compared to the betaine uptake of *C. glutamicum* BetP in *E. coli* MKH13 cells at different external osmolalities. For BetP, betaine transport typically increased with elevated osmolalities. In contrast, BetT1 showed no activation under hyperosmotic stress indicating an osmo-independent choline uptake. Initially, the choline uptake of BetT1 first slightly increases between 0 to 0.2 osmol/kg and this is followed by a steady reduction of the activity with higher osmolalities. Investigation of BetT1 transport properties in presence and absence of sodium revealed a sodium-independent high-affinity, but low capacity choline uptake system (Figure 3.23 and Figure 3.24). The apparent K_m value for BetT1 without sodium is ~44 µM, whereas the affinity decreases with sodium to ~50 µM (Table 3.1). Upon the addition of NaCl, the maximal velocity increases slightly from 6.8 ± 0.5 to 8.9 ± 0.8 nmol/min*mg dw. Furthermore, potential proton coupling of BetT1 was examined at pH 7 (Figure 3.23). Apparently, reducing the pH from 7.5 to 7 did not alter the range of choline accumulation. Moreover, CCCP treatment leads to the decrease of the uptake by a factor of 2, which is not comparable to the abolished choline transport in the case of BetT from *E. coli* (Lamark *et al.*, 1991) or *A. baylyi* BetT2 (Figure 3.7) in presence of the protonophore. The observed reduced choline

transport of *A. baylyi* BetT1 might be attributed to the in general degraded membrane potential caused by CCCP. Taken together, the results indicated BetT1 as osmo-independent transporter being involved rather in choline uptake for catabolism than for osmostress response. Choline uptake of BetT1 does not rely either on proton or sodium coupling suggesting an uniport system entirely driven by the membrane potential adding a new transport mode to the BCCT family.

3.1.9 BetP as model system for *A. baylyi* BetT1

In addition to the crystallization of BetT1 from *A. baylyi*, BetP was used as model system for BetT1. The glycine motif of BetP was mutated to mimic the sequence of BetT1.

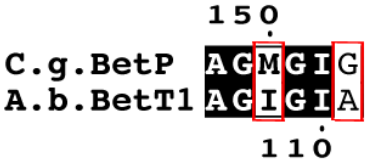

Figure 3.25: Sequence alignment of the glycine motif of BetP and BetT1.
Amino acid sequence alignment of the glycine stretch BetP from *C. glutamicum* (C.g.BetP) to BetT1 from *A. baylyi* (A.b.BetT1). In the structure of BetP, the glycine motif is located in an unwound segment approximately in the middle of TM3 (Ressl *et al.*, 2009). Altered residues within the stretch of BetP and BetT1 are marked in red.

The comparison of the residues of the glycine stretch, which is known to be responsible for the substrate specificity in BCC transporters, shows that the Met150 of BetP is replaced by an isoleucine in BetT1 (Figure 3.25). Instead of the glycine at position 153 in BetP, which is highly conserved in betaine transporters of the BCCT family, an alanine is found for BetT1.
Based on the sequence alignment with *A. baylyi* BetT1 (Figure 3.25), residues within the glycine motif were replaced by point mutations introduced into the vector pASK-IBA5*betP* by site-directed mutagenesis performed by Jessica Devant. The following single and double BetP variants were created:

1) BetP M150I
2) BetP G153A
3) BetP M150I/G153A

3.1.10 Transport properties of BetP variants in *E. coli* MKH13 cells

BetP mutants were synthetized by *E. coli* MKH13 cells and finally [^{14}C]-betaine uptake was measured at different osmotic conditions.

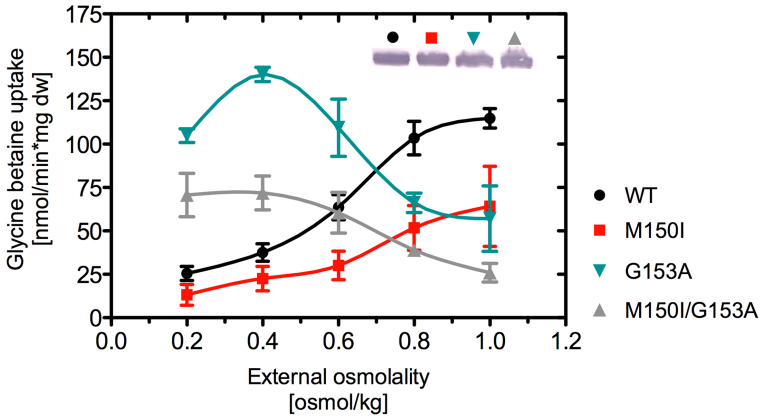

Figure 3.26: Betaine uptake rates of BetP variants in *E. coli* MKH13 cells.
Uptake rates of betaine in nmol per min and mg dry cell weight were measured as a fuction of external osmolality in *E. coli* MKH13 cells expressing the BetP mutants. The errorbars represent ± S.E.M. of triplicate experiments. Immunoblotting against the N-terminal StrepII-tag of the BetP variants in *E. coli* MKH13 membranes let estaminate the same level of protein production.

Figure 3.26 displays the different activation profiles for betaine uptake of the substitution variants of BetP compared to the BetP WT. The single substitution variant BetP M150I shows a regulation pattern comparable to the WT, although the maximum activity at 1 osmol/kg is reduced about 50 %. BetP G153A and the double variant BetP M150I/G153A exhibit significantly altered betaine transport properties. In these cases, the betaine uptake rate is higher at lower osmolalities and decreases upon osmotic upshift. For BetP G153A, the maximum activity of approximately 140 nmol/min*mg dw is reached at 0.4 osmol/kg with an even slightly increased uptake rate as the BetP WT with 115 nmol/min*mg dw at 1 osmol/kg. In contrast, the double mutant achieves only a maximal betaine uptake activity of 75 nmol/min*mg dw.

Subsequently, the [^{14}C]-betaine as well as potential [^{14}C]-choline uptake properties of BetP WT and BetP M150I/G153A in MKH13 cells were compared.

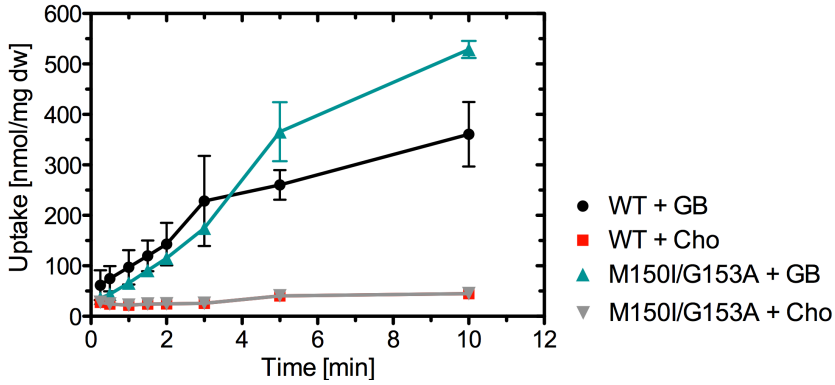

Figure 3.27: Betaine and choline uptake of BetP WT and BetP M150I/G153A in *E. coli* MKH13 cells.

Uptake of either betaine (GB) or choline (Cho) in nmol per mg dry cell weight were measured at 0.6 osmol/kg as a function of time in *E. coli* MKH13 cells expressing BetP WT or BetP M150I/G153A. Uptake was started by adding saturating concentrations of 250 µM [^{14}C]-betaine or 500 µM [^{14}C]-choline. Each value is the mean ± S.E.M of three independent measurements.

Betaine uptake of BetP WT and the double variant BetP M150I/G153A lies in the first 3 minutes in a comparable range of approximately 200 nmol/mg dw (Figure 3.27). At a time point of 10 min, the betaine transport increases up to 520 nmol/mg dw for the mutant, whereas the WT reaches a lower level of uptake with 325 nmol/mg dw. In contrast, no significant choline uptake was observed for BetP M150I/G153A as well for BetP WT.

3.1.11 Transport properties of BetP M150I/G153A in *E. coli* polar lipid proteoliposomes

Since no significant choline transport could be reported for the BetP double variant M150I/G153A in transport measurements in *E. coli* cells, protein was reconstituted in liposomes to gain further insights into the transport properties. Therefore, expression of the double mutant was performed in *E. coli* DH5α^{TM}-T1^{R} and membranes were prepared. After solubilization with DDM, the protein BetP M150I/G153A was further purified by StrepTactin®-affinity chromatography (Section 2.3.4.3). The purified protein was reconstituted with a LPR of 30:1 into preformed liposomes of *E. coli* polar lipids according to the protocol established for BetP reconstitution (Rübenhagen *et al.*, 2000). For transport measurements, extruded proteoliposomes were diluted into buffer (20 mM NaP_i pH 7.5, 25 mM NaCl, 1 µM valinomycin) containing saturating

concentrations of [^{14}C]-betaine or [^{14}C]-choline at 0.6 osmol/kg. Results are compared to the [^{14}C]-betaine uptake of BetP WT under the same experimental conditions.

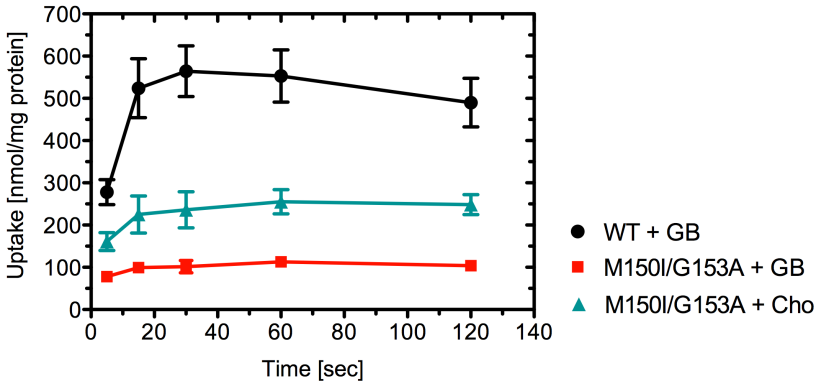

Figure 3.28: Choline and/or betaine uptake of BetP M150I/G153A and BetP WT in *E. coli* proteoliposomes.

Uptake of either choline (Cho) and/or betaine (GB) in nmol per mg protein was measured at 0.6 osmol/kg as a function of time for BetP M150I/G153A as well as for the BetP WT reconstituted into *E. coli* polar lipid liposomes. Uptake was started by adding saturating concentrations of 50 µM [^{14}C]-betaine or 250 µM [^{14}C]-choline, respectively. Each value is the mean ± S.E.M. of at least six independent measurements.

The transport measurement for the BetP variant M150I/G153A reconstituted into liposomes shows compared to BetP WT a pronounced decrease in the betaine uptake rate. Furthermore, BetP M150I/G153A is able to transport choline with a higher activity than observed for betaine (Figure 3.28). The capability of BetP WT in proteoliposomes to transport choline was excluded by former studies (Perez *et al.*, 2011b). Based on these findings, the BetP variant M150I/G153A could be used, beside the native choline transporter BetT1 from *A. baylyi*, as alternative crystallization target to provide first structural insights to the coordination of the substrate choline by an unpolar alanine within the glycine stretch in the BCCT family.

3.2 Discussion

3.2.1 Impact of the glycine stretch in choline transport

Sequence alignments of BCC transporters revealed characteristic conservation patterns within the glycine stretch, which was identified being responsible for the substrate specificity in the BCCT family (Perez *et al.*, 2011b; Ziegler *et al.*, 2010). The conserved sequence of Ala-Gly-Met-Gly-Ile-Gly was found for the sodium-coupled betaine transporter BetP from *C. glutamicum* as well as for BetT2 from *P. aeruginosa*. Instead of the methionine and the last glycine in this motif, an isoleucine and aspartate, respectively, can be indicated for BetT from *E. coli* and BetT2 from *A. baylyi*. In general, *A. baylyi* BetT2 shares the highest identity of 68 % with *E. coli* BetT, whereas identities of 44 %, 42 % and 28 % are reached for *P. aeruginosa* BetT2 and BetT3 as well as *C. glutamicum* BetP, respectively.

BetT from *E. coli* was characterized as proton-coupled choline transporter (Lamark *et al.*, 1991). Within the glycine stretch, the crucial role of the aspartate during proton-coupled choline transport was shown in a BetP mutant, in which the last glycine in the sequence was exchanged against an aspartate (Perez *et al.*, 2011b). Consequently, BetP was turned into a choline transporter by a single point mutation. The crystal structure of BetP G153D demonstrated how choline is coordinated by the aspartate in the glycine stretch in TM3 of BetP. Furthermore, functional analysis revealed the additional capacity of BetP G153D to couple the transport of choline to protons most likely by the transient protonation of the aspartate. The requirement for proton-coupled transport is the presence of a side chain of a residue, which pKa shifts in different transporter states of the alternating access cycle allowing protonation and deprotonation. This proton could be coordinated between the aspartate and the hydroxyl group of choline, which is similar to the coordination in the periplasmic choline-binding protein ChoX (Oswald *et al.*, 2008). In this thesis, proton-coupled choline transport for BetT2 was confirmed in transport measurements in the heterologous host *E. coli* (Figure 3.7). BetT1 from *A. baylyi* shows sequence identities of 50.4 %, 40 % and 30 % to *P. aeruginosa* BetT1, *E. coli* BetT and *C. glutamicum* BetP, respectively. The glycine motifs of BetT1 from *A. baylyi* but also BetT1 and BetT3 from *P. aeruginosa* are less conserved. In the osmoregulatory BetT3 of *P. aeruginosa*, the second glycine is exchanged against a serine and the last position of the stretch comprises a polar threonine instead of an aspartate or glycine (Figure 3.29). Due to

missing kinetic data of BetT3, it can be only speculated, that BetT3 is proton-coupled. Here, two polar residues, most likely by their hydroxyl groups, instead of a charged aspartate might maintain a proton-dependent coordination of choline. The choline transporter BetT1 from *A. baylyi* comprises an unpolar alanine instead of an aspartate or threonine/serine. Consequently, the proton-coupling properties were tested for *A. baylyi* BetT1. The presence of the protonophore only reduced the uptake for BetT1 (Figure 3.23), but did not abolish the transport as for *A. baylyi* BetT2 (Figure 3.7) and BetT from *E. coli* (Lamark *et al*., 1991). The reduced choline transport of BetT1 might be attributed to the decrease of the complete membrane potential of *E. coli* in presence of the protonophore. Compared to *A. baylyi* BetT1, one serine was identified at the last position of the aspartate for the osmo-independent transporter BetT1 from *P. aeruginosa*. The presence of one serine might be not enough for proton coupling, although choline coordination might not be strictly associated with protonation in the BCCT family (Perez *et al*., 2011b).

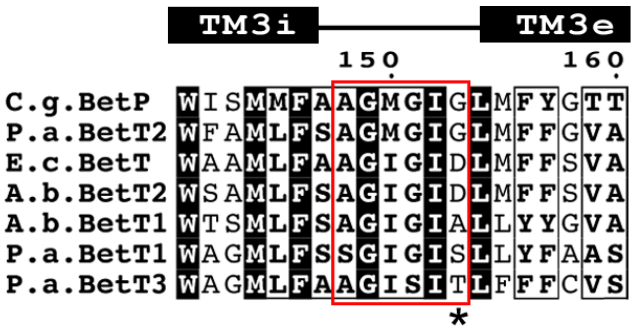

Figure 3.29: Multisequence alignment of the glycine motif of BCCTs from *A. baylyi*, *C. glutamicum* and *P. aeruginosa*.

Multiple amino acid sequence alignment of the glycine stretch (red) of *A. baylyi* BCCTs BetT1 and BetT2 to BetP from *C. glutamicum*, BetT from *E. coli* as well as BetT1-3 from *P. aeruginosa.* Numbering of the residues corresponds to BetP. In the structure of BetP, the glycine motif is located in an unwound segment between the intracellular part and extracellular part of TM3 (TM3i and TM3e) (Ressl *et al*, 2009). The α–helical parts are depicted as black bars on the top of the alignment. The (*) marked residues were shown to be mainly responsible for substrate specificity (Perez *et al*, 2011b).

3.2.2 H^+- vs. Na^+-coupled transport in osmoregulation

The osmo-profile in *E. coli* confirms a primary role of *A. baylyi* BetT2 in osmoprotection (Figure 3.6). This is consistent with *E. coli* BetT, which is activated upon hyperosmotic stress conditions (Lamark *et al*., 1991). Furthermore, BetT2 comprises a hydrophilic C-

terminal domain with a length of 178 amino acids, which is sharing 95 amino acids with the 177 hydrophilic residues of the regulatory domain of BetT from *E. coli* contributing to the high overall sequence identity. Long terminal extensions were shown to contribute to the osmoregulatory and osmosensory properties of choline and betaine transporting BCCTs (Ziegler *et al*., 2010). Due to the high overall identity to BetT1 from *E. coli* and the identical sequence of the glycine stretch, the same functional characteristics (proton-coupling and osmoregulation) were expected for BetT2. *A. baylyi* BetT1 exhibits only a short C-terminal stretch of 20 hydrophilic residues. In contrast, the role of BetT1 from *A. baylyi* was less clear. The absence of long C-terminal extensions corresponds to the finding that the activity of *A. baylyi* BetT1 is not osmoregulated. According to this, the salt-independent choline transporter BetT1 from *P. aeruginosa* as well as also the substrate/product antiporter CaiT from *E. coli* and *Proteus mirabilis* are missing long C-terminal extensions (Malek *et al.*, 2011; Schulze *et al.*, 2010). Moreover, proton-coupled choline transport was excluded for the osmo-independent transporter BetT1 from *A. baylyi* (Figure 3.23). Hence, proton-coupling might be the perquisite of osmo-dependent choline transport.

Compared to the positively charged trimethylammonium compound choline, the zwitterionic betaine was found to be symported with Na^+ ions in osmo-dependent BCCTs. Crystallization and MD simulation allowed the assignment of the residues involved in the formation of sodium-binding sites, namely Na2 and Na1' site, in the sodium-coupled BetP (Khafizov *et al.*, 2012). In the Na2 site, which is conserved also among other LeuT-fold transporters, T467/S468 are mediating crucial side chain interactions with the sodium ion in BetP (Figure 3.30). A similar conserved pattern can be observed also for proton-coupled BCCTs. The Na2 site might be occupied with the positive charge of choline in proton-coupled transporters. Together with the protonable residue within the glycine stretch of osmo-dependent choline transporters, this might fulfill the requirements for the conformational change needed for the translocation of the substrate.

In BetP, the side chains of T246/T250/F380 are responsible for the coordination of sodium at the Na1' site. However, this site is not conserved among FIRL-fold transporters and can be replaced by a positively charged residue (Khafizov *et al.*, 2012). Alternations within these residues are also present among proton- as well as sodium-coupled transporters. In the choline-transporting mutant BetP G153D, the Na1'

site still exists, probably leading to the ability to transport choline additionally in a sodium-coupled way (Perez *et al*, 2011b).

Interestingly, the serine of Na2 is exchanged against a helix-breaking proline as well as the second threonine of Na1' is replaced by a hydrophobic leucine in both osmo-independent transporters BetT1 from *A. baylyi* and *P. aeruginosa* (Figure 3.30). In general, both potential sodium-binding sites in the osmo-independent transporters can be considered as not conserved.

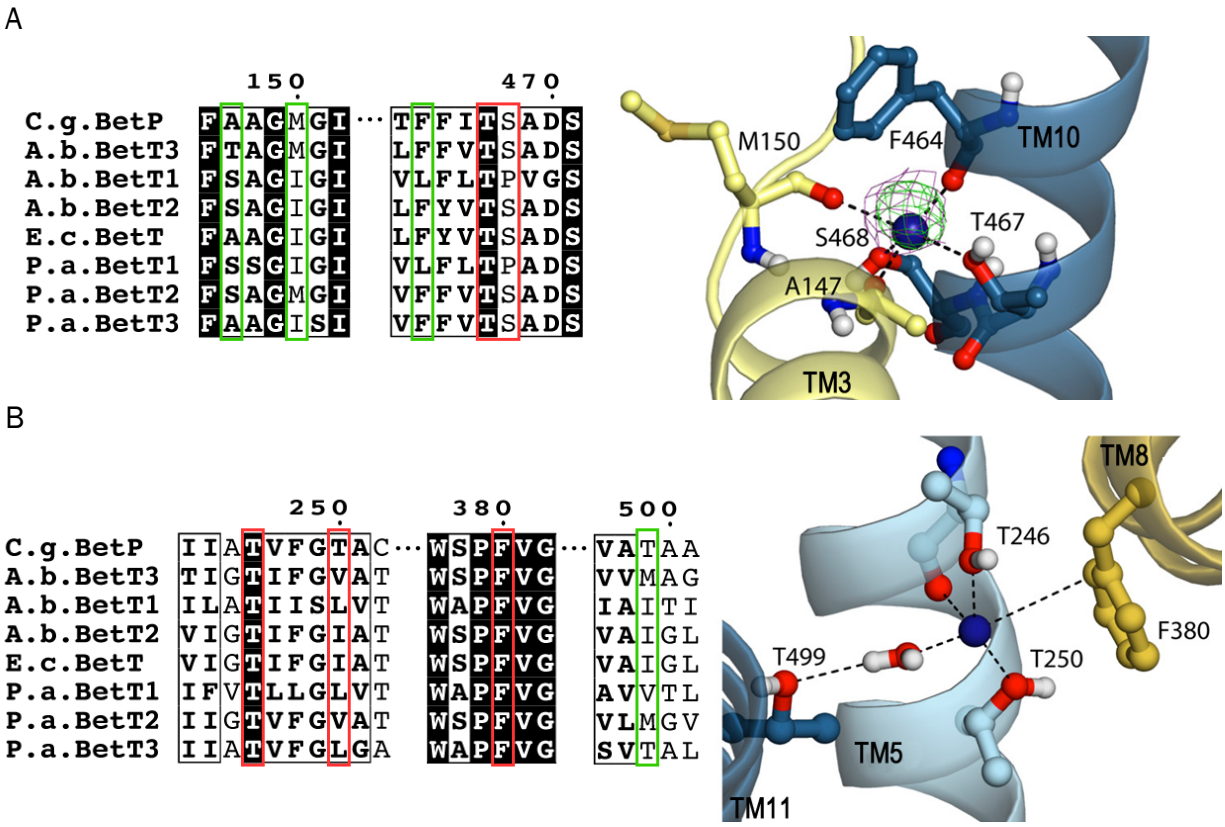

Figure 3.30: Sodium-binding sites in the BCCT family.

Sequence alignment of regions involved in sodium binding in BetP from *C. glutamicum* to BetT1-3 from *A. baylyi* BetT from *E. coli* and BetT1-3 from *P. aeruginosa* (left). Residues framed in red mediate side chain interactions, whereas residues framed in green mediate backbone interactions in BetP. Close-up views of simulation snapshots for the Na2 site (A) and Na1' site (B) of BetP. Simulation snapshot of the Na2 site is superimposed with the F_o-F_c difference density map before placing the ion (contoured at 3.0σ, green) and the $2F_o$-F_c map (contoured at 1.0σ, purple) for PDB 4AIN. Residues and helices are labeled by the according amino acid or transmembrane helix number of BetP, respectively (adapted from Khafizov *et al*., 2012).

3.2.3 Alternative choline uniport systems

The experiments in this thesis indicated *A. baylyi* BetT1 not being sodium- as well as proton-coupled, facilitating choline uniport driven by the membrane potential (Figure 3.23). This is adding a new transport mode not only to the spectra of BCCT family but also to the LeuT-fold transporters. Because choline is also an essential nutrient in eukaryotic cells, our data might be extended to understand eukaryotic choline transporters. In higher eukaryotes, choline plays a role in the synthesis of the membrane phospholipids as well of the neurotransmitter acetylcholine. Choline deficiency affects the expression of genes, which are associated with liver dysfunction and cancer. Furthermore, abnormal choline transport and metabolism have been implicated in a number of neurodegenerative disorders such as Alzheimer's and Parkinsons's desease (Michel *et al.*, 2006). Beside Na^+ and Cl^--dependent high affinity choline transporters CHTs (K_m 0.5 – 3 µM) in cholinergic neurons (Black and Rylett, 2012; Michel *et al.*, 2006), also ubiquitous Na^+-independent intermediate affinity transporters CTLs (choline transporter-like) can be found (Michel *et al*., 2006). Although the choline transporter CTL1 has been reported to be a H^+/choline exchanger (Traiffort *et al.*, 2013), more recent experiments excluded the outward H^+ gradient-dependency. Acidification and alkalization of the intracellular pH as well the addition of the protonophore FCCP decreased the choline uptake only marginal suggesting a membrane potential-dependent choline uptake (Horie *et al.*, 2014). Choline is transported by these transporters with an intermediate affinity of ~10 µM and for CTL1, 10 highly conserved TM domains with intracellular N- and C-termini were predicted (Michel *et al*., 2006).

Polyspecific organic cation transporters (OCTs) are low affinity choline transporters with an apparent K_m of 20 – 200 µM (Michel *et al*., 2006). OCTs translocate choline in a Na^+- and H^+-independent manner (Lozano *et al.*, 2013). As major driving force for choline transport, the membrane potential was identified (Michel *et al*., 2006). These transporters are distributed in liver and kidney (Lozano *et al*., 2013), but representatives were also reported in cholinergic neurons (Nakata *et al.*, 2013). Structure predictions revealed 12 TM domains with termini facing the cytoplasm with highly conserved sequence motifs to the MFS family (Lozano *et al*., 2013). In summary, diverse transport systems for choline were identified and due to the important role of choline, further investigations are required to unravel the precise transport mechanisms.

3.2.4 Crystallization of *A. baylyi* BetT1

The molecular mechanism of choline uniport for *A. baylyi* BetT1 could not be defined yet. Crystallization of the transporter is still ongoing and revealed crystals with the maximum diffraction of 7 Å up to now (Figure 3.18).

Expert pool crystallizability class: 5

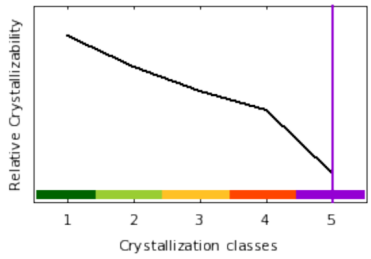

EP crystallization classes
↓Most promising
1 2 3 4 5
↑Least promising

Random forest crystallizability class:4

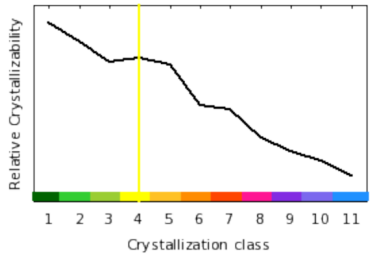

RF crystallization classes
↓Most promising
1 2 3 4 5 6 7 8 9 10 11
Least promising↑

Protein features	
Length	526
Molecular weight	58187
Gravy index	0.70
Isoelectic point	6.41
Instability index	29.74
Predictions	
Transmembrane helices (number)	12
Signal peptides (length)	No
Longest disorder reg.	18
Longest low complexity reg.	19
Coiled coils	0
% disorder residues	10
% coil residues	24
% helix residues	75
% strand residues	1
Predicted surface features	
Surface entropy	-1.06
Surface hydrophobicity	-0.27
Surface rugedness	1.01
Other	
Number of Cys residues	3
Number of Met residues	15
Number of Trp residues	18
Number of Tyr residues	19
Number of Phe residues	34
Epsilon 280	127310
Insertions score	0.02
XtalCoDe construct scoring	

```
1...*...10....*...20....*...30....*...40....*...50....*...60....*...70....*...80....*...90....*..100
MWSKRDEQKTYPPIRLNPFVFWSSAISISIFGMLFVLFPETSQHGLTWIQQQVNQLFGWYYMLVIILSLGFVAWLAFSQVGNIPLGKAQDKPEFGYLVWT

....*..110....*..120....*..130....*..140....*..150....*..160....*..170....*..180....*..190....*..200
SMLFSAGIGIALLYYGVAEPVDHFLRPPEGQGGTVEAAQNAMMYSFLHWGIHGWVLYALVGVTLGYFAFRRDLPLALRSALYPIFGERIHGLVGHMVDGF

....*..210....*..220....*..230....*..240....*..250....*..260....*..270....*..280....*..290....*..300
GILATIISLVTNLGIGALVMISGISYLFPDLPNTSSTLVVTVIMMMLVATLTTVIGIEKGLAWLSRINLRLLYLLLLFVFLTGPTNHLLNGLVQNTGDYL

....*..310....*..320....*..330....*..340....*..350....*..360....*..370....*..380....*..390....*..400
SHFVQKSFDLYLYDKNATGWLASWTIFYWAWWIAWAPFVGMFIARISKGRTIREVVLGVCLIPLGFTLAWISIFGNTAIDLILNHGQQIIGSLVIQDPAL

....*..410....*..420....*..430....*..440....*..450....*..460....*..470....*..480....*..490....*..500
SLFKLLEYLPFHPYVAGIVVVICFVLFLTPVGSGTLMIANLSSQGGSSDSDSPIWLRVFWSIAITIVSIGLLLAGSFSAMQSAVVLCGLPFSVILLLYMF

....*..510....*..520....*.
GLAKALKQETQQPVVESHTTETSGSD
```

Legend

LOOP	loop secondary structure predicted by PSIPRED
HELIX	helix secondary structure predicted by PSIPRED
STRAND	strand secondary structure predicted by PSIPRED
DISORDER	disordered region predicted by DISOPRED2
LOW COMPLEXITY	low complexity region predicted by SEG
COILS	coiled coils region predicted by COILS
TRANSMEMBRANE HELICES	transmembrane helices predicted by TMHMM
SIGNAL PEPTIDES	signal peptites predicted by RPSP

Figure 3.31: Prediction of BetT1 crystallization probability.
The crystallization probability was calculated from the *A. baylyi* BetT1 protein sequence by the XtalPred server (http:// ffas.burnham.org/XtalPred). Disordered regions are underlined in the respective sequence and an arrow indicates the length of the longest disordered region.

The crystallization success rate was investigated by the XtalPred server, which calculates a so-called ''crystallization feasibility'' (Figure 3.31) (Slabinski *et al.*, 2007). Due to long disordered regions at the N- and C-terminus, the crystallization of BetT1 was classified as rather less promising. The unordered regions of BetT1 could explain, why no better diffracting crystals were obtained. In addition, the SERp server proposed three clusters within the BetT1 sequence, which by substitution might enhance the probability for crystallization (Figure 3.32) (Goldschmidt *et al.*, 2007). Successful crystallization for other BCCTs like BetP and CaiT was achieved with the detergent Cymal-5 (Ressl *et al.*, 2009; Schulze *et al.*, 2010). In this thesis, BetT1 crystal growth was only observed in DDM. In comparison to Cymal-5, DDM is forming larger detergent micelles, which stabilize the proteins in solution. Larger sized micelles are known to impede interactions between the protein molecules required for crystal contacts (Gutmann *et al.*, 2007). Modifications like the substitution of the clusters and truncations of the N-terminal His-tag as well as the change to smaller detergents might improve the 3D crystallization of BetT1. Furthermore, a stabilizing effect by re-lipidation of membrane proteins during crystallization was observed in crystallization techniques like HiLiDe (Gourdon *et al.*, 2011). The role of lipids was already discussed also for BetP due to the specific bound negatively charged PG lipids, which were resolved in a crystal structure (Koshy *et al.*, 2013).

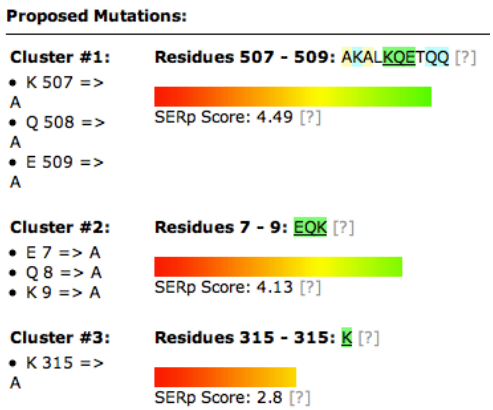

Figure 3.32: Surface Entropy Reduction prediction (SERp) for BetT1.
Clusters for surface entropy reduction to enhance the crystallization probability were estimated from the BetT1 amino acid sequence by the SERp server (http://services.mbi.ucla.edu/SER/).

SERp scores higher than 3 indicate good candidates for mutation. Residues proposed for substitution are shaded green, other mutatable high entropy residues are shaded blue and low entropy residues are shaded yellow.

However, the overall fold of BetT1 will be comparable to trimeric BetP or CaiT. The formation of trimers for BetT1 was already confirmed by BN-PAGE (Figure 3.14). A first homology model for protomeric BetT1 is shown in Figure 3.33. The model was generated by the ModBase server (Pieper *et al.*, 2014).

Figure 3.33: Homology model of *A. baylyi* BetT1.
The homology model of BetT1 was generated using the ModBase server (http://modebase.compbio.ucsf.edu/modebase-cgi/index.cgi) from the crystal structure of BetP from *C. glutamicum* with a sequence identity of 35 % (Ressl *et al.*, 2009; Sand *et al.*, 2014). BetT1 is lacking the N- and C-terminal extensions responsible for osmoregulation.

3.2.5 BetP as model system for BetT1

For an alternative crystallization approach, the model system BetP from *C. glutamicum* was used as a blue print for *A. baylyi* BetT1. Transforming BetP into a transporter with different substrate specificity was already successful in former studies, which benefited from the well-established purification and crystallization protocol (Gärtner, 2014; Perez *et al.*, 2011b). Therefore, the glycine stretch of BetP was mutated in respect to the choline transporter BetT1 from *A. baylyi*. Functional analysis indicated that regulation of betaine transport was dramatically changed for BetP G153A and regulation was lost for M150I/G153A. Interestingly, the pattern of choline transport of BetT1 (Figure 3.22) is comparable to this of the double mutant for betaine (Figure 3.26). It was speculated, that the tight coupling/decoupling of the substrate is responsible for the regulation of transport in BetP (Gärtner, 2014). Apparently, the

plasticity of the glycine stretch, which is supposed to move approximately 6 Å during transport cycle, was altered. Additionally, local protein-protein interactions as well protein-lipid interactions at this site might be changed (Koshy *et al*., 2013). Similar changes in the regulation and uptake rate of betaine in mutants of the glycine stretch were reported before (Gärtner, 2014; Perez *et al.*, 2011b). In proteoliposomes, choline transport was observed for BetP M150I/G153A (Figure 3.28), whereas choline uptake was not observed for BetP in *E. coli* cells. In comparison to cell measurements, purified protein can reconstitute bidirectionally. In BetP M150I/G153A, both sodium-binding sites remained almost unchanged. Exposed sodium-binding sites in BetP, which is embedded in the right orientation in liposomes as it should be in the cell membrane, with or without bound sodium in the outward open conformation might impede binding and transport of the positively charged choline. Transport of substrate can principally function in both directions in secondary transporters. Thus, inward open but outwards oriented BetP M150I/G153A might allow the transport of choline inside of the liposomes, because in this conformation the sodium sites are not exposed. This would explain the missing choline uptake properties of the BetP double mutant in *E. coli* cells. An extended substrate specificity of BetP M150I/G153A to choline would alternatively allow the structural investigation of the coordination of choline by an unpolar alanine within the glycine stretch, if the crystallization of *A. baylyi* BetT1 will fail.

3.2.6 Physiological role of pathogen-relevant choline transport

Pathogenic *P. aeruginosa* is equipped with several BCC transporters. In contrast to *A. baylyi*, *P. aeruginosa* is able to use choline not only as precursor for the osmoprotectant betaine, but also as carbon source. In the pathogenic bacterium, in total three transporter were reported to mediate choline uptake: BetT1, BetT3 and the ABC-transporter CbcXWV (Malek *et al.*, 2011). The impaired choline uptake of the *A. baylyi* double deletion mutant of BetT1 and BetT2 led to the conclusion, that this BCCTs are the only choline transporters in *A. baylyi* (Sand *et al.*, 2014). In *P. aeruginosa* BetT3, analogously to BetT2 from *A. baylyi*, was found to be the major choline transporter upon hyperosmotic stress. The osmo-independent BetT1 and CbcXWV were reported to have a major role for growth *of P. aeruginosa* on choline. Thus, *A. baylyi* BetT1 is rather involved in catabolism than in osmoprotection and is proposed to play a role in the metabolic adaption to choline-rich environments. This

conclusion is supported by the findings of the group of B. Averhoff showing that choline is taken up and oxidized to betaine even in the absence of salt stress in *A. baylyi* (Sand *et al.*, 2014). According to this, Kleber and colleagues discovered that *Acinetobacter calcoaceticus* 69V co-metabolize choline when grown on acetate as carbon source (Kleber *et al.*, 1977). In consequence, the end product betaine of the choline oxidation has to be excreted, what was also observed for *A. baylyi* under isoosmotic conditions. The transport system allowing the efflux of betaine in *A. baylyi* is not identified yet. As potential efflux systems, a counterflow mediated by the osmoregulated betaine transporting BCCTs BetT3 at isotonic conditions was proposed. The counterflow was excluded for *A. baylyi* BeT3 by deletion mutants, which shows still betaine efflux (personal communication B. Averhoff). Additionally, substrate/product antiport of BetT1 could not be confirmed by preloading cells as well as proteoliposomes with betaine (data not shown). It has to be noted, that betaine efflux was not observed under hyperosmotic stress conditions, in which BetT2 is responsible for the uptake of choline uptake as precursor for betaine as osmoprotectant. This is indicating a regulated system for choline in- and betaine-efflux. In consequence, BetT2 might be addressed in further studies as betaine export system under isotonic, down-regulating conditions.

However, *A. baylyi* was not able to use choline as single carbon source. But the oxygen consumption increased independent of high salinity after addition of choline to *A. baylyi* cells. Based on this, it was speculated, that in choline-rich environments choline oxidation might lead to an energetic benefit for the soil bacterium *A. baylyi* (Sand *et al.*, 2014). Choline is a fundamental metabolite in plants. It can be found as component of the membrane lipid phosphatidylcholine, which accounts 40 – 60 % of lipids in non-plastid plant membranes (Moore, 1990). Other membranous environments are colonized by pathogenic *A. baylyi* relatives as *A. baumannii*. As adaption of *Acinetobacter* to membranous environments at infection sites, choline might be provided by phospholipases from abundant host molecules such as phosphatidylcholine and sphingomyelin representing 50 – 90 % of phospholipids in eukaryotic cell membranes (Zachowski, 1993). The screening of different *A. baumannii* strains revealed that the *bet* gene cluster including the osmo-dependent and osmo-independent BCCTs, BetT2 and BetT1, respectively, is widely distributed. It can be found for strains, such as *A. baumannii* ATCC 19606, ATCC 17978, SDF as well as for the multidrug resistant strains AYE and AB0057 (Sand *et al.*, 2014). A study

demonstrated for the pathogen *P. aeruginosa* that the *bet* gene cluster is among the most highly expressed genes in cystic fibrosis patients and choline is actively acquired during infections (Malek *et al.*, 2011; Son *et al.*, 2007). Thus, it can be proposed that the choline oxidation pathway and the choline transporter in combination with distinct phospholipases, which were shown to be important for the pathogenesis of *A. baumannii* (Camarena *et al.*, 2010; Jacobs *et al.*, 2010), play a major role in metabolic adaption of pathogenic *Acinetobacter* to host tissues (Sand *et al*, 2014).

4 Regulatory role of charged clusters in the N-terminal domain of BetP from *Corynebacterium glutamicum*

Several experiments for BetP from *C. glutamicum* as well as for other BCC transporters demonstrated the contribution of their terminal extensions to osmoregulation. BetP exhibits not only a long mainly positively charged C-terminal domain but also a long negatively charged N-terminal domain. Whereas the α-helical C-terminal domain was identified as a chemosensor sensing the increase of internal K^+ concentration upon osmotic upshift (Peter *et al.*, 1998a; Schiller *et al.*, 2004), the functional impact of the N-terminal domain in osmoregulation remains unclear. Truncations of the N-terminal domain renders BetP less osmosensitive in *C. glutamicum* comprising only negatively charged lipids, whereas lose their osmoregulatory properties in the heterologous host *E. coli* with less than 30 % negatively charged lipids. The data suggest that negative charges either from lipids (*C. glutamicum*) or the N-terminal domain (*E. coli*) are absolutely essential for regulation. As negatively charged lipids can compensate for the lack of the N-terminal domain and *vice versa* (Ott *et al.*, 2008), it is assumed that they compete for the same interaction site. Opposite charges of the C-terminal and N-terminal domain of BetP and the relevance of the anionic lipids during osmostress activation let suggest an interaction between these three elements in the regulation mechanism.

4.1 Results

4.1.1 Selection of negatively charged clusters of the N-terminal domain of BetP

The 60 amino acid long N-terminal domain of BetP comprises 15 negatively and only two positively charged residues, which are not conserved among other members of the BCCT family. The negatively charged residues are arranged partially in clusters of 2 – 3 residues: E13/D14 (negatively charged cluster1, NC1); E24/25 (negatively charged cluster2, NC2) and E44/E45/E46 (negatively charged cluster3, NC3). The latter two were identified by the SERp server to impede crystallization (Figure 4.2) (Goldschmidt *et al.*, 2007). The approach of

this server relies on the concept of surface entropy reduction (SER) and identifies flexible, solvent-exposed residues within the protein sequence, which by replacement to residues with lower conformational entropy lead to an increased probability for crystallization (Goldschmidt *et al.*, 2007). As a result, these two clusters revealed SERp scores higher than 3.0 indicating good candidates for mutation. Indeed, diffraction of BetP WT crystals was limited to 6 Å, whereas successful crystallization up to 2.7 Å was performed with a N-terminally truncated mutant BetPΔ29EEE44/45/46AAA (BetPΔ29NC3A) missing NC1 and NC2 due to truncation and exchange of NC3 by alanine substitution (Figure 4.1) (Koshy *et al.*, 2013).

Furthermore, for the N-terminal domains of the BetP WT, NC2 and NC3 are predicted to comprise two potential α-helical segments of 10 – 15 amino acids, respectively (Figure 4.3, BetP WT). In a recently published BetP structure the α-helical structure of the remaining N-terminal domain around the alanine substituted NC3 were resolved from Gln55 to Ala41 (Perez *et al.*, 2012).

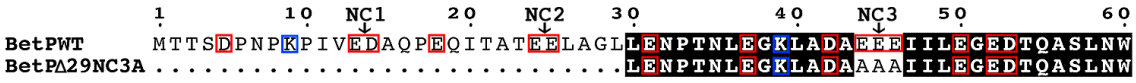

Figure 4.1: Alignment of the N-terminal domain of BetP WT and BetPΔ29NC3A.
Amino acid sequence alignment of the N-terminal domain of BetP WT and the N-terminally truncated crystallization mutant BetPΔ29NC3A. Negatively charged residues are framed red and positively charged residues blue. Negatively charged clusters are indicated for E13/D14 (NC1), E24/E25 (NC2) and E44/E45/E46 (NC3).

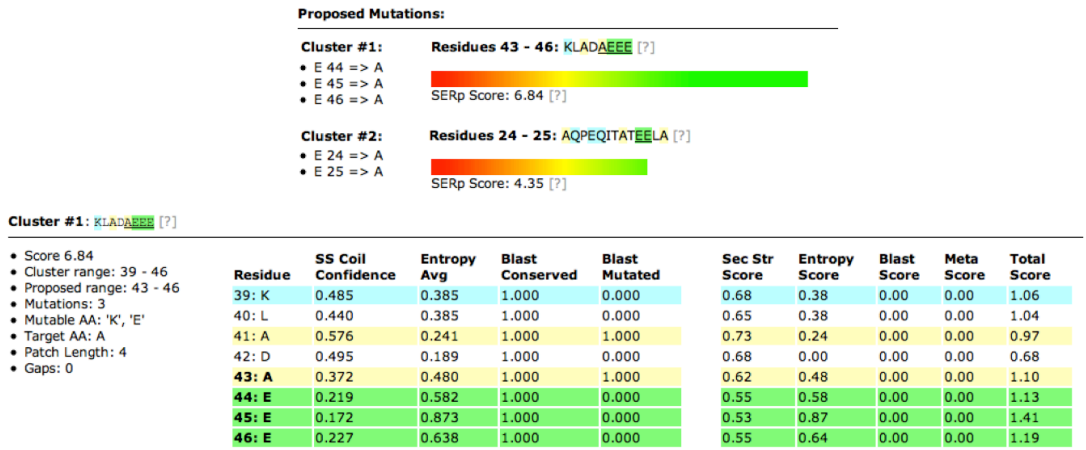

Residue	SS Coil Confidence	Entropy Avg	Blast Conserved	Blast Mutated	Sec Str Score	Entropy Score	Blast Score	Meta Score	Total Score
39: K	0.485	0.385	1.000	0.000	0.68	0.38	0.00	0.00	1.06
40: L	0.440	0.385	1.000	0.000	0.65	0.38	0.00	0.00	1.04
41: A	0.576	0.241	1.000	1.000	0.73	0.24	0.00	0.00	0.97
42: D	0.495	0.189	1.000	0.000	0.68	0.00	0.00	0.00	0.68
43: A	0.372	0.480	1.000	1.000	0.62	0.48	0.00	0.00	1.10
44: E	0.219	0.582	1.000	0.000	0.55	0.58	0.00	0.00	1.13
45: E	0.172	0.873	1.000	0.000	0.53	0.87	0.00	0.00	1.41
46: E	0.227	0.638	1.000	0.000	0.55	0.64	0.00	0.00	1.19

Cluster #2: AQPEQITATEELA [?]

- Score 4.35
- Cluster range: 15 - 27
- Proposed range: 24 - 25
- Mutations: 2
- Mutable AA: 'K', 'E'
- Target AA: A
- Patch Length: 2
- Gaps: 0

Residue	SS Coil Confidence	Entropy Avg	Blast Conserved	Blast Mutated	Sec Str Score	Entropy Score	Blast Score	Meta Score	Total Score
15: A	0.620	0.510	1.000	1.000	0.75	0.51	0.00	0.00	1.26
16: Q	0.647	0.321	1.000	0.000	0.77	0.32	0.00	0.00	1.09
17: P	0.572	0.612	1.000	0.000	0.72	0.61	0.00	0.00	1.34
18: E	0.612	0.612	1.000	0.000	0.75	0.61	0.00	0.00	1.36
19: Q	0.685	0.667	1.000	0.000	0.79	0.67	0.00	0.00	1.46
20: I	0.727	0.570	1.000	0.000	0.81	0.57	0.00	0.00	1.38
21: T	0.695	0.249	1.000	0.000	0.80	0.25	0.00	0.00	1.05
22: A	0.491	0.387	1.000	1.000	0.68	0.39	0.00	0.00	1.07
23: T	0.210	0.485	1.000	0.000	0.55	0.48	0.00	0.00	1.03
24: E	0.047	0.775	1.000	0.000	0.50	0.78	0.00	0.00	1.28
25: E	0.074	0.633	1.000	0.000	0.51	0.63	0.00	0.00	1.14
26: L	0.121	0.342	1.000	0.000	0.52	0.34	0.00	0.00	0.86
27: A	0.285	0.051	1.000	1.000	0.57	0.00	0.00	0.00	0.57

Figure 4.2: Surface Entropy Reduction prediction (SERp).
Clusters for surface entropy reduction were estimated from the BetP protein sequence using the SERp server (http://services.mbi.ucla.edu/SER/). SERp scores higher than 3 indicate good candidates for mutation. Residues proposed for substitution are shaded green, other mutatable high entropy residues are shaded blue and low entropy residues are shaded yellow. SS Coil Confidence for residues being in a coil region, range from 0 – 1.0. Entropy Avg being the average of the side chain entropy of 3 residues, range from 0 for no entropy – 1.0 for high entropy. Blast Conserved describes the conservation of BLAST aligned sequences, range from 0 (no conservation) – 1.0 (fully conserved). Blast Mutated is the fraction of BLAST aligned sequences containing the target residue (A) at this position, range from 0 (none) – 1.0 (all).

In order to evaluate the impact of the selected clusters in osmoregulation, point mutations were introduced individually and together into the vector pASK-IBA5*betP* by site-directed mutagenesis. The clusters in the protein sequence were substituted by alanines leading to the following N-terminal BetP variants:

1) BetP E13A/D14A, hereafter referred to as BetP NC1A
2) BetP E24A/E25A, hereafter referred to as BetP NC2A
3) BetP E44A/E45A/E46A, hereafter referred to as BetP NC3A
4) BetP E13A/D14A/E24A/E25A, hereafter referred to as BetP NC12A
5) BetP E13A/D14A/E24A/E25A/E44A/E45A/E46A, hereafter referred to as BetP NC123A

The impact of the folding for the N-terminal domains of BetP variants was investigated by secondary structure predictions based on the substituted amino acid sequences of the BetP variants.

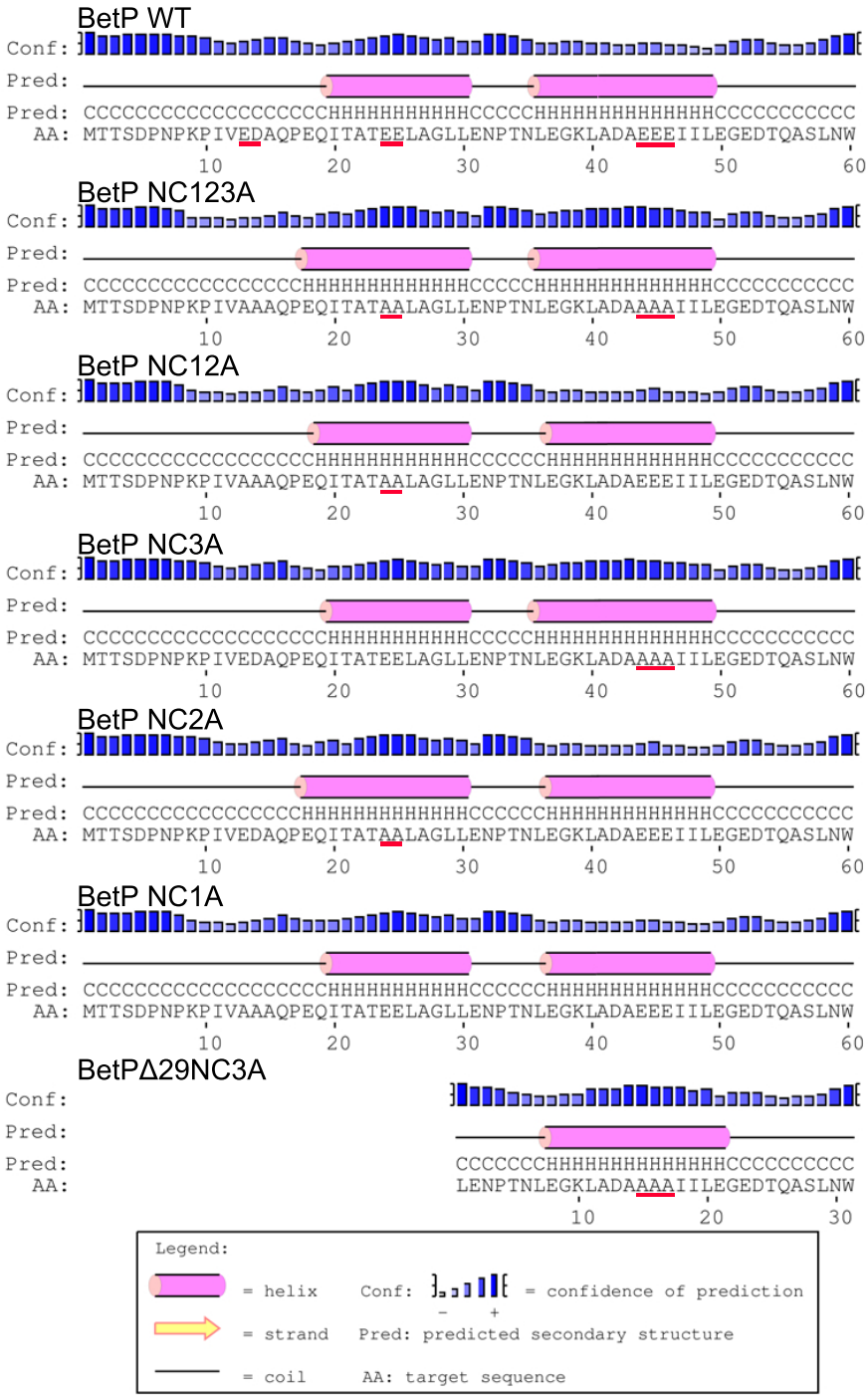

Figure 4.3: Secondary structure of the N-terminal domain of BetP WT and NCA variants. Secondary structure prediction of the N-terminal domain of BetP from *C. glutamicum* was performed by the PSIPRED webserver (McGuffin *et al.*, 2000). Negatively charged clusters and the corresponding alanine substituted positions are indicated by red lines.

The secondary structure predictions (Figure 4.3) suggest that the helical fold is slightly affected by the substitutions of the clusters when the length of the helix as well as the confidence of prediction is compared. For the N-terminal domains of the BetP WT, NC1A, NC2A and NC12A, the second helical segment exhibit only a

low confidence level, whereas BetP NC3A and NC123A showed an increased probability for the helical fold. Interestingly, alanine substitutions of NC2, NC12 and NC123 revealed a longer first helical segment, with Glu18 and Gln19 being still part of the helix.

4.1.2 Transport properties of N-terminal BetP variants in *E. coli* MKH13 cells

The N-terminal modified *betP* mutants were expressed and the corresponding BetP proteins were synthetized in *E. coli* MKH13 cells. Subsequently, [^{14}C]-betaine uptake rates were measured under hyperosmotic conditions in order to evaluate the effect on the osmoregulatory properties of the alanine substituted BetP variants (Figure 4.4). Results are compared to the transport properties of BetP WT under the same experimental conditions.

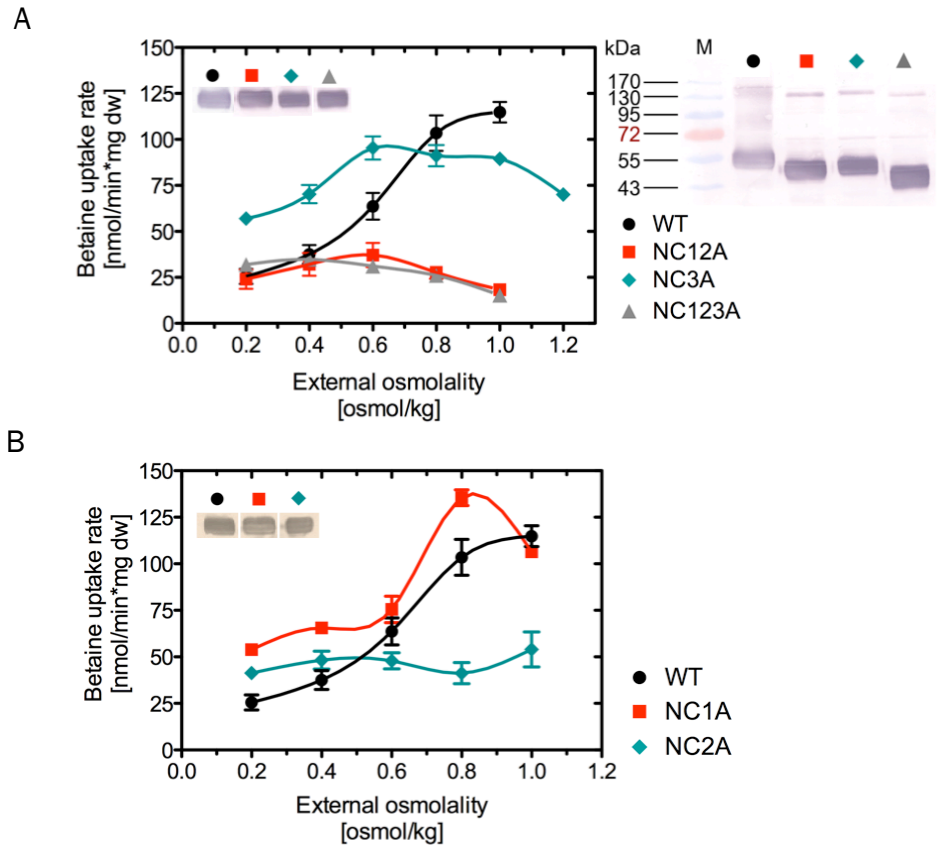

Figure 4.4: Betaine uptake rates of BetP NCA variants in *E. coli* cells.
Uptake rates of betaine in nmol per min and mg dry cell weight were measured in dependence to the external osmolality in *E. coli* MKH13 cells expressing BetP NC123A, NC12A and NC3A (A) as well as BetP NC1A and NC2A (B). Each value is the mean ± S.E.M. of at least three independent measurements. Immunoblotting against the N-terminal StrepII-tag of the BetP variants in *E. coli* MKH13 membranes demonstrates the

same level of synthesis. Additionally, the complete Western Blot shows the migrating behavior of the BetP variants during SDS-PAGE (A, top right). (M) PageRuler™ Prestained Protein Ladder (Thermo Scientific Molecular Biology).

The osmotic profiles of BetP NC12A, NC123A, and NC2A are significantly affected when compared with BetP WT. BetP NC12A and NC123A are constantly down-regulated maintaining wild type basal transport rate over the whole range of osmolality. BetP NC2A is deregulated with a nearly constant betaine uptake rate of slightly above the WT basal activity (Figure 4.4 B). In contrast, BetP NC1A exhibits an osmo-dependent betaine uptake rate with slightly increased uptake rates compared to BetP WT. The uptake rate of BetP NC3A reaches its maximum activity at lower osmolalities (0.6 osmol/kg) than BetP WT (1 osmol/kg) (Figure 4.4 A). Additionally, the maximal uptake rate is reduced by ~ 20 % and the osmo-profile is flattened. The replacement of the N-terminal clusters in the BetP variants NC3A, NC12A and NC123A slightly changed the migration behavior during SDS-PAGE analysis (Figure 4.4 A) indicating either a different folding behavior or even different amount of bound lipids. Aside of the first 20 amino acids indicated as essential *in C. glutamicum* before (Peter *et al.*, 1998a), NC2 can be assigned as the crucial negatively charged cluster within the N-terminal domain regarding osmoregulation of BetP in the heterologous host *E. coli*.

4.1.3 Potential interaction of N- and C-terminal domains

Although NC2 in the N-terminal domain was narrowed down from others and identified to have a crucial function, the contribution of the N-terminal domain to the osmoregulatory mechanism was previously predicted to be indirect via the C-terminal domain (Ott *et al.*, 2008). Certainly, an interaction between the negatively charged cluster E24/E25 with positively charged residues of the C-terminal domain could be assumed. In order to predict potential interacting residues at the C-terminal end, a trimer was modelled based on one protomer with a partially resolved N-terminal domain (chain A, PDB entry code 4AIN) and the protomer with the best-resolved C-terminal domain (chain A, PDB entry code 2WIT) (Figure 4.5) to date. Secondary structure predictions of the N-terminal domain using the PSIPRED webserver (McGuffin *et al.*, 2000) suggested two α-

helical segments separated by a short loop region between residues 31 – 35 (Figure 4.3). This loop region contains a proline residue (Pro33) that could potentially cause a kink changing the orientation of the first half of the N-terminal domain. Taking this potential bending into account, the most plausible interaction partners for the N-terminal domain NC2 with the C-terminal helix were the positively charged R576 and R583 (personal communication Dr. Caroline Koshy, Figure 4.5). Interestingly, these residues are nearly identical with crystal contacts (Figure 4.12) formed by Arg574-Asp356 and Arg584-Glu175 by the C-terminal domain and loops at the periplasmic side of the symmetry related trimer.

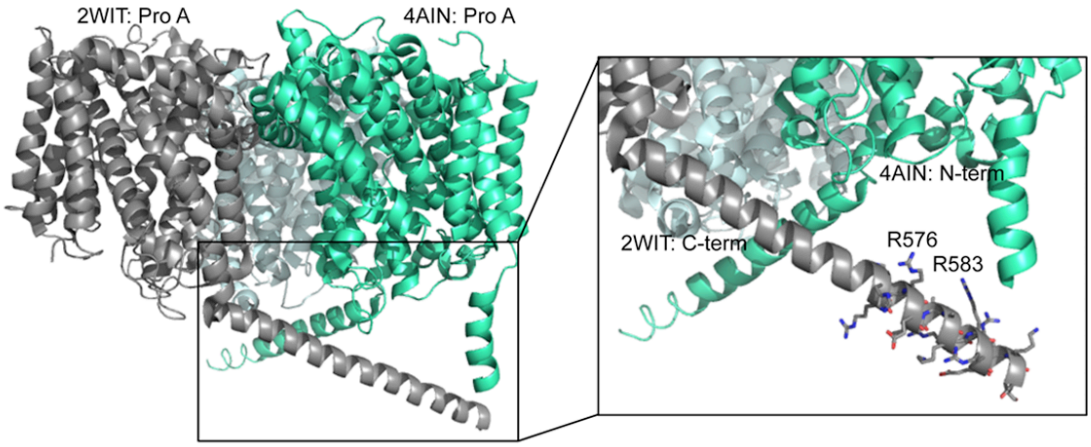

Figure 4.5: Model of potential C-terminal interaction sites.
Protomer A of the BetP trimer (PDB entry code 4AIN) containing the longest resolved N-terminal domain was modelled into the position of protomer C in the BetP trimer, in which protomer A exhibits the longest resolved C-terminal domain (PDB entry code 2WIT). The inset shows potential interactions between the N-terminal domain and Arg576 or Arg583 within the C-terminal domain.

To further investigate potential interactions between NC2 of the N-terminal domain as well as Arg576 and Arg583 of the C-terminal domain, the corresponding residues were replaced by cysteines creating the following different combinations of BetP cysteine variants:

1) BetP E24C/R576C
2) BetP E25C/R576C
3) BetP E24C/R583C
4) BetP E25C/R583C

Single C-terminal cysteine mutants were also required to be examined as controls and therefore site-directed mutagenesis was performed to introduce the following point mutations in BetP:

1) BetP R576C
2) BetP R583C

However, even after several replications, only the cysteine variant BetP R576C could be produced.

4.1.4 Transport properties of cysteine variants of BetP in *E. coli* MKH13 cells

To inspect the transport activity, the double cysteine variants and single C-terminal cysteine variant were synthetized in *E. coli* MKH13 cells and subsequently the uptake of [^{14}C]-betaine was measured under different osmotic conditions.

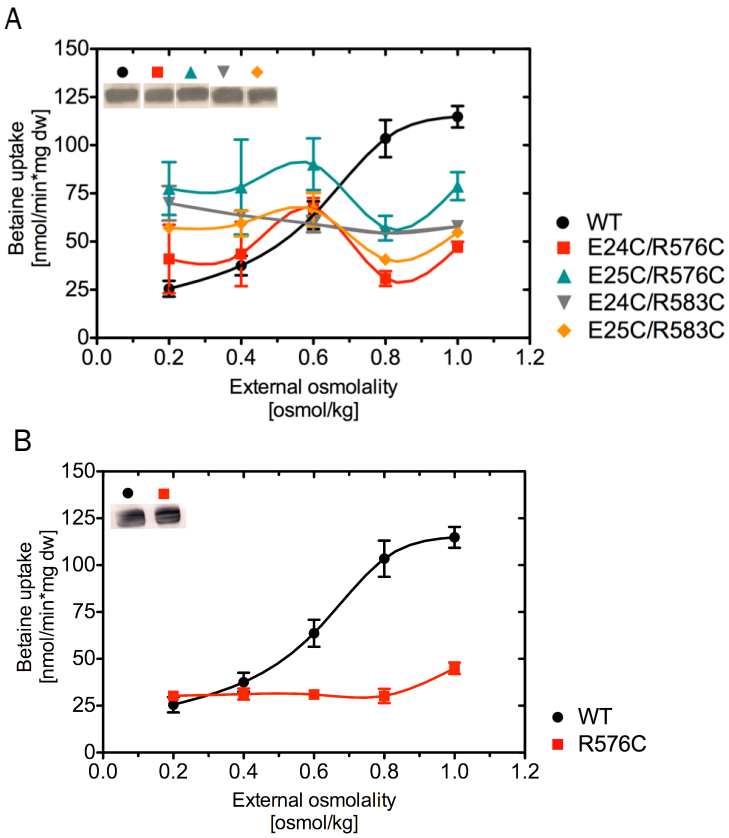

Figure 4.6: Betaine uptake rates of BetP variants with double and single cysteine substitutions in *E. coli* MKH13 cells.

Uptake rates of betaine in nmol per min and mg dry cell weight were measured in dependence to the external osmolality in *E. coli* MKH13 cells expressing N-terminal double cysteine BetP mutants (A) and single cysteine variant BetP R576C (B). Each point shows the average of at least three independent measurements. The errorbars represent ± S.E.M.. Immunoblotting against the N-terminal StrepII-tag of the BetP variants in *E. coli* MKH13 membranes detect a comparable level of protein synthesis.

The double cysteine variants of BetP show in all cases a significant altered osmotic activation profile, although none of the BetP variants abolish activity completely. BetP E24C/R576C, BetP E25C/R576C as well as BetP E25C/R583C show similar osmo-profiles with significantly different uptake rates from basal WT activity for E24C/R576C to 2/3 of maximal WT activity for E25C/R576C (Figure 4.6 A). They all exhibit a more or less pronounced maximal activity at 0.6 osmol/kg. The subsequent decrease of activity is followed by a slight increase at 1.0 osmol/kg. In contrast, BetP E24C/R583C shows a deregulated constitutively active betaine uptake rate at 1/2 of WT activity. Surprisingly, the single C-terminal cysteine variant BetP R576C is down regulated at basal WT activity (Figure 4.7 B), but can be rescued by the additional mutation at E25C in the double cysteine variant (Figure 4.6 A).

4.1.5 Disulfide cross-linking of cysteine variants of BetP

In order to examine the effect of site-directed cross-linking on the oligomerization state of these BetP variants *in vivo*, the double mutants were produced in *E. coli* DH5α^{TM}-T1^{R} cells as described in Section 2.3.1. The membranes of the cells were prepared and incubated for 1 h with copper-o-phenanthroline (CuPh). This oxidant leads to oxidative conditions and induces disulfide bond formation only if the cysteine residues involved are in close proximity. Cleavage of the disulfide bonds was achieved by the addition of the reducing agent TCEP. The same procedure was applied for the single C-terminal cysteine mutant BetP R576C and BetP WT. Non-reducing SDS-PAGE was performed with all samples for Western blot analysis to gain information about the oligomerization state of the different proteins.

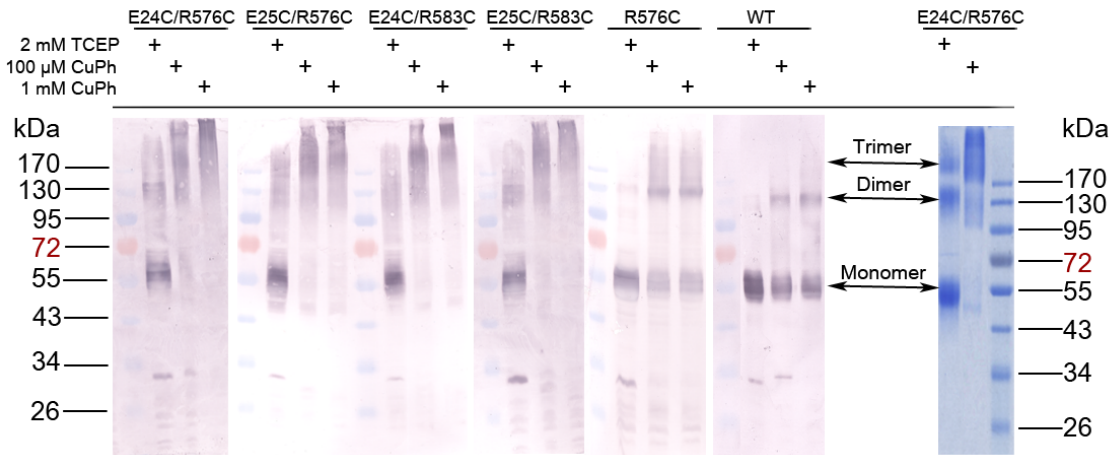

Figure 4.7: Disulfide cross-linking of double cysteine BetP variants within *E. coli* DH5α™-T1^R membranes.

Isolated membranes of *E. coli* DH5α™-T1^R containing BetP variants were reduced by 2 mM TCEP and incubated with either 100 µM or 1 mM CuPh. 40 µg of each sample mixed with non-reducing sample buffer was loaded onto an SDS gel (10 %) and used for Western Blot analysis (left). Exemplarily, a purified protein sample was treated equally and 5 µg was used for non-reducing SDS-PAGE (right). Oligomeric states of BetP are labeled with arrows as monomer, dimer and trimer. As marker PageRuler™ Prestained Protein Ladder (Thermo Scientific Molecular Biology) was used.

After oxidation, trimeric oligomerization states detected in non-reducing SDS-PAGE would imply interactions of the cysteines within the N-terminal and C-terminal domain by disulfide bond formation between adjacent protomers. Monomeric, dimeric and trimeric BetP has the calculated molecular weight of 64.2, 128.4 and 192.6 kDa, respectively.

Upon reduction with TCEP, monomers with the size of ~55 kDa appeared for all double cysteine variants of BetP (Figure 4.7). Trimers at approximately 170 kDa, but no monomers could be observed after the oxidation with either 100 µM or 1 mM CuPh indicating that the lower concentration of the oxidant is sufficient for disulfide bridge formation. At reducing conditions, BetP R576C forms mainly monomers and a weak dimer band at 130 kDa is detectable. The negative control BetP WT shows monomers in each condition. The addition of TCEP to BetP WT leads to monomeric BetP, while the addition of CuPh indicates a weak dimer band.

Further the influence of the site-directed cross-linking by disulfides was investigated at a protein and functional level. Therefore, the cysteine variants of BetP were solubilized from the *E. coli* DH5α™-T1^R membranes and further

purified by StrepTactin®-affinity chromatography (Section 2.3.4.3). All purified protein samples were either incubated with only CuPh or in addition with TCEP followed by non-reducing SDS-PAGE (Figure 4.8).

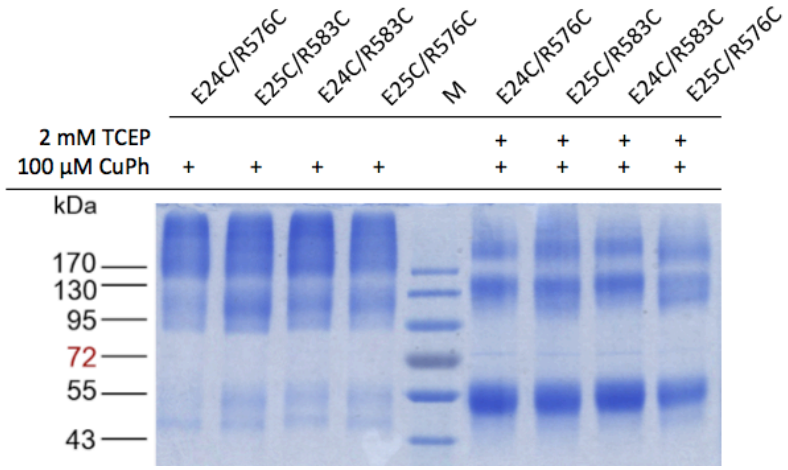

Figure 4.8: Disulfide cross-linking of double cysteine BetP protein in detergent.
Non-reducing SDS-PAGE of purified BetP variant protein in 0.1 % DDM incubated with either only 100 µM CuPh or with 2 mM TCEP. 5 µg of each protein sample mixed with non-reducing sample buffer was applied on the SDS gel (10 %). (M) PageRuler™ Prestained Protein Ladder (Thermo Scientific Molecular Biology).

All double cysteine variants of BetP show oligomerization into dimers and mainly trimers with a size of higher than 170 kDa under oxidizing conditions (Figure 4.8). Under this condition, there are almost no monomers detectable, especially for BetP E24C/R576C indicating that the disulfide bond formation occurs between protomers within trimers. Upon TCEP addition, three clear bands corresponding from top to bottom to trimer, dimer and mainly monomer.

4.1.6 Transport properties of disulfide cross-linked cysteine double variants of BetP in *E. coli* polar lipid proteoliposomes

For functional studies of disulfide cross-linked BetP, samples containing protein at higher oligomers after oxidation with CuPh were used for reconstitution into *E. coli* polar lipids under non-reducing conditions. Prior to uptake measurements of [^{14}C]-betaine at reducing conditions, the proteoliposomes were extruded in buffer containing the reducing agent TCEP. For oxidizing conditions, TCEP was excluded

from buffers. Transport of betaine was measured under different osmotic conditions adjusted with proline.

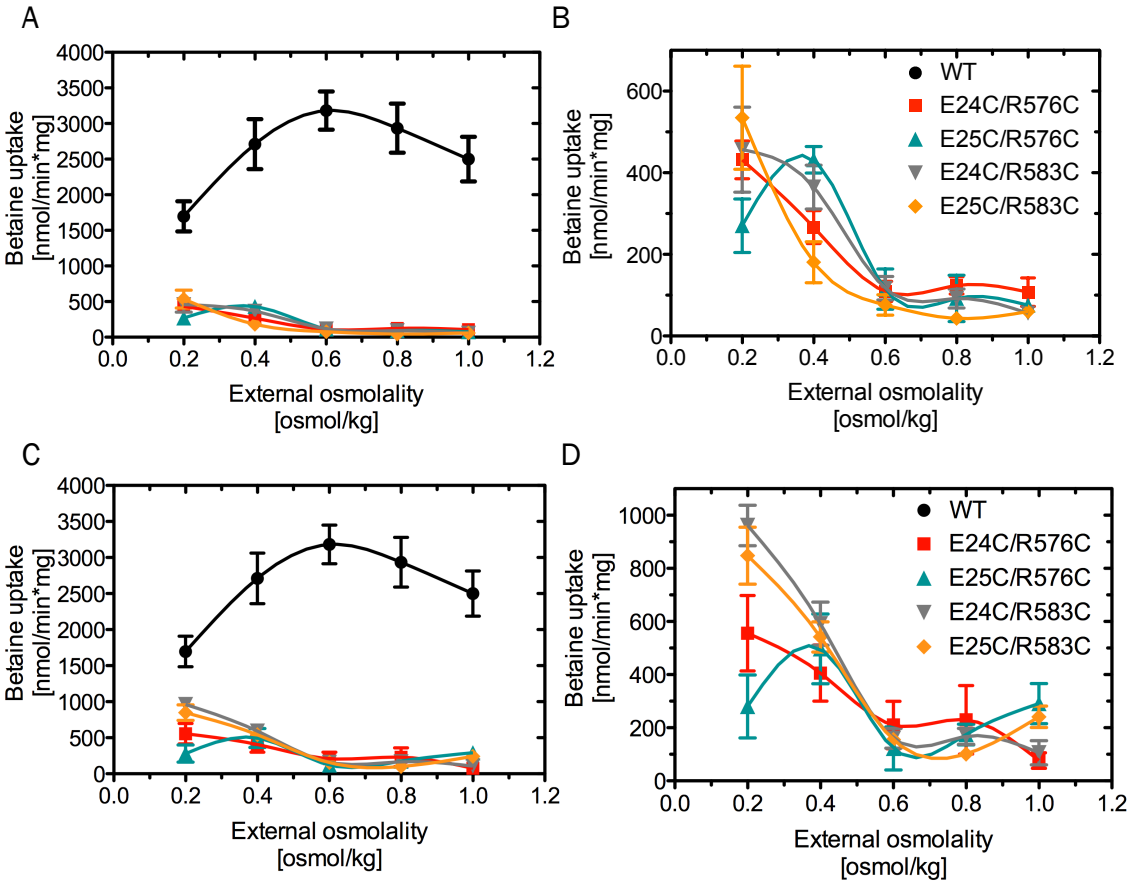

Figure 4.9: Betaine uptake of BetP variants with double cysteine substitutions in *E. coli* polar lipid proteoliposomes.

Uptake of betaine in nmol per min and mg protein was measured as a function of external osmolality for double cysteine BetP variants incooperated in *E. coli* polar lipid liposomes with a LPR of 30:1 at reducing conditions (A, B) and oxidative conditions (C, D). Betaine uptake compared to the BetP WT (left). Zoomed in betaine uptake of the double cysteine BetP variants shown in A and C, independent of the BetP WT for a better comparision between the mutants (right). The measurements represent the mean of at least eight replicates/data point. The errorbars present ± S.E.M..

The measurement under reducing conditions in Figure 4.9 (A – B) resulted in strongly altered activation profiles for all cysteine variants compared to BetP WT and to the aforementioned measurement in cells (Figure 4.6). A pronounced decrease in activity was observed for all mutants, which might be related to a less efficient reconstitution of the cross-linked BetP. Whereas BetP WT reaches the maximal activity at 0.6 osmol/kg, for all mutants except BetP E25C/R576C, the maximum is reached already at the low osmolality of 0.2 osmol/kg. BetP

E25C/R576C shows maximal betaine uptake at 0.4 osmol/kg. All cysteine variants are characterized by a subsequent decrease of the betaine transport in a continuous manner with increasing osmolality. Under oxidizing conditions, there is no difference in the pattern of the osmotic profiles (Figure 4.9 C – D). However, an increase in the maximum betaine uptake activity was observed, which was most pronounced for BetP E24C/R583C and BetP E25C/R583C.

4.1.7 Chemical cross-linking of cysteine double variants of BetP

Chemical cross-linking was performed at different osmotic conditions to investigate the oligomerization behavior during non-activating (0.2 osmol/kg) and activating conditions (0.6 osmol/kg) of the BetP WT and cysteine variants. Here, o-PDM with a tether length of 4 – 9 Å was used. BetP cysteine variants as well as BetP WT were produced in *E. coli* MKH13 cells and membranes were isolated. Membranes were mixed with the corresponding osmotic buffers and subsequently incubated with o-PDM. SDS-PAGE followed by Western blot analysis was carried out (Figure 4.10).

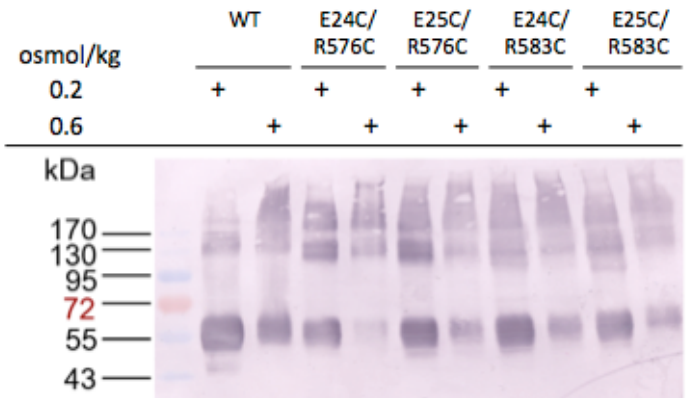

Figure 4.10: Chemical cross-linking of double cysteine BetP variants within *E. coli* MKH13 membranes.
Isolated membranes of *E. coli* MKH13 comprising BetP WT and variants were mixed with osmotic buffers at 0.2 and 0.6 osmol/kg and incubated with 5 mM o-PDM. 15 µg of each sample were applied on an SDS gel (10 %) and used for Western Blot analysis. As marker PageRuler™ Prestained Protein Ladder (Thermo Scientific Molecular Biology) was used.

The tether length of 4 – 9 Å of o-PDM allows the cross-linking of cysteines, which are located in this distance. As a negative control o-PDM was also added to the BetP WT. At 0.2 osmol/kg, BetP WT is present dominantly as monomer, but also

in some extent as dimer (Figure 4.10). Upon osmotic upshift of 0.6 osmol/kg for the WT, unspecific oligomers but also trimers, dimers as well as monomers could be identified for the WT during reducing SDS-PAGE. Oligomerization of BetP is strongly enhanced upon osmotic upshift suggesting that in addition to the terminal interaction network other intratrimeric contacts are strengthened. Whereas under low osmotic conditions the cysteine variants display, beside mainly monomers, also bands for dimers and trimers, high osmotic conditions lead to a diminished amount of monomers. This is observed especially for BetP E24C/R576C. At 0.6 osmol/kg, the BetP cysteine variants show the tendency to form oligomeric states, which monomerize less during SDS-PAGE. Chemical cross-linking of double cysteine BetP let suggest, that at high osmotic conditions, N- and C-terminal domains of adjacent protomers within a trimer are in close proximity contributing to specific and unspecific oligomerization of BetP.

4.2 Discussion

4.2.1 Regulatory interaction of terminal domains

Negative charges in the N-terminal domain were not considered to play a key role in osmoregulation, because N-terminally truncated BetP is still regulated, although with a shifted activity optimum at higher osmolalities (Ott *et al.*, 2008; Peter *et al.*, 1998a). As this effect is reminiscent to the shift that occur when wild type BetP is transferred from a low amount of negative charged lipids (as in *E. coli*) to a higher amount (as in *C. glutamicum*) (Peter *et al.*, 1996), it was assumed that lipids and N-terminal domain compete for the same ionic interactions established with the positively charged C-terminal domain. Interestingly, it was never possible to activate the N-terminally truncated mutant in *E. coli* when the amount of negatively charged lipids is below 30 % suggesting that there might be teamwork between lipids and N-terminal domain.

Two different interaction modes of the N-terminal domain can be assumed (Figure 4.11): (1) interaction with the C-terminal domain of its own protomer corresponding to down-regulation and (2) interaction with the C-terminal domain of the adjacent protomer within the trimer leading to up-regulation. According to this, the N-terminal domain would be as suggested earlier a part of the switch model (Ott *et al.*, 2008), however, with the modification of the switch occurring between adjacent protomers.

Under isotonic conditions, the C-terminal domain is assumed to be oriented towards the membrane surface as the helical fold itself, perhaps even the rigidness of the helix is a parameter in regulation, e.g. the Ala564Pro mutant was constitutively full activated (Becker *et al.*, 2014). In this position, the C-terminal domain might interact with its own N-terminal domain and cytoplasmic loops (Figure 4.11, “red conformation” of the C-terminal domain). This conformation is supported by a yet unpublished crystal structure of BetP, in which a partially resolved C-terminal domain is turning around its own chain (Koshy, 2014). This turn provides an angle in which a potential binding of the positively charged C-terminal domain to the anionic lipid bilayer as well as to its own N-terminal domain is reasonable.

In this down-regulated conformation, the N-terminal domain of BetP might provide a stable interaction by cluster NC3. Lipids can mimic this interaction, however,

this lipid-C-terminal interaction results in an altered response to stress. This is supported by the shifted osmo-profile in NC3A (Figure 4.4 A). High amounts of negatively charged lipids and in competition the negative cluster in the N-terminal domain modulate the amount of stress required to detach the C-terminal domain at up-regulating conditions.

Osmotic stress results in changes in membrane state, e.g., changes in curvature or thickness and in an increase in the K^+ concentration. Both might lead to an alteration in the N-terminal domain/lipid interaction with the C-terminal domain. A re-orientation and conformational change is required to overcome these interactions. Thus, it appears that up-regulation requires the release of the C-terminal domain from interaction with cytoplasmic loops in one protomer. In this context, it was demonstrated that an increase in the K^+ concentration decreases the binding affinity of the C-terminal domain to lipids (Ott *et al*., 2008) suggesting a release of the C-terminal domain under up-regulated conditions. When the C-terminal domain is re-oriented upon osmostress, ionic interactions with central lipids might assist its transient conformation (Figure 4.11, “gray conformation” of C-terminal domain).

The proposed re-orientation is in agreement with the conformational change of the C-terminal domain upon BetP activation, which was verified by PELDOR-derived data, although the movement of the terminal domain could not be described in detail (Nicklisch *et al.*, 2012).

The solved crystal structure of BetP demonstrated an intratrimeric interaction of the helical C-terminal domain with cytoplasmic loops of the adjacent protomer (Ressl *et al*., 2009). Thereby, the C-terminal domain of one protomer is pointing towards TM1 of the adjacent protomer. Unfortunately, this structure could not provide further information about potential interactions with the N-terminal domain, because the N-terminally truncated, surface-engineered BetP variant (BetPΔ29NC3A) was crystallized. Although the elongated conformation of the C-terminal domain was achieved by crystal contacts with negatively charged residues of the symmetry related trimer (Figure 4.12), this artificial conformation was previously discussed as a possible functional state. Moreover, co-crystallization of BetP with Rb^+ ions identified potential K^+-binding sites between the C-terminal domain of one protomer and the cytoplasmic loop 2 of the adjacent protomer (Perez, 2012). That is why it can be suggested that at up-

regulated conditions the C-terminal domain might adopt this conformation via interactions with the N-terminal domain of an adjacent protomers using the negatively charged cluster NC2 (Figure 4.11, "green conformation" of the C-terminal domain). An interaction with negatively charged lipids at the centre of the BetP trimer might support this conformation. Thus, the N-terminal domain and lipids would team up for full activation.

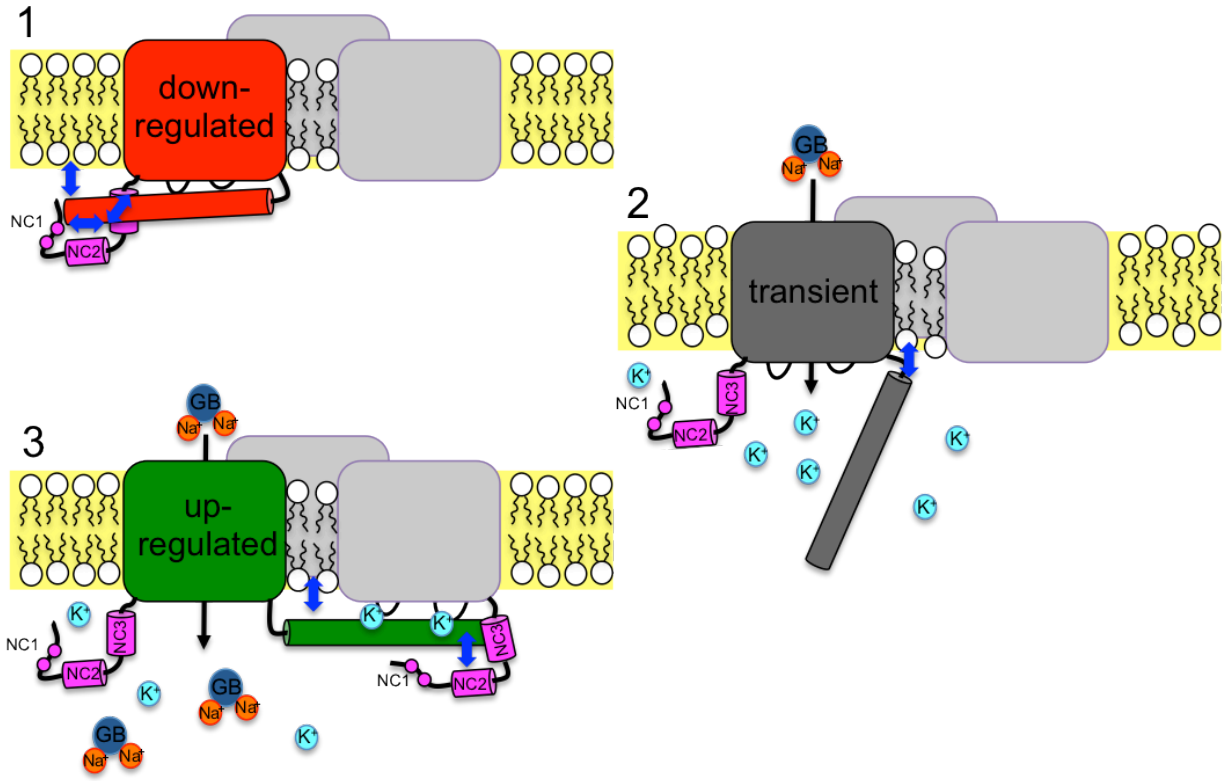

Figure 4.11: Model for a regulatory interaction of terminal domains and lipids.
BetP protomers are shown as plane rectangles embedded into bulk lipids. For clarity, the C-terminal domain is indicated as cylinder and shown only for one protomer (left) in different conformations. Under isotonic conditions, the α-helical C-terminal domain of the protomer interacts with the N-terminal domain and cytoplasmic loops of its own protomer, which is caused by the direct interaction with bulk lipids (1: down-regulated state, red). Osmotic stress results in elevated internal K^+ concentrations and changes in the membrane state triggering a re-orientation of the C-terminal domain (2: transient state, dark gray). Ionic interactions with central lipids might assist this conformation. For fully activated BetP the C-terminal domain of the protomer is protruding towards the adjacent protomer, most likely also due to interactions with central negatively charged lipids. The N-terminal domain of the adjacent protomer provides a stabilizing effect (3: up-regulated state, green). The α-helical segments of the N-terminal domain at NC2 (E24/E25) and NC3 (E44/E45/E46) are depicted as cylinders in magenta. Cluster NC1 (E13/D14) is indicated as magenta circles. The substrates betaine (GB) and coupling Na^+ ions as well as K^+ are shown as circles in blue, orange and light blue, respectively.

4.2.2 Regulatory role of the negatively charged clusters

The cluster NC2 appears to be a hot spot in regulation of BetP. Charges in NC1 and NC3 are still present in BetP NC2A and contribute to the slightly elevated transport rate (Figure 4.4 B), however, they are both not essential for regulation. For NC1 and NC3 the individual substitution against alanine did not prevent regulation, but altered the regulation profile (Figure 4.4).

Secondary structure predictions let suggest that the substitution of the clusters against alanines alters the helical conformation in both helical segments of the N-terminal domain slightly (Figure 4.3). This is also corresponding to the slight change in the migration behavior, which was observed for BetP NC12A and BetP NC123A during SDS-PAGE (Figure 4.4 A).

Beside NC1-3, additional negatively charged residues can be found in proximity of the clusters. This redundancy is also a feature of the C-terminal domain containing a ladder of arginines, which might allow maintaining ionic interactions in different conformations and orientations of the C-terminal domain. For instance, a variation in length of the first helical segment could affect the orientation of Glu18 and Gln19, which can be found as a part of the helix in BetP NC2A but not in the WT, NC1A and NC3A (Figure 4.3).

According to the proposed model, the crucial role of NC2 in osmoregulation and the orientation of the C-terminal domain in the crystal structure (Ressl *et al*., 2009) suggested that the respective negatively charged residues participate in intratrimeric interactions with positively charged residues like Arg576 or Arg583 within the C-terminal domain of the adjacent protomer. Surprisingly, these residues are quite comparable to the crystal contacts formed by Arg574-Asp356 and Arg584-Glu175 by the C-terminal domain and the loops at the periplasmic side of the symmetry related trimer (Figure 4.12) (Ressl *et al*., 2009).

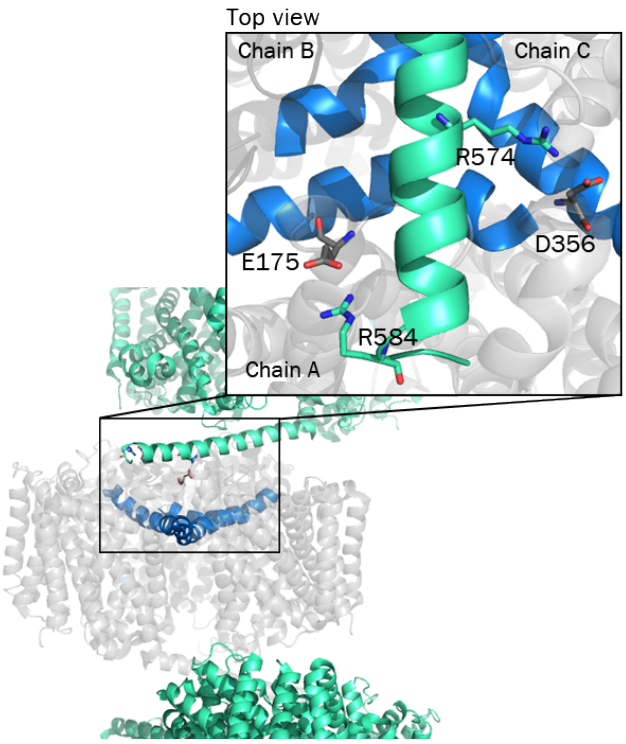

Figure 4.12: Crystal contacts in BetP.
Crystal contacts from symmetry molecules are shown. Residues on the periplasmic side (gray) interact with positively charged residues of the C-terminal helix (green) of a symmetry molecule to form crystal contacts (Inset). For better orientation, h7 is colored blue.

The formation of higher oligomers in cross-linking studies confirmed the capability of the N-terminal domain to physically interact with the adjacent C-terminal domain and that this interaction depends indeed on the amount of osmotic stress (Figure 4.7 and Figure 4.10). Moreover, functional studies of cross-linked BetP in proteoliposomes suggest a positive effect during transport mediated by the interaction of the terminal domains.

Based on the results, Arg576 is a candidate for this interaction as a cross-link between Arg576 and Glu25 rescue the activity to 2/3 of wild type full activity. As expected, this mutant do not show down-regulation properties exhibiting a severely altered osmo-profile (Figure 4.6).

The role of the trimer is to provide interaction partners for the active conformation of the C-terminal domain. In this scenario, the intratrimeric interactions of adjacent protomers may not necessarily contribute to full activation of the trimer, i.e., interaction of the C-terminal domain of protomer 1 (Figure 4.11) with protomer 2 might very well affect only the transport regulation of protomer 1

under certain conditions. Recent studies on a heterotrimeric construct showed the absence of an intratrimeric crosstalk in *E. coli* proteoliposomes (Becker *et al*., 2014). However, as these experimental conditions only allow detecting the K^+ activation and not the physiologically more relevant membrane stimulus, the question of regulatory terminal crosstalk in the BetP trimer still has to be answered.

4.2.3 Comparison to other osmoregulated transport systems

The comparison to two other paradigmatic osmosensing uptake systems, the MFS transporter ProP and the ABC-transporter OpuA, propose some similarities with respect to the regulation mechanism by terminal domains and lipids. The C-terminal domain of ProP from *E. coli* terminates with heptad repeats, composed of a specific sequence of positively and negatively charged as well as hydrophobic residues, which allow the formation of a homodimeric, antiparallel coiled coil structures with adjacent ProP C-termini (Tsatskis *et al.*, 2005; Zoetewey *et al.*, 2003). It is assumed that this structure modulates the threshold for osmotic activation, but is not essential for osmotic activation *per se* (Tsatskis *et al.*, 2005; Tsatskis *et al.*, 2008) because deletion mutants and orthologoues lacking this structural feature are activated at higher osmolalities (Tsatskis *et al.*, 2005; Tsatskis *et al.*, 2008). Interestingly, such a ProP orthologue is found in *C. glutamicum* comprising only an anionic C-terminal domain (Peter *et al.*, 1998b; Tsatskis *et al.*, 2005). Increasing amounts of anionic lipids (CL) shift the activation towards higher osmolalities in E.c.ProP, too, suggesting a direct interaction with the bulk lipids (Tsatskis *et al.*, 2005; Tsatskis *et al.*, 2008).

In OpuA from *Lactoccocus lactis*, the C-terminal domain consists of tandem CBS (cystathione-β-synthase) domains followed by an entirely anionic charged C-terminal stretch (Biemans-Oldehinkel *et al.*, 2006). The CBS domains seem to sense the ionic strength in a lipid-dependent manner. Thus, the CBS pair is assumed to interact directly with bulk lipids (Biemans-Oldehinkel *et al*., 2006). Deletions of the anionic C-terminal domain require an increased osmotic upshift to activate OpuA indicating the remaining C-terminal tail is a modulator of the sensing CBS module (Biemans-Oldehinkel *et al.*, 2006; Mahmood *et al.*, 2006).

The modulating role of terminal domains in the transport regulation of ProP and OpuA seem to be reminiscent to the functional role of the anionic N-terminal domain of BetP. This indicates that common sensing mechanisms involving protein-protein as well as protein-lipid interactions developed independently, since these transporters and terminal domains are not structurally related. A regulation mechanism involving terminal domains can also be found in mammalian transporters like the extensively studied Na^+/H^+ exchanger NHE1, which regulates intracellular pH homeostasis and cell volume (Slepkov *et al.*, 2007). NHE1 possesses a very long C-terminal domain, which consists to 1/3 of charged residues. Indeed, also for NHE1 the C-terminal domain is involved in regulation, here also an interaction with adjacent C-terminal domains is assumed (Hisamitsu *et al.*, 2004), but activity regulation occurs mainly by a sophisticated interplay of several accessory proteins as well as kinases (Malo and Fliegel, 2006; Slepkov *et al.*, 2007).

In summary, the functional role of charged clusters in the N-terminal domain emerging from our data and their competitive and associative interaction with negatively charged lipids is not only an important additional puzzle piece to understand the regulation mechanism of BetP, but might be conserved in other not-trimeric transporters. In this context, a careful extrapolation could provide new insights into stress-regulation of membrane transport processes.

5 Probing conformational dynamics of the trimeric transporter BetP by PELDOR

BetP appeared in 2D and 3D crystal structures as a conformational asymmetric trimer with each protomer in a distinct conformation (Perez *et al.*, 2012; Tsai *et al.*, 2011). In consequence, a crosstalk between the protomers constituting a trimer is suggested. In order to obtain more insights into the oligomeric function of BetP and to evaluate the conformational changes based on crystallographic snapshots in a more native environment, pulsed electron-electron double resonance (PELDOR) in combination with site-directed spin labeling (SDSL) was applied. PELDOR allows the determination of distances between spin labels in a nanometer range to study conformational changes. In this thesis, PELDOR measurements were performed on the three-spin system as well as on the six-spin system of BetP to monitor conformational changes. These conformational rearrangements would be indicated by changes of the average distance or shape of the distance distribution between the spin labels attached to the protein in different conditions.

5.1 Results

5.1.1 Spin label strategy of BetP from *Corynebacterium glutamicum*

The pulsed EPR method PELDOR in combination with SDSL was already successfully applied to determine inter- and intramolecular distances between spin labels in membrane proteins when solubilized in detergent or reconstituted into liposomes (Hubbell and Altenbach, 1994). For SDSL, native amino acids at specific sites in BetP were replaced by cysteine residues, which allow attaching nitroxide spin labels via disulfide bridge formation.

The challenge for the trimeric BetP protein was to find appropriate positions for spin labeling to monitor the conformational changes in the range of PELDOR distances. In addition, these sites would have to be accessible to ensure high labeling efficiencies. In order to investigate the conformationally asymmetric nature of trimeric BetP, initially a three-spin-system was applied. Here, one

accessible residue per protomer, which was supposed to move during conformational change, should be labeled. In symmetric trimers composed of three protomers in identical conformation, only one distance would be detectable, while in the case of different conformational states of the protomers several distances would be detectable (Figure 5.1).

X-ray structures of BetP in the inward open and outward open conformation revealed rather small main chain motions in the range of only 1 to 6 Å, which is far less compared to other LeuT-fold transporters (Krishnamurthy and Gouaux, 2012; Perez *et al.*, 2012; Shimamura *et al.*, 2010). In addition, in a three-spin system for BetP, the intratrimeric distances between moving positions were quite long (~6 nm). Both circumstances together made it difficult to observe distinct differences between conformational states by PELDOR. In consequence, an alternative approach with a six-spin system for trimeric BetP was developed. Correspondingly, this labeling strategy involves two labeled residues within one protomer. Here, the conformational changes are reflected by changes in shorter intraprotomeric distances. Interprotomeric distances are longer than the intraprotomeric ones and therefore distinguishable. However, to address the asymmetry of BetP with this labeling strategy, the shorter intraprotomeric distances should be correlated nevertheless to the longer interprotomeric distances. Despite this limitation of the method, PELDOR was successfully applied for BetP as six-spin system to probe the conformational changes occurring within the protomers at different conditions.

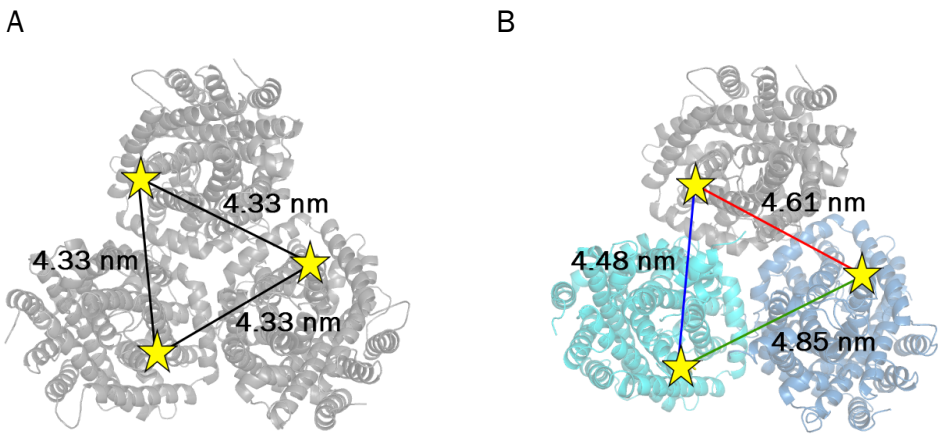

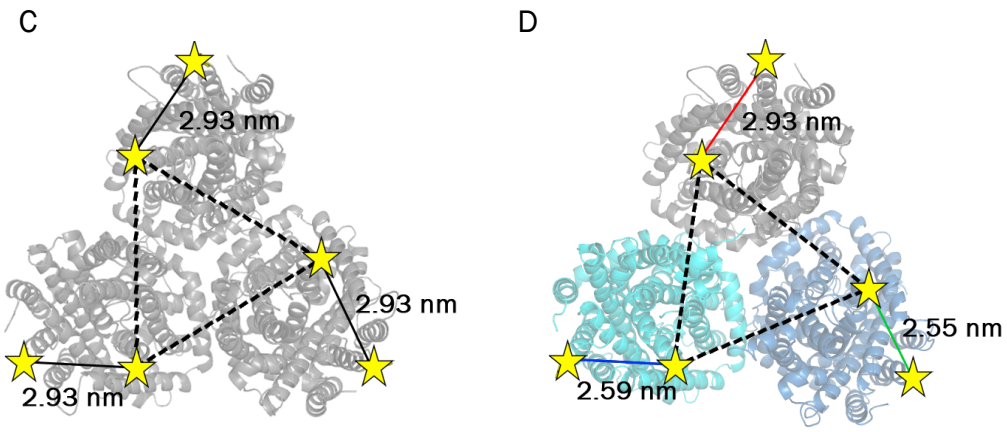

Figure 5.1: Labeling strategies for trimeric BetP.
Models of BetP trimers were created from solved X-ray structures. Symmetric trimers (A, C) consist of three protomers in the inward open conformation (PDB 4DOJ, chain C, gray). Conformational asymmetric trimers (B, D) are composed of protomers in the inward and outward open as well as in the substrate-bound closed conformation (PDB 4DOJ, chain C (gray) and B (blue); PDB 4AIN, chain B (cyan)). Potential labeling sites are represented as stars and distance relations are depicted as Cα – Cα distances between the residues. For the three-spin system, the intratrimeric distances are shown for a symmetric (A) and an asymmetric trimer (B). For the six-spin system, the intraprotomeric distances for protomers in the identical conformation (C) and different conformations (D) are displayed. In this system, some conceivable intratrimeric distances are indicated as dashed lines. Comparable distances within one trimer are colored uniformly black, while unequal distances are colored blue, red and green.

Single cysteine substitutions for the three-spin system were introduced by site-directed mutagenesis into the cysteine-less *betP* gene in the vector pASK-IBA5*betP*C252T (Ott *et al.*, 2008; Rübenhagen *et al.*, 2001) resulting in the BetP variants:

1) BetP S140C/C252T
2) BetP C252T/S516C

Pairs of appropriate labeling sites for BetP were selected at the cytoplasmic as well at the periplasmic side for the six-spin system (Figure 5.2). The following double cysteine BetP variants were created for the six-spin system:

1) BetP S140C/C252T/N488C
2) BetP S140C/C252T/K489C
3) BetP S140C/C252T/W490C

4) BetP C252T/G450C/A514C
5) BetP C252T/G450C/L515C
6) BetP C252T/G450C/S516C

Additionally, replacements at the conserved sodium-binding site Na2, namely T467A/S468A, that inhibit binding and transport of betaine were introduced into selected BetP cysteine variants (Khafizov *et al.*, 2012):

1) BetP S140C/C252T/T467A/S468A/K489C
2) BetP C252T/G450C/T467A/S468A/A514C
3) BetP C252T/G450C/T467A/S468A/S516C

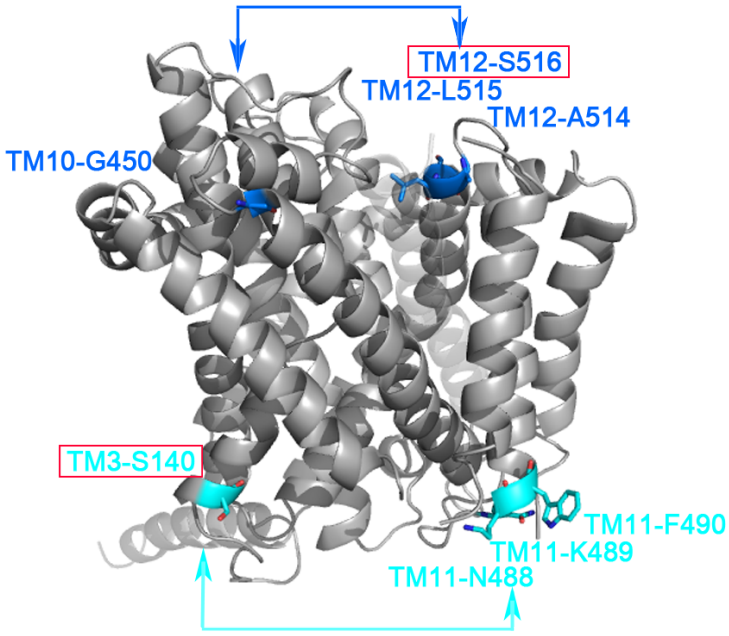

Figure 5.2: Location of labeling sites within the BetP protomer.
Residues selected for cysteine substitution are represented as sticks in the BetP protomer. Residues at the cytoplasmic or periplasmic side of BetP are colored cyan or blue, respectively and labeled with the corresponding amino acid and TM domain. For the three-spin system, positions S140 in TM3 at the cytoplasmic side and S516 in TM12 at the periplasmic side, framed in red, are displayed. In respect to the six-spin system, two residues within the protomer at the same side of the protein were selected at once. The arrows indicate associated residue pairs. At the periplasmic side, the combination of G450 in TM10 with either A514, L515 or S516 in TM12 were studied. The cytoplasmic residue S140 was substituted in conjunction with residues in TM11, namely N488, K489 or F490 for the six-spin system.

5.1.2 Transport properties of BetP cysteine variants in *E. coli* MKH13 cells

In order to exclude negative effects on the osmoregulatory transport properties of the BetP variants due to the diverse cysteine substitutions, the *betP* mutants were expressed and produced in *E. coli* MKH13 cells. [^{14}C]-betaine uptake rates were measured upon increasing hyperosmotic conditions and results are compared to BetP WT (Figure 5.3 Figure 5.6). In addition, the activation profiles for the mutants containing cysteine replacements at the cytoplasmic side of BetP were normalized for a better comparison (Figure 5.4) and in the case of BetP S140C/C252T/K489C, the impact of the residue K489 were analyzed with alternative amino acid substitutions (Figure 5.5).

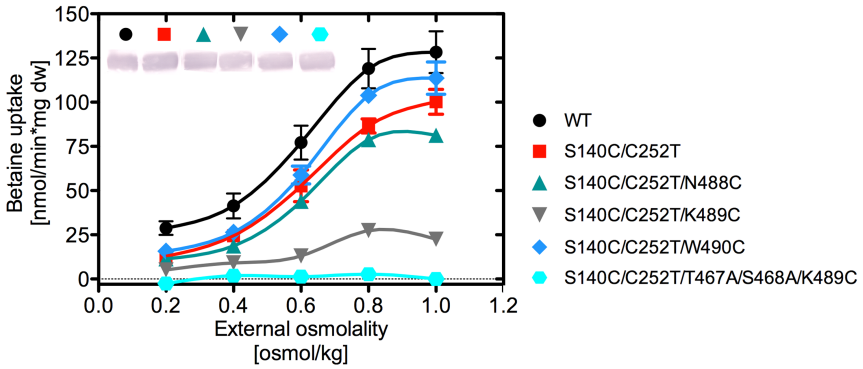

Figure 5.3: Betaine uptake rates of cytoplasmic BetP cysteine variants in *E. coli* MKH13 cells.

Uptake rates of betaine in nmol per min and mg dry cell weight were measured as a function of external osmolality in *E. coli* MKH13 cells expressing cysteine BetP mutants. Each value is the mean ± S.E.M. of at least three independent measurements. Immunoblotting against the N-terminal StrepII-tag of the BetP variants in *E. coli* MKH13 membranes confirmed the same level of protein production.

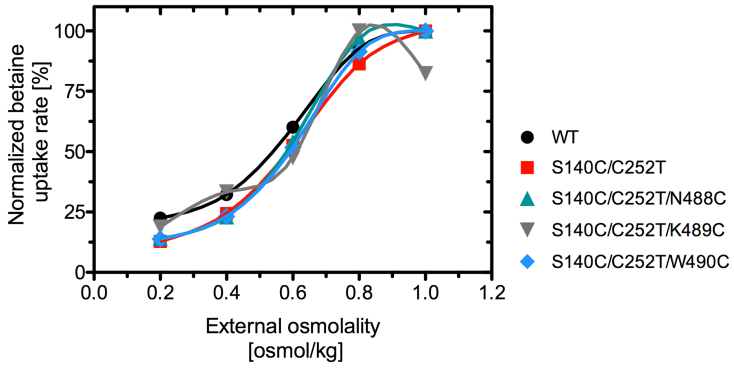

Figure 5.4: Normalized betaine uptake rates of cytoplasmic cysteine variants in *E. coli* MKH13 cells.

Normalized uptake rates of betaine in % as a function of external osmolality are displayed for active BetP cysteine variants from Figure 5.3.

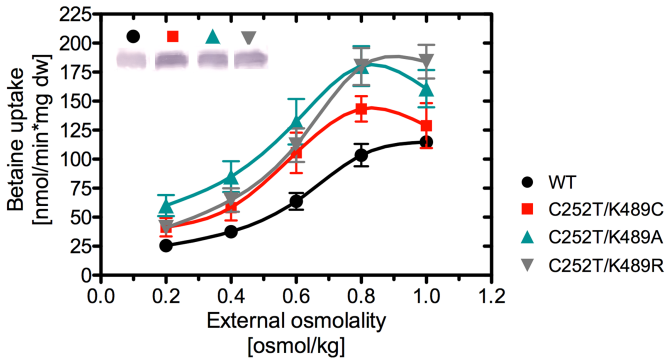

Figure 5.5: Betaine uptake rates of BetP K489 variants in *E. coli* MHK13 cells.
Uptake rates of betaine in nmol per min and mg dry cell weight were measured in dependence to the external osmolality in *E. coli* MKH13 cells producing either BetP K489C, K489A or K489R. The measurements represent the mean of at least three replicates per data point. The errorbars represent ± S.E.M.. Immunoblotting against the N-terminal StrepII-tag of the BetP variants in *E. coli* MKH13 membranes demonstrates the same level of synthesis.

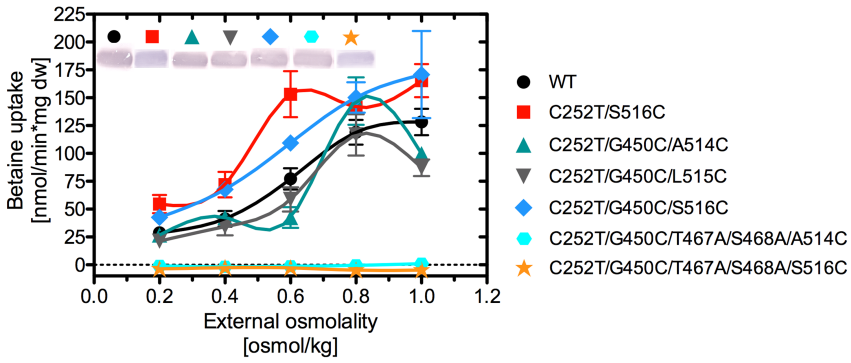

Figure 5.6: Betaine uptake rates of periplasmic BetP cysteine variants in *E. coli* MKH13 cells.
Uptake rates of betaine in nmol per min and mg dry cell weight were measured as a function of external osmolality in *E. coli* MKH13 cells expressing single and double cysteine BetP mutants. Each value is the mean ± S.E.M. of at least three independent measurements. Immunoblotting against the N-terminal StrepII-tag of the BetP variants in *E. coli* MKH13 membranes detect a comparable level of protein synthesis.

Except for BetP S140C/C252T/T467A/S468A/K489C, the cytoplasmic single and double cysteine variants exhibit comparable osmotic activation profiles, which only differ in the maximal uptake rates (Figure 5.3). The most reduced activity was detected for BetP S140C/C252T/K489C, although normalized data indicated that regulation of the transport for this BetP mutant is still maintained (Figure 5.4). Because the replacement of K489 in BetP S140C/C252T/K489C seemed to have an impact on the transport activity level, while BetP S140C/C252T alone exhibit only a slight reduced uptake rate compared to the BetP WT, K489 was

investigated by alternative substitutions in single mutants. Substitutions against a cysteine, an unpolar residue (Ala) as well as against arginine, resulted in higher uptake compared to the BetP WT (Figure 5.5). Like expected, for BetP S140C/C252T/T467A/S468A/K489C as well as the periplasmic BetP variants C252T/G450C/T467A/S468A/A514C and C252T/G450C/T467A/S468A/S516C no active transport was detected due to the disruption of the sodium-binding site Na2, which is essential for betaine symport in BetP (Khafizov *et al.*, 2012). Apart from BetP C252T/S516C, all periplasmic double cysteine variants display a regulation profile with slight alternations in the uptake rate (Figure 5.6).

5.1.3 Purification and site-directed spin labeling

BetP cysteine variants were produced in DH5α^{TM}-T1^{R} cells from which membranes were prepared for further purification by solubilization with DDM and StrepTactin®-affinity chromatography.

The nitroxide spin label methyl methanethiosulfonate (MMTSL) or methane-thiosulfonate (MTSL) was used for spin labeling. A direct comparison between both nitroxide spin labels can be found in Section 7.8.1. In PELDOR measurements, no significant difference between MMTSL and MTSL was observed.

Initially, for site-directed spin labeling of the BetP cysteine variants with the nitroxide spin label MMTSL, diverse methods were tested in order to optimize the label efficiency. Spin labeling was performed in buffers containing either 0.6 % Cymal-5 or 0.1 % DDM, during purification on a Strep-Tactin® Macro-Prep column via the standard gravity flow protocol (Section 2.3.4.3) as well as via fast protein liquid chromatography as described before (Nicklisch *et al.*, 2012). Moreover, spin labeling was conducted after standard StrepTactin®-affinity chromatography in batch with a 10-fold molar excess of the spin label at different pH conditions as well as for different incubation times at RT and 4 °C. As a result, highest label efficiencies were achieved for an incubation at 4 °C over night with protein at 1.5 mg/ml in labeling buffer at pH 7 containing 0.1 % DDM by an increase of the molar excess of the label from 10- to 30-fold. Free spin label was successfully removed by SEC and protein was transferred into either non-activating or

activating conditions and concentrated to approximately 15 mg/ml. The identical procedure was applied for the spin label MTSL.

Samples collected during purification and spin labeling were examined by SDS-PAGE and Western blot analysis. A representative overview of the purification and spin labeling for BetP S140C/C252T is displayed in Figure 5.7 A – C. All BetP variants investigated by PELDOR were compared in SDS-PAGE (Figure 5.7 D) and the corresponding label efficiencies are listed (Table 5.1). Spin label concentration of each sample was determined by cw-EPR at RT. By taking into account the number of the spin labels, which should be bound to the BetP trimer, the determined protein concentration of the sample can be used to estimate the concentration of the spin label for 100 % label efficiency. This can be further correlated to the indeed measured label concentration of the sample. Cw-EPR measurements were performed by Dr. Burkhard Endeward and Dr. Haleh Hashemi Haeri (group of Prof. Dr. Thomas Prisner, Goethe University, Frankfurt am Main).

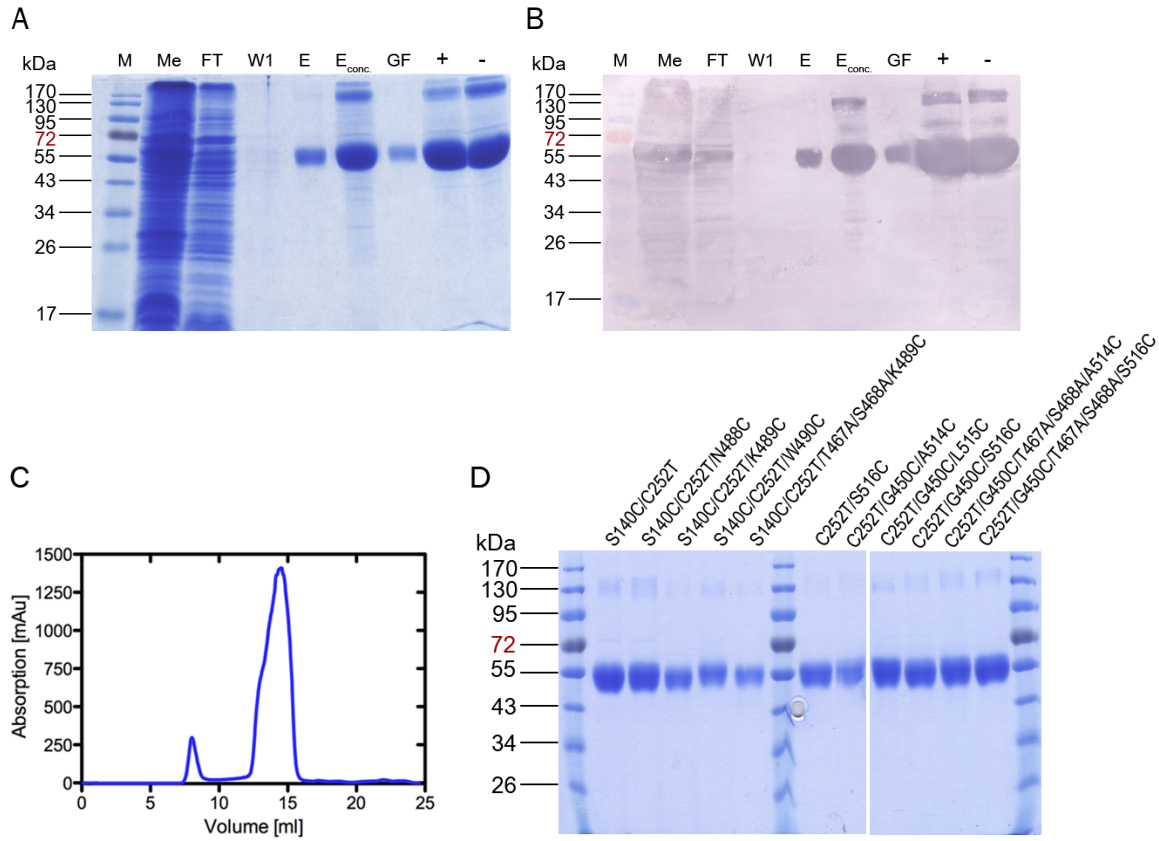

Figure 5.7: Purification and site-directed spin labeling of BetP cysteine variants.
Representative SDS-PAGE (A) and Western Blot (B) of BetP S140C/C252T purification and spin labeling. DDM solubilized *E. coli* DH5α™-T1^R membranes containing BetP

S140C/C252T were applied on a Strep-Tactin® Macro-Prep column, subsequently washed and protein was eluted. 10 µl of the membranes (Me) (10 mg/ml), the flow through of the affinity column (FT), wash 1 (W1) as well as 1 µl of the eluat from the affinity column before and after concentration (E/$E_{conc.}$) were loaded onto the SDS gel (12.5 %). After spin labeling, 1 µl of unconcentrated pooled SEC fractions (GF) as well as the PELDOR samples in activating (+) and non-activating (-) conditions were analyzed. C) To remove free spin label after labeling, preparative SEC was performed. Pooled elution fractions of BetP S140C/C252T after the affinity column (E) were concentrated to 500 µl ($E_{conc.}$), subsequently injected on a Superose 6 10/300 column with a constant flow rate of 0.3 ml/min and the absorption was monitored at 280 nm. D) SDS-PAGE (12.5 %) of all PELDOR samples after spin labeling and preparative SEC. In each case, 1 µl of pooled SEC fractions was analyzed. (M) PageRuler™ Prestained Protein Ladder (Thermo Scientific Molecular Biology) was used.

Table 5.1: Representative label efficiencies of BetP variants

BetP variant	Label efficiency
S140C/C252T	66 ± 13.2 %
S140C/C252T/N488C	73 ± 14.6 %
S140C/C252T/K489C	75 ± 15 %
S140C/C252T/T467A/S468C/K489C	73 ± 14.6 %
S140C/C252T/W490C	66 ± 13.2 %
C252T/G450C/A514C	115 ± 23 %
C252T/G450C/T467A/S468C/A514C	78 ± 15.6 %
C252T/G450C/L515C	123 ± 24.6 %
C252T/G450C/S516C	112 ± 22.4 %
C252T/G450C/T467A/S468C/S516C	140 ± 28 %

Purification of the BetP cysteine variants was performed by the earlier established protocol and single steps of the purification process can be followed for BetP S140C/C252T (Figure 5.7 A – C). All BetP variants run at approximately 55 kDa (Figure 5.7 D). As minimum concentration of the spin label, which is bound to the protein, 100 µM was required for PELDOR. Consequently, for the three-spin system a higher concentration of protein was needed than for the six-spin system. Apart from these mutants mentioned earlier, spin labeling was performed also for other cysteine variants of BetP F165C and E397C resulting in no or too low spin labeling efficiencies, not sufficient for PELDOR (data not shown). Table 5.1 lists the label efficiencies for the cysteine variants of BetP, which were successfully labeled and investigated by PELDOR. In addition, to exclude an unequal distribution of the spin labels in systems with two different labeled positions, the label efficiency was partly determined for each single mutant (data not shown).

Although a protocol for spin labeling of BetP was described before (Nicklisch *et al.*, 2012), thorough optimization of the method was necessary due to the close-to-membrane locations of the cysteine residues. According to this, Table 5.1 illustrates that labeling even at different sides of BetP result in different label efficiencies. Obviously, the cysteine residues at the periplasmic side of BetP are more accessible than at the cytoplasmic side. However, spin labeling efficiencies of 66 – 140 % were reached. Label efficiencies higher than 100 % reflect inaccuracies in determination of the protein concentration by the Bradford assay (Section 2.3.6.1). Cw-EPR revealed less than 5 % free spin labels in the samples after SEC, a concentration, which is acceptable for PELDOR (personal communication Dr. Burkhard Endeward).

5.1.4 Transport properties of spin labeled BetP variants in *E. coli* polar lipid proteoliposomes

To ensure that the BetP mutants investigated by PELDOR are still active after attaching spin labels at the respective sites, BetP variants were reconstituted into *E. coli* polar lipid liposomes. Protein for reconstitution was purified as described earlier by StrepTactin®-affinity chromatography, further spin labeled and not bound spin label was removed by SEC. Subsequently, BetP was reconstituted with the established protocol for BetP reconstitution for transport measurements with a LPR of 30:1 at non-reducing conditions. Functional activity of spin labeled BetP variants was measured by radiochemical [^{14}C]-betaine transport measurements. The BetP variants BetP S140C/C252T/T467A/S468A/K489C, C252T/G450C/T467A/S468A/A514C as well as C252T/G450C/T467A/S468A/S516C represent exceptions, which show in general no activity and were therefore not investigated for transport. However, uptake was measured for labeled mutants, representative for one three-spin as well as one six-spin-system, each at the cytoplasmic and periplasmic side.

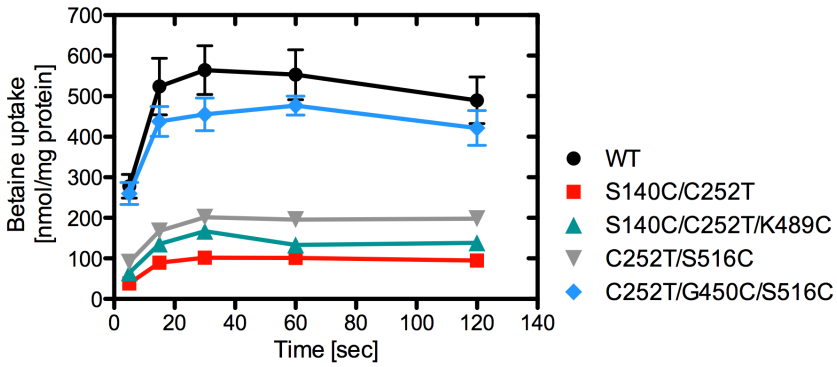

Figure 5.8: Betaine uptake of spin labeled BetP variants in *E. coli* polar lipid proteoliposomes.

Uptake of betaine in nmol per mg protein was measured at 0.6 osmol/kg as a function of time for MTSL-labeled BetP cysteine variants reconstituted into *E. coli* polar lipid liposomes. Uptake was started by adding saturating concentrations of 50 µM [^{14}C]-betaine. Each value is the mean ± S.E.M. of at least six independent measurements.

Betaine uptake measurements indicate that all investigated MTSL-labeled BetP cysteine variants are still active, although at lower activity levels compared to BetP WT (Figure 5.8). Whereas BetP C252T/G450C/S516C shows only a minimal reduced betaine transport activity, the BetP variants S140C/C252T, S140C/C252T/K489C and C252T/S516C display a more pronounced decrease.

5.1.5 PELDOR measurements in detergent

In order to measure distance changes between the spin labels with PELDOR, each BetP variant was transferred into non-activating and activating conditions, respectively. Non-activating condition contained only NaCl to compensate for ionic strength effects, while activating condition for BetP included (1) K^+ as main activation trigger and (2) both substrates, Na^+ and betaine. Na^+ is not active transported by BetP in absence of betaine.

PELDOR data were collected and analyzed by Dr. Burkhard Endeward and Dr. Haleh Hashemi Haeri (group of Prof. Dr. Thomas Prisner, Goethe University, Frankfurt). PELDOR spectra were recorded at 50 K on a Bruker EleXsys E580 spectrometer. Measurements were conducted at X-band (9.6 GHz) or Q-band (33.4 GHz) microwave frequencies using the PELDOR 4-pulse sequence (Pannier *et al*., 2000). To demonstrate the comparability of data, obtained by either X- or Q-band, a direct comparison is represented in the Appendix, Section 7.8.2.

PELDOR analysis was performed like described in section 2.4.3.3 by dividing the experimental PELDOR time trace by the fitted intermolecular contribution of the background resulting in a normalized PELDOR time trace. As an exception, for the six-spin systems at the cytoplasmic side of BetP in detergent, a polynomial background correction was performed to additionally remove the interprotomeric distances from the time trace. In Section 7.8.3, the result of standard and polynomial background correction of the PELDOR time trace is exemplarily indicated for one BetP variant. All traces were analyzed further by Tikhonov regularization to obtain the respective distance distributions. For analysis of experimental data by Tikhonov regularization, the software DeerAnalysis2013 (Jeschke *et al.*, 2006) was used. Detailed PELDOR data for each BetP variant can be found in Section 7.8.7.

Distance distributions were simulated for models of known BetP structures with the rotamer library-based prediction software MMM2015.1 (Multiscale modelling of macromolecular systems) (Polyhach and Jeschke, 2010). Thereby, rotamers for the corresponding labeling sites were computed with the rotamer library R1A_298K_xray (Section 7.8.4).

5.1.5.1 Three-spin system

PELDOR was performed for the cytoplasmic three-spin system BetP S140C/C252T in detergent. The distance distributions derived from Tikhonov regularization of the experimental PELDOR data are compared to simulated distance distributions based on computed rotamers for symmetric and asymmetric BetP models.

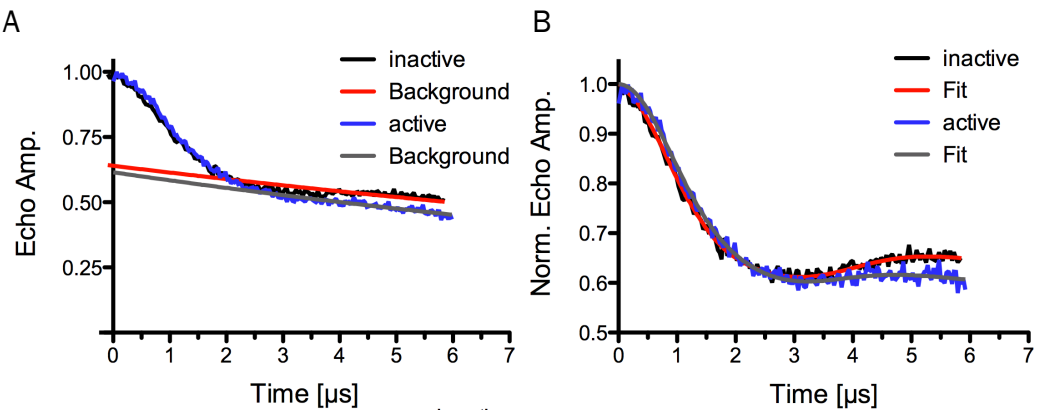

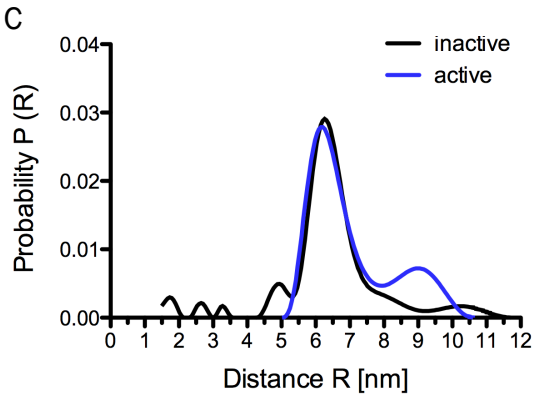

Figure 5.9: PELDOR analysis of BetP S140C/C252T in detergent as three-spin system with labels located at the cytoplasmic side.

Experimental PELDOR measurements were conducted for BetP S140C/C252T in 0.1 % DDM labeled with MMTSL at inactive (black) and active conditions (blue) at Q-band. Corresponding PELDOR time traces for BetP S140C/C252T are displayed as function of time in µs. The echo amplitude (A) and background-corrected normalized echo amplitude (B) are shown with the respective background as well as the fit to the data in red for the inactive and in gray for the active condition, respectively. C) The distance distribution was obtained by Tikhonov regularization (DeerAnalysis2013).

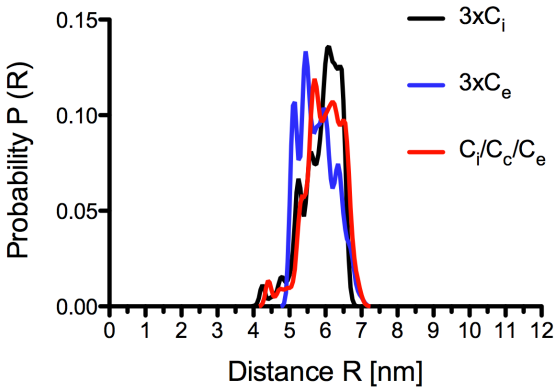

Figure 5.10: Simulated PELDOR distance distribution for BetP S140C/C252T as three-spin system.

Simulated PELDOR distance distributions for BetP S140C/C252T models as symmetric trimer in the inward open (3xC_i, black) and outward open (3xC_e, blue) conformation as well as conformational asymmetric trimer in the inward open, fully occluded (C_c) and outward open state (C_i/C_c/C_e, red). BetP models were created in PyMOL with crystal structures in the inward open (PDB 4DOJ, chain C), fully occluded (PDB 4AIN, chain B) and outward open conformation (PDB 4LLH, chain B). Data was simulated for BetP structures with the software MMM2015.1 (Polyhach and Jeschke, 2010).

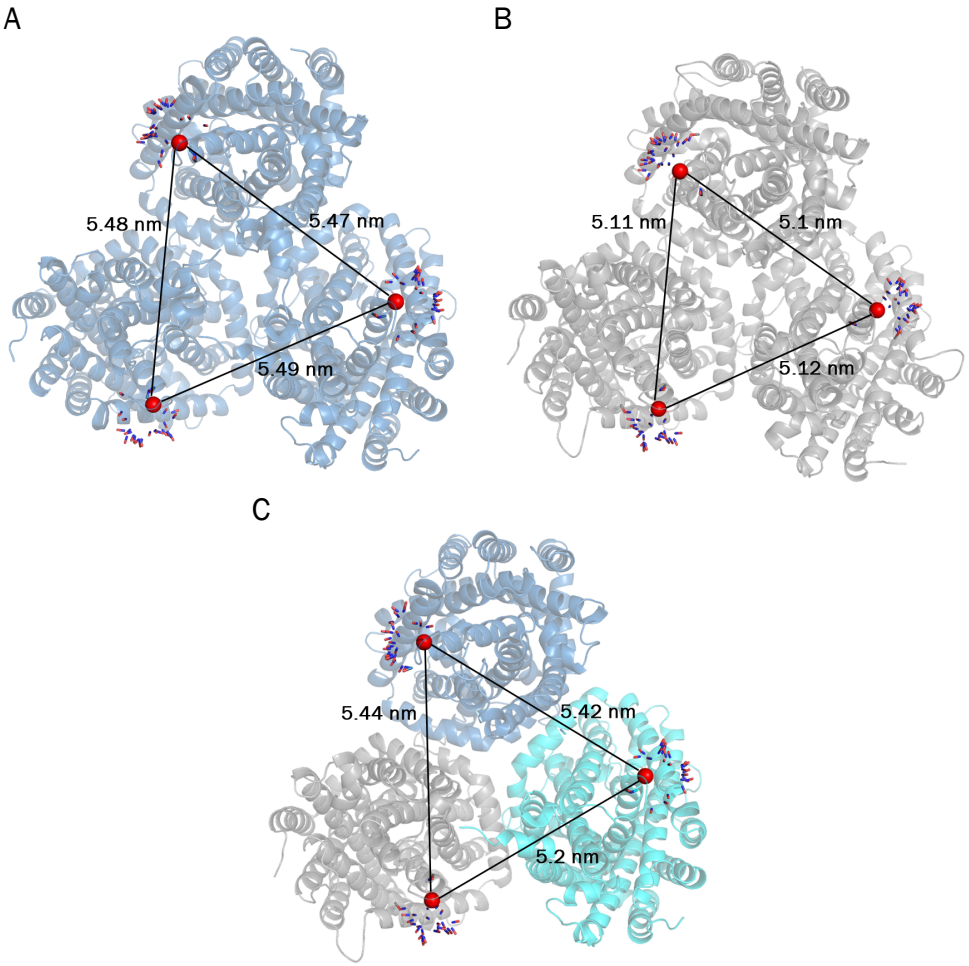

Figure 5.11: Simulated models of BetP S140C/C252T as three-spin system with computed rotamers.

Models of BetP are shown as symmetric trimers consisting of three protomers in either outward open (A, blue) or inward open (B, gray) state. The conformational asymmetric trimer (C) consists of a protomer in the outward and inward facing as well as in the fully occluded (cyan) conformation. The intratrimeric Cα – Cα distances are indicated between S140C. For clarity, the Cα-atom of S140C is depicted as sphere (red), whereas the corresponding rotamers in each respective conformation are depicted as sticks for the NO-atoms of the nitroxide spin labels.

Table 5.2: Cα – Cα and simulated interprotomeric distances of BetP S140C/C252T

Crystal structure$_{Cα-Cα}$			Simulation$_{MMM}$		
3xC_e	3xC_i	$C_e/C_i/C_c$	3xC_e	3xC_i	$C_e/C_i/C_c$
5.48 nm	5.11 nm	5.2 nm 5.42 nm 5.44 nm	5.75 nm	5.87 nm	5.78 nm 5.97 nm 6.05 nm

PELDOR time traces for the three-spin system BetP S140C/C252T were recorded in a time window of 6 µs (Figure 5.9). The length of the time window is too short for precise measurements of the distance peaks larger than 5 nm (Jeschke, 2012). In consequence, no significant distance change could be observed upon

activation of BetP. Distances in simulated symmetric (3xC_i: 5.87 nm; 3xC_e: 5.75 nm) and asymmetric trimers (C_e/C_i/C_c: 5.78 nm, 5.97 nm, 6.05 nm) predicted a change of maximal ~ 0.3 nm, which is quite small compared to the intratrimeric distance of ~6 nm (Table 5.2). This corresponds to the simulated distance distribution (Figure 5.10), in which no significant difference is visible for the various trimeric architectures. The simulated data indicates that the accuracy of this experiment is limited by the rational freedom of the spin labels in combination with long intratrimeric distances. Intratrimeric distances for the three-spin system BetP C252T/S516C were predicted to be even longer.
In summary, the three-spin system demonstrated that the PELDOR method delivered for BetP distances, which are in good agreement with structural data, but the precision is below the one required to resolve different conformational states of BetP.

5.1.5.2 Six-spin system

In order to detect conformational changes by shorter intraprotomeric distances, two positions within one protomer have to be simultaneously labeled, which is leading to a multi-spin system with in total six spin labels. For reliable data of spin systems with multiple spins, the appearance of artifacts known as ghost contributions in the obtained distance distribution has to be excluded (Von Hagens *et al*., 2013). Furthermore, this six-spin label strategy allows only the differentiation between protomers and provides no further information about the constitution of trimers. However, this label strategy enables the determination of conformational changes within BetP protomers in a more native environment. Therefore, intraprotomeric distances between labeled positions within the six-spin system were measured in detergent under non- and activating conditions.

For the interpretation of the following results has to be considered that the distances measured by PELDOR are not unique for certain conformational states of the protomers and there might be no discrimination between specific conformations. Therefore, different states of a protomer could lead to a similar distance, due to the similar arrangement of the spin labeled positions within the helices. Whereas for cytoplasmic labeling sites, the outward open conformation

could not be distinguished from the fully occluded conformation, at the periplasmic side the inward open and fully occluded conformation could not be discriminated (Figure 5.12). According to this, representative distance relations are mainly differentiated between the most differing conformations, in particular the outward and inward open conformation. However, it has to be kept in mind, that the closed conformation might be simultaneously sampled. As a result, each PELDOR experiment on the spin labeled BetP might be a measurement on a combination of protomers in different states.

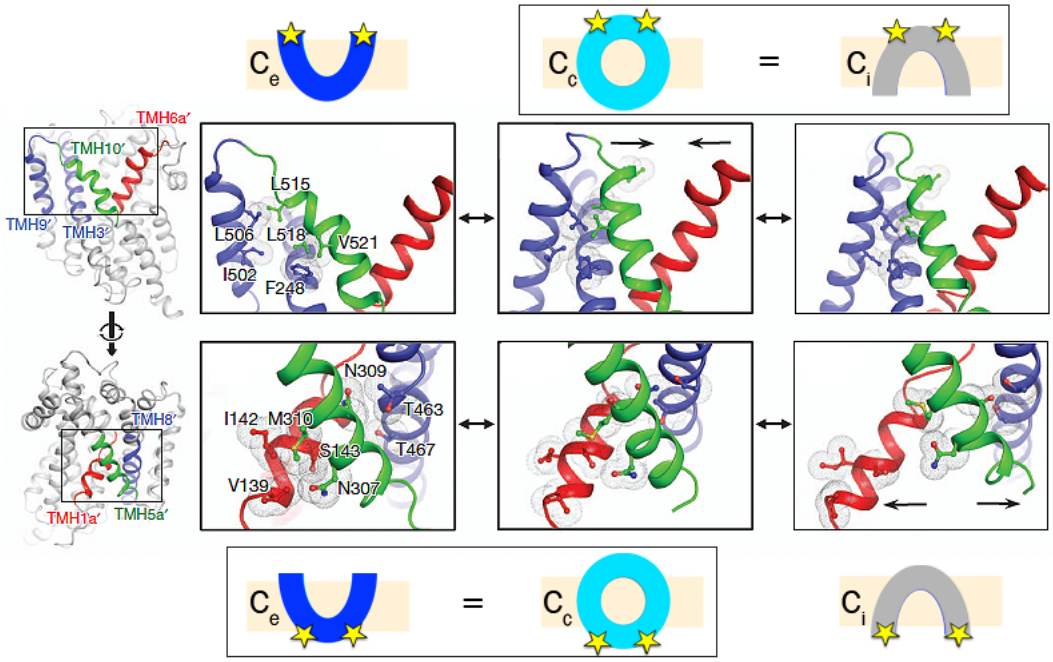

Figure 5.12: Orientation of labeling sites in different conformations of BetP.
Sequence of conformational changes of BetP at both sides of the membrane. Orientation of the helices are displayed for the outward open (C_e, blue), fully occluded (C_c, cyan) and inward open (C_i, gray) conformation. Upper and lower panel illustrate which conformations could not be discriminated by spin labeling at the periplasmic and cytoplasmic side of BetP, due to the same orientation of the helices (adapted from Perez *et al.*, 2012).

Results of the PELDOR measurements are shown for the cytoplasmic BetP variants and are further compared to simulated distance distributions, which are based on computed rotamers for the respective labeling site. Furthermore, intraprotomeric Cα – Cα distances between the labeling sites are indicated for a representative protomer in the outward and inward open conformation with the modeled rotamers for each six-spin system. The indicated Cα – Cα distances give

a general overview of the distance relation and describe the relative trend of the distance change between the spin labeled positions in the different conformations observed in the BetP crystal structures. It have to be noted that the obtained distance distributions might deviate from these distances due to the rational freedom and the size of the spin label itself of 5 - 8 Å (Klare and Steinhoff, 2009), factors which are considered in the rotamer-library based simulation. However, the Cα – Cα distances provide an initial estimation of the obtained data.

In addition, the results for the periplasmic side are illustrated. Beside intraprotomeric also interprotomeric distances are indicated for the periplasmic six-spin systems.

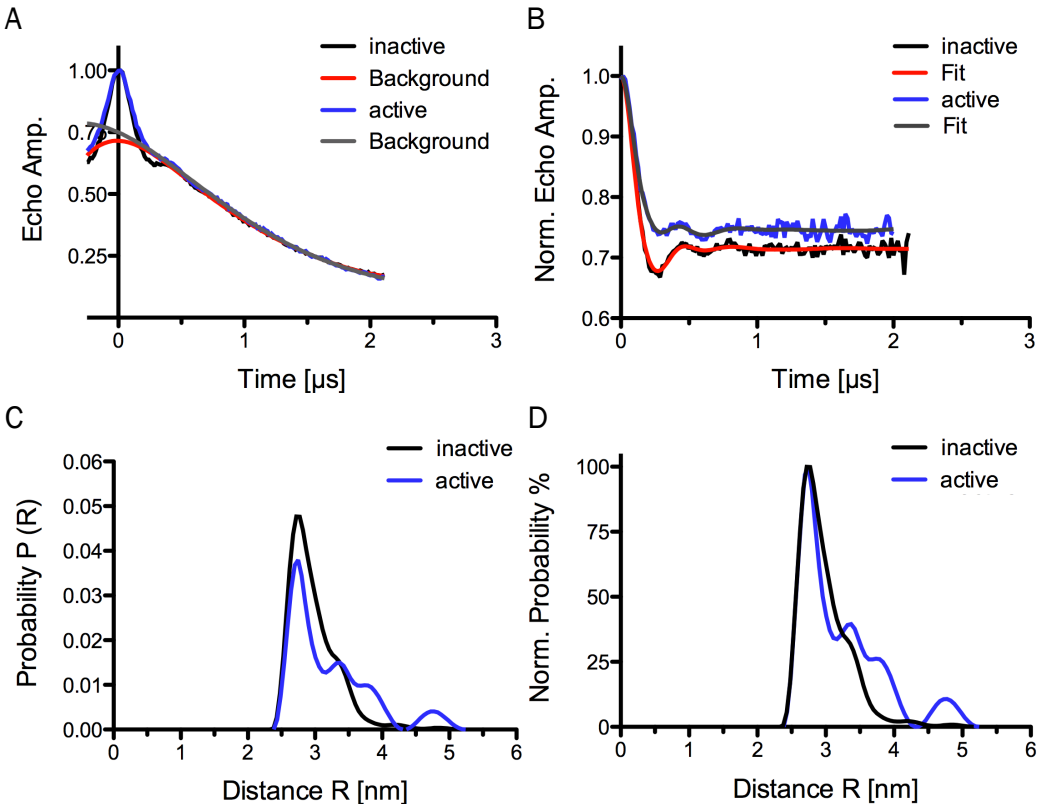

Figure 5.13: PELDOR analysis of BetP S140C/C252T/N488C in detergent as six-spin system with labels located at the cytoplasmic side.

Experimental PELDOR time traces were recorded for BetP S140C/C252T/N488C in 0.1 % DDM labeled with MMTSL at inactive (black) and active conditions (blue) at X-band. Corresponding PELDOR time traces for BetP S140C/C252T/N488C are displayed as function of time in µs. The echo amplitude (A) and background-corrected normalized echo amplitude (B) are shown with the respective background as well as the fit to the data in red for the inactive and in gray for the active condition, respectively. C) The distance

distribution was obtained by Tikhonov regularization (DeerAnalysis2013). D) For a better comparison, the resulting distance distribution was normalized.

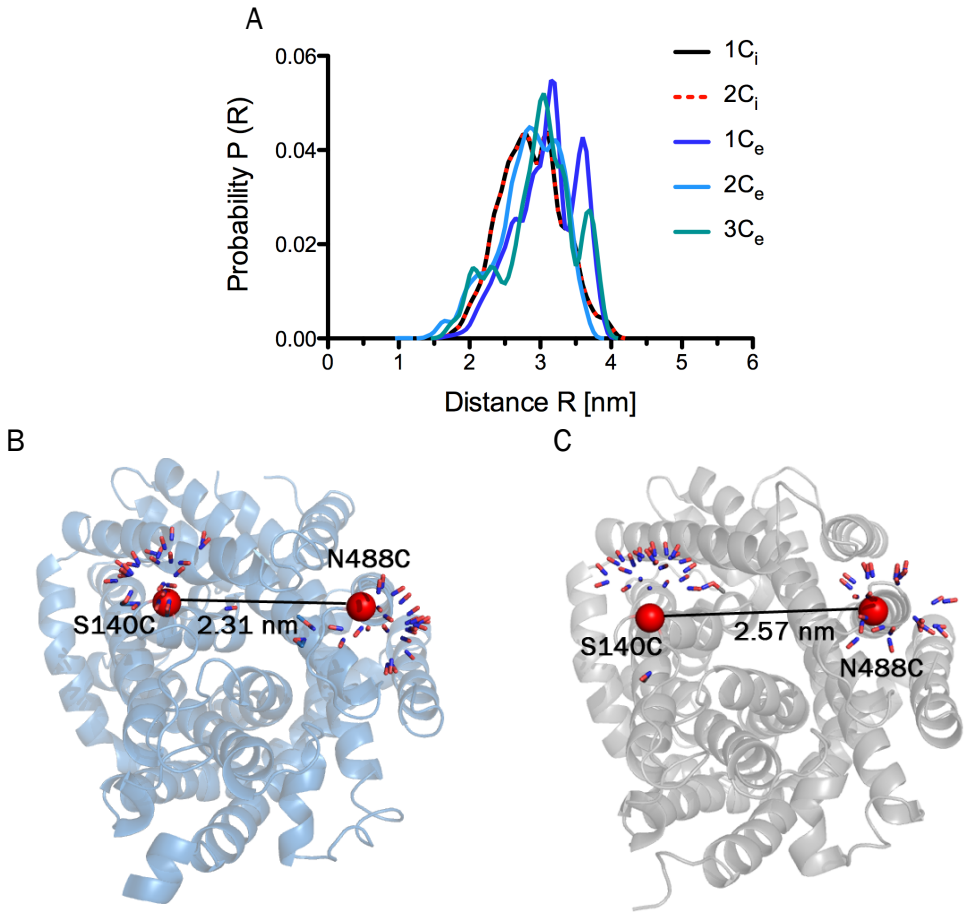

Figure 5.14: Simulated PELDOR distance distribution and representatives of protomeric BetP S140C/C252T/N488C.

A) Simulated PELDOR distance distributions for the BetP S140C/C252T/N488C monomer based on crystal structures in different conformations: inward open state $1C_i$ (PDB 4DOJ, chain C, black) and $2C_i$ (PDB 4C7R, chain A, dashed red) as well as outward open state $1C_e$ (PDB 4DOJ, chain B, dark blue), $2C_e$ (PDB 4LLH, chain A, light blue) and $3C_e$ (PDB 4LLH, chain B, green). In the cytoplasmic view, intraprotomeric Cα – Cα distances between the residues S140C and N488C are indicated with the Cα-atoms as spheres in red. The corresponding rotamers in the outward open (B, $2C_e$, blue) and inward open (C, $1C_i$, gray) conformation are depicted as sticks for the NO-atoms of the nitroxide spin labels. Data were simulated with the MMM software (Polyhach and Jeschke, 2010).

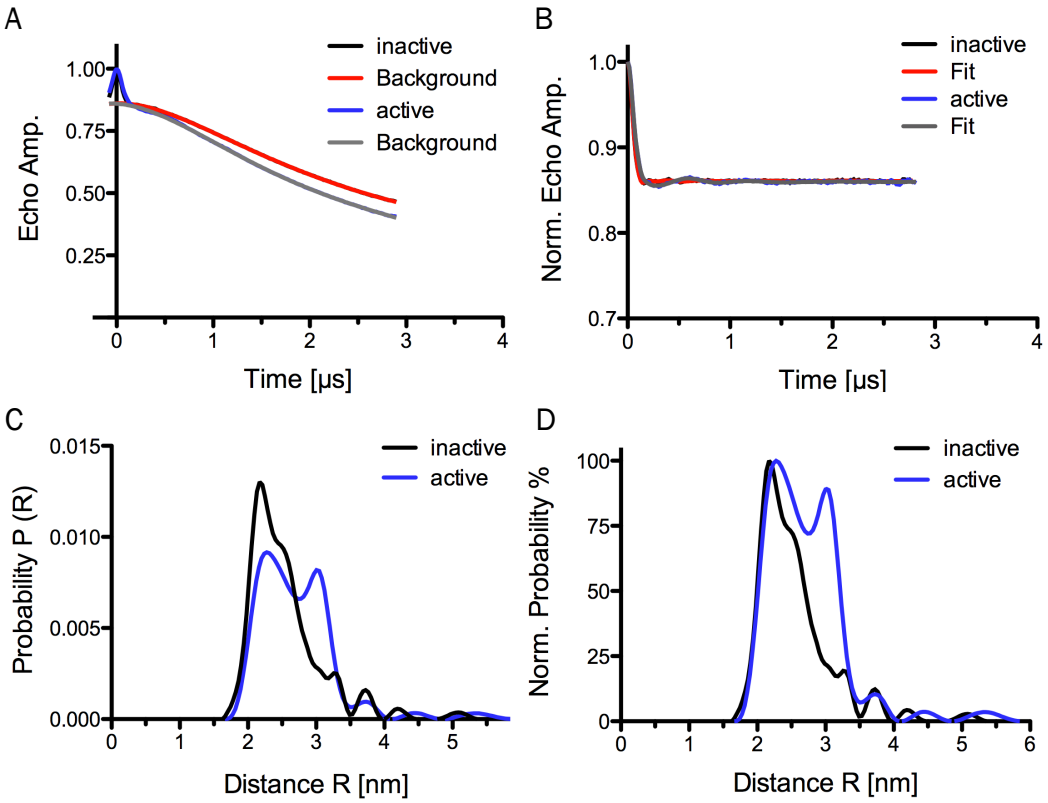

Figure 5.15: PELDOR analysis of BetP S140C/C252T/K489C in detergent as six-spin system with labels located at the cytoplasmic side.

Experimental PELDOR time traces were recorded for BetP S140C/C252T/K489C in 0.1 % DDM labeled with MTSL at inactive (black) and active conditions (blue) at Q-band. Corresponding PELDOR time traces for BetP S140C/C252T/K489C are displayed as function of time in µs. The echo amplitude (A) and background-corrected normalized echo amplitude (B) are shown with the respective background as well as the fit to the data in red for the inactive and in gray for the active condition, respectively. C) The distance distribution was obtained by Tikhonov regularization (DeerAnalysis2013). D) For a better comparison, the resulting distance distribution was normalized.

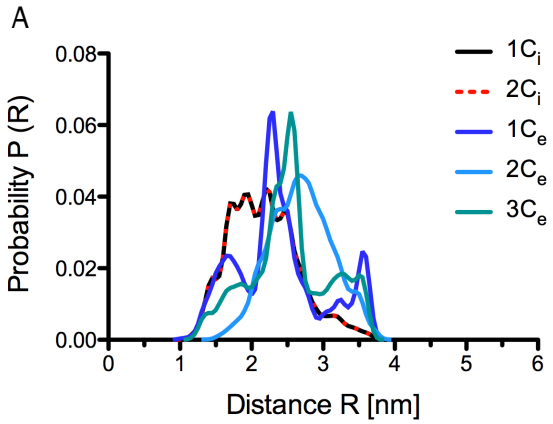

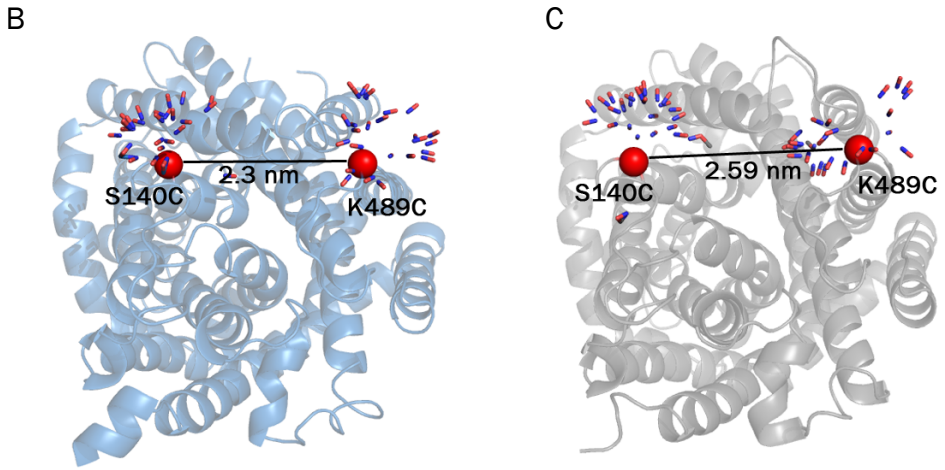

Figure 5.16: Simulated PELDOR distance distribution and representatives of protomeric BetP S140C/C252T/K489C.

A) Simulated PELDOR distance distributions for the BetP S140C/C252T/K489C monomer based on crystal structures in different conformations: inward open state $1C_i$ (PDB 4DOJ, chain C, black) and $2C_i$ (PDB 4C7R, chain A, dashed red) as well as outward open state $1C_e$ (PDB 4DOJ, chain B, dark blue), $2C_e$ (PDB 4LLH, chain A, light blue) and $3C_e$ (PDB 4LLH, chain B, green). In the cytoplasmic view, intraprotomeric Cα – Cα distances between the residues S140C and K489C are indicated with the Cα-atoms as spheres in red. The corresponding rotamers in the outward open (B, $2C_e$, blue) and inward open (C, $1C_i$, gray) conformation are depicted as sticks for the NO-atoms of the nitroxide spin labels. Data were simulated with the MMM software (Polyhach and Jeschke, 2010).

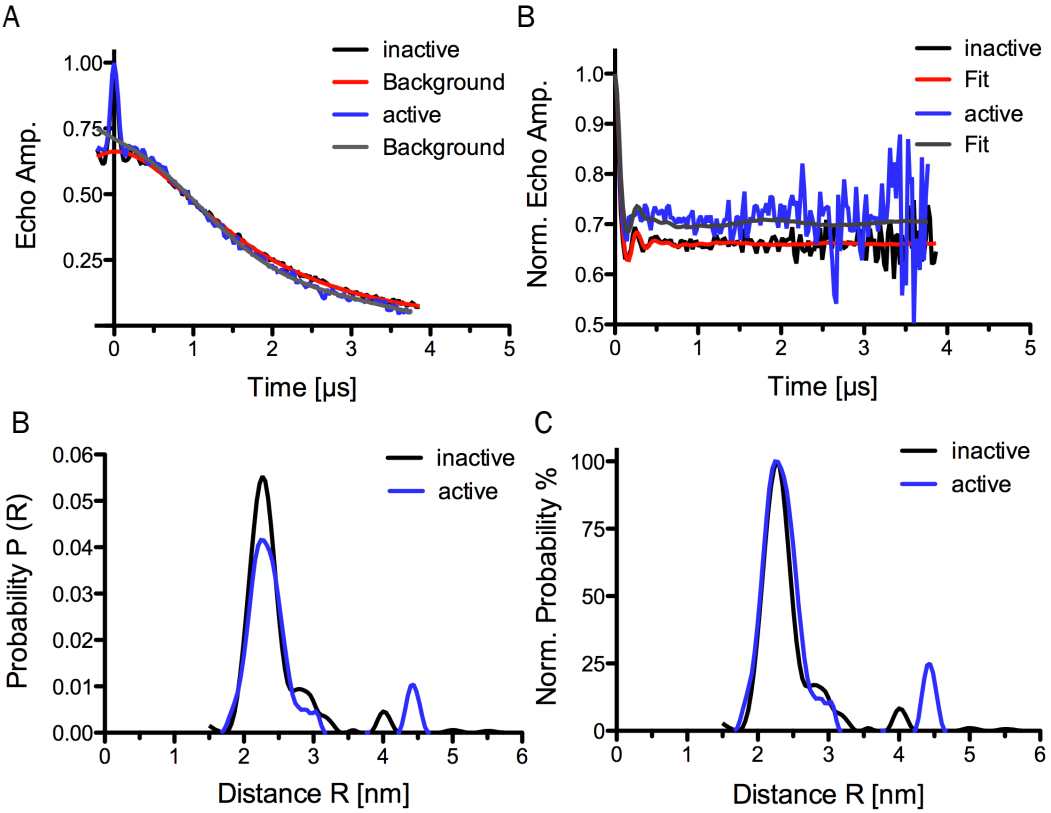

Figure 5.17: PELDOR analysis of BetP S140C/C252T/T467A/S468A/K489C in detergent as six-spin system with labels located at the cytoplasmic side.

Experimental PELDOR time traces were recorded for BetP S140C/C252T/T467A/S468A/K489C in 0.1 % DDM labeled with MMTSL at inactive (black) and active conditions (blue) at X-band. Corresponding PELDOR time traces for BetP S140C/C252T/T467A/S468A/K489C are displayed as function of time in µs. The echo amplitude (A) and background-corrected normalized echo amplitude (B) are shown with the respective background as well as the fit to the data in red for the inactive and in gray for the active condition, respectively. C) The distance distribution was obtained by Tikhonov regularization (DeerAnalysis2013). D) For a better comparison, the resulting distance distribution was normalized.

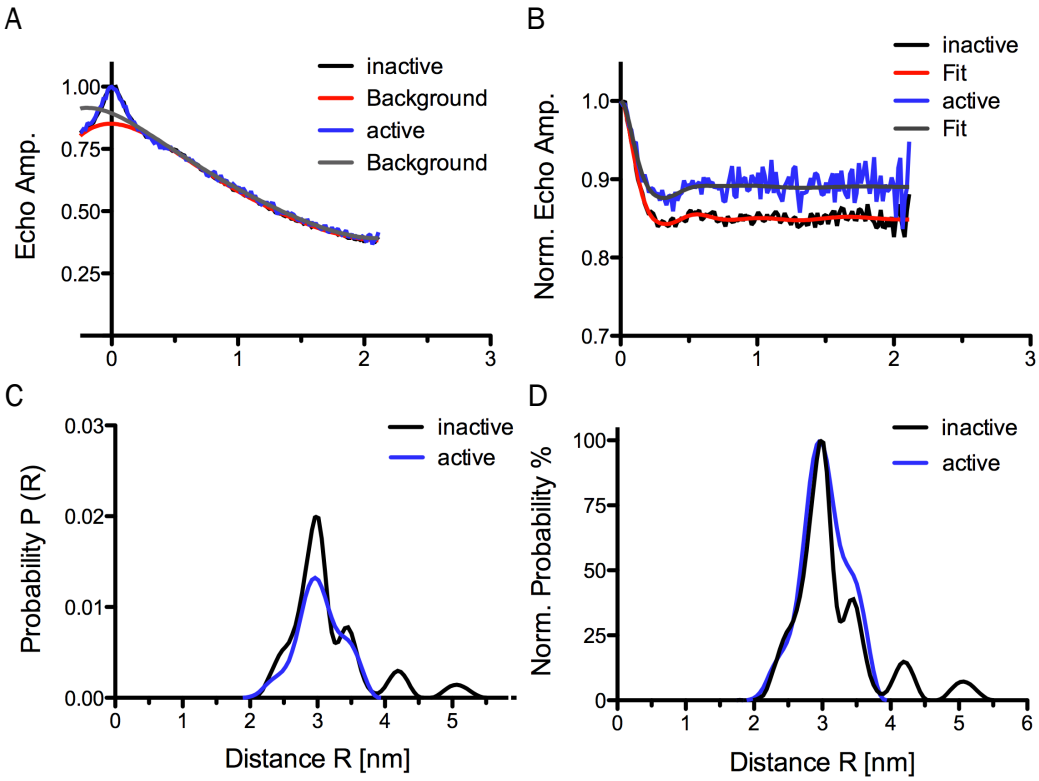

Figure 5.18: PELDOR measurements of BetP S140C/C252T/W490C in detergent as six-spin system with labels located at the cytoplasmic side.

Experimental PELDOR time traces were recorded for BetP S140C/C252T/W490 in 0.1 % DDM labeled with MMTSL at inactive (black) and active conditions (blue) at X-band. Corresponding PELDOR time traces for BetP S140C/C252T/W490 are displayed as function of time in µs. The echo amplitude (A) and background-corrected normalized echo amplitude (B) are shown with the respective background as well as the fit to the data in red for the inactive and in gray for the active condition, respectively. C) The distance distribution was obtained by Tikhonov regularization (DeerAnalysis2013). D) For a better comparison, the resulting distance distribution was normalized.

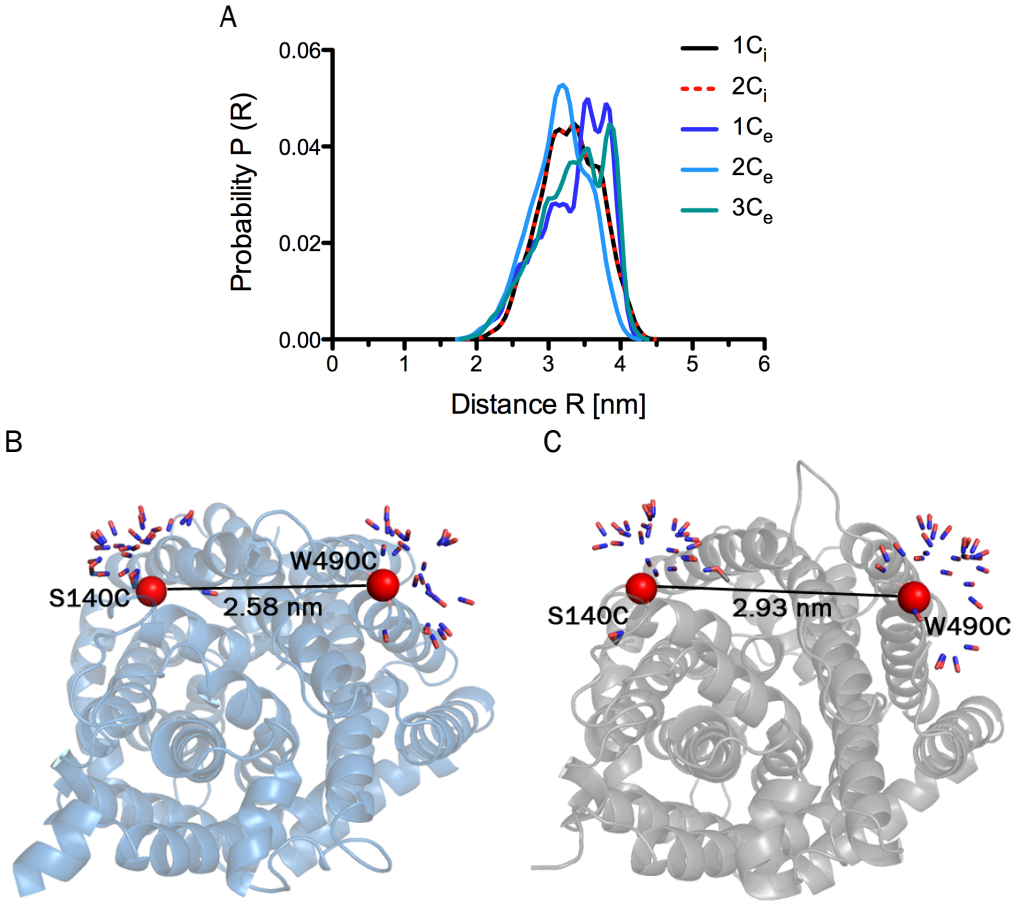

Figure 5.19: Simulated PELDOR distance distribution and representatives of protomeric BetP S140C/C252T/W490C.

A) Simulated PELDOR distance distributions for the BetP S140C/C252T/K489C monomer based on crystal structures in different conformations: inward open state 1Ci (PDB 4DOJ, chain C, black) and 2Ci (PDB 4C7R, chain A, dashed red) as well as outward open state 1Ce (PDB 4DOJ, chain B, dark blue), 2Ce (PDB 4LLH, chain A, light blue) and 3Ce (PDB 4LLH, chain B, green). In the cytoplasmic view, intraprotomeric Cα – Cα distances between the residues S140C and W490C are indicated with the Cα-atoms as spheres in red. The corresponding rotamers in the outward open (B, 2Ce, blue) and inward open (C, 1Ci, gray) conformation are depicted as sticks for the NO-atoms of the nitroxide spin labels. Data were simulated with the MMM software (Polyhach and Jeschke, 2010).

Table 5.3: Cα - Cα and simulated intraprotomeric distances for the cytoplasmic BetP six-spin systems

	Crystal structure$_{Cα-Cα}$		Simulation$_{MMM}$	
	2Ce	**1Ci**	**2Ce**	**1Ci**
S140C – N488C	2.31 nm	2.57 nm	2.82 nm	2.85 nm
S140C – K489C	2.3 nm	2.59 nm	2.68 nm	2.16 nm
S140C – W490C	2.58 nm	2.93 nm	3.14 nm	3.28 nm

PELDOR time traces were recorded for the cytoplasmic BetP six-spin systems in a time window of 2 – 4 µs. Although long interprotomeric distances (> 5 nm) are present in the cytoplasmic six-spin systems of BetP, the short distances were successfully separated from these by a polynomial background correction of the data (Figure 5.13, Figure 5.15, Figure 5.17, Figure 5.18 A – B). For the distinct separation of the shorter intraprotomeric from the longer interprotomeric distances, a background of a polynomial shape instead of the common mono-exponential background was used to filter the short distances out in the background corrected PELDOR time trace (personal communication Dr. Burkhard Endeward, Goethe University, Frankfurt). In all cases, the main distance peaks for the cysteine variants appear between 2 – 3.5 nm.

BetP S140C/C252C/N488C shows under inactivating conditions a main peak at 2.8 nm with a small shoulder at 3.4 nm (Figure 5.13). Upon activation, a slight increase of the shoulder can be detected, however, this increase is insignificant (Figure 5.13). In contrast, BetP S140C/C252T/K489C shows a significant change in the experimental distance distribution by splitting from the main distance at 2.3 nm at non-activating conditions to two distances at 2.3 nm and 3 nm with almost the same probability under fully activating conditions (Figure 5.15). Table 5.3 lists the intraprotomeric Cα – Cα distance relation between the residues S140 and K489 in one outward open and inward open crystal structure, respectively. The increase of the experimental intraprotomeric distance for BetP S140C/C252T/K489C might imply a conformational change from the outward to the inward facing state upon activation when compared to these distances. Although there might be a transition into another conformation indicated by the second longer peak, the shorter distance is still present for BetP S140C/C252T/K489C in the activated condition. Remarkably, this conformational change can be abolished for BetP S140C/C252C/T467A/S468A/K489C, which is impaired in the ability to transport betaine (Figure 5.6), because the main sodium-binding site T467/S468 is distorted. A single distance peak at ~2.3 nm suggests for inactive BetP S140C/C252C/T467A/S468A/K489C one distinct conformational state (Figure 5.17). For BetP S140C/C252C/W490C with a main peak at 3 nm and a less pronounced shoulder at 3.3 nm, no significant change upon activation could be observed (Figure 5.18).

Table 5.3 summarizes the intraprotomeric Cα – Cα distances between the native residues in the crystal structures and the simulated average spin-spin distances by the software package MMM (Polyhach *et al.*, 2011; Polyhach and Jeschke, 2010) for protomeric BetP cysteine variants exemplarily in the outward and inward open conformation. In addition, Figure 5.14, Figure 5.16 and Figure 5.19 presents the corresponding BetP models with the most populated rotamers, which were predicted by the rotamer library R1A_298K_xray. This rotamer library was chosen for data analysis, because the standard rotamer library at cryogenic and ambient temperature, R1A_175K and R1A_289K, respectively, showed very low numbers of rotamers at specific sites leading to an artificial splitting of distance distributions (Section 7.8.4). For an adequate comparison, simulated distance distributions are displayed for different inward open and outward open BetP crystal structures.

The differences between the simulated average spin-spin distances in both states are less pronounced for S140C/C252T/N488C, S140C/C252T/W490C and S140C/C252T/K489C as well as do not follow the same trend when compared to the measured Cα – Cα distances in the crystal structures (Table 5.3). However, the experimental obtained distance peaks are in a comparable range of the simulated spin-spin distances.

The comparison of the experimental data with the computed distance distributions is far from trivial. No significant distance change between the outward and inward open conformation of BetP S140C/C252T/N488C and S140C/C252T/W490C can be detected in the simulated distance distributions (Figure 5.14 and Figure 5.19) as well as in the simulated average distances (Table 5.3). This correlates with the observed experimental distance distributions for these mutants (Figure 5.13 and Figure 5.18). In contrast, the trend of the simulation of BetP S140C/C252T/K489C differs from the predicted Cα – Cα distances. Whereas the inward open conformation is indicated by a longer distance in the crystal structure, within the simulation the different outward open conformations are characterized by longer distances (Figure 5.16). This divergence might be attributed to the different conformational freedom of the rotamers in the different conformations (Table 7.4, Section 7.8.4).

In consequence, the computed distance distributions are significantly affected by the rotamer number (Table 7.4, Section 7.8.4) and distribution as indicated in

Figure 5.16. In general, the simulated distributions are slightly broader and more heterogenic than the experimental ones.

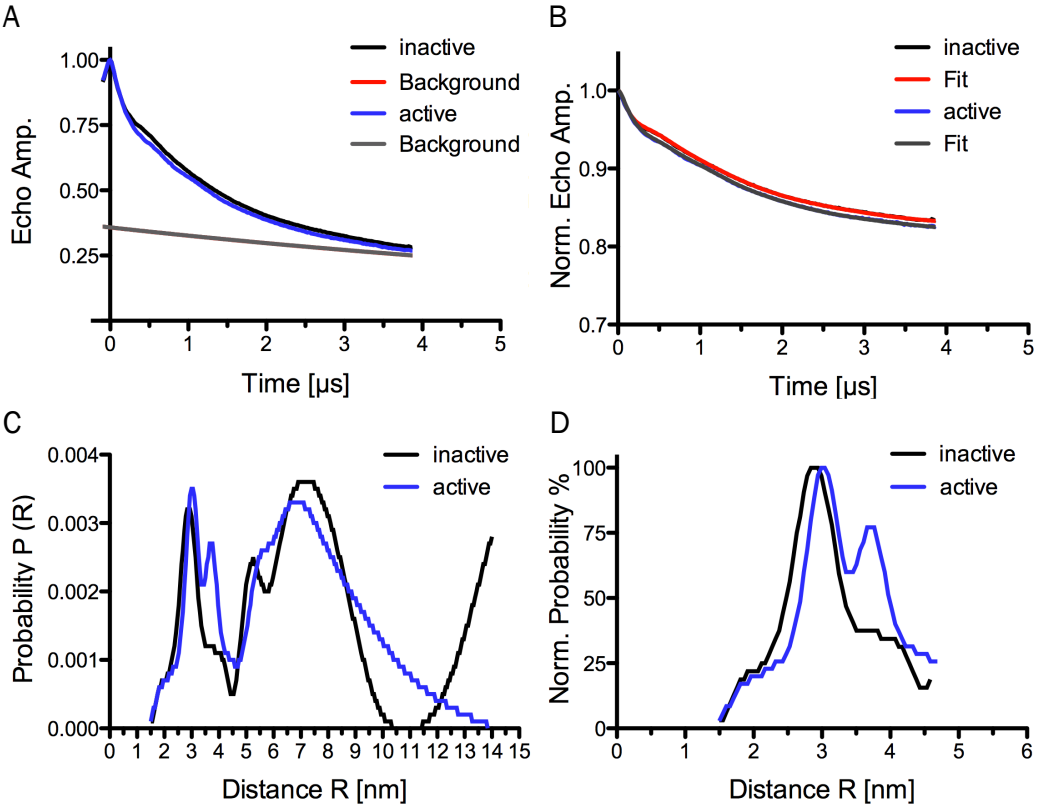

Figure 5.20: PELDOR measurements of BetP C252T/G450C/A514C in detergent as six-spin system with labels located at the periplasmic side.

Experimental PELDOR time traces were recorded for BetP C252T/G450C/A514C in 0.1 % DDM labeled with MMTSL at inactive (black) and active conditions (blue) at Q-band. Corresponding PELDOR time traces for BetP C252T/G450C/A514C are displayed as function of time in µs. The echo amplitude (A) and background-corrected normalized echo amplitude (B) are shown with the respective background as well as the fit to the data in red for the inactive and in gray for the active condition, respectively. C) The distance distribution was obtained by Tikhonov regularization (DeerAnalysis2013). D) For a better comparison, the first part of the resulting distance distribution was normalized.

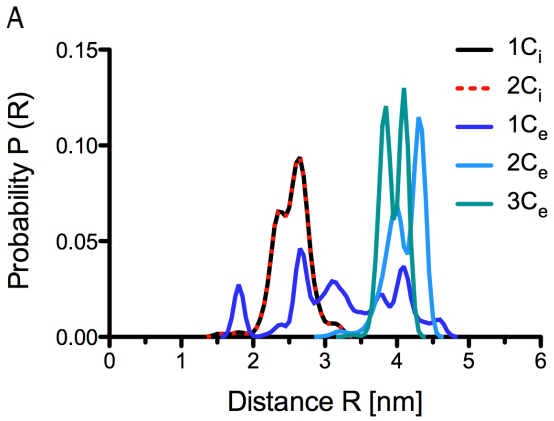

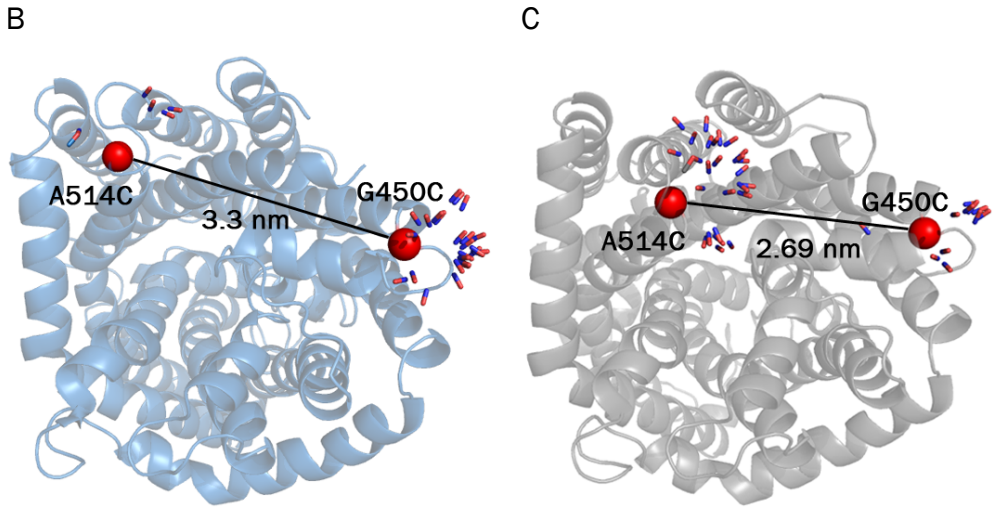

Figure 5.21: Simulated PELDOR distance distribution and representatives of protomeric BetP C252T/G450C/A514C.

A) Simulated PELDOR distance distributions for the BetP C252T/G450C/A514C monomer based on crystal structures in different conformations: inward open state $1C_i$ (PDB 4DOJ, chain C, black) and $2C_i$ (PDB 4C7R, chain A, dashed red) as well as outward open state $1C_e$ (PDB 4DOJ, chain B, dark blue), $2C_e$ (PDB 4LLH, chain A, light blue) and $3C_e$ (PDB 4LLH, chain B, green). In the periplasmic view, intraprotomeric Cα – Cα distances between the residues G450C and A514C are indicated with the Cα-atoms as spheres in red. The corresponding rotamers in the outward open (B, $2C_e$, blue) and inward open (C, $1C_i$, gray) conformation are depicted as sticks for the NO-atoms of the nitroxide spin labels. Data was simulated with the MMM software (Polyhach and Jeschke, 2010).

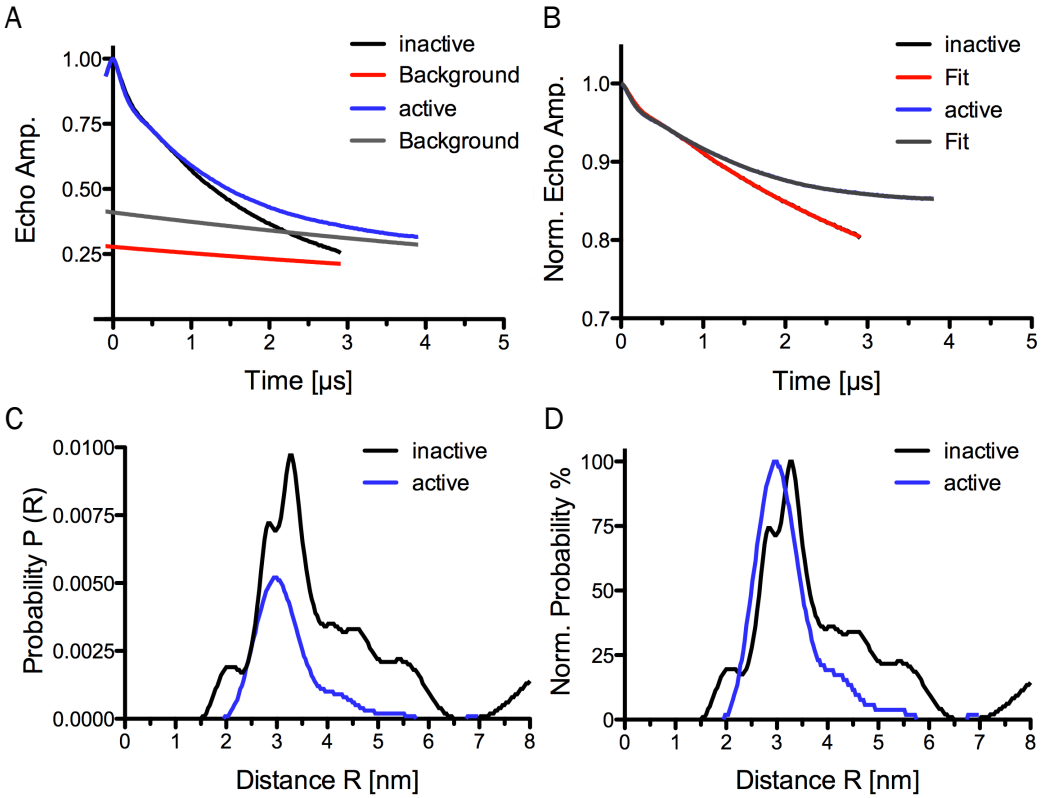

Figure 5.22: PELDOR measurements of BetP C252T/G450C/T467A/A514C in detergent as six-spin system with labels located at the periplasmic side.
Experimental PELDOR time traces were recorded for BetP C252T/G450C/T467A/S468A/A514C in 0.1 % DDM labeled with MMTSL at inactive (black) and active conditions (blue) at Q-band. Corresponding PELDOR time traces for BetP C252T/G450C/T467A/S468A/A514C are displayed as function of time in µs. The echo amplitude (A) and background-corrected normalized echo amplitude (B) are shown with the respective background as well as the fit to the data in red for the inactive and in gray for the active condition, respectively. C) The distance distribution was obtained by Tikhonov regularization (DeerAnalysis2013). D) For a better comparison, the resulting distance distribution was normalized.

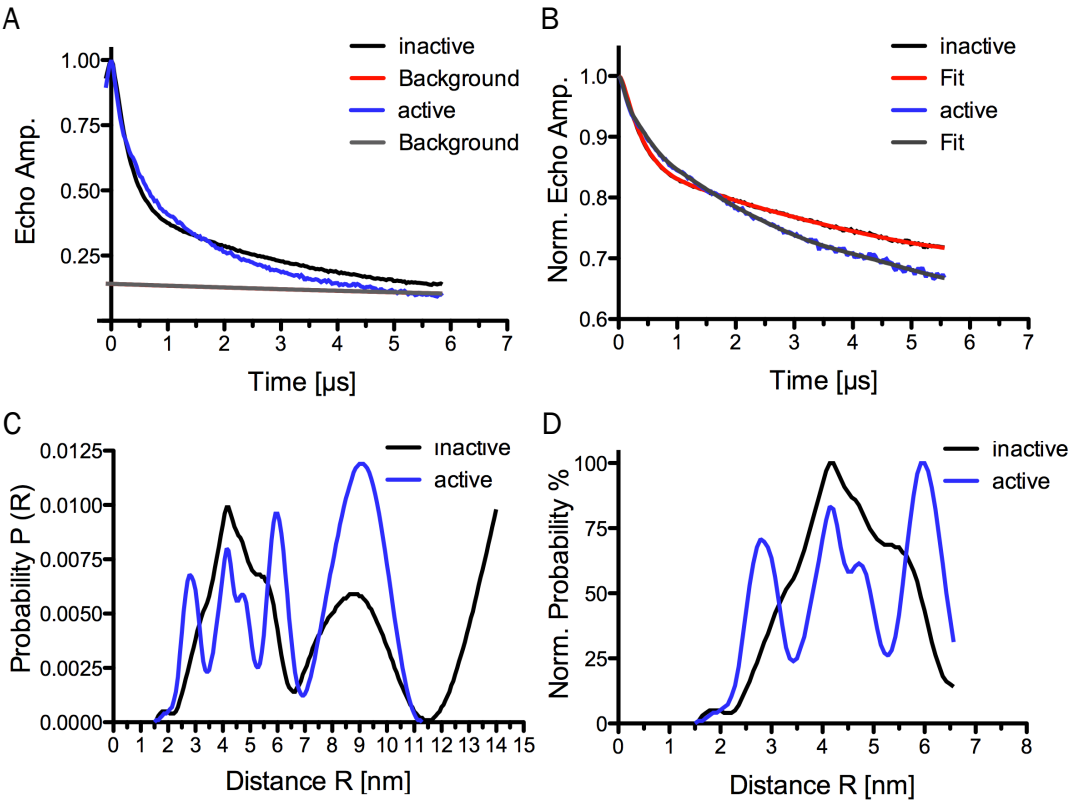

Figure 5.23: PELDOR measurements of BetP C252T/G450C/L515C in detergent as six-spin system with labels located at the periplasmic side.
Experimental PELDOR time traces were recorded for BetP C252T/G450C/L515C in 0.1 % DDM labeled with MMTSL at inactive (black) and active conditions (blue) at Q-band. Corresponding PELDOR time traces for BetP C252T/G450C/L515C are displayed as function of time in µs. The echo amplitude (A) and background-corrected normalized echo amplitude (B) are shown with the respective background as well as the fit to the data in red for the inactive and in gray for the active condition, respectively. C) The distance distribution was obtained by Tikhonov regularization (DeerAnalysis2013). D) For a better comparison, the first half of the resulting distance distribution was normalized.

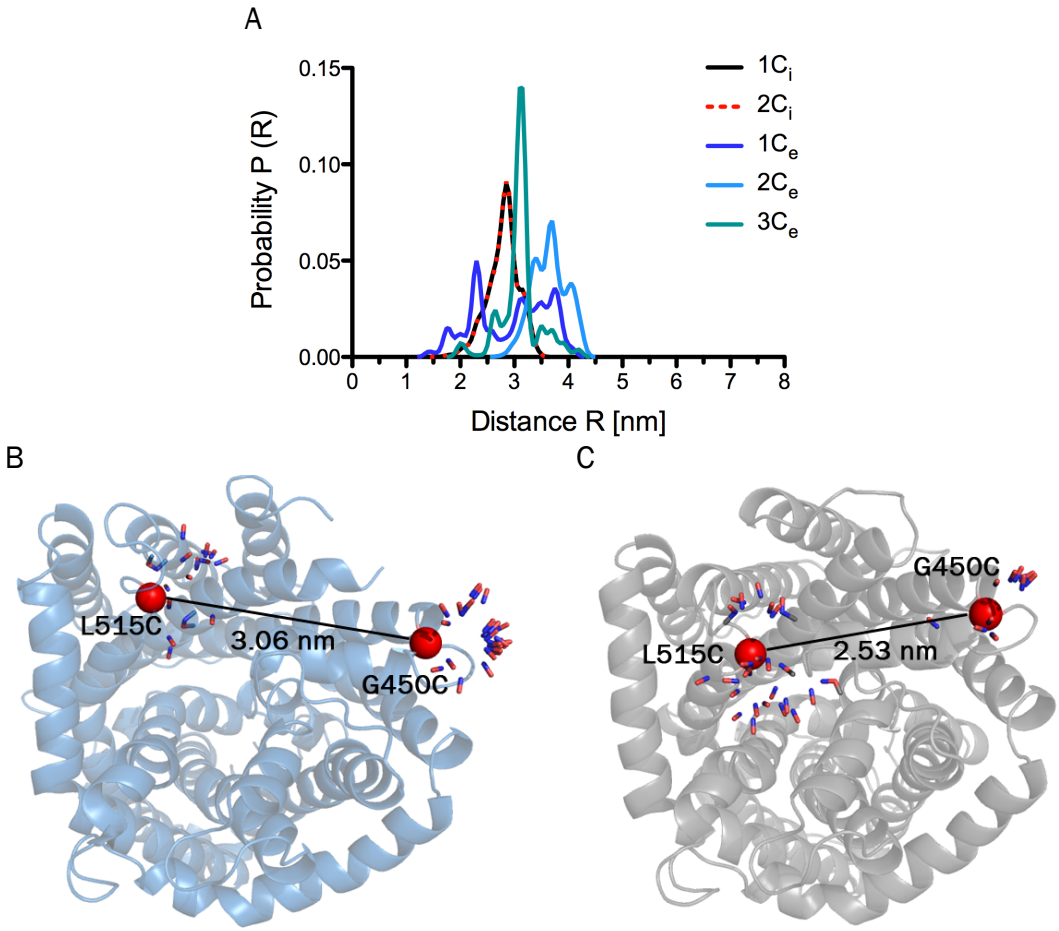

Figure 5.24: Simulated PELDOR distance distribution and representatives of protomeric BetP C252T/G450C/L515C.

A) Simulated PELDOR distance distributions for the BetP C252T/G450C/L515C monomer based on crystal structures in different conformations: inward open state $1C_i$ (PDB 4DOJ, chain C, black) and $2C_i$ (PDB 4C7R, chain A, dashed red) as well as outward open state $1C_e$ (PDB 4DOJ, chain B, dark blue), $2C_e$ (PDB 4LLH, chain A, light blue) and $3C_e$ (PDB 4LLH, chain B, green). In the periplasmic view, intraprotomeric Cα – Cα distances between the residues G450C and L515C are indicated with the Cα-atoms as spheres in red. The corresponding rotamers in the outward open (B, $2C_e$, blue) and inward open (C, $1C_i$, gray) conformation are depicted as sticks for the NO-atoms of the nitroxide spin labels. Data was simulated with the MMM software 1 (Polyhach and Jeschke, 2010).

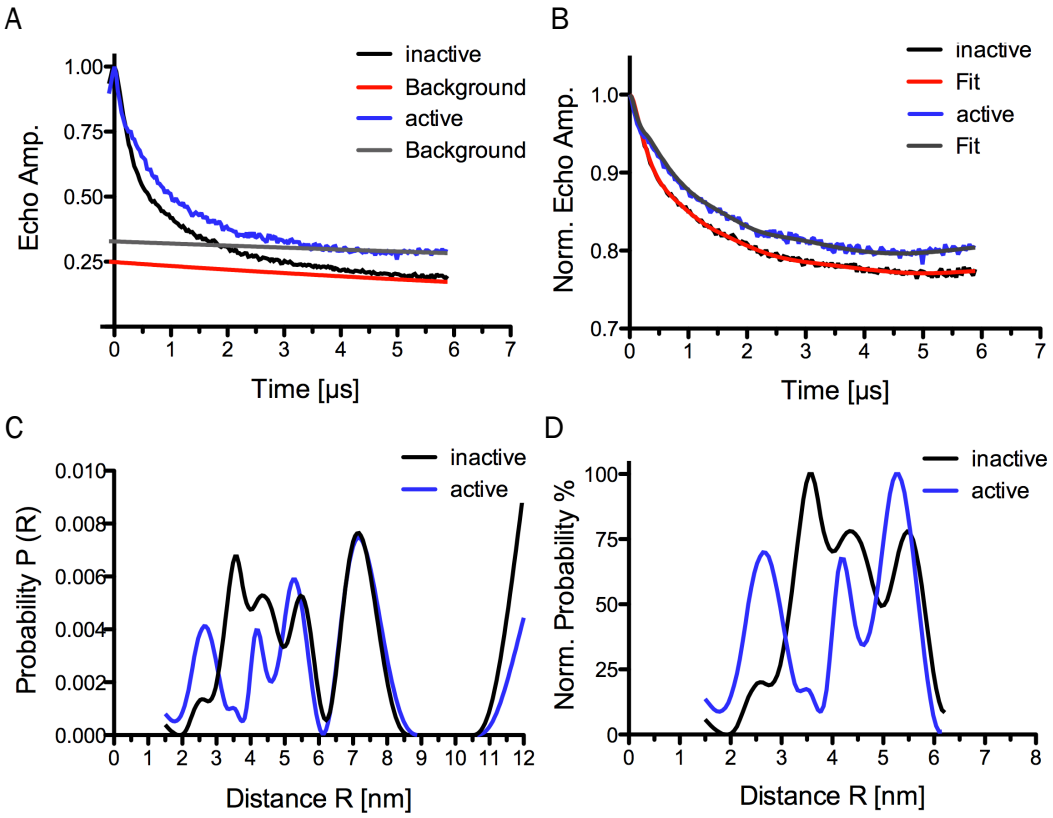

Figure 5.25: PELDOR measurements of BetP C252T/G450C/S516C in detergent as six-spin system with labels located at the periplasmic side.

Experimental PELDOR time traces were recorded for BetP C252T/G450C/S516C in 0.1 % DDM labeled with MTSL at inactive (black) and active conditions (blue) at Q-band. Corresponding PELDOR time traces for BetP C252T/G450C/S516C are displayed as function of time in µs. The echo amplitude (A) and background-corrected normalized echo amplitude (B) are shown with the respective background as well as the fit to the data in red for the inactive and in gray for the active condition, respectively. C) The distance distribution was obtained by Tikhonov regularization (DeerAnalysis2013). D) For a better comparison, the first half of the resulting distance distribution was normalized.

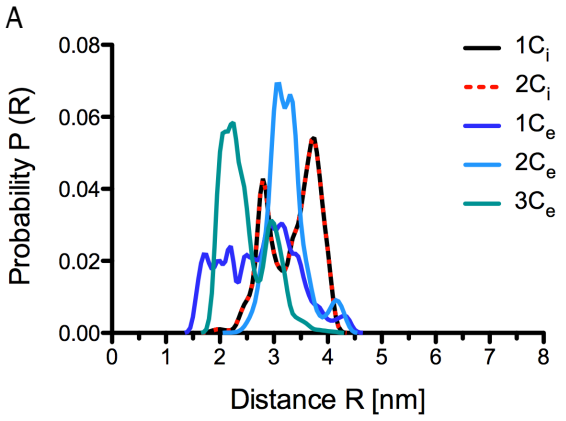

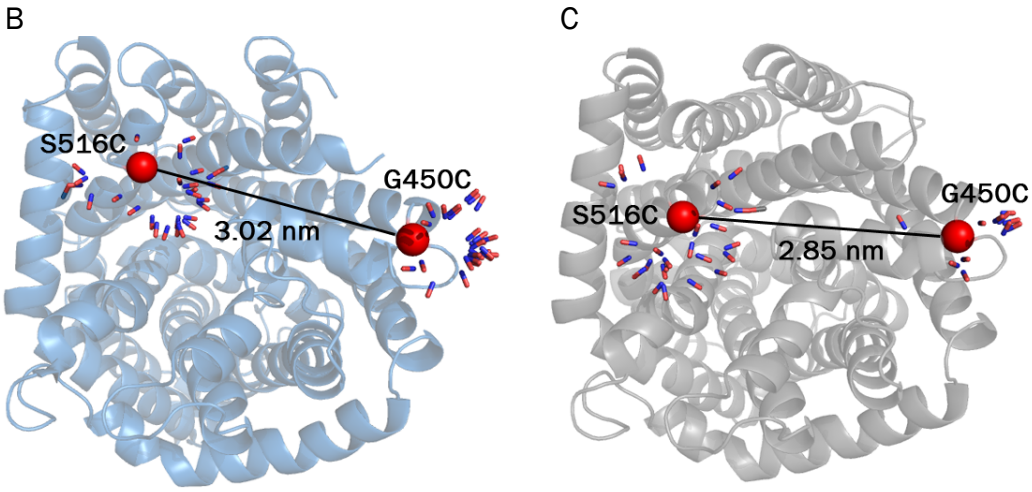

Figure 5.26: Simulated PELDOR distance distribution and representatives of protomeric BetP C252T/G450C/S516C.

A) Simulated PELDOR distance distributions for the BetP C252T/G450C/S516C monomer based on crystal structures in different conformations: inward open state $1C_i$ (PDB 4DOJ, chain C, black) and $2C_i$ (PDB 4C7R, chain A, dashed red) as well as outward open state $1C_e$ (PDB 4DOJ, chain B, dark blue), $2C_e$ (PDB 4LLH, chain A, light blue) and $3C_e$ (PDB 4LLH, chain B, green). In the periplasmic view, intraprotomeric Cα – Cα distances between the residues G450C and S516C are indicated with the Cα-atoms as spheres in red. The corresponding rotamers in the outward open (B, $2C_e$, blue) and inward open (C, $1C_i$, gray) conformation are depicted as sticks for the NO-atoms of the nitroxide spin labels. Data was simulated with the MMM software (Polyhach and Jeschke, 2010).

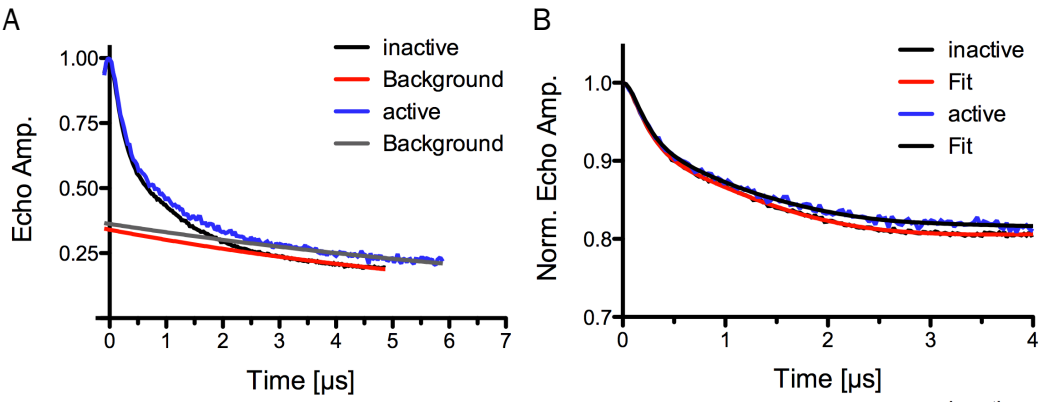

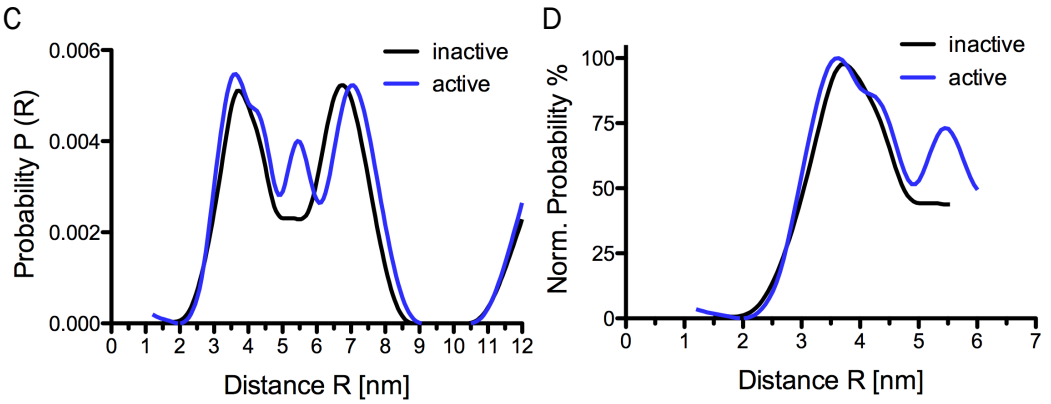

Figure 5.27: PELDOR measurements of BetP C252T/G450C/T467A/S468A/S516C in detergent as six-spin system with labels located at the periplasmic side.

Experimental PELDOR time traces were recorded for BetP C252T/G450C/T467A/S468A/S516C in 0.1 % DDM labeled with MTSL at inactive (black) and active conditions (blue) at Q-band. Corresponding PELDOR time traces for BetP C252T/G450C/T467A/S468A/S516C are displayed as function of time in µs. The echo amplitude (A) and background-corrected normalized echo amplitude (B) are shown with the respective background as well as the fit to the data in red for the inactive and in gray for the active condition, respectively. C) The distance distribution was obtained by Tikhonov regularization (DeerAnalysis2013). D) For a better comparison, the first half of the resulting distance distribution was normalized.

Table 5.4: Cα – Cα and simulated intraprotomeric distances for the periplasmic BetP six-spin systems

	Crystal structure$_{Cα-Cα}$		Simulation$_{MMM}$	
	2C$_e$	**1C$_i$**	**2C$_e$**	**1C$_i$**
G450C – A514C	3.3 nm	2.69 nm	4.09 nm	2.53 nm
G450C – L515C	3.06 nm	2.53 nm	3.63 nm	2.78 nm
G450C – S516C	3.02 nm	2.85 nm	3.23 nm	3.33 nm

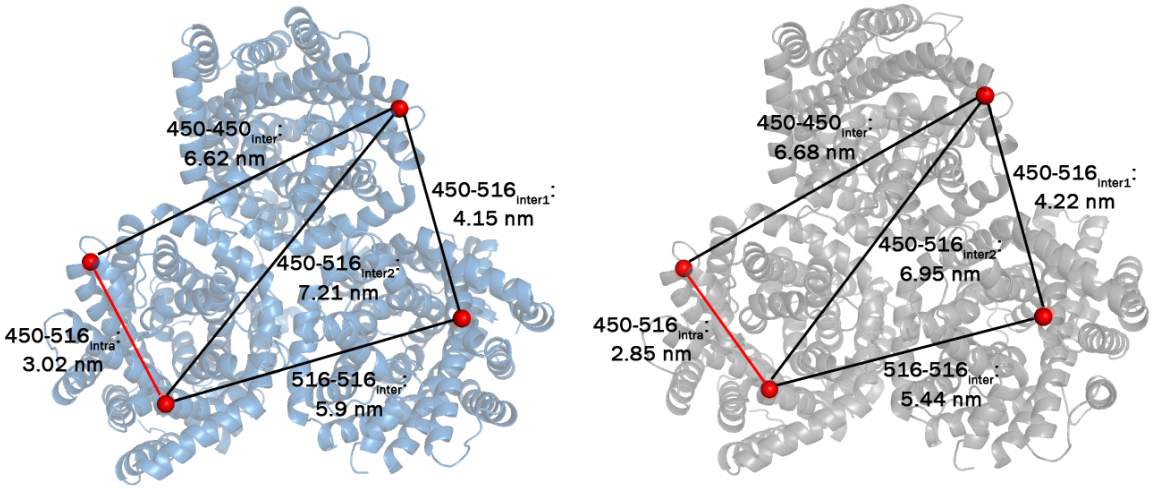

Figure 5.28: Representative intra- and interprotomeric distances for symmetric BetP C252T/G450C/S516C as six-spin system.

The conformational symmetric BetP trimer models were created with the solved X-ray structures of BetP protomers in the outward open ($2C_e$, blue) and inward open ($1C_i$, gray) conformation. The native residues G450 and S516 are selected as labeling sites and the corresponding Cα-atoms are represented as red spheres. Intraprotomeric distances are colored red, the interprotomeric distances are colored black and the distance relations are depicted as Cα – Cα distances between the corresponding residues.

Table 5.5: Cα – Cα and simulated interprotomeric distances for the periplasmic BetP six-spin systems

	Crystal structure$_{Cα-Cα}$		**Simulation$_{MMM}$**	
	3 x $2C_e$	**3 x $1C_i$**	**3 x $2C_e$**	**3 x $1C_i$**
G450C – A514C$_{inter1}$	4.67 nm	4.7 nm	4.9 nm	5.35 nm
G450C – A514C$_{inter2}$	7.38 nm	7.37 nm	8.51 nm	7.73 nm
G450C – G450C$_{inter}$	6.62 nm	6.68 nm	7.21 nm	7.25 nm
A514C – A514C$_{inter}$	6.37 nm	6.25 nm	7.53 nm	6.42 nm
G450C – L515C$_{inter1}$	4.44 nm	4.57 nm	5.13 nm	4.6 nm
G450C – L515C$_{inter2}$	7.12 nm	7.03 nm	8.15 nm	7.12 nm
G450C – G450C$_{inter}$	6.62 nm	6.68 nm	7.21 nm	7.25 nm
L515C – L515C$_{inter}$	5.82 nm	5.66 nm	6.99 nm	5.21 nm
G450C – S516C$_{inter1}$	4.15 nm	4.22 nm	4.4 nm	3.92 nm
G450C – S516C$_{inter2}$	7.21 nm	6.95 nm	7.67 nm	7.32 nm
G450C – G450C$_{inter}$	6.62 nm	6.68 nm	7.21 nm	7.25 nm
S516C – S516C$_{inter}$	5.9 nm	5.44 nm	6.1 nm	5.41 nm

Figure 5.20 – Figure 5.27 show the results of the experimental and simulated PELDOR measurements for the six-spin systems at the periplasmic side of diverse BetP variants in detergent. PELDOR time traces were recorded with time windows of 4 – 6 µs. In contrast to the measurements for the cytoplasmic six-spin systems, the intraprotomeric distances were not sufficiently separated from the longer interprotomeric distances in the periplasmic BetP mutants. For these measurements, distance populations have been detected between 2 – 10 nm. Due to the insufficient accuracy of long distances, for time windows of 6 µs distances around 7 nm or even longer are not reliable (Jeschke, 2012). In consequence, the analysis will focus on the first part of the distance distribution (<5 nm), which is still sufficient for 4 µs PELDOR time traces and the expected distances within a protomer. In addition, the experimental results are compared to the simulated data based on the single protomers in the outward and inward open conformations. Therefore, the probability was normalized only for the first part of the distance distribution, which contains the more relevant information of the intraprotomeric distances.

The analysis of the PELDOR time traces of BetP C252T/G450C/A514C indicated that under non-activating conditions, the distance distribution exhibits a peak at 3 nm. Upon activation, the distance at 3 nm shifts slightly to longer distances and at 3.7 nm an additional peak appears (Figure 5.20). Based on the intraprotomeric Cα – Cα distances (Table 5.4), the presence of a second longer distance suggests a change from the inward facing to the outward open state. This corresponds very well to the simulated distance distribution (Figure 5.21). As for the cytoplasmic side, the inactivation of BetP C252T/G450C/A514C by the additional substitutions of the essential sodium-binding site (T467/S468) were investigated. BetP C252T/G450C/T467A/S468A/A514C was identified to be impaired in the betaine transport activity and consequently a less significant difference could be observed (Figure 5.22). Taking the short PELDOR time trace window into account, the differences are in the order of the uncertainty, expected from the background correction.

BetP C252T/G450C/L515C is characterized by very broad distance distribution with a main peak at 4.2 nm and a shoulder at approximately 5.5 nm at inactive conditions (Figure 5.23). Addition of the main activation trigger K^+ and betaine as substrate let separate the distance distribution into at least two peaks at 2.9 nm, and 4.3 nm with a shoulder at 4.8 nm and a distance around 6.1 nm. The latter distance is too long for a reliable interpretation. Here, the occurrence of the significant smaller distance at 2.9 nm indicates a change from the outward facing to the inward open state, if compared with proposed intraprotomeric Cα – Cα distances for the respective states (Table 5.4). The longer intraprotomeric distance corresponding to the outward open transporter (Cα – Cα: 3.3 nm, MMM: 3.63 nm) seems to overlap with other longer interprotomeric distances within the broad distance distribution under inactive conditions in the six-spin system. This is matching to the simulated distance distribution, in which peaks for the outward open conformation can be detected at 4 nm (Figure 5.24).

The analysis of the experimental data of BetP C252T/G450C/S516C revealed at inactivating conditions a distance distribution at 3.65 nm up to 5.6 nm, whereas the activated BetP variant exhibits high probabilities for the distance of 2.7 nm and a distance distribution between 4.2 nm and 5.4 nm (Figure 5.25), which might be interpreted as two distances. However, the distances are outside of the reliability of the PELDOR data. Interestingly, upon activation of this BetP variant,

again a short distance could be detected, which might correspond to the inward open conformation when comparing the trend of Cα – Cα distances (Table 5.4). According to this, the transporter is suggested to undergo the transition from outward open to the inward open conformation as seen for BetP C252T/G450C/L515C. The longer distance is again assumed to overlap with the longer interprotomeric distances. In contrast to C252T/G450C/L515C, there is no significant difference between the different states in the rotamer-predicted distance distribution for C252T/G450C/S516C visible. Calculations for this mutant excluded ghost contributions due to multi-spin effects (Section 7.8.5) and therefore the observed distance changes can be assumed as significant. As expected, for the non-activatable mutant C252T/G450C/T467A/S468A/S516C, no significant change in the main peak population upon activation was demonstrated (Figure 5.27). From the three labeling pairs in total at the periplasmic side of BetP, two showed the appearance of a shorter distance in the presence of K^+ and the substrates Na^+/betaine. Interestingly, BetP C252T/G450C/A514C, which is adjacent to residue L515C, was characterized by an opposite movement. This unexpected result leaded to a revision of this specific position in diverse BetP structures. It was found, that A514 is located at a very flexible loop between TM11 and TM12. Moreover, this residue is even not resolved in all structures due its flexibility (personal communication Dr. Caroline Koshy). Thus, the deviating result for C252T/G450C/A514C was attributed to the high flexibility at this position, which was considered in further discussions. As for the cytoplasmic side, the simulated distance distributions were similar for the inward open crystal structures but differed between the outward open conformations. Although $1C_i$ (PDB 4DOJ, chain A) is in particular a substrate-bound conformation (C_iS), it is directly comparable to 2Ci (PDB 4C7R, chain A). In contrast, the differences between the outward open conformations are more pronounced than expected. Here, the calculated distance distributions are significantly affected by the rotamer number and distribution (Section 7.8.4, Table 7.4). In general, the simulated distributions were more heterogenic than the experimental distance distributions.

The combination of intra- and interprotomeric distances is exemplarily indicated in Figure 5.28 and is included in Table 5.5 for symmetric trimers in the inward and outward facing orientation. The number, the length and broad distributions of

the distances impede a precise assignment of the detected distances in the experimentally measured to the simulated interprotomeric distances, which is too complicated due to the trimeric appearance of BetP. However, the detected distances are within the realms of possibility if compared within Table 5.5. Although the existence of asymmetric trimers might be considered here, the imprecise assignment of the distances make a further discrimination difficult and was therefore not pursued further.

5.1.6 PELDOR measurements in *E. coli* polar lipid proteoliposomes

For BetP the regulatory role of specific lipids was indicated by biochemical as well as structural data (Koshy *et al.*, 2013; Rübenhagen *et al.*, 2000). Therefore, BetP was incorporated into *E. coli* polar lipid liposomes for PELDOR measurements. Reconstitution of spin labeled BetP variants allows the distance measurements by PELDOR in even more native conditions than in detergent. BetP variants were purified and spin labeled as described before. For reconstitution of selected BetP cysteine variants into *E. coli* polar liposomes with a LPR of 20:1, the protocol established by Sascha Niklisch (Nicklisch *et al.*, 2012) was used. The less harsh reconstitution method combining extraction of the detergent by Bio-Beads during dialysis increase the yield of incorporated spin labeled protein. According to the approach earlier, the distances for reconstituted BetP were measured under non- and activating conditions by PELDOR for the six-spin system. At inactivating conditions, no difference between the internal and external Na^+ concentration of the proteoliposomes was present. In contrast, at activating conditions BetP variants reconstituted into liposomes were activated by internal K^+, whereas the substrates betaine and Na^+ were provided from the outside. Additionally, valinomycin was added to the samples to facilitate a membrane potential.
PELDOR measurements were performed for the cytoplasmic BetP variants S140C/C252T/N488C, S140C/C252T/K489C and S140C/C252T/W490C as well as for the periplasmic six-spin systems BetP C252T/G450C/L515C and C252T/G450C/S516C reconstituted into liposomes. Additionally, also the data of the betaine transport impaired mutants S140C/C252T/T467A/S468A/K489C and BetP C252T/G450C/T467A/S468A/S516C is presented.

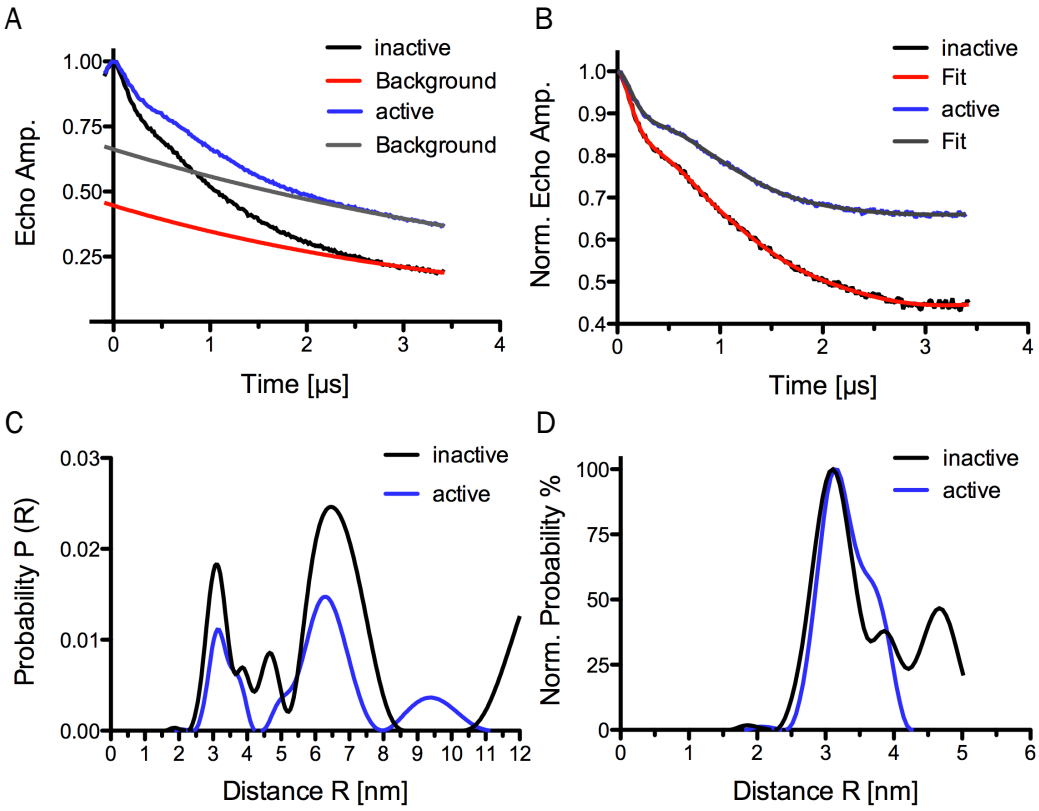

Figure 5.29: PELDOR measurements of BetP S140C/C252T/N488C reconstituted into *E. coli* lipid liposomes as six-spin system at the cytoplasmic side.

Experimental PELDOR time traces were recorded for BetP S140C/C252T/N488C reconstituted into *E. coli* polar lipid liposomes and labeled with MMTSL at inactive (black) and active conditions (blue) at Q-band. Corresponding PELDOR time traces for BetP S140C/C252T/N488C are displayed as function of time in µs. The echo amplitude (A) and background-corrected normalized echo amplitude (B) are shown with the respective background as well as the fit to the data in red for the inactive and in gray for the active condition, respectively. C) The distance distribution was obtained by Tikhonov regularization (DeerAnalysis2013). D) For a better comparison, the first half of the resulting distance distribution was normalized.

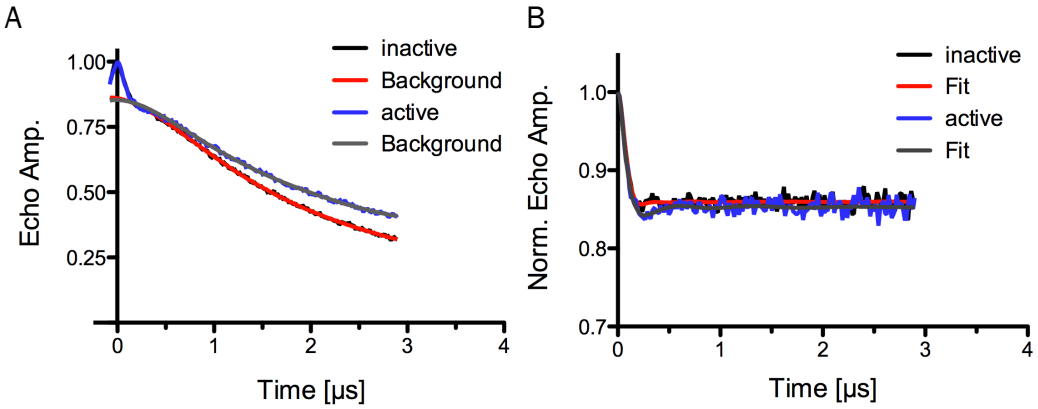

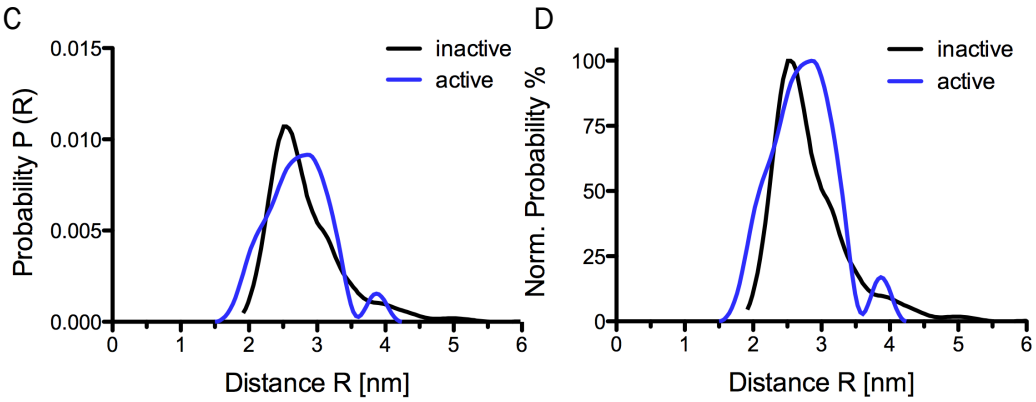

Figure 5.30: PELDOR measurements of BetP S140C/C252T/K489C reconstituted into *E. coli* lipid liposomes as six-spin system at the cytoplasmic side.

Experimental PELDOR time traces were recorded for BetP S140C/C252T/K489C reconstituted into *E. coli* polar lipid liposomes and labeled with MTSL at inactive (black) and active conditions (blue) at Q-band. Corresponding PELDOR time traces for BetP S140C/C252T/K489C are displayed as function of time in µs. The echo amplitude (A) and background-corrected normalized echo amplitude (B) are shown with the respective background as well as the fit to the data in red for the inactive and in gray for the active condition, respectively. C) The distance distribution was obtained by Tikhonov regularization (DeerAnalysis2013). D) For a better comparison, the resulting distance distribution was normalized.

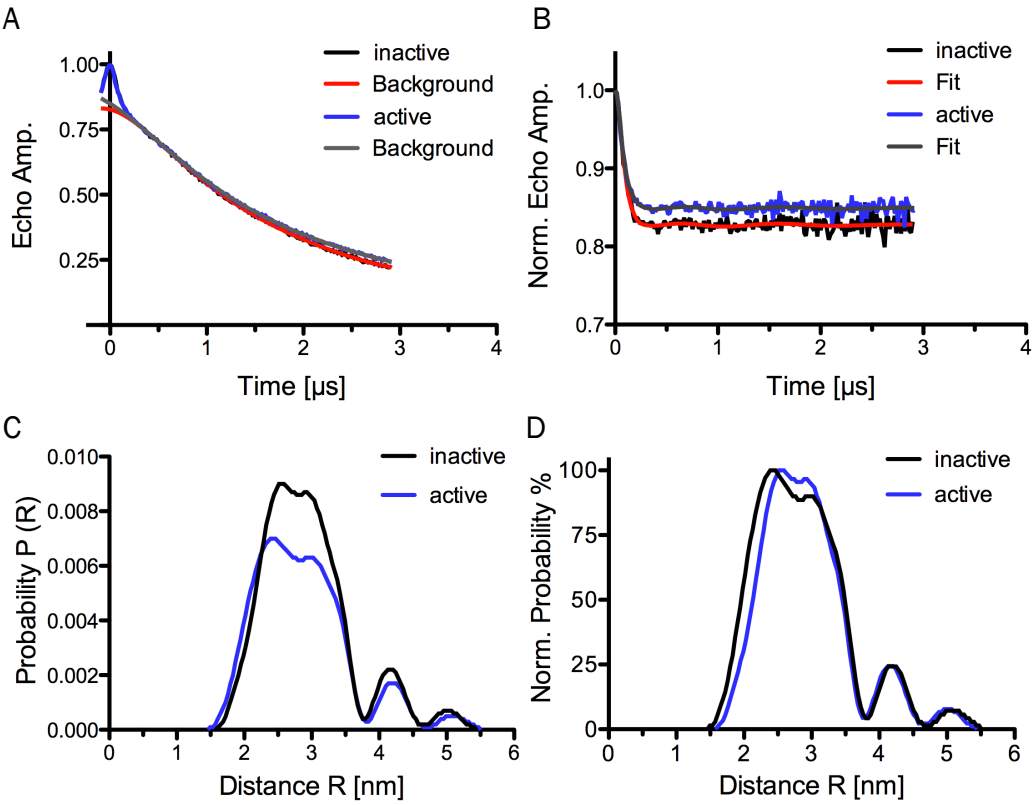

Figure 5.31: PELDOR measurements of BetP S140C/C252T/T467A/S468A/K489C reconstituted into *E. coli* lipid liposomes as six-spin system at the cytoplasmic side.

Experimental PELDOR time traces were recorded for BetP S140C/C252T/T467A/S468A/K489C reconstituted into *E. coli* polar lipid liposomes and labeled with MMTSL at inactive (black) and active conditions (blue) at Q-band. Corresponding PELDOR time traces for BetP S140C/C252T/T467A/S468A/K489C are displayed as function of time in µs. The echo amplitude (A) and background-corrected normalized echo amplitude (B) are shown with the respective background as well as the fit to the data in red for the inactive and in gray for the active condition, respectively. C) The distance distribution was obtained by Tikhonov regularization (DeerAnalysis2013). D) For a better comparison, the resulting distance distribution was normalized.

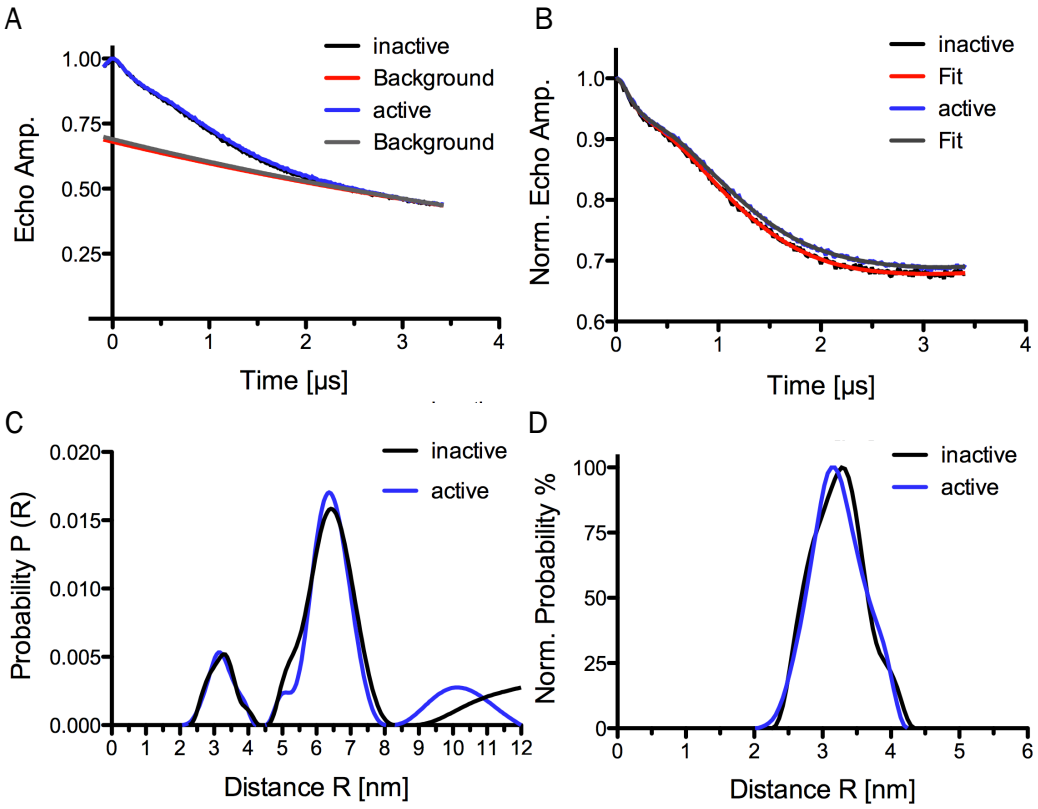

Figure 5.32: PELDOR measurements of BetP S140C/C252T/W490C reconstituted into *E. coli* lipid liposomes as six-spin system at the cytoplasmic side.

Experimental PELDOR time traces were recorded for BetP S140C/C252T/W490C reconstituted into *E. coli* polar lipid liposomes and labeled with MMTSL at inactive (black) and active conditions (blue) at Q-band. Corresponding PELDOR time traces for BetP S140C/C252T/W490C are displayed as function of time in µs. The echo amplitude (A) and background-corrected normalized echo amplitude (B) are shown with the respective background as well as the fit to the data in red for the inactive and in gray for the active condition, respectively. C) The distance distribution was obtained by Tikhonov regularization (DeerAnalysis2013). D) For a better comparison, the first half of the resulting distance distribution was normalized.

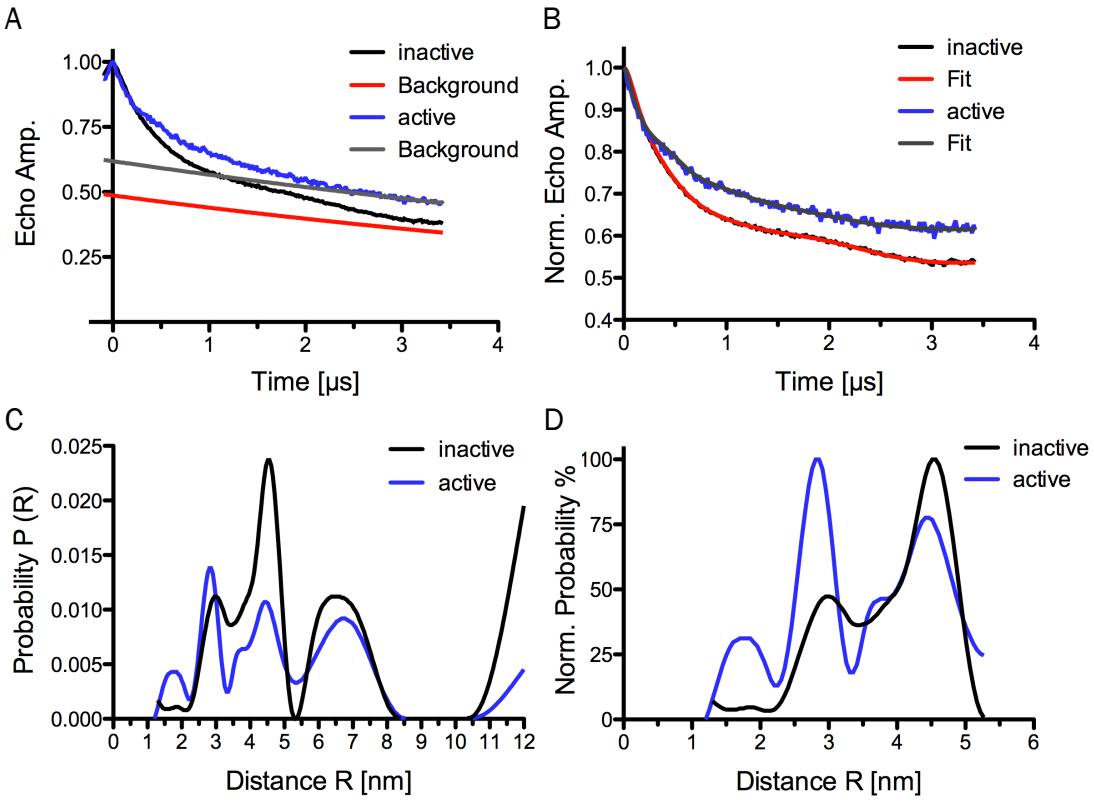

Figure 5.33: PELDOR measurements of BetP C252T/G450C/L515C reconstituted into *E. coli* lipid liposomes as six-spin system at the periplasmic side.

Experimental PELDOR time traces were recorded for BetP C252T/G450C/L515C reconstituted into *E. coli* polar lipid liposomes and labeled with MMTSL at inactive (black) and active conditions (blue) at Q-band. Corresponding PELDOR time traces for BetP C252T/G450C/L515C are displayed as function of time in µs. The echo amplitude (A) and background-corrected normalized echo amplitude (B) are shown with the respective background as well as the fit to the data in red for the inactive and in gray for the active condition, respectively. C) The distance distribution was obtained by Tikhonov regularization (DeerAnalysis2013). D) For a better comparison, the first half of the resulting distance distribution was normalized.

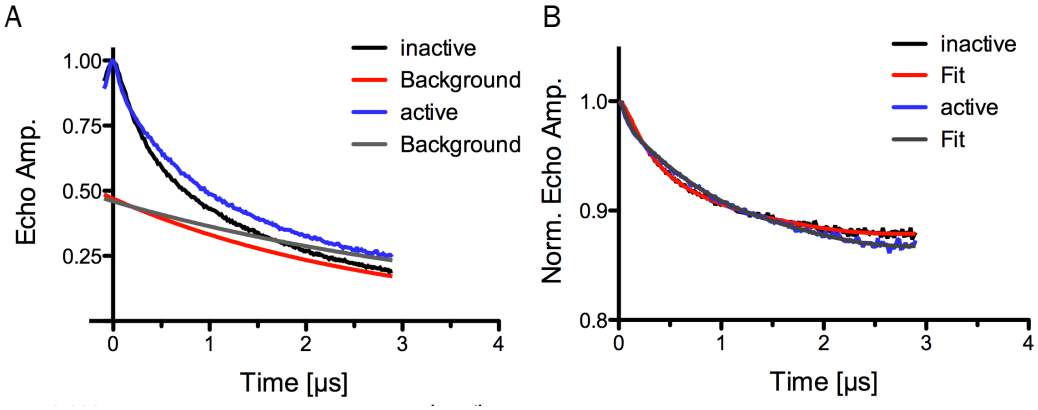

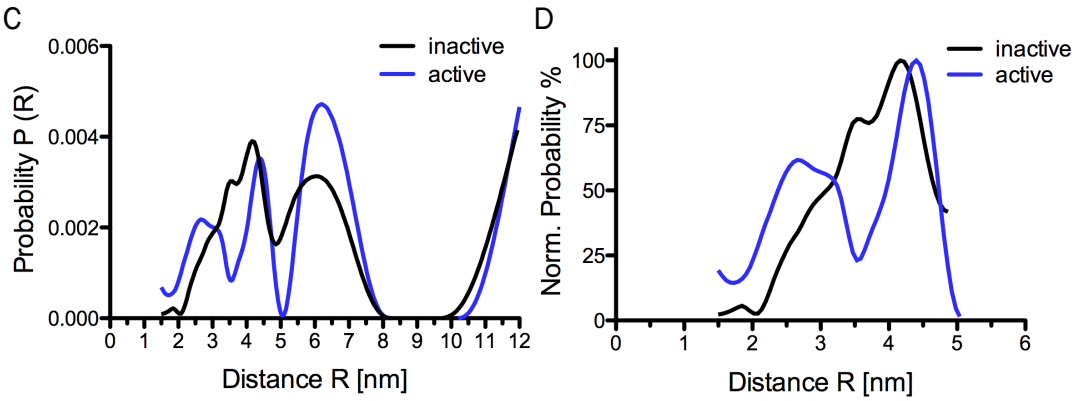

Figure 5.34: PELDOR measurements of BetP C252T/G450C/S516C reconstituted into *E. coli* lipid liposomes as six-spin system at the periplasmic side.

Experimental PELDOR time traces were recorded for BetP C252T/G450C/S516C reconstituted into *E. coli* polar lipid liposomes and labeled with MTSL at inactive (black) and active conditions (blue) at Q-band. Corresponding PELDOR time traces for BetP C252T/G450C/S516C are displayed as function of time in µs. The echo amplitude (A) and background-corrected normalized echo amplitude (B) are shown with the respective background as well as the fit to the data in red for the inactive and in gray for the active condition, respectively. C) The distance distribution was obtained by Tikhonov regularization (DeerAnalysis2013). D) For a better comparison, the first half of the resulting distance distribution was normalized.

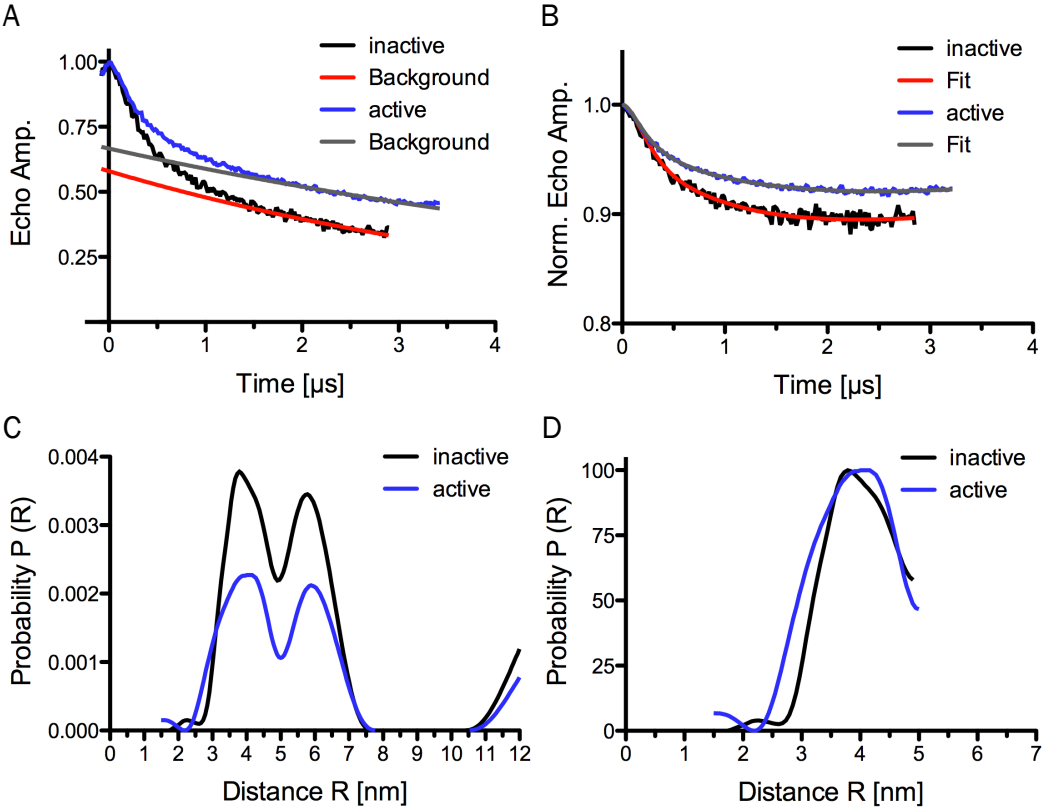

Figure 5.35: PELDOR measurements of BetP C252T/G450C/T467A/S468A/S516C reconstituted into *E. coli* lipid liposomes as six-spin system at the periplasmic side.

Experimental PELDOR time traces were recorded for BetP C252T/G450C/T467A/S468A/S516C reconstituted into *E. coli* polar lipid liposomes and labeled with MTSL at inactive (black) and active conditions (blue) at Q-band. Corresponding PELDOR time traces for BetP C252T/G450C/T467A/S468A/S516C are displayed as function of time in µs. The echo amplitude (A) and background-corrected normalized echo amplitude (B) are shown with the respective background as well as the fit to the data in red for the inactive and in gray for the active condition, respectively. C) The distance distribution was obtained by Tikhonov regularization (DeerAnalysis2013). D) For a better comparison, the first half of the resulting distance distribution was normalized.

PELDOR time traces were recorded for the reconstituted six-spin systems in time windows of approximately 3 to maximal 3.5 µs. The intraprotomeric distances were only partly separated from longer interprotomeric distances. Thus, main distance peaks can be observed between 2 – 9 nm. Because the study is focusing on the shorter intraprotomeric distances (< 5 nm), the probability was normalized for the first part of the distance distribution.

For the reconstituted cytoplasmic six-spin system BetP S140C/C252T/N488C under inactive as well as active conditions a main peak at 3.2 nm was detected (Figure 5.29). Whereas upon activation only a shoulder at 3.7 nm appears, additional distance distributions above 3.5 nm, which are not considered as significant, are visible in the inactive condition. A direct comparison to the data obtained for this mutant in detergent showed that the main population can be found already at 2.8 nm instead of 3.2 nm (Figure 5.13). In contrast to the detergent sample, in the case of BetP S140C/C252T/K489C, in proteoliposomes a broad distance distributions in both conditions can be observed. Thereby, the non-activated condition is characterized by a main peak at 2.6 nm instead 2.3 nm identified in detergent. Upon addition of betaine and K^+ to the proteoliposome system, the main distance shifts to 2.9 nm, which is comparable to the population at 3 nm in Figure 5.15 and was suggested to correspond to the inward open conformation of the transporter. The broad distance distribution in both conditions might indicate a heterogenic composition of conformational states. The betaine transport deficient mutant BetP S140C/C252T/T467A/S468A/K489C shows no distance change upon activation (Figure 5.31). Moreover, also a broad distance distribution from 2 to 3.5 nm was detected, which is directly comparable to the range where the inactive and active state of BetP S140C/C252T/K489C have been found (Figure 5.30). As in detergent, for

reconstituted BetP S140C/C252T/W490C no significant alteration were observed between the two different conditions (Figure 5.32). The main peaks can be found for the respective mutant at 3.3 nm.

At the periplasmic side, for BetP C252T/G450C/L515C instead of a broad distribution with a main peak at 4.2 nm in detergent (Figure 5.23), the distance distribution seperates into two populations of 3 and 4.6 nm for the proteoliposome system under non-activating conditions (Figure 5.33). Upon activation a low probability peak can be found below 2 nm, which is most probably the result of the detection of hyperfine modulation artifacts from weakly coupled deuterium nuclei (personal communication Dr. Burkhard Endeward). This distance should not be further considered due to the strongly decreasing sensitivity of PELDOR below 2 nm. In addition, there is a pronounced increase in the the population of 2.9 nm, which is directly comparable to the six-spin system in detergent. This short distance was suggested to represent the fraction of the inward open transporter. At inactive conditions, the obtained distance distribution of reconstituted BetP C252T/G450C/S516C is characterized by a broad population around 4 nm. The addition of the activating factors K^+ and betaine let split the broad population into a peak at 2.7 nm and another at 4.5 nm (Figure 5.34). The short intraprotomeric distance is corresponding to the population of 2.7 nm in detergent (Figure 5.25). The appearance of a shorter distance was interpreted to demonstrate the inward open state of BetP. Like in detergent, BetP C252T/G450C/T467A/S468A/S516C in proteoliposomes displays no significant change upon activation (Figure 5.35).

In general, the obtained data for the cytoplasmic six-spin BetP systems show a more heterogenic composition with broader distances. For the cytoplasmic BetP variants a common trend of a shift to longer distances of about 0.3 – 0.4 nm was detected, which might indicate an effect by the lipid surrounding. In contrast, the distances at the periplasmic site show the identical transition from the outward facing to the inward facing state of BetP upon activation. Moreover, a shift to longer distances was not observed for the periplasmic BetP variants.

5.2 Discussion

5.2.1 Investigation of conformational asymmetry in BetP by PELDOR

One major goal of the PELDOR analysis was to address the nature of the conformational asymmetry of trimeric BetP not constrained by crystal contacts. The following three scenarios can be imagined linking activation of BetP to the conformational mix: (1) symmetric trimers due to the synchronization of the alternating access, (2) structural asymmetric trimers because of a constitutive cycling or (3) random cycling of the protomers independently through the states.

In the past, BetP was already studied in terms of a potential crosstalk in order to explain the observed conformational asymmetry. Artificial monomerization of BetP by substitution of periplasmic residues at the trimer interface identified the monomer, albeit with a reduced transport activity level, as functional unit for transport catalysis. Additionally, the monomer did not show transport regulation (Perez *et al*., 2011a). Consequently, the trimeric architecture was suggested as prerequisite for regulation.

A functional crosstalk within BetP was deduced from the observed interaction between the elongated C-terminal domain and mainly the cytoplasmic loop 2 of the adjacent protomer in the crystal structure (Ressl *et al*., 2009). A comparable interaction leading to an allosteric regulation by adjacent protomers was also found in the trimeric Amt-1 transporter (Loque *et al.*, 2007; Loque *et al.*, 2006). Consequently, a functional significance was assumed for the interprotomeric interaction. In particular, the observed conformational asymmetry in 2D and 3D crystals pointed towards the presence of a conformational crosstalk. In this context, the asymmetry strongly suggests a conformational coupling between the protomers within a trimer, which might facilitate the conversion of the individual protomers from out- to the inward facing state by reducing the rate-limiting steps (Tsai *et al*., 2011). Beside symmetric trimers, conformational asymmetric trimers were reported only in crystal structures and therefore the influence by crystal contacts could not be ruled out. Notably, in all asymmetric structures of 3D crystals, protomer C is forced into the inward facing state by crystal contacts at the periplasmic side with the C-terminal domain of protomer A of the symmetry related trimer. But because crystal contacts differ significantly in 2D and 3D crystal structures, the appearance of the asymmetry might be not just artificial

and raises the question if either symmetric or asymmetric trimers represent the physiologically relevant state. The situation can be related to trimeric AcrB. Based on a structural asymmetry observed for AcrB, evidence for a conformational crosstalk was provided (Murakami *et al.*, 2006; Seeger *et al.*, 2006).

More recently, a heterotrimer approach excluded an interprotomeric crosstalk in regulation (Becker *et al*., 2014). Experiments revealed that a single protomer in a trimeric environment has the capacity to transport betaine as well as to respond to osmotic stress even when the adjacent protomers are inhibited in function (substitution of substrate- and Na^+-binding site) and regulation (deletion of C-terminal domain). As a result, no negative dominance from inactivated adjacent protomers occurred. Conclusively, the regulatory competence of the C-terminal domain was suggested to be only relevant for its protomer itself. However, the contribution of the N-terminal domain in a potential crosstalk was not considered and moreover these experiments were performed in proteoliposomes, in which the role of the more relevant membrane stimulus cannot be assessed (Becker *et al*., 2014). A further argument against a regulatory crosstalk of BetP is provided by 2D crystal structures of BetPΔC45. In this mutant, the important inter-protomeric interaction site provided by the C-terminal domain is not existent, however, the trimers form asymmetric trimers, too (Tsai *et al*., 2011). Despite the wealth of data, the presence of asymmetric BetP trimers in 2D and 3D crystals can still not be explained.

In contrast to the rare examples as AcrB and Amt-1 for which a conformational crosstalk was demonstrated, a crosstalk was excluded for trimeric Glt_{Ph} by comparable pulsed EPR studies (Section 1.2). Here, an identical label strategy to our study was applied for Glt_{Ph} from *Pyrococcus horikoshii* to probe structure as well as the state distribution of the subunits within the trimer (Georgieva *et al.*, 2013; Hänelt *et al.*, 2013). In contrast to BetP, the crystal structures of asymmetric Glt_{Ph} predicted for the alternating access cycle, large movements of 2 nm of the transport domain across the membrane. According to the large conformational change, PELDOR enabled the identification of the conformational ensemble for Glt_{Ph} in detergent and proteoliposomes. However, the underlying alternating access mechanism of Glt_{Ph}, the “elevator-model” (Akyuz *et al.*, 2015)

significantly differs from the transport mechanism proposed for BetP (Perez *et al.*, 2012).

For PELDOR measurements in BetP, TM3 was selected as most promising candidate. In particular, the unwound glycine stretch in the middle of TM3 is involved in the substrate coordination (Perez *et al.*, 2012; Ressl *et al.*, 2009) and moves during the alternating access mechanism. In the three-spin system, one distance between the spin labeled positions would indicate symmetric trimers, whereas several distances would indicate asymmetric trimers. However, as the movements in BetP are below 6 Å, the three-spin system was at its limit. In fact, the distance change between TM3 could not be accurately detected within the trimer. Although an overlay between an inward and outward open conformation indicated a vertical movement within the protomer of 5.3 Å of the respective residue S140 (Figure 5.36), this movement is almost not detectable within the intratrimeric distance change. Representative Cα – Cα distances for BetP S140C are listed for the different conformations in Table 5.6. In addition, the Cα – Cα distance length of approximately ~5 nm in the crystal structure between the Cα-atoms of the residues is leading to main distance peaks at 6 nm in the experimental distance distribution, the sensitivity limit for applied 4-pulse PELDOR and the relaxation properties of the sample.

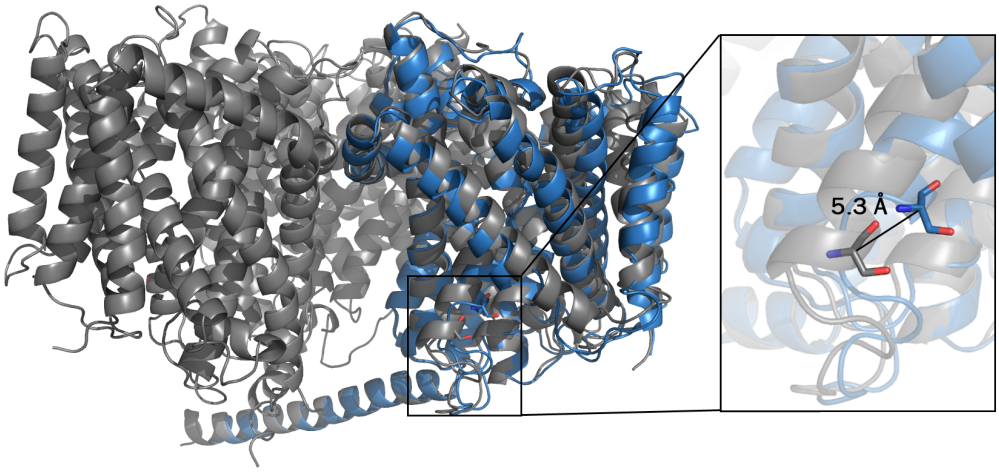

Figure 5.36: Conformational change of labeling site S140C.
Protomer A in the inward open state (PDB 4C7R, chain A, gray) is superimposed by a protomer in the outward open conformation (PDB 4DOJ, chain B, blue) within the trimer. The Cα – Cα distance of movement of the native residue S140 is depicted by a black line (Inset).

The overlay of the structure in the inward open and outward open state of BetP indicated alternative labeling sites, for which a more pronounced movement is predicted. These sites are located at the peripheral boarders of BetP, which as protomer itself has already a diameter of approximately 5 nm. In comparison to the cytoplasmic side, the periplasmic side exhibit more potential candidates, however, both sides are characterized by long intratrimeric distances. In Table 5.6, few representatives for alternative labeling sites for the cytoplasmic and periplasmic side are listed. At the periplasmic side, residue S516C might present an appropriate labeling site (Figure 5.37). The predicted movement within the quite long intratrimeric distances is 10 Å (1 nm). Although functional analysis indicated for BetP C252T/S516C the suitability for further investigations (Figure 5.6 and Figure 5.8), PELDOR measurements were not performed at that stage due to the distance limitations in the standard 4-pulse PELDOR method.

Table 5.6: Cα – Cα distances for three-spin systems of BetP

		Symmetric trimer		Asymmetric trimer
Residue	**ProΔC$_e$/C$_i$**	**3xC$_e$**	**3xC$_i$**	**C$_e$/C$_i$/C$_c$**
S140$_{cp}$	5.3 Å	5.24 nm	5.1 nm	5.2/5.26/53.8 nm
G299$_{cp}$	5.2 Å	8 nm	8.6 nm	7.45/7.74/8.5 nm
L508$_{pp}$	6.7 Å	8.97 nm	7.46 nm	7.6/8.27/8.31 nm
S516$_{pp}$	4.7 Å	6.48 nm	5.44 nm	5.58/5.98/6.25 nm

ProΔC$_e$/C$_i$: Cα – Cα distance of the conformational change of the respective residue at the cytoplasmic ($_{cp}$) or periplasmic ($_{pp}$) site within the protomer; C$_e$: outward open, PDB 4DOJ, chain B; C$_i$: inward open, PDB 4C7R, chain A; C$_c$: closed (PDB 4AIN, chain B)

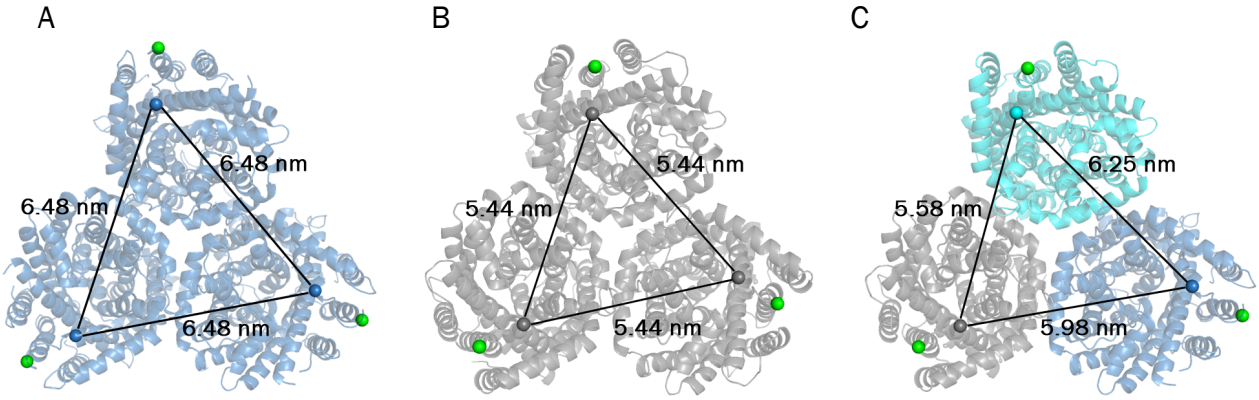

Figure 5.37: Cα – Cα distances for alternative three-spin system at the periplasmic side of BetP.

The intratrimeric Cα – Cα distances are indicated for the three-spin system BetP S516C as symmetric trimers in the outward open (A, PDB 4DOJ, chain B, blue) and inward open state (B, PDB 4C7R, chain A, gray) as well as asymmetric trimer with a protomer in the outward and inward open as well as the fully occluded (PDB 4AIN, chain B, cyan) state.

Additionally, the position of L508 is presented. The Cα-atoms of residue S516 and L508 are depicted as spheres, colored in the corresponding color of the conformation or green, respectively.

To overcome the distance limitations, the group of Prof. Dr. Thomas Prisner (Dr. Philipp Spindler, Goethe University, Frankfurt) was working on the optimization of the method. In order to increase the measurable distance, the 4-pulse sequence was changed to 7 pulses for PELDOR analysis. First attempts to study the three-spin system BetP S140C are presented in the Section 7.8.6. To obtain reliable results, also larger intratrimeric changes as for BetP C252T/S516C should be studied by 7-pulse CP PELDOR.
With the optimized method in hand, further investigations are required to elucidate the distribution of conformational states within the BetP trimer. Although longer distances might be measurable in future, it has to be considered, that there might be difficulties to differentiate between asymmetric trimers and a mixture auf symmetric trimers in different conformations. Here, the correlation between the short intraprotomeric and longer interprotomeric distances in the six-spin system of BetP might provide further insights, however, demonstrating a challenging task.

5.2.2 Investigation of alternating access in BetP by PELDOR

So far, the transport mechanism of BetP was solely predicted by static snapshots of crystal structures in different states, which were interpreted as distinct conformations of the alternating access cycle. On the basis of the three major conformations: outward open – closed – inward open – the mechanism was described as a hybrid of rigid body movements and individual flexing of symmetry-related helices (Perez *et al*., 2012) (Figure 5.38).

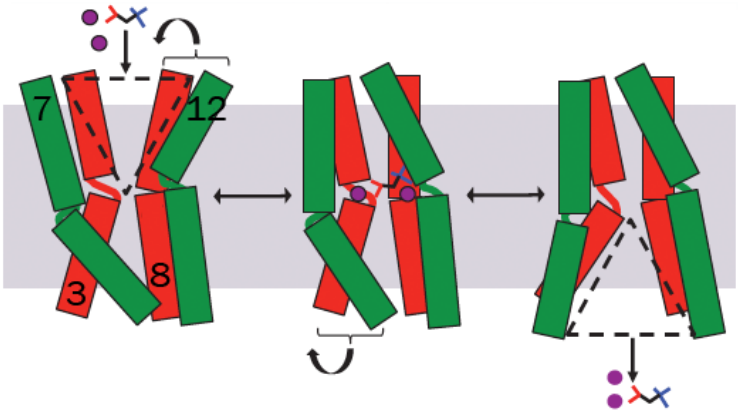

Figure 5.38: Model of the alternating access mechanism of BetP.
Sequence of opening and closure of the gating main chains of BetP underlying the alternating access mechanism. From left to right, schematic drawings of the outward open, fully occluded and inward open conformation. Arrows indicate the closing of the periplasmic gates, TM7 and TM12, after substrate and ion binding, as well as the opening of the cytoplasmic gate between TM3 and TM8. Betaine is shown in black, blue and red, sodium ions in purple (adapted from Perez *et al*., 2012).

Based on the crystal structures, rigid body movements of the scaffold motif (TM5/6 and TM10/11) relative to the 4-helix bundle (TM3/4 and TM8/9) were indicated. Thereby, the scaffold tilts 13° away from an axis running through the centre of BetP normal to the plane of the membrane (Perez *et al*., 2012). Additional gating-like movements were observed for TM3 and TM8 at the cytoplasmic side and TM12 at the periplasmic side of BetP.

In comparison, the conformational rearrangements in the crystal structures of BetP were less pronounced as for other LeuT-fold transporters (Krishnamurthy and Gouaux, 2012; Shimamura *et al*., 2010). It was suggested that the restricted movements are related to its exclusive specificity to betaine. However, more pronounced movements of BetP in a more native environment could not be ruled out (Perez *et al*., 2012).

In the present work, additional insights into the conformational changes of BetP were provided by PELDOR in a more native environment. At the cytoplasmic side of BetP, a conformational change by a distance shift between the first helix of the 4-helix bundle, TM3 (S140C), and TM11 (K489C) was demonstrated in detergent (Figure 5.15). In particular, to the main distance at 2.3 nm, a second 0.7 nm longer peak appeared upon activation. The comparison between inward and outward open crystal structures predicted a spring-like movement of 0.5 nm and a tilt of ~13° in TM3 being responsible for the opening of the cytoplasmic pathway

to release the substrate (Figure 5.39) (Perez *et al*., 2012). The question remains open, why for residue K489C the distance change can be observed but not for neighbouring N488C and W490C (Figure 5.13 and Figure 5.18). As a control, BetP S140C/C252T/T467A/S468A/K489C, which is transport impaired, does not show any change in distances exhibiting only a single peak. Therefore, we can be confident that the changes in S140C/K489C are functionally significant, while the adjacent positions, N488 and W490, are less suitable for labeling for PELDOR.

In summary, we conclude that upon activation, PELDOR reports a shift at the cytoplasmic side, which would correspond according to the crystal structures to the transition from outward/closed to inward open state. The absence of differences for the three-spin system S140C/C252T at both conditions support that changes at the cytoplasmic side measured by PELDOR and changes derived from the crystal structure are in the same order of magnitude (Figure 5.9). This is quite different to what was reported for LeuT. In the inward open X-ray structure of LeuT from *A. aeolicus*, the first helix in the 4-helix bundle TM1, corresponding to BetP TM3, was characterized by a pronounced displacement of 1.2 nm and a tilt of 45°(Figure 5.39) (Krishnamurthy and Gouaux, 2012). Interestingly, this huge movement could not be observed in PELDOR measurements for LeuT TM1 and TM9 (BetP TM11), which are directly comparable to the studied spin labeling sites in BetP (Figure 5.39 and Figure 5.40 A) (Kazmier *et al.*, 2014b). Although no distance change was detected for TM1 and TM9 with a single peak at 4 nm for all conditions, the broad distance distribution was assigned to the flexibility of TM1 (Figure 5.40 A). Moreover, the distance distribution between TM1 and TM9 for LeuT, which additionally was substituted with Y268A as for the crystallization mutant resulting in the inward facing conformation, revealed conformations which are not sampled in the WT background (Figure 5.40 A) (Kazmier *et al.*, 2014b).

Another example for some discrepancies between crystal structure and PELDOR distances is the conformational change in the Na^+/hydantoin transporter Mhp1 from *Microbacterium liquefaciens*. A transition between different states at the comparable site, namely TM1 (F30C) and TM9 (T338C), was demonstrated for the Mhp1 by PELDOR (Figure 5.40 B) (Kazmier *et al.*, 2014a). Here, a distance change of about 1 nm toward shorter distances was observed and interpreted as

isomerization into the outward facing state, although the hinge-like movement of TM1 was not reported in the inward open conformation of Mhp1 in the crystal structure (Figure 5.39 and Figure 5.40 B) (Kazmier *et al.*, 2014a; Shimamura *et al.*, 2010). Subsequently, the distance change might result from rearrangements of TM9, not TM1 (Figure 5.39). Particularly, the predicted Cα – Cα distances of 3.75 nm for the inward open and 3.06 nm for the outward open state ($\Delta C_i/C_e$: 0.69 nm) (Table 5.7) of Mhp1 revealed peaks within the experimental distance distribution at ~5 nm and ~4 nm (Figure 5.40 B).

Compared to that, the Cα – Cα distance of 2.25 nm and 2.76 nm for the inward open and outward open X-ray structure of BetP ($\Delta C_i/C_e$: 0.5 nm), respectively, resulted in peaks at 2.3 nm and 3 nm (Δ: 0.7 nm). The smaller change (1 nm vs. 0.7 nm) in the distance distribution is in agreement with the for BetP predicted less pronounced movements at this site.

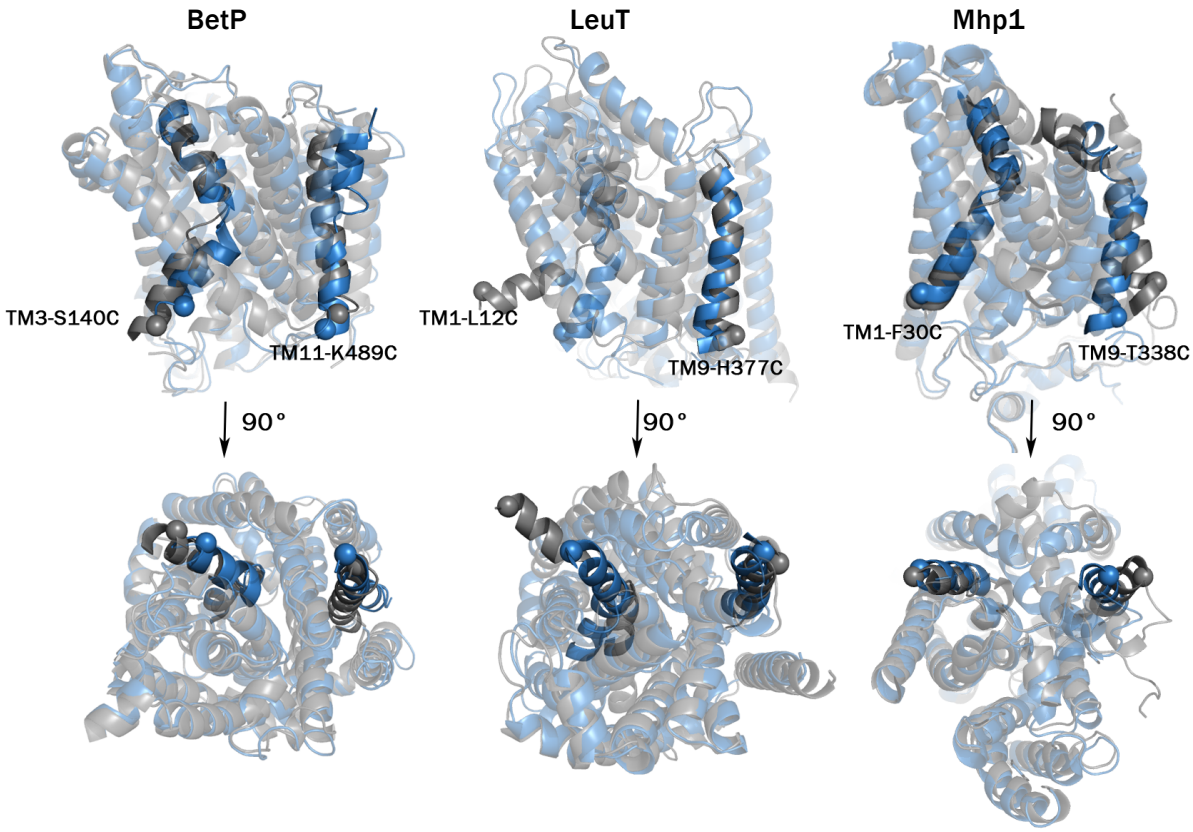

Figure 5.39: Superimposition of crystal structures in the inward open and outward open conformation of LeuT-fold transporters with cytoplasmic view.

Upper row, side views of the overlays of the outward open (blue) and inward open (gray) crystal structures are presented, from left to right, for BetP from *C. glutamicum*, LeuT from *A. aeolicus* and Mhp1 from *M. liquefaciens.* Lower row, the cytoplasmic views are displayed for the superimposed structures. Investigated labeling sites are indicated with

TM domain and with the corresponding residue. The Cα-atoms of the residues are depicted as spheres. The outward open state is represented by BetP PDB 4DOJ, chain B; LeuT PDB 3TT1 and Mhp1 PDB 2JLN, whereas the inward open conformation is illustrated by BetP PDB 4C7R, chain A; LeuT PDB 3TT3 and Mhp1 PDB 2X79.

Table 5.7: Cα – Cα distances between outward and inward open conformation for BetP, LeuT and Mhp1

	C_e	C_i
BetP TM3(S140C) – TM11(K489C)	2.25 nm	2.76 nm
LeuT TM1(L12C) – TM9(H377C)	2.85 nm	4.31 nm
Mhp1 TM1(F30C) – TM9(T388C)	3.06 nm	3.75 nm

BetP C_e: PDB 4DOJ, chain B; BetP C_i: PDB 4C7R, chain A ; LeuT C_e: PDB 3TT1; LeuT C_i: PDB 3TT3; Mhp1 C_e: PDB 2JLN, Mhp1 C_i: PDB 2X79

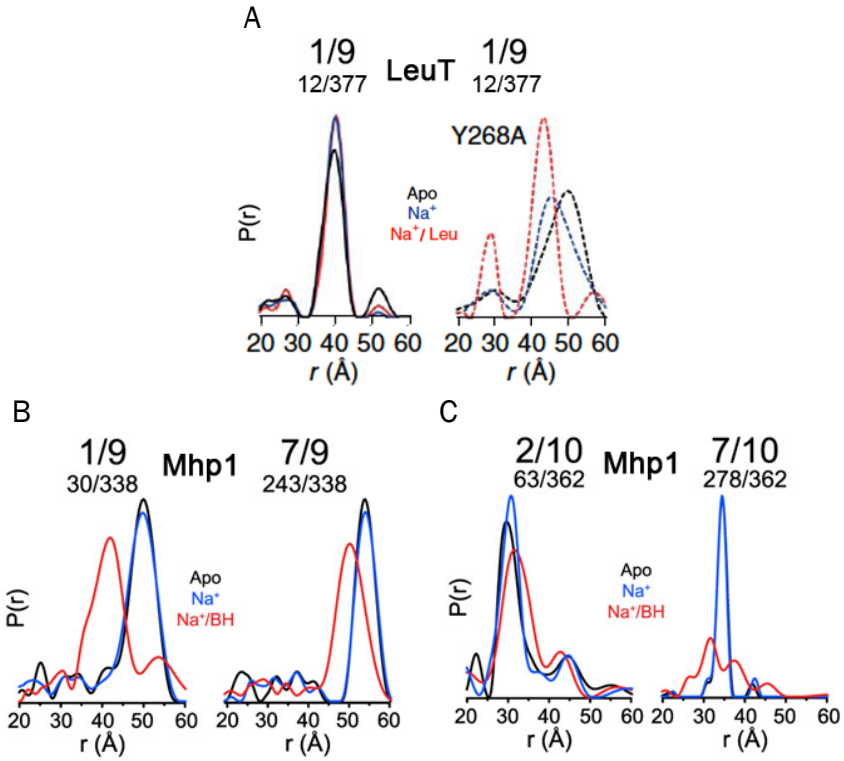

Figure 5.40: Experimental distance distribution of LeuT and Mhp1.
Distance distributions obtained by PELDOR for the cytoplasmic side for LeuT (A) and Mhp1 (B) as well as the periplasmic side for Mhp1 (C). For LeuT, the distance distribution is indicated additionally for LeuT Y268A (right). PELDOR measurements for each pair were performed in the apo (black), Na^+-bound (Na^+, blue) and Na^+- and substrate-bound (Na^+/Leu or Na^+/BH, red) conditions. As substrate either leucine (Leu) or benzyl-hydantoin (BH) was applied (adapted from Kazmier *et al.*, 2014a, Kazmier *et al.*, 2014b).

At the periplasmic side for BetP C252T/G450C/A514C, C252T/G450C/L515C and C252T/G450C/S516C, movements of TM10 relative to TM12 were monitored by PELDOR (Figure 5.20, Figure 5.23, Figure 5.25). In BetP, TM12 is

believed to undergo a gating-like movement of 5.7 Å and a tilt of 41° to the membrane normal, which is required for the opening or closure of the periplasmic pathway (Figure 5.41) (Perez *et al*., 2012). For BetP C252T/G450C/L515C and C252T/G450C/S516C upon activation, shorter distance peaks appear (Figure 5.23 and Figure 5.25). Simulations by the rotamer library for C252T/G450C/L515C indicated shorter distances for the inward open crystal structures (Figure 5.24). The longer distance corresponding to the outward open conformation might overlay with interprotomeric distances, which were not sufficiently separated from the intraprotomeric distances by background correction of the PELDOR spectra. It can be assumed, that the opening movement of TM10 and TM12 might be more pronounced than anticipated from the crystal structure. Although the same trend was observed for the distance distribution of C252T/G450C/S516C, simulations were not conclusive. Additionally, experimental distances for BetP C252T/G450C/A514C showed the opposite trend, which make interpretation at this point difficult (Figure 5.20). For LeuT, alternative EPR methods, namely spin label mobility and NiEDDA accessibility measurements, for the corresponding site in TM10 (BetP TM12) with N397C, L400C, D404C and F405C at the periplasmic side implied as well structural rearrangements, too, although no larger conformational change was observed in the X-ray structures (Figure 5.41) (Claxton *et al.*, 2010). Therefore, the result was related to the movement captured by the crystal structure of Mhp1 (Figure 5.41) (Claxton *et al.*, 2010). Interestingly, PELDOR distance measurements between TM10 (F362C) in conjunction with TM2 (V63C) or TM7 (V278C) instead of TM8 (TM10 BetP) in Mhp1 did not report respective changes (Figure 5.40 C) (Kazmier *et al*., 2014a).

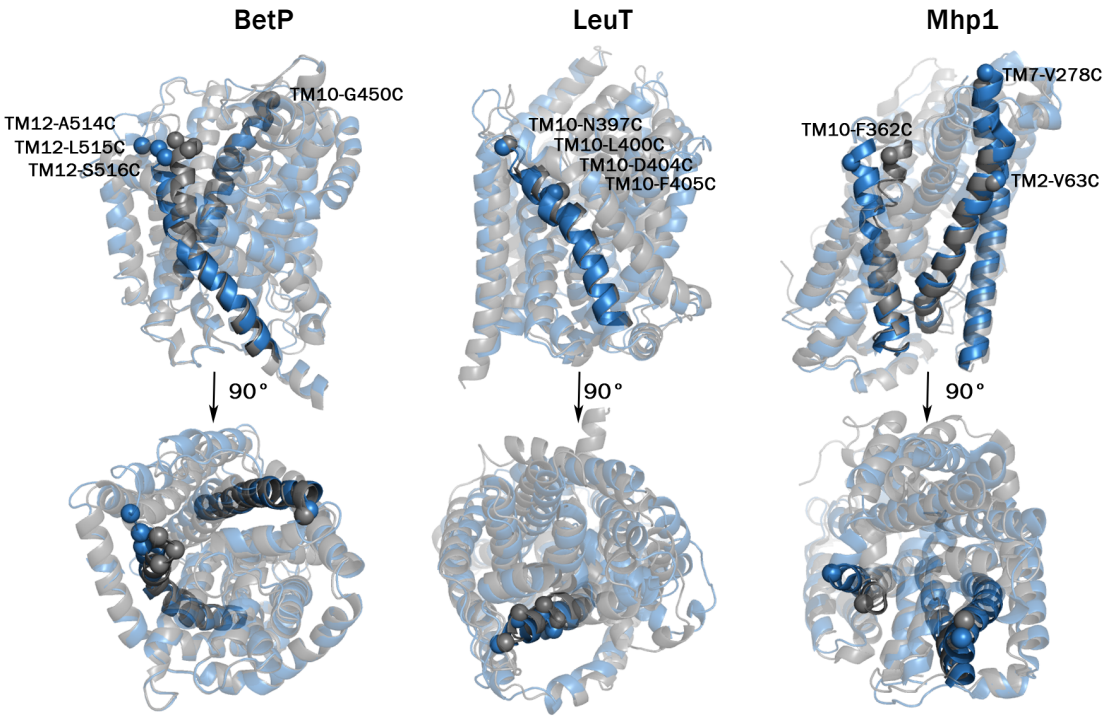

Figure 5.41: Superimposition of crystal structures in the inward open and outward open conformation of LeuT-fold transporters with periplasmic view.
Upper row, side views of the overlays of the outward open (blue) and inward open (gray) crystal structures are presented, from left to right, for BetP from *C. glutamicum*, LeuT from *A. aeolicus* and Mhp1 from *M. liquefaciens.* Lower row, the periplasmic views are displayed for the superimposed structures. Investigated labeling sites are indicated with TM domain and with the corresponding residue. The Cα-atoms of the residues are depicted as spheres. The outward open state is represented by BetP PDB 4DOJ, chain B; LeuT PDB 3TT1 and Mhp1 PDB 2JLN, whereas the inward open conformation is illustrated by BetP PDB 4C7R, chain A; LeuT PDB 3TT3 and Mhp1 PDB 2X79.

In summary, beside common features, also significant differences to the crystal structures were found for LeuT and Mhp1, respectively. The data on LeuT were interpreted in a way that already the presence of Na^+ without substrate favors the outward facing conformation, whereas for Mhp1 only binding of Na^+ together with the substrate is leading to a shift towards the outward open conformation (Kazmier *et al.*, 2014a, Kazmier *et al.*, 2014b). In contrast to BetP, which was investigated at inactive (Na^+) and active conditions (Na^+/K^+/betaine), Mhp1 and LeuT were studied in the apo condition as well as in presence of Na^+ and Na^+/substrate (Figure 5.40). Furthermore, observed multicomponent distributions imply for both transporters being in equilibrium between multiple states. This is consistent with the bimodal distance distribution obtained for the cytoplasmic BetP variant upon activation. The simulated data of BetP for the different crystal

structures do not allow at the moment a precise assignment of the obtained distance distribution to distinct conformations of BetP. The simulated distance distributions are strongly affected by the low rotamer numbers, which were predicted by the rotamer library in the software MMM2015.1 (Polyhach and Jeschke, 2010). As a result, the used outward open crystal structures (PDB 4DOJ, chain B; PDB 4LLH chain A and B) do not show similar trends in the computed distance distributions. Especially, the outward open conformation of PDB 4DOJ is not suitable for simulations by either the standard rotamer library R1A_175K or R1A_298K as well as for R1A_298K_xray due to low rotamer numbers (Table 7.4). Furthermore, it has to be kept in mind that all outward open structures were only obtained for the crystallization mutant of BetP with the additional mutation G153D in the glycine stretch. This substitution enabled the transport of choline in a Na^+- as well as H^+-coupled mechanism. However, Na^+-coupled betaine transport is still maintained, which is a strong argument for a WT like outward open conformation in this mutant.

In particular, the classification of the transition of BetP S140C/C252T/K489C is difficult. With respect to the Cα – Cα distances, the splitting of the main peak into a second longer distance peak might indicate the transition from outward to inward facing state upon activation. The observed shorter distances for BetP C252T/G450C/L515C and BetP C252T/G450C/S516C upon activation, which base on the Cα – Cα distances correspond as well to the inward open conformation (Table 5.4). In contrast, the simulation for S140C/C252T/K489C supposes the change from inward to outward open, which again is corresponding to the simulation of periplasmic site for BetP C252T/G450C/A514C. For Mhp1 and LeuT, the distance distributions were more consistent with simulations. In both cases, additional MD simulations with attached dummy nitroxide spin labels were carried out (Kazmier *et al*., 2014a; Kazmier *et al*., 2014b). Consequently, subsequent MD simulations for BetP might enable the reliable classification of the experimental distance distribution and are already on going in the group of Dr. Lucy Forrest (National Institute of Neurological Disorders and Stroke, Rockville, MD, USA). Nevertheless, the experimental distance distributions in detergent indicated conformational changes at sites, which were predicted to move based on the crystal structures of BetP. Differences to the other LeuT-fold transporters have to be considered in the light of the osmoregulatory function of BetP. Further

insights to the conformational changes were obtained by distance measurements for selected sites reconstituted into liposomes. Consistent with the data in detergent, no conformational change was observed for BetP S140C/C252T/ N488C and W490C, but a shifting broad distance distribution was identified for S140C/C252T/K489C (Figure 5.29, Figure 5.30 and Figure 5.32). Broad distances already at inactive conditions might suggest increased flexibilities between the labeling sites in TM3 and TM11 already upon reconstitution. The betaine transport deficient mutant as well shows a very broad distance distribution, which did not further alter upon activation, indicating the influence of the lipid bilayer, but not of the activating conditions (Figure 5.31). Additionally, as a common pattern, the distances revealed from proteoliposomes for cytoplasmic mutants, were characterized by longer distances compared to those obtained in detergent. This situation was not present for the experiments for the periplasmic side. The increased distances at the cytoplasmic side might be related to PG lipids, which are located in a cavity between the protomers at the trimeric interface (Koshy *et al*., 2013). Here, residue S140 of TM3 is in close proximity to this PG lipids and the residue itself or the spin label attached to the residue might interact with the lipids (Figure 5.42). Furthermore, a change in the distance between the protomers on the cytoplasmic side due to a change of the tilt angle of the protomers with respect to the membrane plane was identified for BetP in 2D crystals (Tsai *et al*., 2011). Previous PELDOR studies suggested a rotation of 15° of the individual protomers within the trimer based on the spin labeled C-terminal domain (Nicklisch *et al.*, 2012). However, it has to be noted that although the label efficiency for the proteoliposome measurements was comparable to that in detergent, due to the reconstitution procedure, less protein was present in these samples. Therefore, the observed shift at the cytoplasmic side might be at the border of the detection limit.

At the periplasmic side, for BetP C252T/G450C/L515C and S516C in proteoliposomes upon activation (Figure 5.33 and Figure 5.34), short distance peaks can be compared directly to the detergent measurements (Figure 5.23 and Figure 5.25). The distance distribution of BetP C252T/G450C/L515C exhibits at inactive conditions already a short distance peak with a lower probability, which increases twice upon activation. In the case of BetP C252T/G450C/S516C, at

inactive conditions a broad distance distribution already containing short distances can be observed.

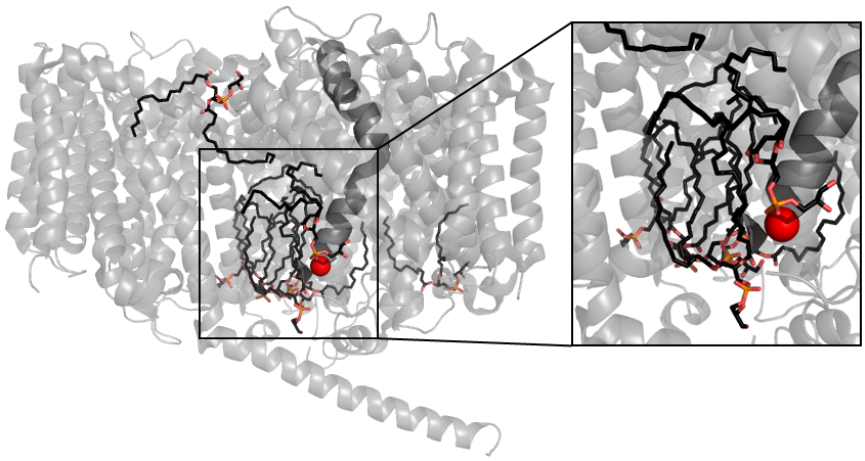

Figure 5.42: BetP crystal structure with bound PG lipids.
BetP trimer (PDB 4C7R) with bound PG lipids depicted as sticks in black. The Cα-atom of residue S140 in TM3 at the cytolasmic site is indicated as sphere.

The experimental distributions in proteoliposomes were in general broader than in detergent, however, main distance distributions showed comparable patterns upon activation. In a more recent study, the physical nature of stimuli required for BetP activation was investigated in more detail (Maximov *et al*., 2014). Beside the relevant K^+ stimulus, a second type of stimulus related to the physiological state of the membrane was identified. In particular, the second stimulus could be mimicked by the amphiphile tetracaine for BetP in cells, but not in proteoliposomes. Since the molecular activity of BetP in proteoliposomes in the presence of a sufficiently high internal K^+ concentration is similar to that of fully activated BetP in cells, it was suggested that reconstituted BetP is already in a pre-activated state. As a possible reason for this, a different conformation of BetP upon integration into proteoliposomes as compared to the insertion into the plasma membrane of the cell was considered (Maximov *et al*., 2014). In the present work, broad distance distributions as well as distances, which were detected upon activation of BetP in detergent, were already observed at inactive condition for BetP reconstituted into liposomes. Here, the data provided additional evidence that reconstituted BetP might be in a pre-activated state sampling multiple conformations.

With respect to the Cα – Cα distances of crystal structures, a preliminary model of the conformational changes of BetP can be suggested: (1) the outward open/closed conformation might be populated in presence of Na^+, (2) upon addition of the activation trigger K^+ and the substrate betaine, a conformational change to the inward facing conformation of BetP is favored. This is supported by the increase of the distance of the cytoplasmic side and the decrease of the distance at the periplasmic side. Whereas in scenario 1 the conformational rearrangment between the residues at the periplasmic side in the outward open conformation might be more pronounced than anticipated, the observed distance changes for the cytoplasmic side are in agreement with the less prounounced movement in the crystal structure. Additionally, reconstituted BetP might be in a pre-activated state already in absence of K^+, which was indicated by multiple conformations. Further validation of this model by MD simulations is required.

6 Conclusions and Perspectives

The results of this thesis provided first insights into the physiological role and regulation of pathogen-relevant choline transporters, Bet1 and BetT2 belonging to the BCCT family. Functional analysis of BetT1 identified a high affinity, but low capacity choline transporter that might function as an uniporter, adding a new mechanistic concept not only to the BCCT family but also to the LeuT-like fold transporters. On the contrary, BetT2 takes part in the bacterial osmostress response by the accumulation of choline, which is converted into the compatible solute betaine to counteract hyperosmotic stress. The ability to adapt to osmostress conditions might ensure the survival of *Acinetobacter* species on any surface. In particular, the colonization of pathogenic *Acinetobacter* on medical equipment represents a high risk factor. The determination of an atomic structure might help to identify alternative strategies to counteract this delirious pathogenic species. Heterologous expression as well as purification of BetT1 was successful. 3D crystallization trials yielded crystals diffracting to 8 Å. Further optimizations by site-directed mutagenesis and the application of alternative crystallization methods, as HiLiDe (Gourdon *et al*., 2011), have to be adopted to improve diffraction. Atomic structures will not only have a clinical impact, but also will provide further insights into the coordination of choline in the BCCT family, either in a uniport mechanism for BetT1 or proton-coupled way for BetT2. Especially, it will shed light to the unique C-terminal domain of BetT2. Although the C-terminal domain of BCCTs was already associated with osmoregulatory function, the identified ATP-binding motif of BetT2 might represent an additional regulatory component.

Our collaborators identified a coordinated interplay of choline uptake and betaine efflux depending on the osmotic condition. Choline accumulated by BetT1 at low osmotic conditions is excreted in the form of betaine. At high external osmolality, BetT2 derived choline is converted into betaine, which is in turn accumulated to counteract hyperosmotic stress. Further studies are required to identify the unknown betaine efflux system in *Acinetobacter*. Additionally, further functional analysis have to be performed to examine for a substrate:product antiport for BetT1 or the ability of BetT2 to export betaine at low osmotic conditions.

Moreover, in the framework of this thesis, the regulatory role of the N-terminal domain of BetP was investigated in detail. Our data imply a regulatory role of negatively charged clusters within the N-terminal domain. Functional analysis identified the cluster E24/E25 to be crucial for osmoregulation in the heterologous host *E. coli*, which comprises only 30 % of anionic lipids. Because increased amounts of negatively charged lipids, as it is present in *C. glutamicum*, can compensate for the lack of the N-terminal domain, lipids and the N-terminus were assumed to compete for the same interaction site in BetP. The C-terminal domain was considered as potential interaction partner, because of its orientation in the crystal structure as well as its binding affinities to membrane surfaces and N-terminal peptides (Ott *et al*., 2008). Cross-linking studies between the N- and C-terminal domains revealed a potential interaction between these domains of adjacent protomers. Based on this work, a regulation mechanism emerged in which the C-terminal domain switches between interactions with the N-terminal domain of its own protomer to the N-terminal domain of an adjacent protomer. Further studies have to be performed to characterize the potential interaction in more detail. Because only the N-terminal truncated BetP protein resulted in well diffracting crystals, alternative crystallization approaches and the recently advanced electron microscopy based structural investigations might shed light to the structure of the N-terminal domain of the BetP wild type. Secondary structure predictions suggested two α-helical segments separated by a short loop region containing a proline. This prediction might point towards an intrinsic flexible N-terminal domain.

The competitive and associative interaction between terminal domains and negatively charged lipids is not only assumed for BetP, but comparable interactions are also proposed for other osmosensing uptake systems such as ProP and OpuA (Biemans-Oldehinkel *et al.*, 2006; Mahmood *et al.*, 2006; Tsatskis *et al.*, 2005; Tsatskis *et al.*, 2008). Although these transporters and terminal domains are not structurally related, common sensing and regulatory mechanisms involving protein-protein as well as protein-lipid interactions seem to be present in these transporters. In this context, the data obtained in this work, provide new insights into stress-regulation of membrane transport processes.

In the last part of this thesis, conformational changes within the BetP trimer were probed by PELDOR in combination with site-directed spin labeling to provide further insights into the oligomeric function of BetP at inactive and active conditions. Long intratrimeric distances between positions, which were predicted to undergo less pronounced movements as expected at the beginning of the project, exceeded the detection limit of 4-pulse PELDOR. Following a modification of the spin labeling strategy, a sophisticated multi-spin system of six spin labels within a trimer was developed. Shorter intraprotomeric distances could be successfully measured between two spin labeled residues in one protomer. This six-spin system enabled us to obtain a more dynamic picture of conformational changes within the BetP protomer. Thus, the conformational dynamics in BetP, solely predicted by crystal structures before, could be verified. In comparison to the transport mechanism of other LeuT-fold transporters, namely LeuT and Mhp1, the reported conformational changes from the inward to outward open conformation of BetP based on crystal structures, were substantially less pronounced. Distance measurements by PELDOR helped in measuring the extent of conformational changes in BetP and to test whether the transporter states observed in crystal structures occur physiologically or are restrained due to crystal contacts. The results of this thesis exemplarily verified conformational rearrangements at the periplasmic and cytoplasmic side of BetP solubilized in detergent and reconstituted into liposomes. Distance changes between TM10 and TM12 can be related to the predicted gating-like movement of TM12 in the crystal structures. At the cytoplasmic side of BetP, between TM3 and TM11 smaller distance shifts as compared to Mhp1 are consistent with the hinge-like movement of only ~5 Å in the BetP crystal structure. In order to classify the obtained distance distributions to precise conformations at inactive and active conditions, MD simulations are being performed in collaboration of the group of Dr. Lucy Forrest (National Institute of Neurological Disorders and Stroke, Rockville, MD, USA). This will provide the last puzzle piece for the interpretation of the obtained data. However, the small range distance changes correspond well to the restricted conformational rearrangements observed in the crystal structures. Based on this, it can be assumed that the restricted movements are related to BetP's exclusive specificity to the osmolyte betaine. The compatible solute betaine is known to be excluded from the first hydration shell of a protein and

thereby promote the right folding of proteins. More hydrated substrate pathways due to more pronounced rearrangements might be disadvantageous for the efficient betaine transport in a micromolar affinity range of BetP. In agreement to this hypothesis, ionic networks were identified, which are restricting the flexibility by the linkage of bundle helices (Gärtner *et al.*, 2011). Although BetP shares the LeuT-fold with other transporters, it can be suggested that differences in the transport mechanism have evolved in order to adapt to the requirements of the respective transporters regarding their substrate and function.

7 Appendix

7.1 Members of the BCCT family

Table 7.1: Functionally characterized members of the BCCT family

BCCT (Ref.)	Organism	Substrate	Driving force/ Direction	Total No. (aa)	N-term No. (aa)	C-term No. (aa)	Sequence identity to BetP (%)
BetP (Peter *et al*., 1996)	*Corynebacterium glutamicum*	GB	smf/sym	595	58	50	100
OpuD (Kappes *et al*., 1996)	*Bacillus subtilis*	GB	smf/sym	512	4	24	43
BetL (Sleator *et al*., 1999)	*Listeria monocytogenes*	GB	smf/sym	507	3	20	41
BetH (Lu *et al*., 2004)	*Hallobacillus trueperi*	GB	smf/sym	505	3	18	41
BetT (Fan *et al*., 2003)	*Haemophilus influenzae*	Cho	sym	669	6*	174*	39
BetM (Vermeulen and Kunte, 2004)	*Marinococcus halophilus*	GB	smf/sym	493	3	7	38
LcoP (Steger *et al*., 2004)	*Corynebacterium glutamicum*	E/GB	smf/sym	630	43	96	37
BetT3 (Malek *et al*., 2011)	*Pseudomonas aeruginosa*	Cho	pmf/sym	661	12*	168*	37
BetT1 (Malek *et al*., 2011)	*Pseudomonas aeruginosa*	Cho	pmf/sym	516	1*	28*	36
EctT (Kuhlmann *et al*., 2011)	*Virgibacillus pantothenticus*	E/HE	smf/sym	501	7	14	36
BetT3 (Sand *et al*., 2011)	*Acinetobater baylyi*	GB	smf/sym	660	11*	164*	35
ButA (Baliarda *et al*., 2003)	*Tetragenococcus halophila*	GB	smf/sym	539	34	15	33
OpuD (Naughton *et al*., 2009)	*Vibrio cholera*	GB	smf/sym	539	34	15	33
EctM (Vermeulen and Kunte, 2004)	*Marinococcus halophilus*	E/HE	smf/sym	439	10	25	33
BetT (Laloknam *et al*., 2006)	*Aphanothece halophytica*	GB	smf/sym	564	36	38	32
BetP (Naughton *et al*., 2009)	*Vibrio parahaemolyticus*	GB	smf/sym	523	41	14	32
BetU (Ly et al., 2004)	*Escherichia coli*	GB	smf/sym	667	17	162	31
BetS (Boscari *et al*., 2002)	*Sinorhizobium meliloti*	GB/PB	smf/sym	706	52	167	31
BetT (Chen and Beattie, 2008)	*Pseudomonas syringae*	Cho/Ac	pmf/sym	667	14	160	30
BetT (Lamark *et al*., 1991)	*Escherichia coli*	Cho	pmf/sym	667	14	175	30
CudT (Rosenstein *et al*., 1999)	*Staphylococcus xylosus*	Cho	pmf/sym	540	7	36	30
BetT1 (Sand *et al*., 2014)	*Acinetobater baylyi*	Cho	uni	526	18*	23*	30

BCCT (Ref.)	Organism	Substrate	Driving force/ Direction	Total No. (aa)	N-term No. (aa)	C-term No. (aa)	Sequence identity to BetP (%)
EctP (Weinand *et al*., 2007)	*Corynebacterium glutamicum*	E/P/GB	smf/sym	615	21	102	29
BetT2 (Sand *et al*., 2014)	*Acinetobater baylyi*	Cho	pmf/sym	686	19*	177*	28
DddT (Todd *et al*., 2010)	*Psychrobacter sp.*	GB/DMSP	smf/sym	550	25	17	28
CaiT (Eichler *et al*., 1994)	*Escherichia coli*	C/γ-BB	anti	504	10	5	25
PmCaiT (Schulze *et al*., 2010)	*Proteus mirabilis*	C/γ-BB	anti	514	15	10	25

Ac: acetylcholine; C: carnitine; Cho: choline; DMPS: dimethylsulfoniopropiate; E: ectoine; γ-BB: γ-butyrobetaine; GB: glycine betaine; HE: hydroxyectoine; P: proline; PB: proline betaine; smf: sodium motive force; pmf: proton motive force; sym: symport; anti: substrate:product antiport
*lengths of the N-terminal and C-terminal domains were predicted by TMHMM (www.cbs.dtu.dk/services/TMHMM-2.0/)

7.2 Sequence alignment of BetP, OpuD, BetT, EctT, LcoP and CaiT

Amino acid sequence of the BCC transporters BetP and LcoP from *Corynebacterium glutamicum*, OpuD from *Bacillus subtilis*, EctT from *Virgibacillus pantothenticus* and *Escherichia coli* BetT were aligned using ESPript (Robert and Gouet, 2014).

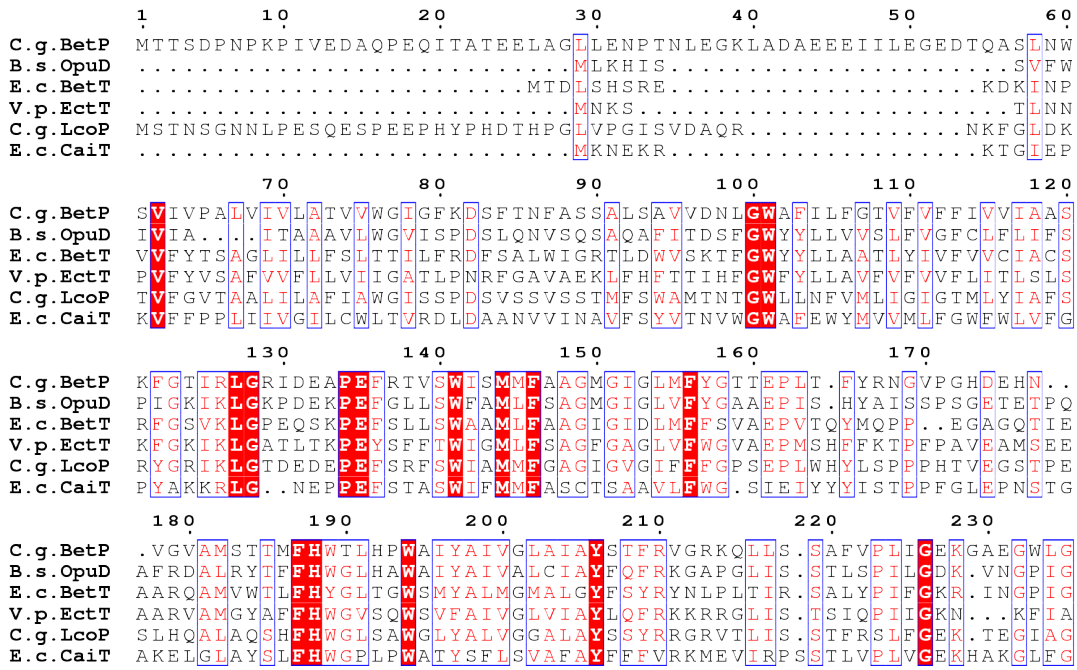

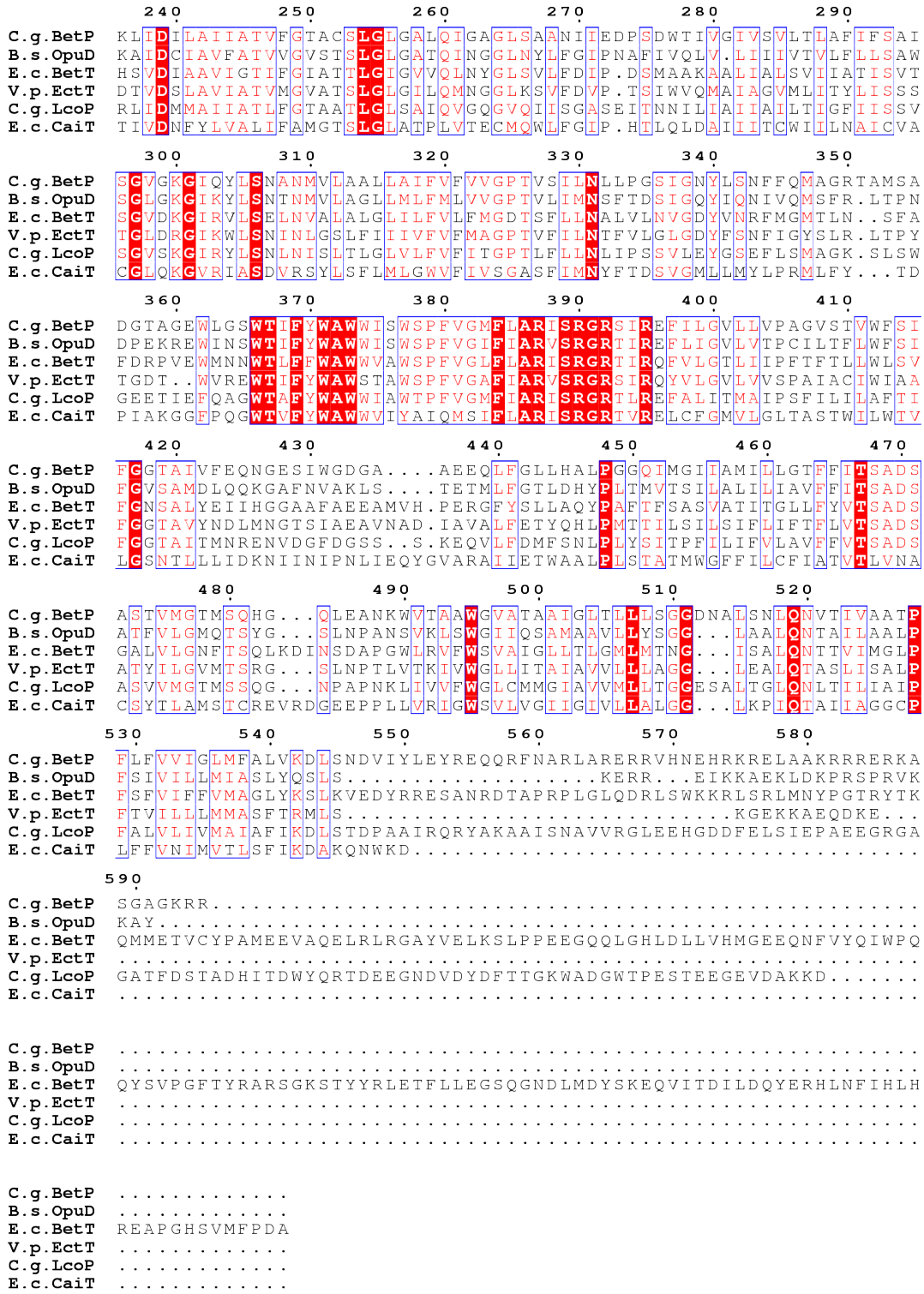

Figure 7.1: Amino acid sequence alignment of BetP, OpuD, BetT, EctT, LcoP and CaiT. The sequences of *B. subtilis* OpuD, *E. coli* BetT and CaiT and *V. pantothenticus* EctT and *C. glutamicum* LcoP were aligned against BetP from *C. glutamicum*.

7.3 Sequence alignment of BetP, BetT and A.b.BetT1 – 3

Amino acid sequence of BetP from *C. glutamicum*, BetT from *E. coli* and BetT1 – 3 from *Acinetobacter baylyi* were aligned using ESPript (Robert and Gouet, 2014).

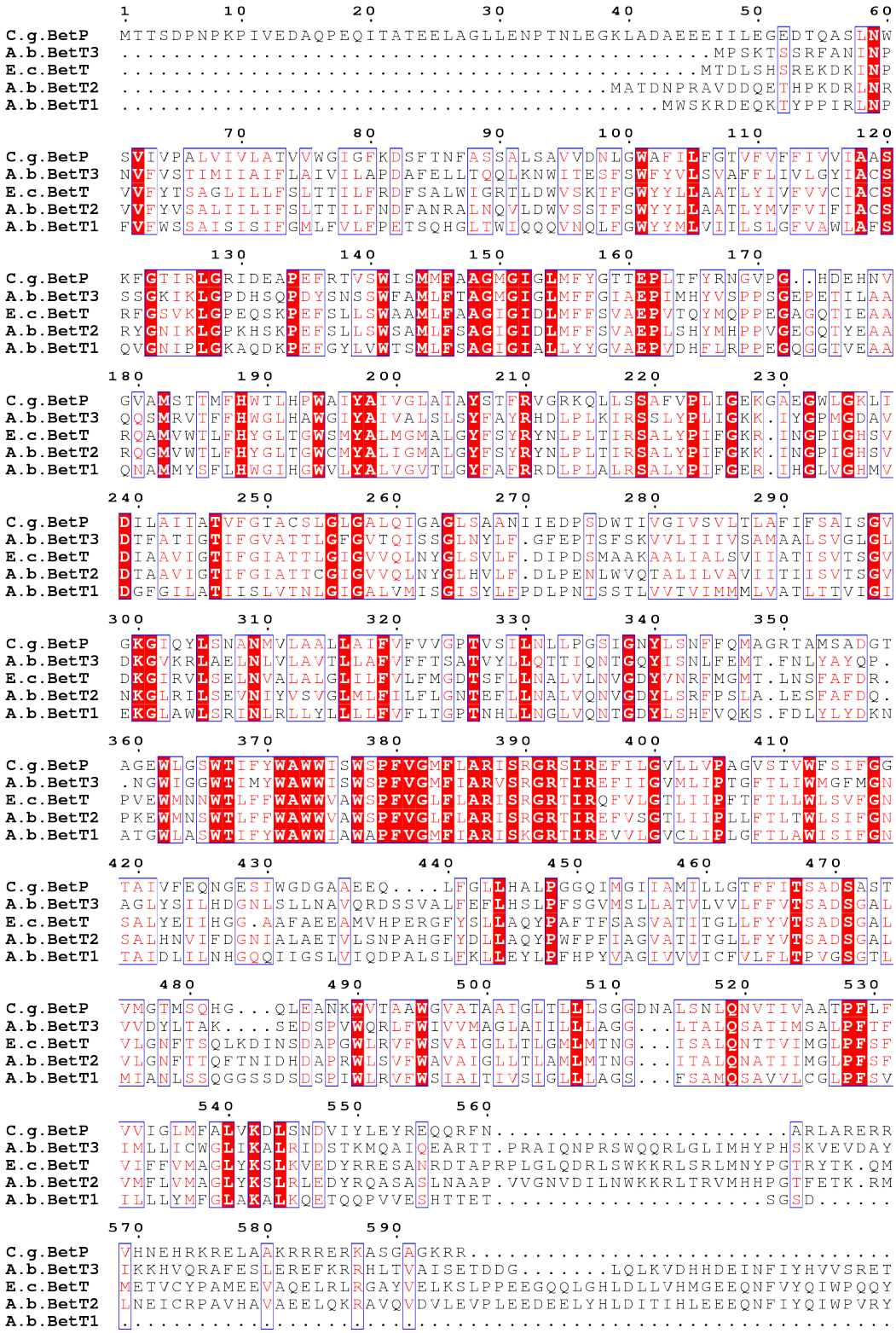

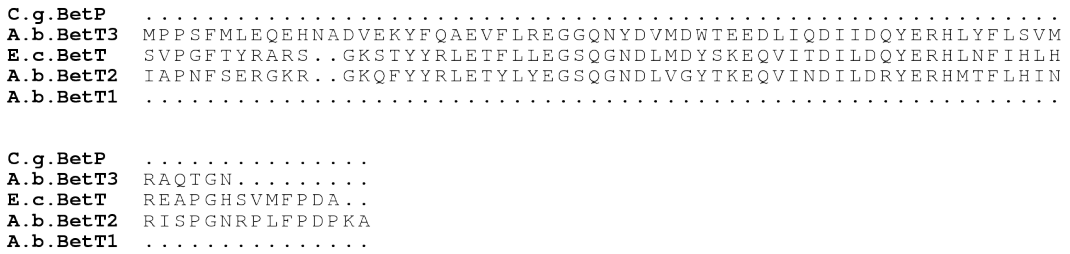

Figure 7.2: Amino acid sequence alignment of BetP, BetT3, BetT, BetT2 and BetT1.
The sequences of *A. baylyi* BetT1 – 3 and *E. coli* BetT were aligned against BetP from *C. glutamicum*.

7.4 Sequence alignment of BetP, BetT, A.b.BetT1 -3 and P.a.BetT1 – 3

Amino acid sequence of BetP from *C. glutamicum*, BetT from *E. coli*, BetT1 – 3 from *A. baylyi* and BetT1 – 3 from *Pseudomonas aeruginosa* were aligned in ESPript (Robert and Gouet, 2014).

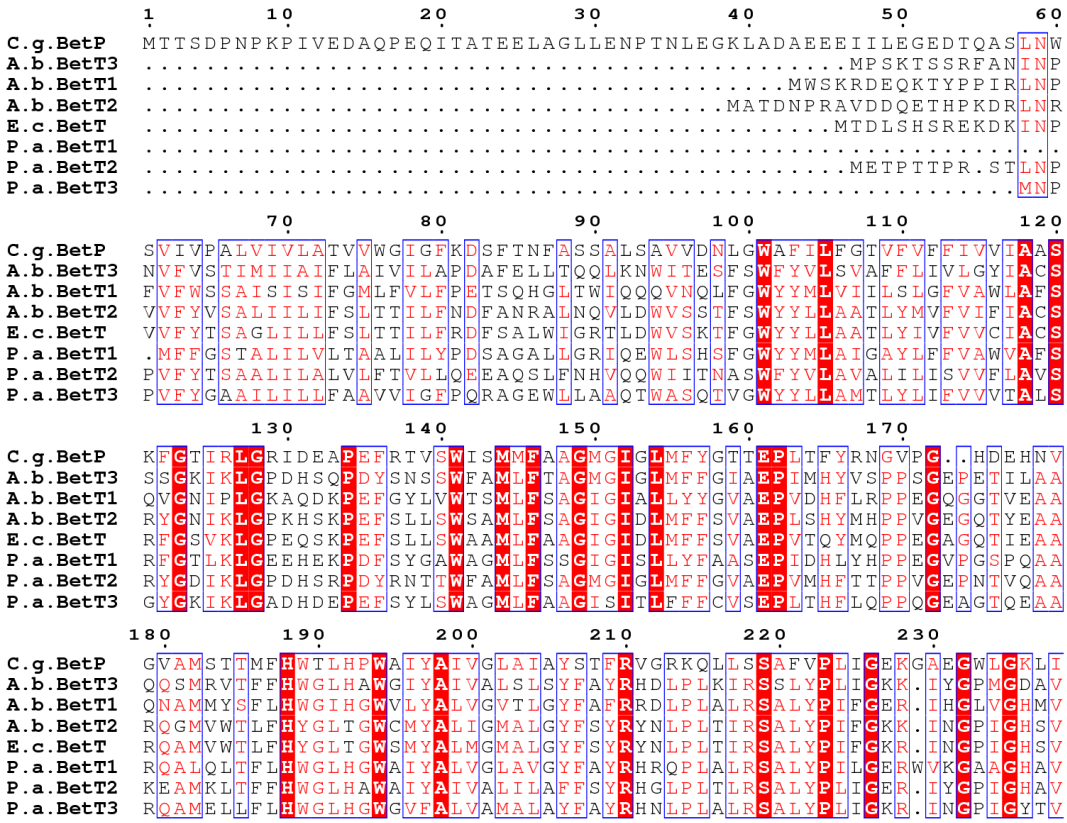

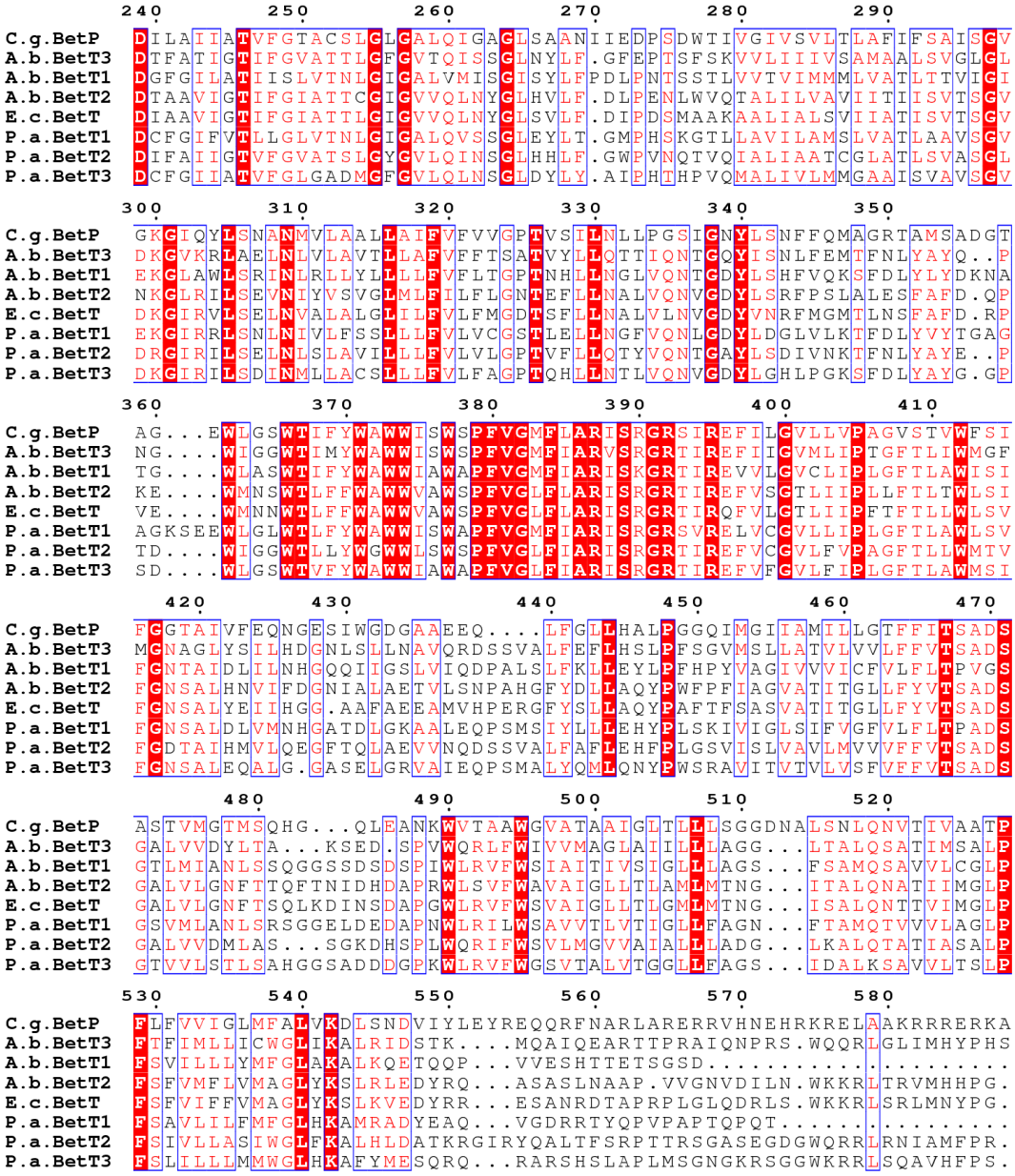

Figure 7.3: Amino acid sequence alignment of BetP, BetT, A.b.BetT1 - 3 and P.a.BetT1 - 3.

The sequences of *E. coli* BetT, *A. baylyi* BetT1 – 3 and *P. aeruginosa* BetT1 - 3 were aligned against BetP from *C. glutamicum*.

7.5 Nucleotide sequence alignment of BetT2 from *Acinetobacter baylyi*

The 2061 bp long *betT2* gene fragment was cloned into the pBAD/HisA vector using the restriction endonucleases SacI and EcoRI. The success of cloning was confirmed by sequencing with the corresponding pBAD forward and pBAD reverse

primer.

```
for             CTGCAGCTTTTTATCGCAACTCTCTACTGTTTCTCCATACCCGTTTTTTGGGCTAACAGG 60
BetT2           ------------------------------------------------------------

for             AGGAATTAACCATGGGGGGTTCTCATCATCATCATCATCATGGTATGGCTAGCATGACTG 120
BetT2           ------------------------------------------------------------

for             GTGGACAGCAAATGGGTCGGGATCTGTACGACGATGACGATAAGGATCGATGGGGATCCG 180
BetT2           ------------------------------------------------------------

                SacI
for             AGCTCTGTATGGCAACAGATAATCCAAGAGCAGTTGATGATCAAGAGACTCATCCAAAAG 240
BetT2           --------ATGGCAACAGATAATCCAAGAGCAGTTGATGATCAAGAGACTCATCCAAAAG 52
                        **************************************************

for             ATCGTTTAAATCGTGTGGTCTTTTATGTTTCTGCCCTTATTATTTTAATATTTTCACTCA 300
BetT2           ATCGTTTAAATCGTGTGGTCTTTTATGTTTCTGCCCTTATTATTTTAATATTTTCACTCA 112
                ************************************************************

for             CCACGATTTTATTTAATGATTTTGCTAATCGTGCATTAAATCAAGTACTGGATTGGGTCA 360
BetT2           CCACGATTTTATTTAATGATTTTGCTAATCGTGCATTAAATCAAGTACTGGATTGGGTCA 172
                ************************************************************

for             GCTCTACCTTTAGCTGGTACTACTTGTTGGCAGCCACCTTATATATGGTGTTTGTCATTT 420
BetT2           GCTCTACCTTTAGCTGGTACTACTTGTTGGCAGCCACCTTATATATGGTGTTTGTCATTT 232
                ************************************************************

for             TTATTGCCTGCTCTCGTTATGGCAATATCAAGCTAGGACCCAAACACTCGAAGCCTGAGT 480
BetT2           TTATTGCCTGCTCTCGTTATGGCAATATCAAGCTAGGACCCAAACACTCGAAGCCTGAGT 292
                ************************************************************

for             TTAGTCTGTTAAGCTGGTCGGCCATGCTCTTTTCGGCAGGGATCGGCATTGATTTGATGT 540
BetT2           TTAGTCTGTTAAGCTGGTCGGCCATGCTCTTTTCGGCAGGGATCGGCATTGATTTGATGT 352
                ************************************************************

for             TCTTCTCGGTGGCAGAGCCGTTATCGCATTATATGCATCCGCCAGTGGGTGAGGGACAGA 600
BetT2           TCTTCTCGGTGGCAGAGCCGTTATCGCATTATATGCATCCGCCAGTGGGTGAGGGACAGA 412
                ************************************************************

for             CTTATGAAGCTGCGCGTCAGGGCATGGTCTGGACACTATTTCACTATGGACTGACAGGCT 660
BetT2           CTTATGAAGCTGCGCGTCAGGGCATGGTCTGGACACTATTTCACTATGGACTGACAGGCT 472
                ************************************************************

for             GGTGTATGTATGCCTTGATTGGTATGGCACTGGGTTATTTTAGTTATCGTTATAATTTAC 720
BetT2           GGTGTATGTATGCCTTGATTGGTATGGCACTGGGTTATTTTAGTTATCGTTATAATTTAC 532
                ************************************************************

for             CACTCACGATCCGCTCTGCCTTGTATCCAATTTTTGGTAAGAAAATTAATGGCCCGATTG 780
BetT2           CACTCACGATCCGCTCTGCCTTGTATCCAATTTTTGGTAAGAAAATTAATGGCCCGATTG 592
                ************************************************************

for             GACATAGTGTGGATACTGCTGCCGTCATCGGAACAATTTTTGGTATTGCGACGACTTGCG 840
BetT2           GACATAGTGTGGATACTGCTGCCGTCATCGGAACAATTTTTGGTATTGCGACGACTTGCG 652
                ************************************************************
```

```
for             GTATTGGTGTCGTACAACTGAATTATGGACTACACGTTT---------------------- 879
BetT2           GTATTGGTGTCGTACAACTGAATTATGGACTACACGTTTTATTCGATTTACCTGAAAATT 712
                ************************************
                ------------------------------------------------------------
BetT2           TATGGGTTCAAACTGCCCTCATTTTGGTTGCCGTCATTATTACCATTATTTCTGTGACTT 772

                ------------------------------------------------------------
BetT2           CAGGTGTCAATAAAGGTTTACGGATTTTGTCTGAGGTTAACATTTATGTTTCTGTTGGCC 832

                ------------------------------------------------------------
BetT2           TGATGCTGTTTATTTTATTTTTGGGCAATACCGAGTTTTTACTCAATGCACTTGTTCAAA 892

                ------------------------------------------------------------
BetT2           ACGTGGGAGATTATCTAAGCCGTTTTCCAAGTCTGGCGCTAGAAAGTTTTGCTTTTGATC 952

                ------------------------------------------------------------
BetT2           AACCGAAAGAATGGATGAATAGTTGGACGCTGTTTTTCTGGGCATGGTGGGTGGCGTGGT 1012

                ------------------------------------------------------------
BetT2           CTCCATTTGTGGGGCTGTTTCTTGCACGTATTTCACGTGGACGTACCATTCGTGAGTTTG 1072

rev             ---------------------------------------CCTGGCTCTCCATTTTTGGAA 21
BetT2           TATCTGGGACCTTGATTATTCCGTTGCTGTTTACCTTAACCTGGCTCTCCATTTTTGGAA 1132
                                                      **********************
rev             ATAGTGCGCTACACAATGTCATCTTTGATGGCAATATTGCACTTGCTGAAACAGTCCTTT 81
BetT2           ATAGTGCGCTACACAATGTCATCTTTGATGGCAATATTGCACTTGCTGAAACAGTCCTTT 1192
                ************************************************************
rev             CCAATCCTGCACATGGTTTTTACGATTTACTGGCACAATACCCATGGTTTCCATTTATTG 141
BetT2           CCAATCCTGCACATGGTTTTTACGATTTACTGGCACAATACCCATGGTTTCCATTTATTG 1252
                ************************************************************
rev             CGGGCGTGGCAACCATTACAGGATTACTGTTTTATGTGACTTCGGCAGATTCTGGTGCAT 201
BetT2           CGGGCGTGGCAACCATTACAGGATTACTGTTTTATGTGACTTCGGCAGATTCTGGTGCAT 1312
                ************************************************************
rev             TGGTTCTGGGTAACTTCACCACACAATTTACCAATATTGATCACGATGCGCCGCGCTGGC 261
BetT2           TGGTTCTGGGTAACTTCACCACACAATTTACCAATATTGATCACGATGCGCCGCGCTGGC 1372
                ************************************************************
rev             TGAGTGTGTTTTGGGCAGTGGCGATTGGTTTATTGACCTTGGCTATGCTGATGACCAATG 321
BetT2           TGAGTGTGTTTTGGGCAGTGGCGATTGGTTTATTGACCTTGGCTATGCTGATGACCAATG 1432
                ************************************************************
rev             GAATTACTGCACTGCAAAATGCCACCATCATCATGGGGTTACCGTTTAGTTTCGTGATGT 381
BetT2           GAATTACTGCACTGCAAAATGCCACCATCATCATGGGGTTACCGTTTAGTTTCGTGATGT 1492
                ************************************************************
rev             TTCTGGTGATGGCAGGTCTGTATAAATCCTTGCGGCTTGAAGATTATCGACAGGCCAGCG 441
BetT2           TTCTGGTGATGGCAGGTCTGTATAAATCCTTGCGGCTTGAAGATTATCGACAGGCCAGCG 1552
                ************************************************************
rev             CCAGTTTAAATGCTGCTCCAGTAGTGGGTAATGTCGATATTCTGAACTGGAAAAAGCGCT 501
BetT2           CCAGTTTAAATGCTGCTCCAGTAGTGGGTAATGTCGATATTCTGAACTGGAAAAAGCGCT 1612
```

```
                ************************************************************
rev             TAACGCGTGTGATGCATCATCCTGGAACGTTTGAAACCAAACGCATGCTCAATGAAATCT 561
BetT2           TAACGCGTGTGATGCATCATCCTGGAACGTTTGAAACCAAACGCATGCTCAATGAAATCT 1672
                ************************************************************
rev             GTCGTCCCGCTGTACATGCAGTTGCAGAGGAGTTACAAAAACGCGCGGTACAAGTGGATG 621
BetT2           GTCGTCCCGCTGTACATGCAGTTGCAGAGGAGTTACAAAAACGCGCGGTACAAGTGGATG 1732
                ************************************************************
rev             TACTTGAAGTGCCACTTGAAGAAGATGAAGAACTTTACCATTTGGATATTACGATCCATT 681
BetT2           TACTTGAAGTGCCACTTGAAGAAGATGAAGAACTTTACCATTTGGATATTACGATCCATT 1792
                ************************************************************
rev             TGGAAGAAGAGCAAAACTTTATCTATCAGATCTGGCCTGTCCGTTATATTGCACCCAATT 741
BetT2           TGGAAGAAGAGCAAAACTTTATCTATCAGATCTGGCCTGTCCGTTATATTGCACCCAATT 1852
                ************************************************************
rev             TTAGTGAGCGAGGCAAGCGAGGCAAGCAGTTTTACTATCGTCTGGAAACCTATCTTTATG 801
BetT2           TTAGTGAGCGAGGCAAGCGAGGCAAGCAGTTTTACTATCGTCTGGAAACCTATCTTTATG 1912
                ************************************************************
rev             AAGGTTCGCAAGGCAATGACCTTGTGGGTTATACCAAAGAGCAGGTGATCAACGATATTT 861
BetT2           AAGGTTCGCAAGGCAATGACCTTGTGGGTTATACCAAAGAGCAGGTGATCAACGATATTT 1972
                ************************************************************
rev             TAGATCGCTATGAACGCCACATGACCTTCTTACATATTAATCGTATTAGTCCGGGTAATC 921
BetT2           TAGATCGCTATGAACGCCACATGACCTTCTTACATATTAATCGTATTAGTCCGGGTAATC 2032
                ************************************************************
                                          EcoRI
rev             GCCCGCTATTTCCAGATCCTAAAGCCTAGGGAATTCGAAGCTTGGCTG 969
BetT2           GCCCGCTATTTCCAGATCCTAAAGCCTAG------------------- 2061
                ****************************
```

Figure 7.4: Sequencing result of the *betT2* gene cloned into pBAD/HisA vector.
The *betT2* gene sequence (blue letters) was aligned against the results after sequencing for the forward (for) and reverse (rev) pBAD primers. Within the sequence of the forward primer can be found the -10 promoter region and ribosome-binding site, which are highlighted in gray and green, respectively. The translations initiation codon of the pBAD/HisA vector is highlighted in pink, whereas the N-terminal polyhistidine region is shown in yellow. The recognition sites for the endonucleases are colored red and labeled with the corresponding name of the endonuclease. The sequence identity between the primer and gen sequence is depicted by stars.

7.6 Crystallization screens

Table 7.2: 96-well crystallization screen "DDM" for *A. baylyi* BetT1

	A	B	C	D	E	F
1	0.1 M $(NH_4)_2SO_4$ 0.1 M HEPES pH 7.5 9 % PEG 4000 22 % Glycerol	0.1 M M $MgCl_2$ 0.1 M Tris pH 7.5 19.5 % PEG 400	0.1 M NaCl 0.04 M Tris pH 8 24.5 % PEG 350	0.02 M bis Tris pH 7 12.5 % PEG 2000	0.05 M $Mg(CH_3COO)_2$ 0.05 M CH_3COONa pH 5.4 21.5 % PEG 400	0.1 M NaCl 0.05 M Glycine pH 9.5 30.5 % PEG 300
2	0.1 M $(NH_4)_2SO_4$ 0.1 M HEPES pH 7.5 10 % PEG 4000 22 % Glycerol	0.1 M $MgCl_2$ 0.1 M Tris pH 7.5 20 % PEG 400	0.1 M NaCl 0.04 M Tris pH 8 25 % PEG 350	0.02 M bis Tris pH 7 13 % PEG 2000	0.05 M $Mg(CH_3COO)_2$ 0.05 M CH_3COONa pH 5.4 22 % PEG 400	0.1 M NaCl 0.05 M Glycine pH 9.5 31 % PEG 300
3	0.1 M $(NH_4)_2SO_4$ 0.1 M HEPES pH 7.5 11 % PEG 4000 22 % Glycerol	0.1 M $MgCl_2$ 0.1 M Tris pH 7.5 20.5 % PEG 400	0.1 M NaCl 0.04 M Tris pH 8 25.5 % PEG 350	0.02 M bis Tris pH 7 13.5 % PEG 2000	0.05 M $Mg(CH_3COO)_2$ 0.05 M CH_3COONa pH 5.4 22.5 % PEG 400	0.1 M NaCl 0.05 M Glycine pH 9.5 31.5 % PEG 300
4	0.1 M $(NH_4)_2SO_4$ 0.1 M HEPES pH 7.5 13 % PEG 4000 22 % Glycerol	0.1 M $MgCl_2$l 0.1 M Tris pH 7.5 21 % PEG 400	0.1 M NaCl 0.04 M Tris pH 8 26.5 % PEG 350	0.02 M bis Tris pH 7 14 % PEG 2000	0.05 M $Mg(CH_3COO)_2$ 0.05 M CH_3COONa pH 5.4 23 % PEG 400	0.1 M NaCl 0.05 M Glycine pH 9.5 32 % PEG 300
5	0.1 M $(NH_4)_2SO_4$ 0.1 M HEPES pH 7.5 14 % PEG 4000 22 % Glycerol	0.1 M $MgCl_2$ 0.1 M Tris pH 7.5 21.5 % PEG 400	0.1 M NaCl 0.04 M Tris pH 8 26.5 % PEG 350	0.02 M bis Tris pH 7 14.5 % PEG 2000	0.05 M $Mg(CH_3COO)_2$ 0.05 M CH_3COONa pH 5.4 23.5 % PEG 400	0.1 M NaCl 0.05 M Glycine pH 9.5 32.5 % PEG 300
6	0.1 M $(NH_4)_2SO_4$ 0.1 M HEPES pH 7.5 12 % PEG 4000 22 % Glycerol	0.1 M $MgCl_2$ 0.1 M Tris pH 7.5 22 % PEG 400	0.1 M NaCl 0.04 M Tris pH 8 27 % PEG 350	0.02 M bis Tris pH 7 15 % PEG 2000	0.05 M $Mg(CH_3COO)_2$ 0.05 M CH_3COONa pH 5.4 24 % PEG 400	0.1 M NaCl 0.05 M Glycine pH 9.5 33 % PEG 300
7	0.1 M $(NH_4)_2SO_4$ 0.1 M HEPES pH 7.5 12 % PEG 4000 12 % PEG 4000	0.1 M $MgCl_2$ 0.1 M Tris pH 7.5 22.5 % PEG 400	0.1 M NaCl 0.04 M Tris pH 8 27.5 % PEG 350	0.02 M bis Tris pH 7 15.5 % PEG 2000	0.05 M $Mg(CH_3COO)_2$ 0.05 M CH_3COONa pH 5.4 24.5 % PEG 400	0.1 M NaCl 0.05 M Glycine pH 9.5 33.5 % PEG 300
8	0.1 M $(NH_4)_2SO_4$ 0.1 M HEPES pH 7.5 12 % PEG 4000 12 % PEG 4000	0.1 M $MgCl_2$ 0.1 M Tris pH 7.5 23 % PEG 400	0.1 M NaCl 0.04 M Tris pH 8 28 % PEG 350	0.02 M bis Tris pH 7 16 % PEG 2000	0.05 M $Mg(CH_3COO)_2$ 0.05 M CH_3COONa pH 5.4 25 % PEG 400	0.1 M NaCl 0.05 M Glycine pH 9.5 34 % PEG 300
9	0.1 M $(NH_4)_2SO_4$ 0.1 M HEPES pH 7.5 12 % PEG 4000 21 % Glycerol	0.1 M $MgCl_2$ 0.1 M Tris pH 7.5 23 % PEG 400	0.1 M NaCl 0.04 M Tris pH 8 28.5 % PEG 350	0.02 M bis Tris pH 7 16.5 % PEG 2000	0.05 M $Mg(CH_3COO)_2$ 0.05 M CH_3COONa pH 5.4 25.5 % PEG 400	0.1 M NaCl 0.05 M Glycine pH 9.5 34.5 % PEG 300
10	0.1 M $(NH_4)_2SO_4$ 0.1 M HEPES pH 7.5 12 % PEG 4000 23 % Glycerol	0.1 M $MgCl_2$ 0.1 M Tris pH 7.5 24 % PEG 400	0.1 M NaCl 0.04 M Tris pH 8 29 % PEG 350	0.02 M bis Tris pH 7 17 % PEG 2000	0.05 M $Mg(CH_3COO)_2$ 0.05 M CH_3COONa pH 5.4 26 % PEG 400	0.1 M NaCl 0.05 M Glycine pH 9.5 35 % PEG 300
11	0.1 M $(NH_4)_2SO_4$ 0.1 M HEPES pH 7.5 12 % PEG 4000 24 % Glycerol	0.1 M $MgCl_2$ 0.1 M Tris pH 7.5 24.5 % PEG 400	0.1 M NaCl 0.04 M Tris pH 8 29.5 % PEG 350	0.02 M bis Tris pH 7 17.5 % PEG 2000	0.05 M $Mg(CH_3COO)_2$ 0.05 M CH_3COONa pH 5.4 26.5 % PEG 400	0.1 M NaCl 0.05 M Glycine pH 9.5 35.5 % PEG 300
12	0.1 M $(NH_4)_2SO_4$ 0.1 M HEPES pH 7.5 12 % PEG 4000 25 % Glycerol	0.1 M $MgCl_2$ 0.1 M Tris pH 7.5 25 % PEG 400	0.1 M NaCl 0.04 M Tris pH 8 30 % PEG 350	0.02 M bis Tris pH 7 18 % PEG 2000	0.05 M $Mg(CH_3COO)_2$ 0.05 M CH_3COONa pH 5.4 27 % PEG 400	0.1 M NaCl 0.05 M Glycine pH 9.5 36 % PEG 300

Table 7.3: 24-well crystallization screen "DDM" for *A. baylyi* BetT1

	1	2	3	4	5	6
A	0.07 M NaCl 0.05 M Na_3-Citrate pH 4,25 20.5 % PEG	0.07 M NaCl 0.05 M Na_3-Citrate pH 4,25 21 % PEG	0.07 M NaCl 0.05 M Na_3-Citrate pH 4,25 21.5 % PEG	0.07 M NaCl 0.05 M Na_3-Citrate pH 4,25 22 % PEG	0.07 M NaCl 0.05 M Na_3-Citrate pH 4,25 22.5 % PEG	0.07 M NaCl 0.05 M Na_3-Citrate pH 4,25 23 % PEG
B	0.07 M NaCl 0.05 M Na_3-Citrate pH 4.5 20.5 % PEG	0.07 M NaCl 0.05 M Na_3-Citrate pH 4.5 21 % PEG	0.07 M NaCl 0.05 M Na_3-Citrate pH 4.5 21.5 % PEG	0.07 M NaCl 0.05 M Na_3-Citrate pH 4.5 22 % PEG	0.07 M NaCl 0.05 M Na_3-Citrate pH 4.5 22.5 % PEG	0.07 M NaCl 0.05 M Na_3-Citrate pH 4.5 23 % PEG
C	0.07 M NaCl 0.05 M Na_3-Citrate pH 4,75 20.5 % PEG	0.07 M NaCl 0.05 M Na_3-Citrate pH 4,75 21 % PEG	0.07 M NaCl 0.05 M Na_3-Citrate pH 4,75 21.5 % PEG	0.07 M NaCl 0.05 M Na_3-Citrate pH 4,75 21.5 % PEG	0.07 M NaCl 0.05 M Na_3-Citrate pH 4,75 22.5 % PEG	0.07 M NaCl 0.05 M Na_3-Citrate pH 4,75 23 % PEG
D	0.07 M NaCl 0.05 M Na_3-Citrate pH 5 20.5 % PEG	0.07 M NaCl 0.05 M Na_3-Citrate pH 5 21 % PEG	0.07 M NaCl 0.05 M Na_3-Citrate pH 5 21.5 % PEG	0.07 M NaCl 0.05 M Na_3-Citrate pH 5 22 % PEG	0.07 M NaCl 0.05 M Na_3-Citrate pH 5 22.5 % PEG	0.07 M NaCl 0.05 M Na_3-Citrate pH 5 23 % PEG

7.7 Surface Entropy Reduction prediction for *A. baylyi* BetT1

A surface entropy reduction prediction (SERp, http://services.mbi.ucla.edu/SER/) was performed on the basis of the amino acid sequence of BetT1 from *A. baylyi* to determine clusters, which have to be substituted to enhance crystallizability.

Proposed Mutations:

Cluster #1: **Residues 507 - 509:** AKALKQETQQ [?]
- K 507 => A
- Q 508 => A
- E 509 => A

SERp Score: 4.49 [?]

Cluster #2: **Residues 7 - 9:** EQK [?]
- E 7 => A
- Q 8 => A
- K 9 => A

SERp Score: 4.13 [?]

Cluster #3: **Residues 315 - 315:** K [?]
- K 315 => A

SERp Score: 2.8 [?]

Cluster #1: AKALKQETQQ [?]
- Score 4.49
- Cluster range: 503 - 512
- Proposed range: 507 - 509
- Mutations: 3
- Mutable AA: 'K', 'E', 'Q'
- Target AA: A
- Patch Length: 3
- Gaps: 0

Residue	SS Coil Confidence	Entropy Avg	Blast Conserved	Blast Mutated	Sec Str Score	Entropy Score	Blast Score	Meta Score	Total Score
503: A	0.016	0.385	0.000	0.000	0.00	0.38	0.00	0.00	0.38
504: K	0.016	0.333	1.000	0.000	0.00	0.33	0.00	0.00	0.33
505: A	0.047	0.385	1.000	1.000	0.00	0.38	0.00	0.00	0.38
506: L	0.082	0.385	0.000	0.000	0.00	0.38	0.00	0.00	0.38
507: K	0.104	0.705	0.000	0.000	0.00	0.71	0.00	0.00	0.71
508: Q	0.129	0.945	0.000	0.000	0.32	0.94	0.00	0.00	1.27
509: E	0.103	0.805	1.000	0.000	0.46	0.81	0.00	0.00	1.27

Cluster #2: EQK [?]

- Score 4.13
- Cluster range: 7 - 9
- Proposed range: 7 - 9
- Mutations: 3
- Mutable AA: 'K', 'E', 'Q'
- Target AA: A
- Patch Length: 3
- Gaps: 0

Residue	SS Coil Confidence	Entropy Avg	Blast Conserved	Blast Mutated	Sec Str Score	Entropy Score	Blast Score	Meta Score	Total Score
7: E	0.264	0.801	0.000	1.000	0.57	0.80	0.00	0.00	0.87
8: Q	0.211	0.945	0.000	0.000	0.54	0.94	0.00	0.00	0.99
9: K	0.293	0.848	0.000	0.000	0.58	0.85	0.00	0.00	0.92

Cluster #3: K [?]

- Score 2.8
- Cluster range: 315 - 315
- Proposed range: 315 - 315
- Mutations: 1
- Mutable AA: 'K'
- Target AA: A
- Patch Length: 1
- Gaps: 0

Residue	SS Coil Confidence	Entropy Avg	Blast Conserved	Blast Mutated	Sec Str Score	Entropy Score	Blast Score	Meta Score	Total Score
315: K	0.567	0.749	0.000	0.000	0.73	0.75	0.00	0.00	1.48

Color-coding Legend:

- Patch proposed for mutation is shaded gray in **bold** face
- Residues proposed for mutation are shaded dark green
- Other mutable high entropy residues (KEQ) are shaded blue
- Low entropy residues (A) shaded yellow

Score Legend:

- SS Coil Confidence: PSIPRED confidence for a residue being in a coil region. Range 0 ... 1.0.
- Entropy Avg: Side chain entropy averaged in window of 3 residues. Range 0 (no entropy, Ala) ... 1.0 (highest entropy, Gln).
- Blast Conserved: Fraction of BLAST aligned sequences that showed conservation. Range 0 (no conservation) ... 1.0 (fully conserved).
- Blast Mutated: Fraction of BLAST aligned sequences that contained a target residue (A) at this position. Range 0 (none) ... 1.0 (all).
- *See Intro for the calculation of model scores from these raw values.*

Figure 7.5: Surface Entropy Reduction prediction (SERp) for BetT1.
Clusters for surface entropy reduction to enhance the crystallization probability were estimated from the BetT1 amino acid sequence by the SERp server (http://services.mbi.ucla.edu/SER/). SERp scores higher than 3 indicate good candidates for mutation. Residues proposed for substitution are shaded green, other mutatable high entropy residues are shaded blue and low entropy residues are shaded yellow. The corresponding score legend is shown below the results.

7.8 PELDOR

7.8.1 MTSL vs. MMTSL

In the current work, two nitroxide spin labels were used, namely methanethiosulfonate (MTSL;(1-Oxyl-2,2,5,5-tetramethyl-Δ3-pyrroline-3-methyl) methanethiosulfonate) and methyl methanethiosulfonate (MMTSL; (1-Oxyl-2,2,5,5-tetramethylpyrrolidin-3-yl) methyl methanethiosulfonate). Whereas MTSL is commonly utilized as paramagnetic spin label in PELDOR experiments, MMTSL is the ring unsaturated analog (Figure 7.6). In order to exclude differences in the distance measurements due to a different conformational freedom of the spin labels, PELDOR experiments were performed with BetP S140C/C252T/K489C as six-spin system labeled with MMTSL and MTSL, respectively.

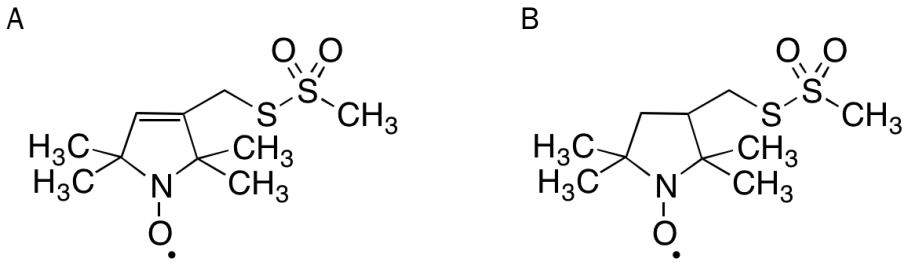

Figure 7.6: MTSL vs. MMTSL.

The structural formula is displayed for MTSL (A) and the ring unsaturated analog MMTSL (B), respectively.

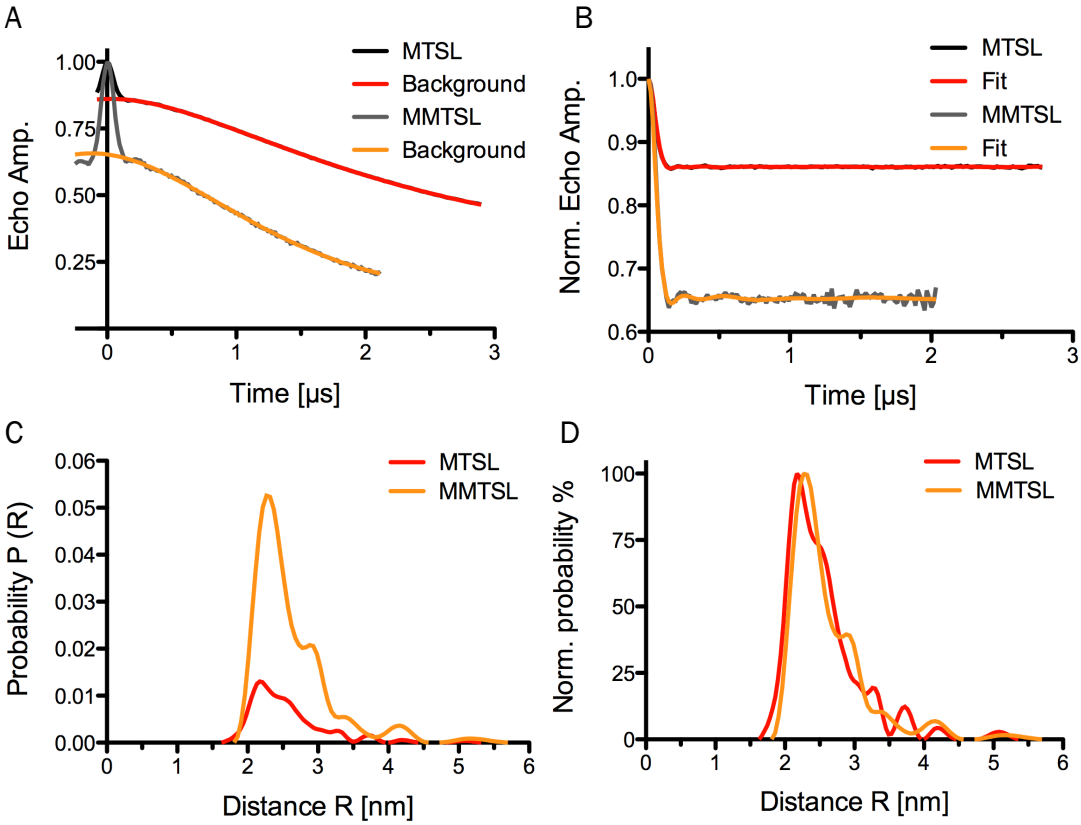

Figure 7.7: PELDOR analysis of BetP S140C/C252T/K489C in detergent labeled with MTSL and MMTSL at inactive conditions.

Experimental PELDOR time traces for BetP S140C/C252T/K489C in 0.01 % DDM and spin labeled by either MTSL (black) or MMTSL (gray), are displayed as function of time in µs at inactive conditions. The echo amplitude (A) and background-corrected normalized echo amplitude (B) is shown with the respective background as well as the fit to the data in red for MTSL and in orange for MMTSL, respectively. The distance distribution was obtained by Tikhonov regularization (C) and for clarity the distance distribution was normalized for a better comparison (D).

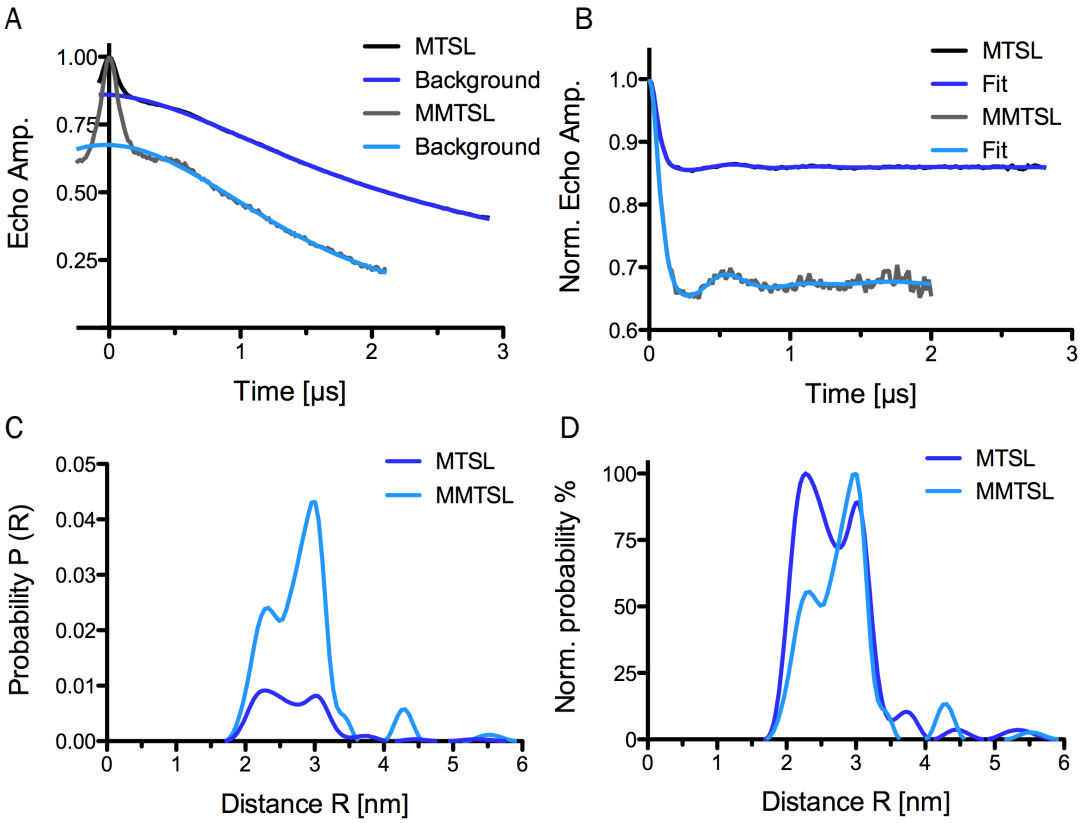

Figure 7.8: PELDOR analysis of BetP S140C/C252T/K489C in detergent labeled with MTSL and MMTSL at active conditions.

Experimental PELDOR time traces for BetP S140C/C252T/K489C in 0.01 % DDM and spin labeled by either MTSL (black) or MMTSL (gray), are displayed as function of time in µs at active conditions. The echo amplitude (A) and background-corrected normalized echo amplitude (B) is shown with the respective background as well as the fit to the data in red for MTSL and in orange for MMTSL, respectively. The distance distribution was obtained by Tikhonov regularization (C) and for clarity the distance distribution was normalized for a better comparison (D).

The direct comparison of the data, either at non-activating or activating conditions, showed that no significant difference could be assigned between the spin labels. Both obtained distance distributions showed main peaks at comparable distances at inactive as well as active conditions (Figure 7.7 and Figure 7.8). The differences in the modulation depth are based on the used X- or Q-Band Spectrometer frequency and the thereby different pulse length as well as spectral densities. Hence, the data of either MMTSL or MTSL labeled probes can be compared.

7.8.2 X-Band vs. Q-Band

For this thesis, PELDOR experiments were conducted on a Bruker EleXsys E580 spectrometer operating either at X-band (9.6 GHz) or Q-band (33.7 GHz) frequencies with the standard 4-pulse 'dead time free' PELDOR sequence. To exclude differences in the resulting PELDOR analysis due to different frequencies, PELDOR spectra were recorded for BetP S140C/C252T/N488C at X-band and Q-band microwave frequencies and the obtained results were subsequently compared.

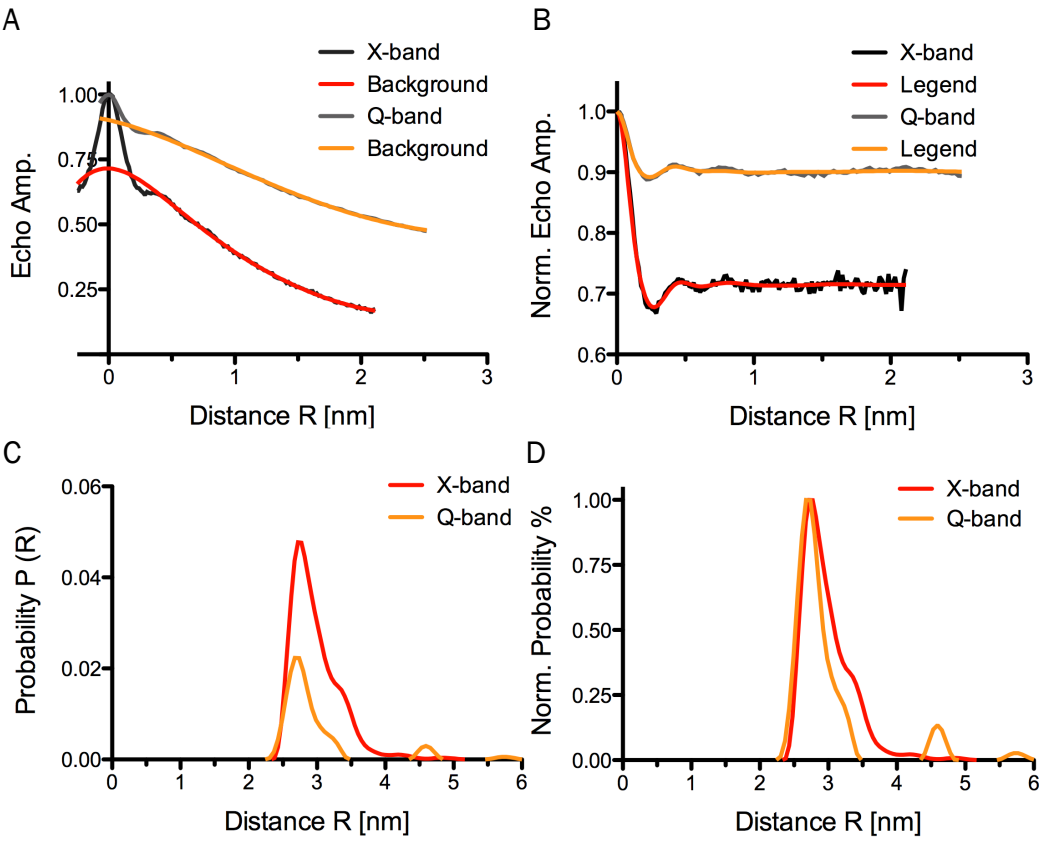

Figure 7.9: PELDOR analysis at X- and Q-band frequencies of BetP S140C/C252T/N488C in detergent at inactive conditions.

Experimental PELDOR time traces at X-band (black) and Q-band (gray) frequencies for BetP S140C/C252T/N488C, spin labeled by MMTSL. The PELDOR spectra are displayed as function of time in µs at inactive conditions in 0.01 % DDM. The echo amplitude (A) and background-corrected normalized echo amplitude (B) is shown with the respective background as well as the fit to the data in red at X-band and in orange for Q-band, respectively. The distance distribution was obtained by Tikhonov regularization (C) and for clarity the distance distribution was normalized for a better comparison (D).

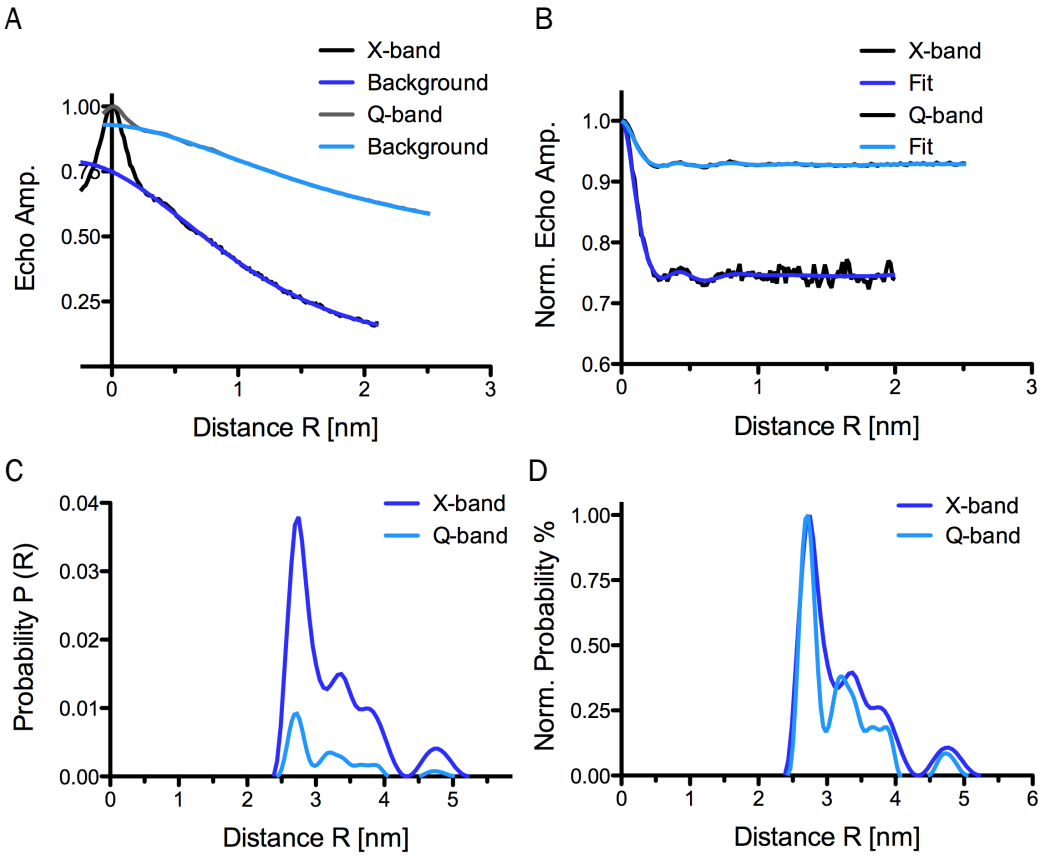

Figure 7.10: PELDOR analysis at X- and Q-band frequencies of BetP S140C/C252T/N488C at active conditions.

Experimental PELDOR time traces at X-band and Q-band frequencies for BetP S140C/C252T/N488C, spin labeled by MMTSL. The PELDOR spectra are displayed as function of time in µs at inactive conditions in 0.01 % DDM. The echo amplitude (A) and background-corrected normalized echo amplitude (B) is shown with the respective background as well as the fit to the data in dark blue at X-band and in light blue for Q-band, respectively. The distance distribution was obtained by Tikhonov regularization (C) and for clarity the distance distribution was normalized for a better comparison (D).

The comparison of the data, either at non-activating or activating conditions, revealed that no significant difference could be observed due to the use of either X- or Q-band. Main peaks at comparable distances were detected in the resulting distance distributions at inactive as well as active conditions (Figure 7.9 and Figure 7.10). Differences can be related to the different used pulse length. Thus, the data of either X- or Q-band measured probes can be compared.

7.8.3 Polynomial background correction

For time traces of BetP variants in detergent as six-spin systems with labels located at the cytoplasmic side, a polynomial background correction was performed to remove longer interprotomeric distances. Figure 7.11 exemplarily compares the results of standard and polynomial background correction with different time windows.

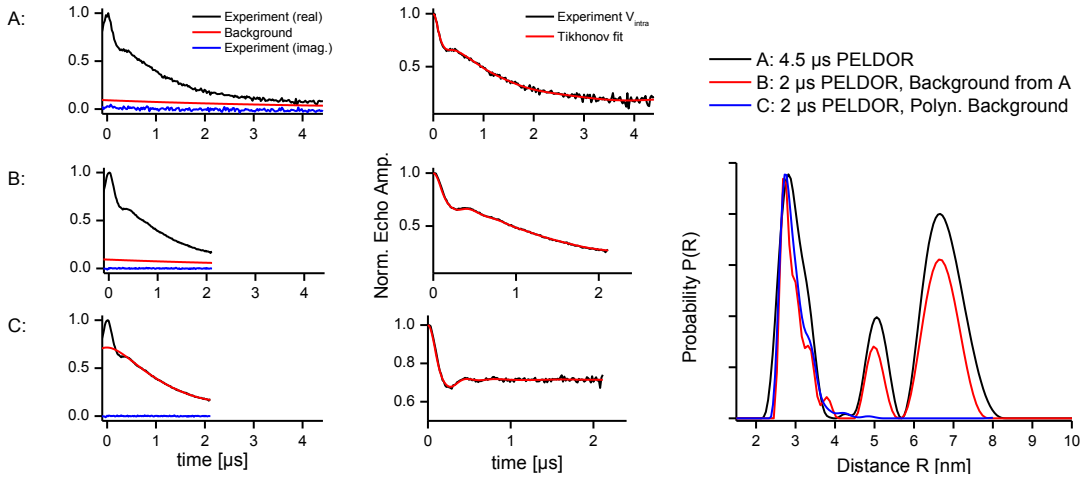

Figure 7.11: Polynomial background correction of BetP S140C/C252T/N488C in detergent as six-spin system with labels located at the cytoplasmic side.
PELDOR time traces are displayed for the MMTSL labeled six-spin system BetP S140C/C252T/N488C in 0.1 % DDM as function of time in µs. The echo amplitude (left column) is shown with the standard intermolecular background contribution (red) for a time frame of 4.5 µs (A) and 2 µs (B) as well as with the polynomial background (red) for 2 µs (C). The corresponding background-corrected normalized echo amplitudes (right column) of the experimental data (black) is shown with the respective Tikhonov fit in red. The distance distribution was obtained by Tikhonov regularization (DeerAnalysis2013) of the background-corrected time traces. Figure was provided by Dr. Burkhard Endeward.

Figure 7.11 illustrates the Tikhonov-derived distance distributions, which are based on different background correction procedures and different time windows. For the standard fitting of the intermolecular background with time windows of 4.5 µs and 2 µs, longer interprotomeric distances can be observed. In contrast, the polynomial background correction results in a distance distribution indicating only the intraprotomeric distance of 3 nm. In this way, the shorter intraprotomeric distances were successfully separated from longer interprotomeric distances (> 5 nm) by a polynomial background correction.

7.8.4 MMM simulation of BetP

Distance distributions were simulated for diverse BetP variants with the rotamer library approach of the software package MMM2015.1. The standard applied rotamer library R1A for the spin label MTSL can be calculated for cryogenic (R1A_175K) and ambient (R1A_289K) temperatures. However, the standard rotamer library showed in some cases a very low number of rotamers, especially at position S140C and G450C at 175 K and 298 K, respectively (Table 7.4). Beside the standard library, alternative libraries based on the same rotamers with different relative probabilities of the rotamers are available. After recommendation of Yehan Polyhach (personal communication Dr. B. Endeward) the rotamer library R1A_298K_xray was applied for BetP. A direct comparison of the rotamers predicted by the standard library at cryogenic and ambient temperature with the alternative library R1A_298K_xray for the labeling sites in different BetP conformations is indicated in Table 7.4. Furthermore, the simulated distance distribution of R1A_298K and R1A_298K_xray are directly compared for the sites at the cytoplasmic side and subsequently for the periplasmic side of BetP.

Table 7.4: Calculated rotamers

	R1A_175K		R1A_298K					R1A_298K_Xray				
	$1C_i$	$1C_e$	$1C_i$	$2C_i$	$1C_e$	$2C_e$	$3C_e$	$1C_i$	$2C_i$	$1C_e$	$2C_e$	$3C_e$
S140C	70	1	71	71	1	46	43	91	91	11	67	67
N488C	40	4	44	44	61	32	66	71	71	81	57	84
K489C	60	82	49	49	64	120	92	75	75	97	128	101
W490C	100	126	125	125	130	138	138	131	131	133	139	131
G450C	3	25	1	1	13	25	5	11	11	37	39	27
A514C	7	8	14	14	13	1	4	35	35	18	5	35
L515C	39	77	36	36	38	1	3	76	76	85	19	12
S516C	62	89	59	59	84	75	84	81	81	99	89	91

conformations: inward open $1C_i$ (PDB 4DOJ, chain C) and $2C_i$ (PDB 4C7R, chain A); outward open $1C_e$ (PDB 4DOJ, chain B), $2C_e$ (PDB 4LLH, chain A) and $3C_e$ (PDB 4LLH, chain B)

*outliers are colored red

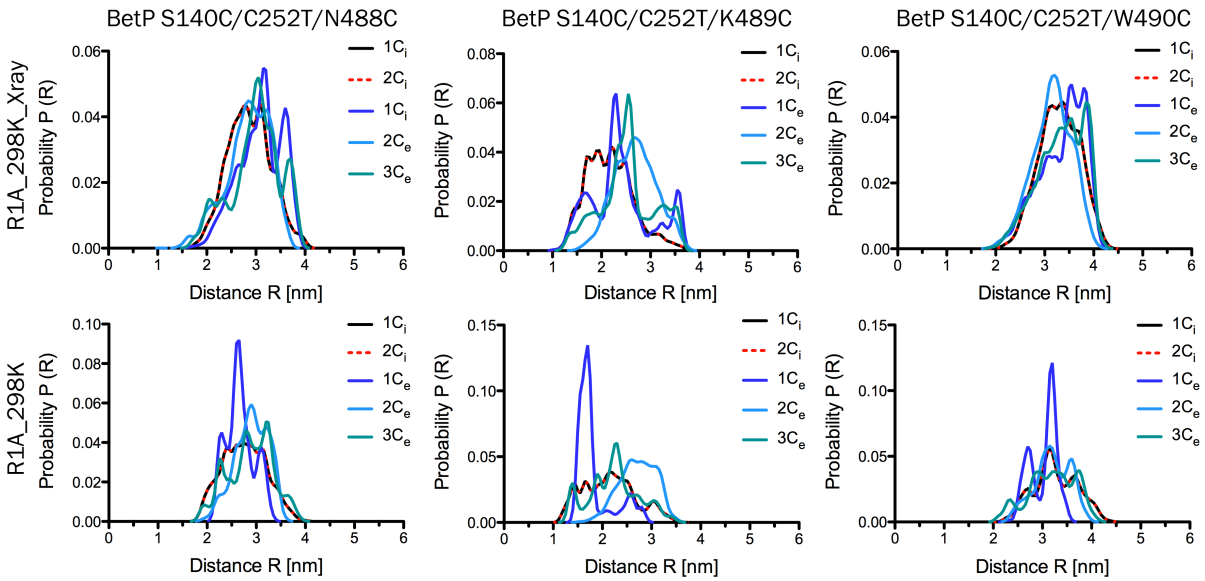

Figure 7.12: Simulated PELDOR distance distribution of protomeric BetP variants at the cytoplasmic side.

Simulated PELDOR distance distributions for cytoplasmic BetP variants as single protomers based on crystal structures in different conformations: inward open state $1C_i$ (PDB 4DOJ, chain C, black) and $2C_i$ (PDB 4C7R, chain A, dashed red) as well as outward open state $1C_e$ (PDB 4DOJ, chain B, dark blue), $2C_e$ (PDB 4LLH, chain A, light blue) and $3C_e$ (PDB 4LLH, chain B, green). Data was simulated by the use of the rotamer library R1A_298K_xray (first row) and R1A_298K (second row) in the MMM software (Polyhach and Jeschke, 2010).

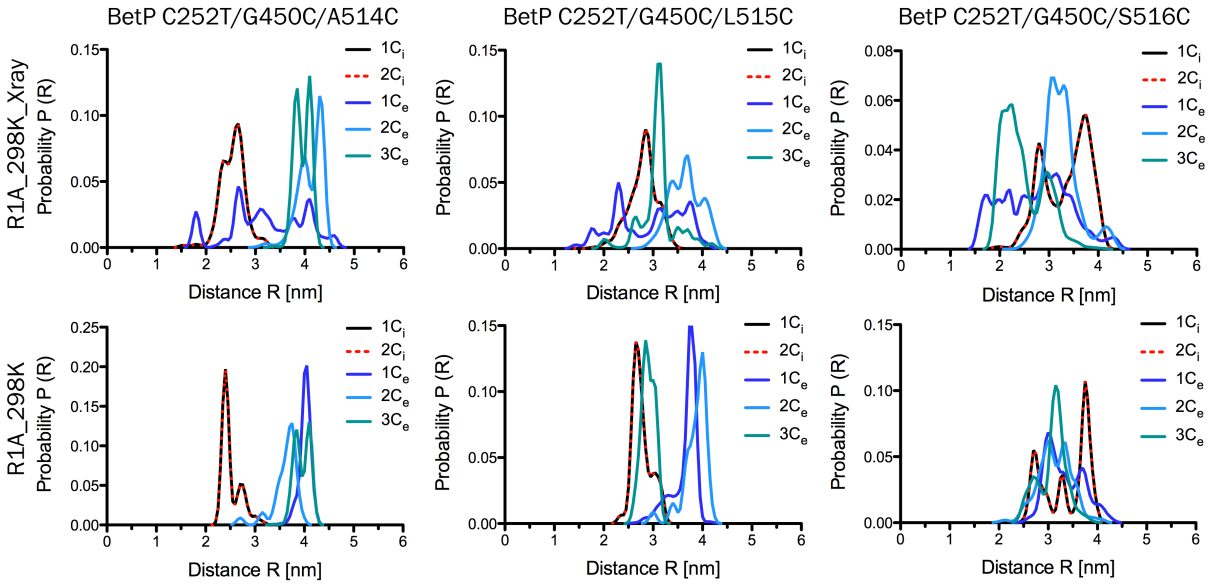

Figure 7.13: Simulated PELDOR distance distribution pf protomeric BetP variants at the periplasmic side.

Simulated PELDOR distance distributions for periplamic BetP variants as single protomers based on crystal structures in different conformations: inward open state $1C_i$ (PDB 4DOJ, chain C, black) and $2C_i$ (PDB 4C7R, chain A, dashed red) as well as outward open state $1C_e$ (PDB 4DOJ, chain B, dark blue), $2C_e$ (PDB 4LLH, chain A, light blue) and

$3C_e$ (PDB 4LLH, chain B, green). Data was simulated by the use of the rotamer library R1A_298K_xray (first row) and R1A_298K (second row) in the MMM software (Polyhach and Jeschke, 2010).

The distance distributions in the different conformations are significantly affected by the rotamer number and distribution. Low rational freedom for the label at position S140C and G450C for rotamer library R1A_175K and R1A_298K in specific conformations are indicated with less rotamers (outlier, Table 7.4). In consequence, the distance distributions are very heterogenic and follow not the trends, which are implied by the crystal structures. For the cytoplasmic as well as for the periplasmic spin labeling pairs the obtained distance distributions with the rotamer library R1A_298K show less differences between the outward and inward open states of the crystal structures. For R1A_298K_xray only one outlier is found and therefore the ladder rotamer library was used for comparison to the experimental data.

7.8.5 Examination of multi-spin effects in the BetP six-spin system

If more than two spin labels are present in a biomolecule, the sum and difference frequencies of dipolar couplings occur depending on the label efficiency and inversion efficiency. This might lead to artifacts, known as ghost contributions, in the distance distribution of multi-spin systems. This ghost distances can be suppressed by power scaling of the form factor with an exponent $\xi_N = 1/(1-N)$, where N is the number of spins.

Therefore, the distance distribution was calculated by MMM2015.1 for the BetP six-system BetP G450C/C252T/S516C in the outward open conformation. Based on this, the PELDOR time traces were simulated by taking the multi-spin effects into consideration. The time traces were further analyzed at different time windows by Tikhonov regularization with application of the ghost option in DeerAnalysis2013. Calculations were performed by Dr. B. Endeward (group of Prof. Dr. Thomas Prisner, Goethe-University, Frankfurt am Main).

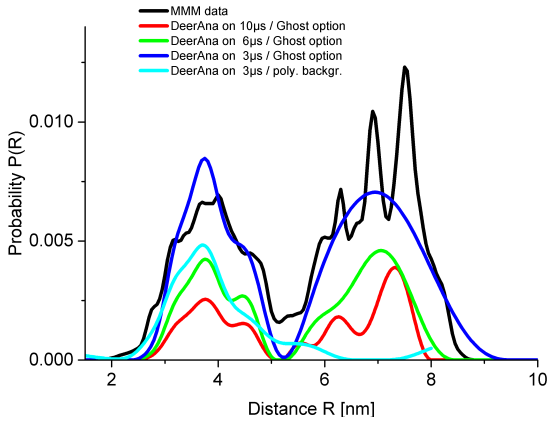

Figure 7.14: Multi-spin effects of BetP G450C/C252T/S516C.
Distance distributions for BetP G450C/C252T/S516C obtained by Tikhonov regularization with DeerAnalysis2013 considering multi-spin effects.

Figure 7.14 indicates, that differences due to multi-spin effects in the six-spin system G450C/C252T/S516C are smaller than the distance changes considered in the analysis of the experimental PELDOR results (Figure 5.23 and Figure 5.24).

7.8.6 7-pulse CP-PELDOR of BetP

The long intratrimeric distance of roughly 60 Å between the spin labeled position of S140C in the BetP trimer could not be resolved by standard 4-pulse PELDOR (Figure 5.9). In consequence, the standard 4-pulse sequence was modified into a 7-pulse PELDOR sequence, based on a short CP (Carr-Purcell) refocusing sequence (7-pulse CP-PELDOR) (Carr and Purcell, 1954), to increase the observation time window and therefore the measurable distance range as well as accuracy for non-deuterated protein complexes in detergent (Spindler *et al.*, 2015). Method optimization and analysis of recorded data was performed by Dr. Philipp Spindler and Dr. Burkhard Endeward (group of Prof. Dr. Thomas Prisner, Goethe-University, Frankfurt am Main).

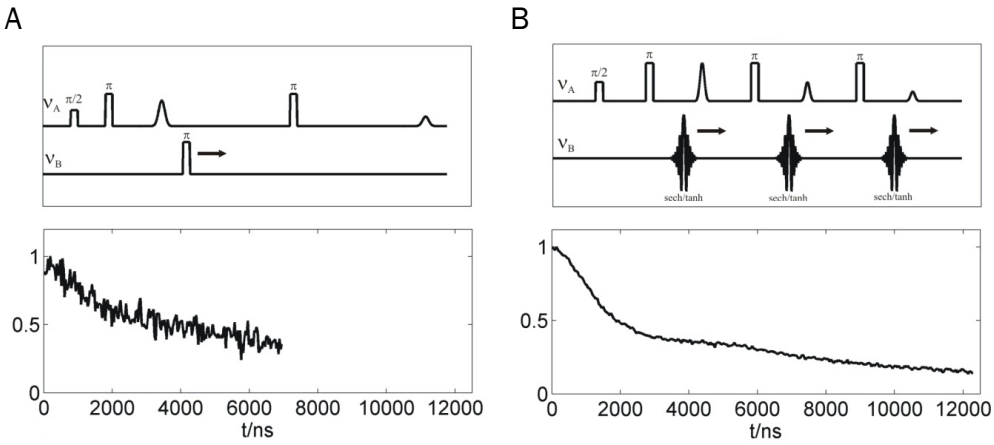

Figure 7.15: Comparison of PELDOR time traces of BetP S140C/C252T.
Dipolar evolution time trace obtained with standard 4-pulse PELDOR sequence (A) and with the 7-pulse CP-PELDOR sequence (B). Both experiments were carried out at 50 K. The 7-pulse signal was recorded over 2.5 h with a 50 MHz bandwith sech/tanh pump pulses, whereas the 4-pulse signal was averaged over 1 h with 12 ns rectangular pump pulse (adapted from Spindler *et al*., 2014)

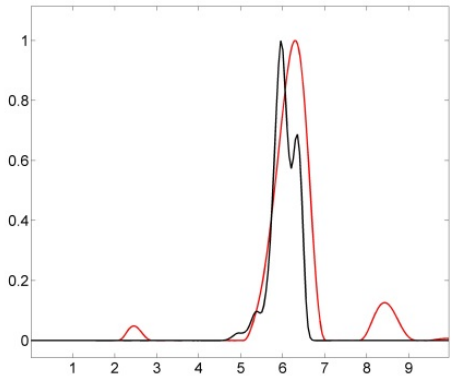

Figure 7.16: Comparison of experimental and simulated distance distribution for trimeric BetP S140C/C252T.
The experimental distance distribution of BetP S140C/C252T at inactivating conditions in 0.1 % DDM obtained by the 7-pulse CP-PELDOR and subsequent Tikhonov regularization (black) is compared to the simulated distance distribution for the corresponding BetP variant based on the crystal structure PDB 4DOJ (red) by MMM2015.1 (Polyhach and Jeschke, 2010) (Spindler *et al*., 2015).

The accuracy of distance determinations by PELDOR is limited by the flexibility of the spin labels and the maximal achievable observation time window, which again is limited by the transversal relaxation time T_2 of the unpaired electron spin (Spindler *et al*., 2015). The short relaxation time T_2 of the MTSL spin label, arising from the dynamics of interactions between the unpaired electron spin and the proton nuclear spin close by, did allow to obtain a maximum observation time

window of 7 µs for BetP with the standard 4-pulse sequence (Figure 7.15). This time window is too short to separate the intermolecular decay function properly and to obtain enough resolution in the distance distribution to identify the small distance differences predicted by the BetP crystal structures (Figure 5.10). Therefore, the 7-pulse CP-PELDOR sequence was applied with additional adiabatic pulses as inversion pump pulses. This kind of pulses is characterized by better inversion probability compared to rectangular pulses. As a result, the observation time window could be extended to 12.5 µs for non-deuterated spin-labeled BetP in detergent (Figure 7.15 B). Additionally, a strongly improved time trace with better signal-to-noise can be observed. The obtained distance distribution for BetP S140C/C252T indicates a splitting into two distance peaks at 5.9 and 6.5 nm with comparable probabilities (Figure 7.16) implying an asymmetry of BetP. The shorter distance is corresponding to the simulated distance distribution for the asymmetric trimer of PDB 4DOJ (outward open occluded/outward open/inward open), for which only one distance can be observed. For further reliable interpretation of the data, an adequate strategy for data simulation has to be developed to classify the obtained distance distribution. Moreover, additional BetP mutants have to be investigated at inactive and active conditions in detergent and reconstituted into liposomes.

7.8.7 Summary of PELDOR data

7.8.7.1 PELDOR measurements on the three-spin system in detergent

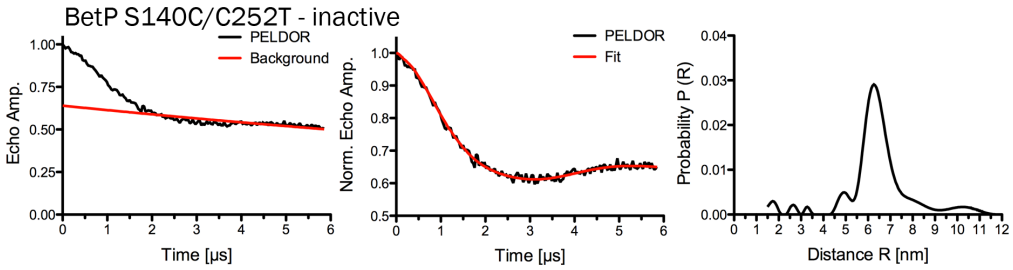

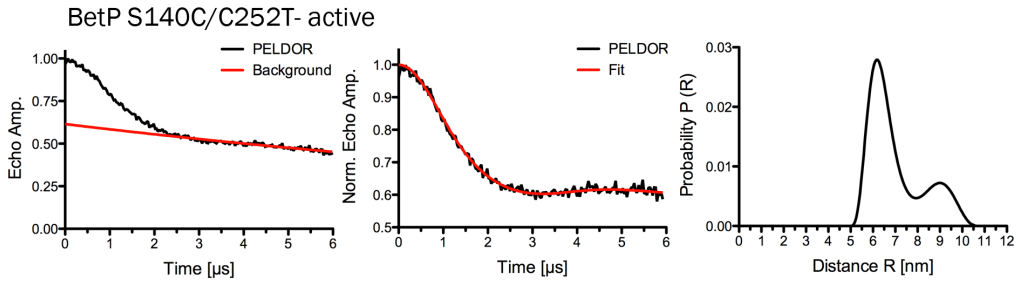

Figure 7.17: PELDOR analysis of BetP S140C/C252T in detergent as three-spin system at the cytoplasmic side.

Experimental PELDOR measurements were conducted for BetP S140C/C252T labeled with MMTSL at inactive and active conditions in 0.1 % DDM at Q-band. Corresponding PELDOR time traces for BetP S140C/C252T are displayed as function of time in µs. The echo amplitude (first column) and background-corrected normalized echo amplitude (second column) are shown with the respective background as well as the fit to the data in red. The distance distribution was obtained by Tikhonov regularization (DEERAnalysis2013) (third column).

7.8.7.2 PELDOR measurements on the six-spin system in detergent

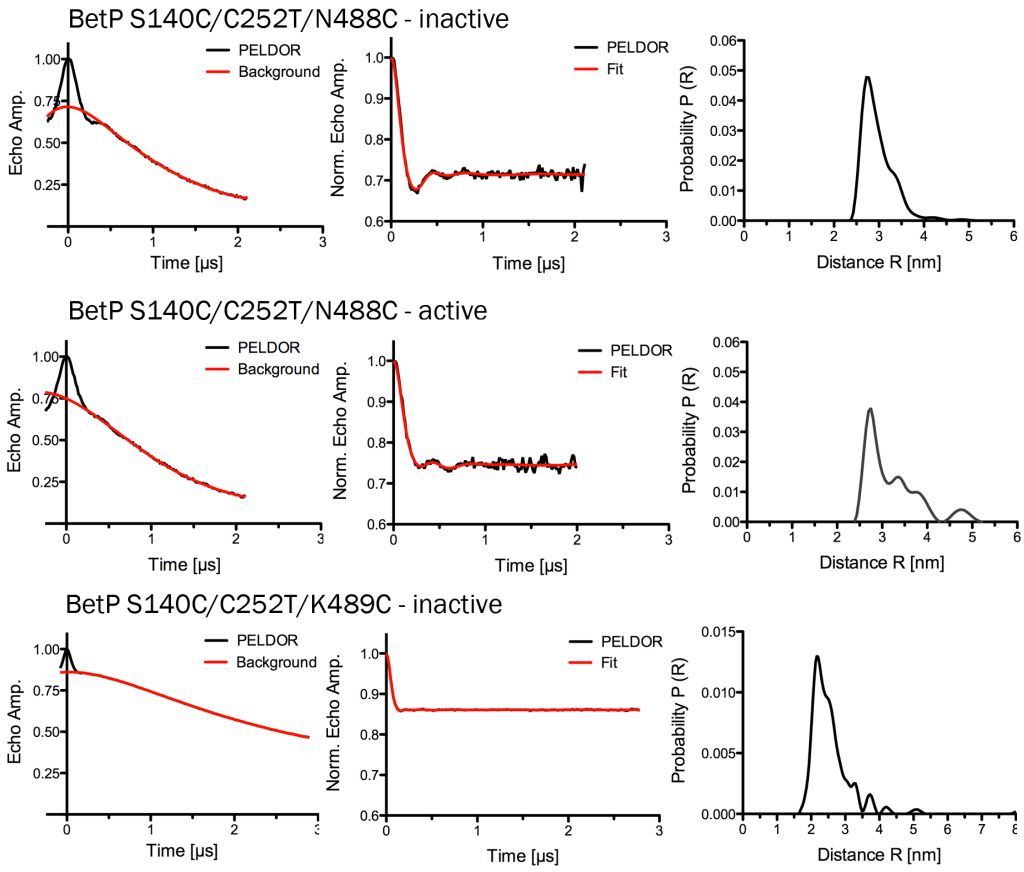

BetP S140C/C252T/K489C - active

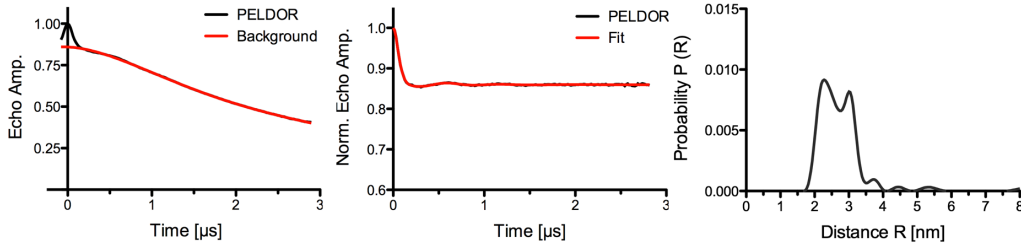

BetP S140C/C252T/W490C - inactive

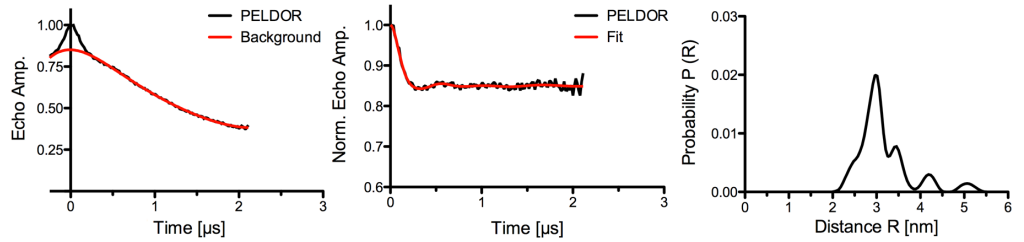

BetP S140C/C252T/W490C - active

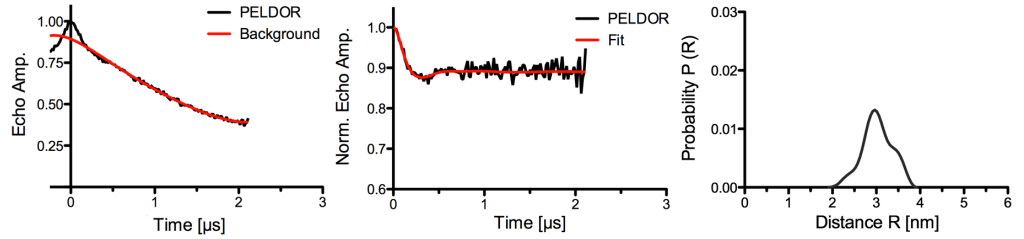

BetP S140C/C252T/T467A/S468A/K489C - active

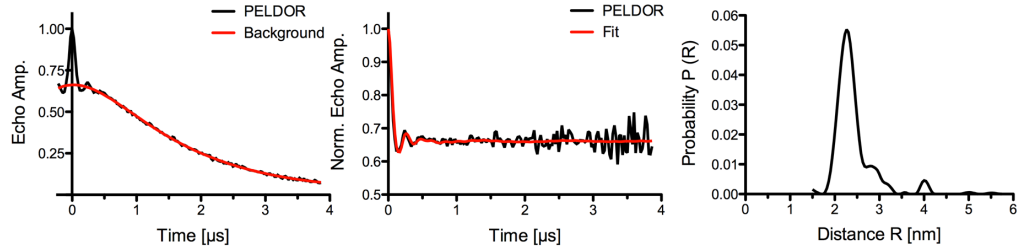

BetP S140C/C252T/T467A/S468A/K489C - inactive

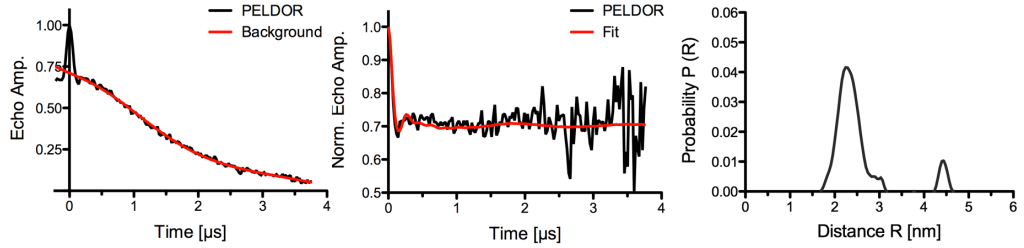

BetP C252T/G450C/A514C - inactive

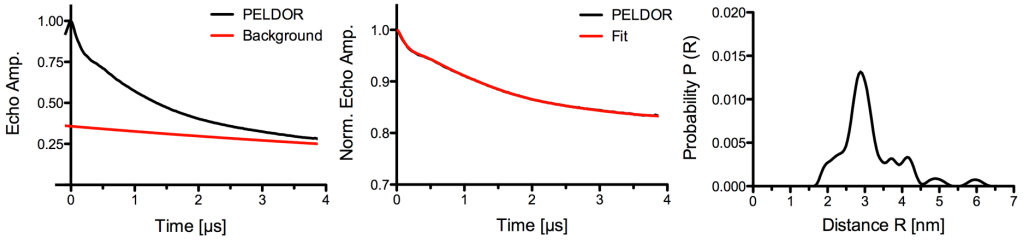

BetP C252T/G450C/A514C - active

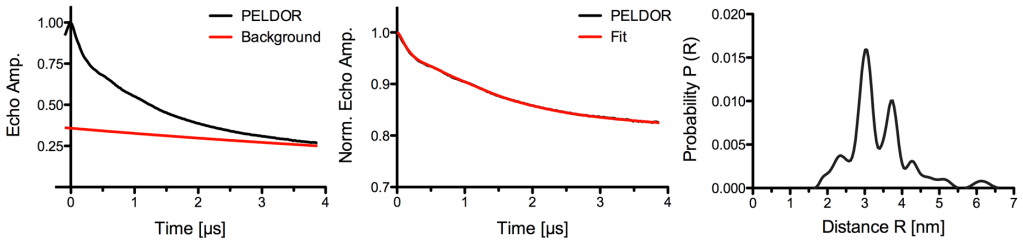

BetP C252T/G450C/L515C - inactive

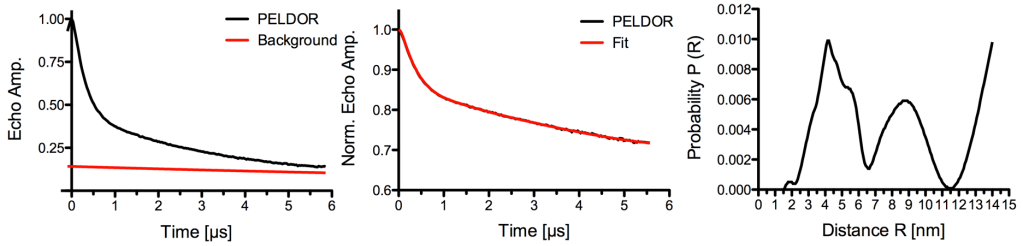

BetP C252T/G450C/L515C- active

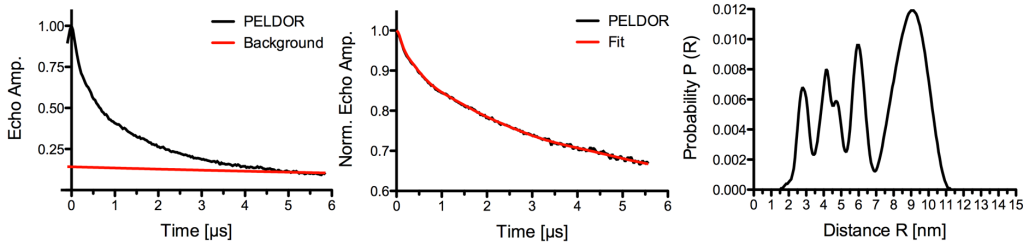

BetP C252T/G450C/S516C - inactive

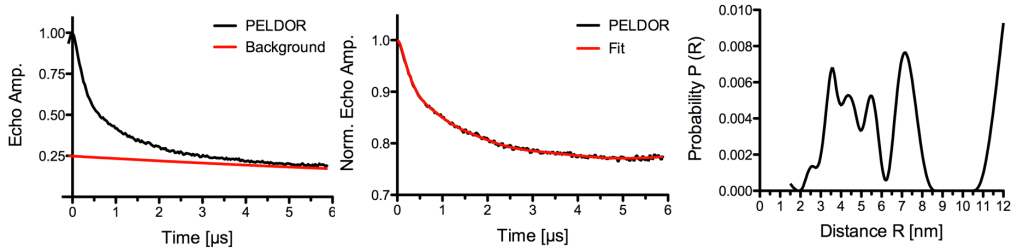

BetP C252T/G450C/S516C- active

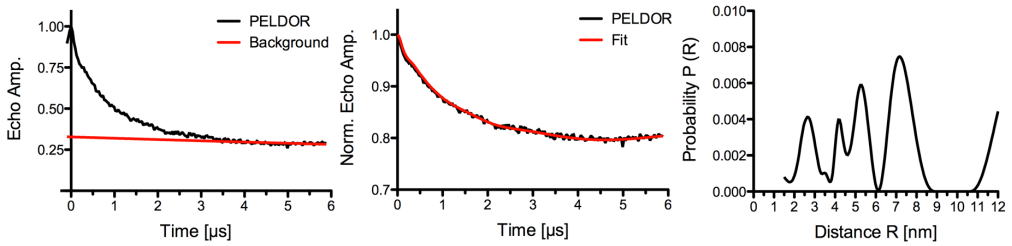

BetP C252T/G450C/T467A/S468A/A514C - inactive

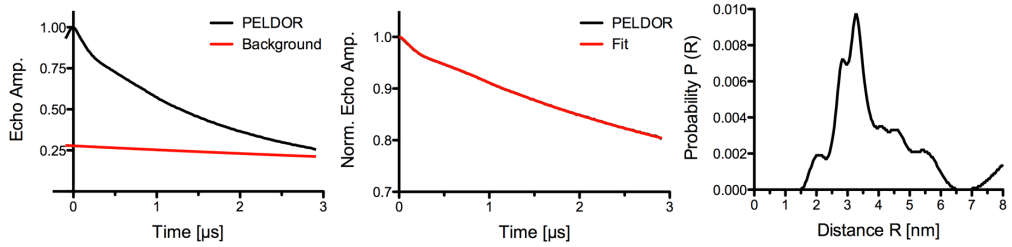

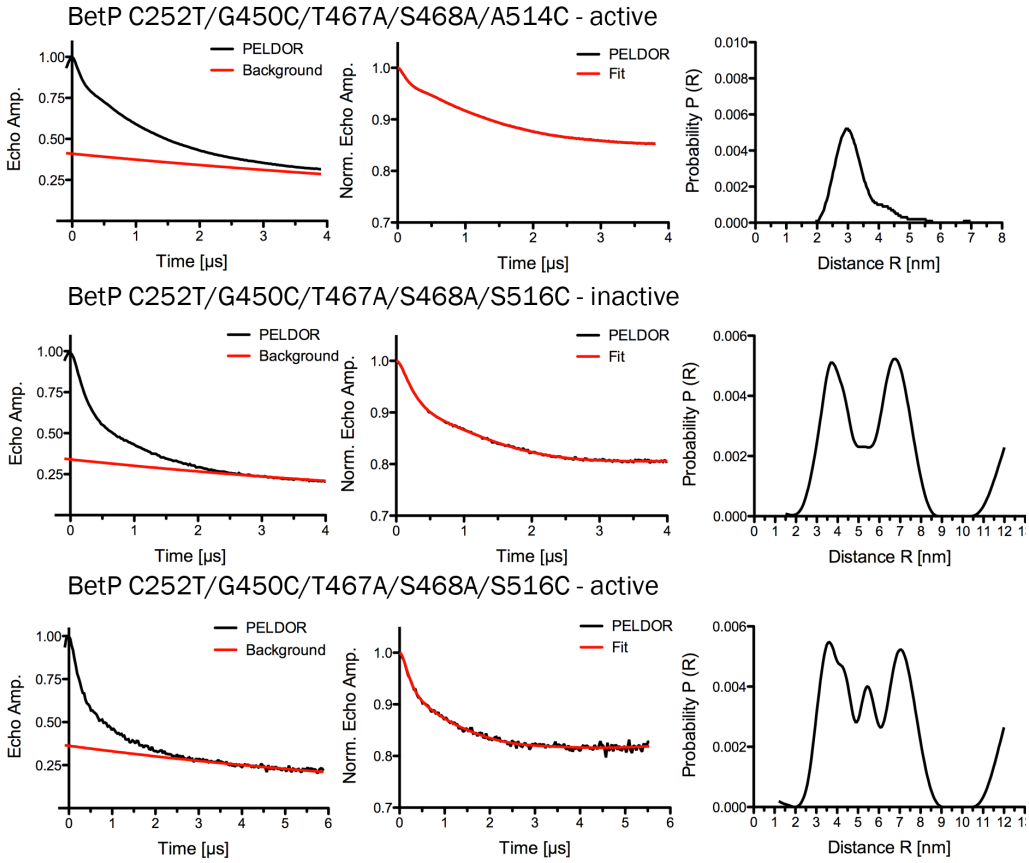

Figure 7.18: PELDOR analysis of BetP variants in detergent as six-spin system.
Experimental PELDOR time traces were recorded for BetP variants labeled with either MMTSL or MTSL at inactive and active conditions in 0.1 % DDM at X- or Q-band. Corresponding PELDOR time traces are displayed as function of time in µs. The echo amplitude (first column) and background-corrected normalized echo amplitude (second column) are shown with the respective background as well as the fit to the data in red. The distance distribution was obtained by Tikhonov regularization (DEERAnalysis2013) (third column).

7.8.7.3 PELDOR measurements on the six-spin system in proteoliposomes

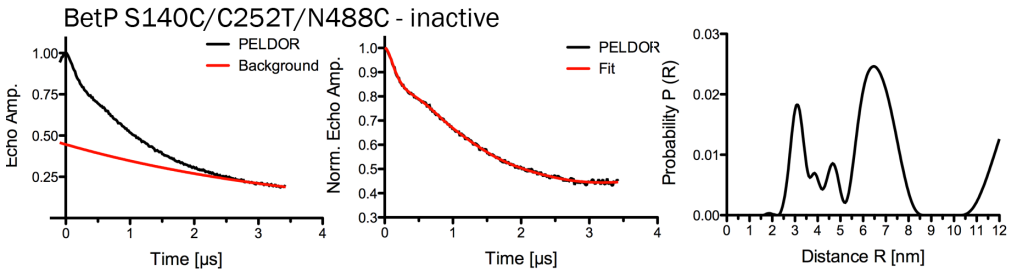

BetP S140C/C252T/N488C - active

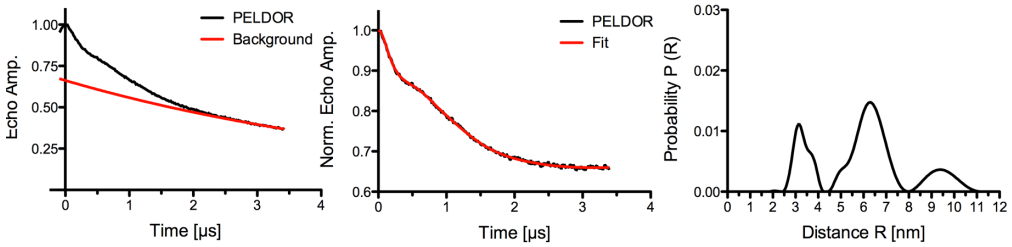

BetP S140C/C252T/K489C - inactive

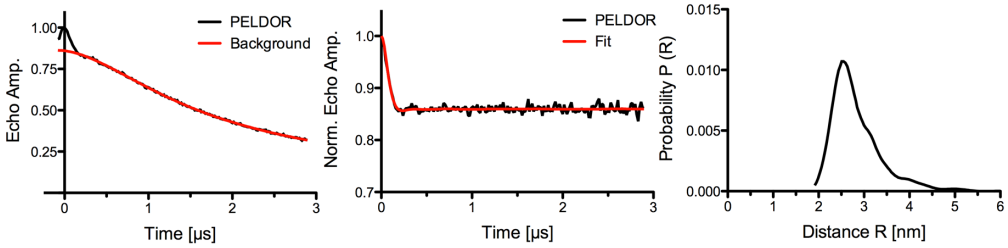

BetP S140C/C252T/K489C - active

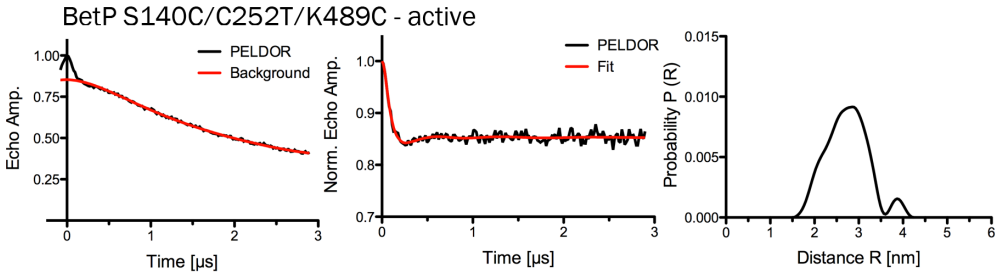

BetP S140C/C252T/W490C - inactive

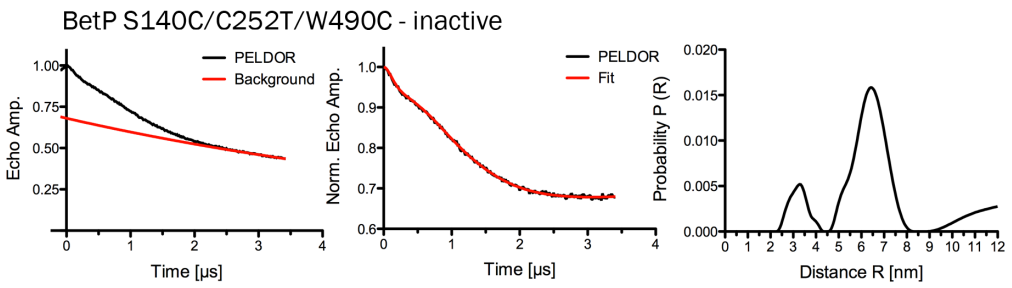

BetP S140C/C252T/W490C - active

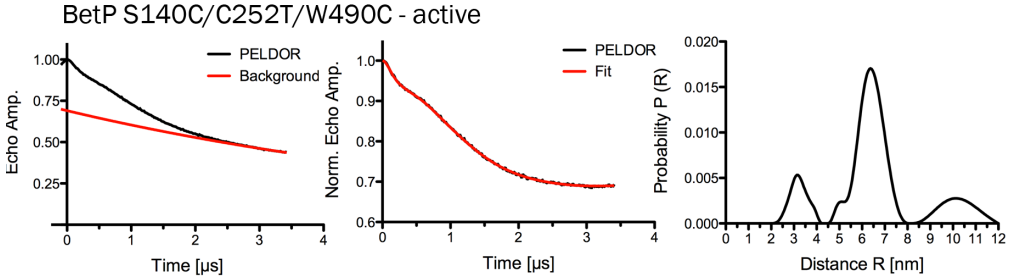

BetP S140C/C252T/T467A/S468A/K489C - active

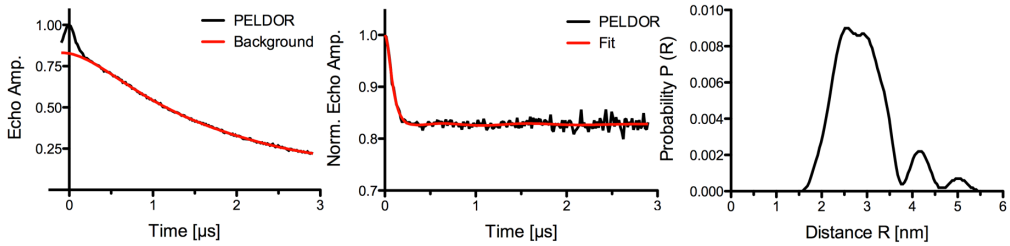

BetP S140C/C252T/T467A/S468A/K489C - inactive

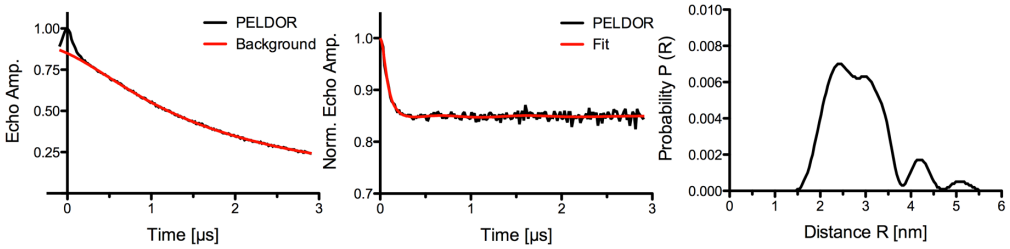

BetP C252T/G450C/L515C - inactive

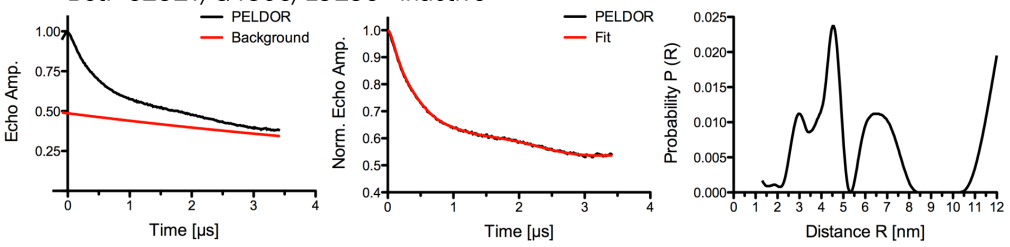

BetP C252T/G450C/L515C- active

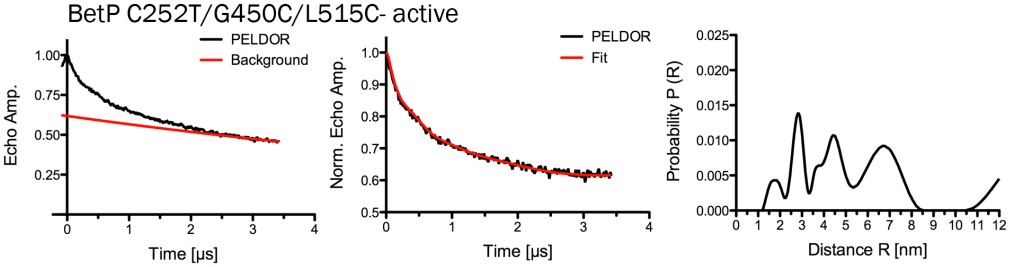

BetP C252T/G450C/S516C - inactive

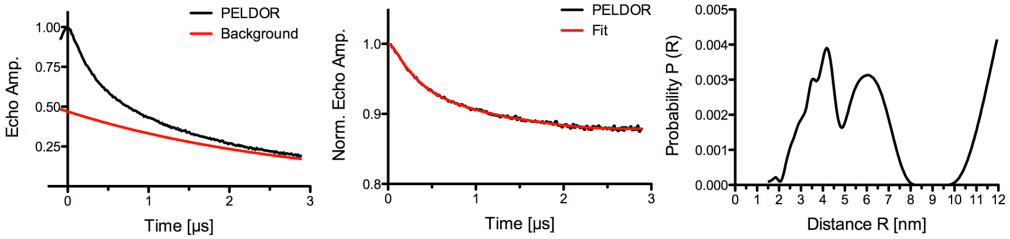

BetP C252T/G450C/S516C- active

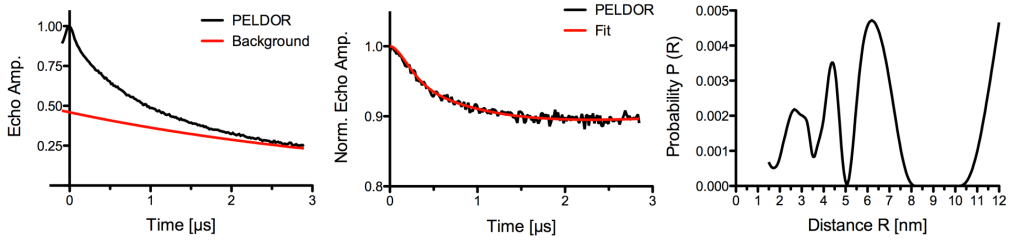

BetP C252T/G450C/T467A/S468A/S516C - inactive

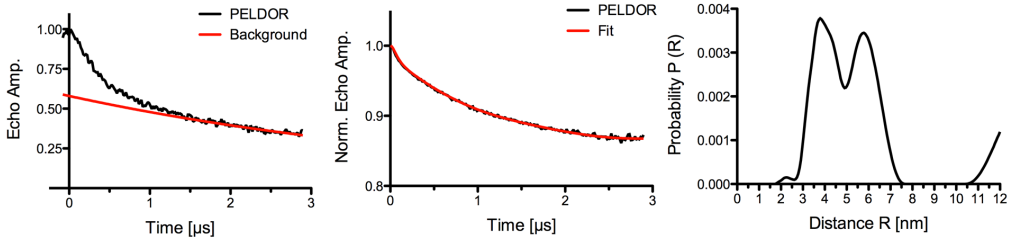

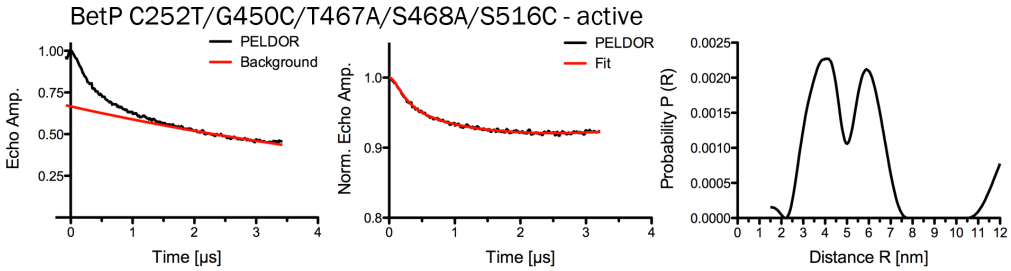

Figure 7.19: PELDOR analysis of BetP as six-spin system in proteoliposomes.

Experimental PELDOR time traces were recorded for BetP variants reconstituted into *E. coli* polar lipid liposomes, labeled with either MMTSL or MTSL at inactive and active conditions at X- or Q-band. Corresponding PELDOR time traces are displayed as function of time [µs]. The echo amplitude (first column) and background-corrected normalized echo amplitude (second column) are shown with the respective background as well as the fit to the data in red. The distance distribution was obtained by Tikhonov regularization (DEERAnalysis2013) (third column).

References

Abee, T., and Wouters, J.A. 1999. Microbial stress response in minimal processing. *Int J Food Microbiol*. 50:65-91.

Abramson, J., Smirnova, I., Kasho, V., Verner, G., Kaback, H.R., and Iwata, S. 2003. Structure and mechanism of the lactose permease of Escherichia coli. *Science*. 301:610-615.

Akyuz, N., Georgieva, E.R., Zhou, Z., Stolzenberg, S., Cuendet, M.A., Khelashvili, G., Altman, R.B., Terry, D.S., Freed, J.H., Weinstein, H., Boudker, O., and Blanchard, S.C. 2015. Transport domain unlocking sets the uptake rate of an aspartate transporter. *Nature*. 518:68-73.

Arakawa, T., and Timasheff, S.N. 1985. The Stabilization of Proteins by Osmolytes. *Biophysical Journal*. 47:411-414.

Baliarda, A., Robert, H., Jebbar, M., Blanco, C., and Le Marrec, C. 2003. Isolation and Characterization of ButA, a Secondary Glycine Betaine Transport System Operating in Tetragenococcus halophila. *Curr Microbiol*. 47:347-351.

Barbe, V., Vallenet, D., Fonknechten, N., Kreimeyer, A., Oztas, S., Labarre, L., Cruveiller, S., Robert, C., Duprat, S., Wincker, P., Ornston, L.N., Weissenbach, J., Marliere, P., Cohen, G.N., and Medigue, C. 2004. Unique features revealed by the genome sequence of Acinetobacter sp. ADP1, a versatile and naturally transformation competent bacterium. *Nucleic Acids Res*. 32:5766-5779.

Becker, M., Maximov, S., Becker, M., Meyer, U., Wittmann, A., and Krämer, R. 2014. Analysis of putative protomer crosstalk in the trimeric transporter BetP: The heterotrimer approach. *Biochim Biophys Acta*. 1837:888-898.

Berlau, J., Aucken, H., Malnick, H., and Pitt, T. 1999. Distribution of Acinetobacter Species on Skin of Healthy Humans. *Eur J Clin Microbiol Infect Dis*. 18:179-183.

Biemans-Oldehinkel, E., Mahmood, N.A., and Poolman, B. 2006. A sensor for intracellular ionic strength. *Proc Natl Acad Sci U S A*. 103:10624-10629.

Black, S.A., and Rylett, R.J. 2012. Choline transporter CHT regulation and function in cholinergic neurons. *Cent Nerv Syst Agents Med Chem*. 12:114-121.

Boscari, A., Mandon, K., Dupont, L., Poggi, M.C., and Le Rudulier, D. 2002. BetS Is a Major Glycine Betaine/Proline Betaine Transporter Required for Early Osmotic Adjustment in Sinorhizobium meliloti. *Journal of Bacteriology*. 184:2654-2663.

Bradford, M.M. 1976. A rapid and sensitive method for the quantitation of microgram quantities of protein utilizing the principle of protein-dye binding. *Analytical biochemistry*. 72:248-254.

Brown, A.D. 1976. Microbial Water Stress. *Bacteriol Rev*. 40:803-846.

Camarena, L., Bruno, V., Euskirchen, G., Poggio, S., and Snyder, M. 2010. Molecular mechanisms of ethanol-induced pathogenesis revealed by RNA-sequencing. *PLoS Pathog*. 6:e1000834.

Carr, H.Y., and Purcell, E.M. 1954. Effects of Diffusion on Free Precession in Nuclear Magnetic Resonance Experiments. *Physical Review*. 94:630-638.

Chayen, N.E. 2004. Turning protein crystallisation from an art into a science. *Curr Opin Struct Biol*. 14:577-583.

Chayen, N.E., and Saridakis, E. 2008. Protein crystallization: from purified protein to diffraction-quality crystal. *Nat Methods*. 5:147-153.

Chen, C., and Beattie, G.A. 2008. Pseudomonas syringae BetT is a low-affinity choline transporter that is responsible for superior osmoprotection by choline over glycine betaine. *J Bacteriol*. 190:2717-2725.

Chen, T., Siu, L., Lee, Y., Chen, C., Huang, L., Wu, R.C., Cho, W., and Fung, C. 2008. Acinetobacter baylyi as a Pathogen for Opportunistic Infection. *J Clin Microbiol*. 46:2938-2944.

Chung, C.T., Niemela, S.L., and Miller, R.H. 1989. One-step preparation of competent Escherichia coli: transformation and storage of bacterial cells in the same solution. *Proc Natl Acad Sci U S A*. 86:2172-2175.

Claxton, D.P., Quick, M., Shi, L., de Carvalho, F.D., Weinstein, H., Javitch, J.A., and McHaourab, H.S. 2010. Ion/substrate-dependent conformational dynamics of a bacterial homolog of neurotransmitter:sodium symporters. *Nature structural & molecular biology*. 17:822-829.

Dauter, Z. 1999. Data-collection strategies. *Acta Cryst.* 55:1703-1717.

de Berardinis, V., Durot, M., Weissenbach, J., and Salanoubat, M. 2009. Acinetobacter baylyi ADP1 as a model for metabolic system biology. *Curr Opin Microbiol*. 12:568-576.

Devant, J. 2014. Cholin-Transporter der BCCT-Famile. *Bachelorarbeit Goethe Universität Frankfurt*.

Dinnbier, U., Limpinsel, E., Schmid, R., and Bakker, E.P. 1988. Transient accumulation of potassium glutamate and its replacement by trehalose during adaptation of growing cells of Escherichia coli K-12 to elevated sodium chloride concentrations. *Arch Microbiol*. 150:348-357.

Doughari, H.J., Ndakidemi, P.A., Human, I.S., and Benade, S. 2011. The Ecology, Biology and Pathogenesis of Acinetobacter spp.: An Overview. *Microbes and Environments*. 26:101-112.

Eichler, K., Bourgis, F., Buchet, A., Kleber, H.P., and Mandrandberthelot, M.A. 1994. Molecular Characterization of the Cai Operon Necessary for Carnitine Metabolism in Escherichia-Coli. *Molecular Microbiology*. 13:775-786.

Elliot, J., and Janik, A. 1969. Transformation of Acinetobacter calo-aceticus (Bacterium anitratum). *J Bacteriol.* 98:281-288.

Faham, S., Watanabe, A., Besserer, G.M., Cascio, D., Specht, A., Hirayama, B.A., Wright, E.M., and Abramson, J. 2008. The crystal structure of a sodium galactose transporter reveals mechanistic insights into Na+/sugar symport. *Science*. 321:810-814.

Fan, X., Pericone, C.D., Lysenko, E., Goldfine, H., and Weiser, J.N. 2003. Multiple mechanisms for choline transport and utilization in Haemophilus influenzae. *Molecular Microbiology*. 50:537-548.

Fang, Y., Jayaram, H., Shane, T., Kolmakova-Partensky, L., Wu, F., Williams, C., Xiong, Y., and Miller, C. 2009. Structure of a prokaryotic virtual proton pump at 3.2 A resolution. *Nature*. 460:1040-1043.

Farwick, M., Siewe, R.M., and Krämer, R. 1995. Glycine Betaine Uptake after Hyperosmotic Shift in Corynebacterium glutamicum. *J Bacteriol*. 177:4690-4695.

Forrest, L.R., Krämer, R., and Ziegler, C. 2011. The structural basis of secondary active transport mechanisms. *Biochim Biophys Acta*. 1807:167-188.

Forrest, L.R., Zhang, Y.W., Jacobs, M.T., Gesmonde, J., Xie, L., Honig, B.H., and Rudnick, G. 2008. Mechanism for alternating access in neurotransmitter transporters. *Proc Natl Acad Sci U S A*. 105:10338-10343.

Förster, T. 1948. Zwischenmolekulare Energiewanderung Und Fluoreszenz. *Annalen Der Physik*. 2:55-75.

Garman, E. 1999. Cool data: quantity AND quality. *Acta Crystallogr D Biol Crystallogr*. 55:1641-1653.

Gärtner, R.M. 2014. Towards a molecular mechanism of ectoine transport. *Dissertation Goethe Universität Frankfurt*.

Gärtner, R.M., Perez, C., Koshy, C., and Ziegler, C. 2011. Role of bundle helices in a regulatory crosstalk in the trimeric betaine transporter BetP. *J Mol Biol*. 414:327-336.

Gasteiger, E., Wilkins, M.R., Bairoch, A., Sanchez, J.C., Williams, K.L., Appel, R.D., and Hochstrasser, D.F. 1999. protein identification and analysis tools on the expasy server. *Methods Mol Biol*. 112:531-552.

Ge, L., Perez, C., Waclawska, I., Ziegler, C., and Muller, D.J. 2011. Locating an extracellular K+-dependent interaction site that modulates betaine-binding of the Na+-coupled betaine symporter BetP. *Proc Natl Acad Sci U S A*. 108:E890-898.

Georgieva, E.R., Borbat, P.P., Ginter, C., Freed, J.H., and Boudker, O. 2013. Conformational ensemble of the sodium-coupled aspartate transporter. *Nature structural & molecular biology*. 20:215-221.

Giacomini, K.M., and Sugiyama, Y. 2011. Chapter 5. Membrane Transporters and Drug Response. *New York McGraw-Hill*.

Goldschmidt, L., Cooper, D.R., Derewenda, Z.S., and Eisenberg, D. 2007. Toward rational protein crystallization: A Web server for the design of crystallizable protein variants. *Protein Sci*. 16:1569-1576.

Gourdon, P., Andersen, J.L., Hein, K.L., Bublitz, M., Pedersen, B.P., Liu, X.Y., Yatime, L., Nyblom, M., Nielsen, T.T., Olesen, C., Moller, J.V., Nissen, P., and Morth, J.P. 2011. HiLiDe-Systematic Approach to Membrane Protein Crystallization in Lipid and Detergent. *Crystal Growth & Design*. 11:2098-2106.

Gutmann, D.A., Mizohata, E., Newstead, S., Ferrandon, S., Postis, V., Xia, X., Henderson, P.J., van Veen, H.W., and Byrne, B. 2007. A high-throughput method for membrane protein solubility screening: the ultracentrifugation dispersity sedimentation assay. *Protein Sci*. 16:1422-1428.

Haardt, M., Kempf, B., Faatz, E., and Bremer, E. 1995. The osmoprotectant proline betaine is a major substrate for the binding-protein-dependent transport system ProP of Escherichia coli K-12. *Mol Gen Genet*. 246:783-786.

Hänelt, I., Wunnicke, D., Bordignon, E., Steinhoff, H.J., and Slotboom, D.J. 2013. Conformational heterogeneity of the aspartate transporter Glt(Ph). *Nature structural & molecular biology*. 20:210-214.

Hellmich, U.A., and Glaubitz, C. 2009. NMR and EPR studies of membrane transporters. *Biol Chem*. 390:815-834.

Hisamitsu, T., Pang, T., Shigekawa., M., and Wakabayashi, S. 2004. Dimeric Interaction between the Cytoplasmic Domains of the Na+/H+ Exchanger NHE1 Revealed by Symmetrical Intermolecular Cross-Linking and Selective Co-immunoprecipitation. *Biochemistry*. 43:11135-11143.

Hoischen, C., and Krämer, R. 1990. Membrane Alteration Is Necessary but Not Sufficient for Effective Glutamate Secretion in Corynebacterium glutamicum. *J Bacteriol.* 172:3409-3416.

Holtmann, G., and Bremer, E. 2004. Thermoprotection of Bacillus subtilis by Exogenously Provided Glycine Betaine and Structurally Related Compatible Solutes: Involvement of Opu Transporters. *Journal of Bacteriology*. 186:1683-1693.

Horie, A., Ishida, K., Watanabe, Y., Shibata, K., and Hashimoto, Y. 2014. Membrane transport mechanisms of choline in human intestinal epithelial LS180 cells. *Biopharm Drug Dispos*. 35:532-542.

Hubbell, W.L., and Altenbach, C. 1994. Investigation of structure and dynamics in membrane proteins using site-directed spin labeling. *Current Opinion in Structural Biology*. 4:566-573.

Ilari, A., and Savino, C. 2008. Protein structure determination by x-ray crystallography. *Methods Mol Biol*. 452:63-87.

Jacobs, A.C., Hood, I., Boyd, K.L., Olson, P.D., Morrison, J.M., Carson, S., Sayood, K., Iwen, P.C., Skaar, E.P., and Dunman, P.M. 2010. Inactivation of phospholipase D diminishes Acinetobacter baumannii pathogenesis. *Infection and immunity*. 78:1952-1962.

Jardetzky, O. 1966. Simple allosteric model for membrane pumps. *Nature*. 211:969-970.

Jeschke, G. 2012. DEER distance measurements on proteins. *Annu Rev Phys Chem*. 63:419-446.

Jeschke, G., Chechik, V., Ionita, P., Godt, A., Zimmermann, H., Banham, J., Timmel, C.R., Hilger, D., and Jung, H. 2006. DeerAnalysis2006 - a Comprehensive Software Package for Analyzing Pulsed ELDOR Data. *App. Magn. Reson.* 30:473-498.

Jung, H., Buchholz, M., Clausen, J., M., N., Revermann, A., Schmid, R., and Jung, K. 2002. CaiT of Escherichia coli, a new tranporter catalyzing L-carnitine/gamma-butyrobetaine exchange. *J Biol Chem*. 277:39251-39258.

Junttila, J., and Brander, M. 1989. Listeria monocytogenes Septicemia Associated with Consumption of Salted Mushrooms. *Scand J Infect Dis*. 21:119-342.

Kapfhammer, D., Karatan, E., Pflughoeft, K.J., and Watnick, P.I. 2005. Role for glycine betaine transport in Vibrio cholerae osmoadaptation and biofilm formation within microbial communities. *Applied and environmental microbiology*. 71:3840-3847.

Kappes, R.M., Kempf, B., and Bremer, E. 1996. Three transport systems for the osmoprotectant glycine betaine operate in Bacillus subtilis: characterization of OpuD. *J Bacteriol*. 178:5071-5079.

Kazmier, K., Sharma, S., Islam, S.M., Roux, B., and McHaourab, H.S. 2014a. Conformational cycle and ion-coupling mechanism of the Na+/hydantoin transporter Mhp1. *Proc Natl Acad Sci U S A*. 111:14752–14757.

Kazmier, K., Sharma, S., Quick, M., Islam, S.M., Roux, B., Weinstein, H., Javitch, J.A., and McHaourab, H.S. 2014b. Conformational dynamics of ligand-dependent alternating access in LeuT. *Nature structural & molecular biology*. 21:472-479.

Kempf, B., and Bremer, E. 1998. Uptake and synthesis of compatible solutes as microbial stress responses to high-osmolality environments. *Arch Microbiol*. 170:319–330.

Kempf, M., and Rolain, J.M. 2012. Emergence of resistance to carbapenems in Acinetobacter baumannii in Europe: clinical impact and therapeutic options. *International journal of antimicrobial agents*. 39:105-114.

Khafizov, K., Perez, C., Koshy, C., Quick, M., Fendler, K., Ziegler, C., and Forrest, L.R. 2012. Investigation of the sodium-binding sites in the sodium-coupled betaine transporter BetP. *Proc Natl Acad Sci U S A*. 109:E3035-3044.

Khafizov, K., Staritzbichler, R., Stamm, M., and Forrest, L.R. 2010. A study of the evolution of inverted-topology repeats from LeuT-fold transporters using AlignMe. *Biochemistry*. 49:10702-10713.

Killmann, H., Benz, R., and Braun, V. 1996. Properties of the FhuA channel in the Escherichia coli outer membrane after deletion of FhuA portions within and outside the predicted gating loop. *J Bacteriol*. 178:6913-6920.

Klare, J.P., and Steinhoff, H.J. 2009. Spin labeling EPR. *Photosynthesis research*. 102:377-390.

Kleber, H.-P., Seim, H., Aurich, H., and Strack, E. 1977. Verwertung von Trimethylammoniumverbindungen durch Acinetobacter calcoaceticus. *Arch Microbiol*. 112:201-206.

Koshy, C. 2014. Insights into the functional and regulatory mechanisms of the osmoregulated Na+/glycine betaine symporter BetP from Corynebacterium glutamicum: A structural and computational study. *Dissertation Goethe Universität Frankfurt*.

Koshy, C., Schweikhard, E.S., Gartner, R.M., Perez, C., Yildiz, O., and Ziegler, C. 2013. Structural evidence for functional lipid interactions in the betaine transporter BetP. *EMBO J*. 32:3096-3105.

Krämer, R., and Ziegler, C. 2009. Regulative interactions of the osmosensing C-terminal domain in the trimeric glycine betaine transporter BetP from Corynebacterium glutamicum. *Biol Chem*. 390:685-691.

Krishnamurthy, H., and Gouaux, E. 2012. X-ray structures of LeuT in substrate-free outward-open and apo inward-open states. *Nature*. 481:469-474.

Krogh, A., Larsson, B., von Heijne, G., and Sonnhammer, E.L.L. 2001. Predicting Transmembrane Protein Topology with a Hidden Markov Model: Application to Complete Genome. *JMB.* 305:567-580.

Kuhlmann, A.U., Hoffmann, T., Bursy, J., Jebbar, M., and Bremer, E. 2011. Ectoine and hydroxyectoine as protectants against osmotic and cold stress: uptake through the SigB-controlled betaine-choline- carnitine transporter-type carrier EctT from Virgibacillus pantothenticus. *J Bacteriol.* 193:4699-4708.

Kyhse-Andersen, J. 1984. Electroblotting of Multiple Gels: a Simple Apparatus without Buffer Tank for Rapid Transfer of Proteins from Polyacrylamide to Nitrocellulose. *Journal of Biochemical and Biophysical Methods.* 10:203-209.

La Scola, B., and Raoult, D. 2004. Acinetobacter baumannii in human body louse. *Emerg Infect Dis.* 10:1671-1673.

Laemmli, U.K. 1970. Cleavage of Structural Proteins during the Assembly of the Head of Bacteriophage T4. *Nature.* 227:680-685.

Laloknam, S., Tanaka, K., Buaboocha, T., Waditee, R., Incharoensakdi, A., Hibino, T., Tanaka, Y., and Takabe, T. 2006. Halotolerant cyanobacterium Aphanothece halophytica contains a betaine transporter active at alkaline pH and high salinity. *Applied and environmental microbiology.* 72:6018-6026.

Lamark, T., Kaasen, I., Eshoo, M.W., Falkenberg, P., McDougall, J., and Strøm, A.R. 1991. DNA sequence and analysis of the bet genes encoding the osmoregulatory choline?glycine betaine pathway of Escherichia coli. *Molecular Microbiology.* 5:1049-1064.

Loque, D., Lalonde, S., Looger, L.L., von Wiren, N., and Frommer, W.B. 2007. A cytosolic trans-activation domain essential for ammonium uptake. *Nature.* 446:195-198.

Loque, D., Yuan, L., Kojima, S., Gojon, A., Wirth, J., Gazzarrini, S., Ishiyama, K., Takahashi, H., and von Wiren, N. 2006. Additive contribution of AMT1;1 and AMT1;3 to high-affinity ammonium uptake across the plasma membrane of nitrogen-deficient Arabidopsis roots. *Plant J.* 48:522-534.

Lozano, E., Herraez, E., Briz, O., Robledo, V.S., Hernandez-Iglesias, J., Gonzalez-Hernandez, A., and Marin, J.J. 2013. Role of the plasma membrane transporter of organic cations OCT1 and its genetic variants in modern liver pharmacology. *Biomed Res Int.* 2013:692071.

Lu, W., Zhao, B., Feng, D., and Yang, S. 2004. Cloning and characterization of the Halobacillus trueperi betH gene, encoding the transport system for the compatible solute glycine betaine. *FEMS microbiology letters.* 235:393-399.

Lund, A., Shiotani, M., and Shimada, S. 2011. Principles and Applications of ESR Spectroscopy. *Springer.*

Ly, A., Henderson, J., Lu, A., Culham, D.E., and Wood, J.M. 2003. Osmoregulatory Systems of Escherichia coli: Identification of Betaine-Carnitine-Choline Transporter Family Member BetU and Distributions of betU and trkG among Pathogenic and Nonpathogenic Isolates. *Journal of Bacteriology.* 186:296-306.

Madej, M.G., Soro, S.N., and Kaback, H.R. 2012. Apo-intermediate in the transport cycle of lactose permease (LacY). *Proc Natl Acad Sci U S A.* 109:E2970-2978.

Magoon, M.W., Wright, J.R., Baritussio, A., Williams, M.C., Goerke, J., Benson, B.J., Hamilton, R.L., and Clements, J.A. 1982. Subfractionation of Lung Surfactant: Implications for Metabolism and Surface Activity. *Biochimica et Biophysica Acta.* 750:18-31.

Mahmood, N.A., Biemans-Oldehinkel, E., Patzlaff, J.S., Schuurman-Wolters, G.K., and Poolman, B. 2006. Ion specificity and ionic strength dependence of the osmoregulatory ABC transporter OpuA. *J Biol Chem.* 281:29830-29839.

Malek, A.A., Chen, C., Wargo, M.J., Beattie, G.A., and Hogan, D.A. 2011. Roles of three transporters, CbcXWV, BetT1, and BetT3, in Pseudomonas aeruginosa choline uptake for catabolism. *J Bacteriol.* 193:3033-3041.

Malo, M.E., and Fliegel, L. 2006. Physiological role and regulation of the Na+/H+ exchanger. C*an J Physiol Pharmacol.* 84:1081-1095.

Maximov, S., Ott, V., Belkoura, L., and Krämer, R. 2014. Stimulus analysis of BetP activation under in vivo conditions. *Biochim Biophys Acta.* 1838:1288-1295.

McGuffin, L.J., Bryson, K., and Jones, D.T. 2000. The PSIPRED protein structure prediction server. *Bioinformatics Applications Note.* 16:404-405.

Mchaourab, H.S., Steed, P.R., and Kazmier, K. 2011. Toward the fourth dimension of membrane protein structure: insight into dynamics from spin-labeling EPR spectroscopy. *Structure.* 19:1549-1561.

McRee, D.E. 1993. Practical protein crystallography. *San Diego: Academic Press.*

Meiboom, S., and Gill, D. 1958. Modified Spin-Echo Method for Measuring Nuclear Relaxation Times. *Review of Scientific Instruments.* 29:688.

Messerschmidt, A. 2007. X-Ray Crystallography of Biomacromolecules. *WILEY-VCH Verlag GmbH & Co. KGaA*

Michel, V., Yuan, Z., Ramsubir, S., and Bakovic, M. 2006. Choline transport for phospholipid synthesis. *Exp Biol Med (Maywood).* 231:490-504.

Miller, A., and Tanner, J. 2008. Essentials of Chemical Biology: Structure and Dynamics of Biological Macromolecules. *Wiley.*

Milov, A.D., Ponomarev, A.B., and Tsvetkov, Y.D. 1984. Electron Electron Double-Resonance in Electron-Spin Echo - Model Biradical Systems and the Sensitized Photolysis of Decalin. *Chemical Physics Letters.* 110:67-72.

Moore, T.S. 1990. Biosynthesis of phosphatidylinositol. *Inositol Metab Plant.* 9:107-112.

Morbach, S., and Krämer, R. 2005. Structure and function of the betaine uptake system BetP of Corynebacterium glutamicum: strategies to sense osmotic and chill stress. *J Mol Microbiol Biotechnol.* 10:143-153.

Motulsky, H. 1999. Analyzing Data with GraphPad Prism. G*raphPad Software, Inc.*

Mullis, K.B., and Faloona, F.A. 1987. Specific synthesis of DNA in vitro via a polymerase-catalyzed chain reaction. *Methods in enzymology.* 155:335-350.

Murakami, S., Nakashima, R., Yamashita, E., Matsumoto, T., and Yamaguchi, A. 2006. Crystal structures of a multidrug transporter reveal a functionally rotating mechanism. *Nature.* 443:173-179.

Murphy, D.M. 2009. EPR (Electron Paramagnetic Resonance) Spectroscopy of Polycrystalline Oxide Systems. *WILEY-VCH Verlag GmbH & Co. KGaA.*

Nakata, T., Matsui, T., Kobayashi, K., Kobayashi, Y., and Anzai, N. 2013. Organic cation transporter 2 (SLC22A2), a low-affinity and high-capacity choline transporter, is preferentially enriched on synaptic vesicles in cholinergic neurons. *Neuroscience.* 252:212-221.

Naughton, L.M., Blumerman, S.L., Carlberg, M., and Boyd, E.F. 2009. Osmoadaptation among Vibrio species and unique genomic features and physiological responses of Vibrio parahaemolyticus. *Applied and environmental microbiology.* 75:2802-2810.

Nicklisch, S.C., Wunnicke, D., Borovykh, I.V., Morbach, S., Klare, J.P., Steinhoff, H.J., and Krämer, R. 2012. Conformational changes of the betaine transporter BetP from Corynebacterium glutamicum studied by pulse EPR spectroscopy. *Biochim Biophys Acta.* 1818:359-366.

Oren, A. 1999. Bioenergetic aspects of halophilism. *Microbiol Mol Biol Rev.* 63:334-348.

Oswald, C., Smits, S.H., Hoing, M., Sohn-Bosser, L., Dupont, L., Le Rudulier, D., Schmitt, L., and Bremer, E. 2008. Crystal structures of the choline/acetylcholine substrate-binding protein ChoX from Sinorhizobium meliloti in the liganded and unliganded-closed states. *J Biol Chem.* 283:32848-32859.

Ott, V., Koch, J., Spate, K., Morbach, S., and Krämer, R. 2008. Regulatory properties and interaction of the C- and N-terminal domains of BetP, an osmoregulated betaine transporter from Corynebacterium glutamicum. *Biochemistry.* 47:12208-12218.

Özcan, N., Ejsing, C.S., Shevchenko, A., Lipski, A., Morbach, S., and Krämer, R. 2007. Osmolality, temperature, and membrane lipid composition modulate the activity of betaine transporter BetP in Corynebacterium glutamicum. J *Bacteriol.* 189:7485-7496.

Özcan, N., Krämer, R., and Morbach, S. 2005. Chill activation of compatible solute transporters in Corynebacterium glutamicum at the level of transport activity. *J Bacteriol.* 187:4752-4759.

Pannier, M., Veit, S., Godt, A., Jeschke, G., and Spiess, H.W. 2000. Dead-Time Free Measurement of Dipole–Dipole Interactions between Electron Spins. *J Magn Reson*. 142: 331-340.

Peleg, A.Y., Seifert, H., and Paterson, D.L. 2008. Acinetobacter baumannii: emergence of a successful pathogen. *Clin Microbiol Rev.* 21:538-582.

Perez, C. 2012. Structural and functional studies on the osmoregulated trimeric Na+/betaine symporter BetP from Corynebacterium glutamicum. *Dissertation Goethe Universität Frankfurt.*

Perez, C., Faust, B., Mehdipour, A.R., Francesconi, K.A., Forrest, L.R., and Ziegler, C. 2014. Substrate-bound outward-open state of the betaine transporter BetP provides insights into Na+ coupling. *Nature communications.* 5:4231.

Perez, C., Khafizov, K., Forrest, L.R., Krämer, R., and Ziegler, C. 2011a. The role of trimerization in the osmoregulated betaine transporter BetP. *EMBO Rep.* 12:804-810.

Perez, C., Koshy, C., Ressl, S., Nicklisch, S., Krämer, R., and Ziegler, C. 2011b. Substrate specificity and ion coupling in the Na+/betaine symporter BetP. *EMBO J.* 30:1221-1229.

Perez, C., Koshy, C., Yildiz, O., and Ziegler, C. 2012. Alternating-access mechanism in conformationally asymmetric trimers of the betaine transporter BetP. N*ature.* 490:126-130.

Pesin, S.R., and Candia, O.A. 1982. Acetylcholine concentration and its role in ionic transport by the corneal epithelium. *Invest. Ophthalmol. Vis. Sci.* 22:651-659.

Peter, H., Burkovski, A., and Krämer, R. 1996. Isolation, characterization, and expression of the Corynebacterium glutamicum betP gene, encoding the transport system for the compatible solute glycine betaine. *J Bacteriol.* 178:5229-5234.

Peter, H., Burkovski, A., and Krämer, R. 1998a. Osmo-sensing by N- and C-terminal extensions of the glycine betaine uptake system BetP of Corynebacterium glutamicum. *J Biol Chem.* 273:2567-2574.

Peter, H., Weil, B., Burkovski, A., Krämer, R., and Morbach, S. 1998b. Corynebacterium glutamicum Is Equipped with Four Secondary Carriers for Compatible Solutes: Identification, Sequencing, and Characterization of the Proline/Ectoine Uptake System, ProP, and the Ectoine/Proline/Glycine Betaine Carrier, EctP. *J Bacteriol.* 180:6005-6012.

Pieper, U., Webb, B.M., Dong, G.Q., Schneidman-Duhovny, D., Fan, H., Kim, S.J., Khuri, N., Spill, Y.G., Weinkam, P., Hammel, M., Tainer, J.A., Nilges, M., and Sali, A. 2014. ModBase, a database of annotated comparative protein structure models and associated resources. *Nucleic Acids Res.* 42:D336-346.

Polyhach, Y., Bordignon, E., and Jeschke, G. 2011. Rotamer libraries of spin labelled cysteines for protein studies. *Phys Chem Chem Phys.* 13:2356-2366.

Polyhach, Y., and Jeschke, G. 2010. Prediction of favourable sites for spin labelling of proteins. *Spectroscopy.* 24:651-659.

Prasad, R. 1996. Manual on Membrane Lipids. *Springer.*

Rath, A., and Deber, C.M. 2013. Correction factors for membrane protein molecular weight readouts on sodium dodecyl sulfate-polyacrylamide gel electrophoresis. *Anal Biochem.* 434:67-72.

Reginsson, G.W., and Schiemann, O. 2011a. Pulsed-electron-electron double resonance: beyond nanometre distance measurements on biomolecules. *Biochem J.* 353-363:353-363.

Reginsson, G.W., and Schiemann, O. 2011b. Studying biomolecular complexes with pulsed electron-electron double resonance spectroscopy. *Biochemical Society transactions.* 39:128-139.

Ressl, S., Terwisscha van Scheltinga, A.C., Vonrhein, C., Ott, V., and Ziegler, C. 2009. Molecular basis of transport and regulation in the Na(+)/betaine symporter BetP. *Nature.* 458:47-52.

Reyes, N., Ginter, C., and Boudker, O. 2009. Transport mechanism of a bacterial homologue of glutamate transporters. *Nature.* 462:880-885.

Rigaud, J.L., Pitard, B., and Levy, D. 1995. Reconstitution of Membrane-Proteins into Liposomes - Application to Energy-Transducing Membrane-Proteins. B*iochimica Et Biophysica Acta-Bioenergetics.* 1231:223-246.

Robert, X., and Gouet, P. 2014. Decephering key features in protein structures with the new ENDscript server. *Nucleic Acids Res.* 42:320-324.

Rosenstein, R., Futter-Bryniok, D., and Gotz, F. 1999. The choline-converting pathway in Staphylococcus xylosus C2A: genetic and physiological characterization. *J Bacteriol.* 181:2273-2278.

Rübenhagen, R., Morbach, S., and Krämer, R. 2001. The osmoreactive betaine carrier BetP from Corynebacterium glutamicum is a sensor for cytoplasmic K+. *EMBO J.* 20:5412-5420.

Rübenhagen, R., Rönsch, H., Jung, H., Krämer, R., and Morbach, S. 2000. Osmosensor and Osmoregulator Properties of the Betaine Carrier BetP from Corynebacterium glutamicum in Proteoliposomes. *J Biol Chem.* 275:735-741.

Saier, M.H., Yen, M.R., Noto, K., Tamang, D.G., and Elkan, C. 2009. The Transporter Classification Database: recent advances. *Nucleic Acids Res.* 37.

Sand, M., de Berardinis, V., Mingote, A., Santos, H., Gottig, S., Muller, V., and Averhoff, B. 2011. Salt adaptation in Acinetobacter baylyi: identification and characterization of a secondary glycine betaine transporter. *Arch Microbiol.* 193:723-730.

Sand, M., Mingote, A.I., Santos, H., Muller, V., and Averhoff, B. 2013. Mannitol, a compatible solute synthesized by Acinetobacter baylyi in a two-step pathway including a salt-induced and salt-dependent mannitol-1-phosphate dehydrogenase. *Environmental microbiology.* 15:2187-2197.

Sand, M., Stahl, J., Waclawska, I., Ziegler, C., and Averhoff, B. 2014. Identification of an osmo-dependent and an osmo-independent choline transporter in Acinetobacter baylyi: implications in osmostress protection and metabolic adaptation. *Environmental microbiology.* 16:1490-1502.

Schaffner, W., and Weissmann, C. 1973. A rapid, sensitive, and specific method for the determination of protein in dilute solution. *Anal Biochem.* 56:502-514.

Schägger, H., and von Jagow, G. 1991. Blue native electrophoresis for isolation of membrane protein complexes in enzymatically active form. *Anal Biochem.* 199:223-231.

Schiemann, O., Piton, N., Plackmeyer, J., Bode, B.E., Prisner, T.F., and Engels, J.W. 2007. Spin labeling of oligonucleotides with the nitroxide TPA and use of PELDOR, a pulse EPR method, to measure intramolecular distances. *Nature protocols.* 2:904-923.

Schiller, D., Krämer, R., and Morbach, S. 2004. Cation specificity of osmosensing by the betaine carrier BetP of Corynebacterium glutamicum. *FEBS Lett.* 563:108-112.

Schiller, D., Ott, V., Krämer, R., and Morbach, S. 2006. Influence of membrane composition on osmosensing by the betaine carrier BetP from Corynebacterium glutamicum. *J Biol Chem.* 281:7737-7746.

Schmidt, T.G.M., Koepke, J., Frank, R., and Skerra, A. 1996. Molecular interaction between the Strep-tag affinity peptide and its cognate target, streptavidin. *Journal of Molecular Biology.* 255:753-766.

Schulze, S., Koster, S., Geldmacher, U., Terwisscha van Scheltinga, A.C., and Kuhlbrandt, W. 2010. Structural basis of Na(+)-independent and cooperative substrate/product antiport in CaiT. *Nature.* 467:233-236.

Seeger, M.A., Schiefner, A., Eicher, T., Verrey, F., Diederichs, K., and Pos, K.M. 2006. Structural Asymmetry of AcrB Trimer Suggests a Peristaltic Pump Mechanism. *Science.* 313:1295-1298.

Shaffer, P.L., Goehring, A., Shankaranarayanan, A., and Gouaux, E. 2009. Structure and mechanism of a Na+-independent amino acid transporter. *Science.* 325:1010-1014.

Sheehan, D. 2009. Physical Biochemistry: Principles and Applications. *Wiley.*

Shimamura, T., Weyand, S., Beckstein, O., Rutherford, N.G., Hadden, J.M., Sharples, D., Sansom, M.S.P., Iwata, S., Henderson, P.J.F., and Cameron, A.D. 2010. Molecular Basis of Alternating Access Membrane Transport by the Sodium-Hydantoin Transporter Mhp1. *Science.* 328:470-473.

Slabinski, L., Jaroszewski, L., Rychlewski, L., Wilson, I.A., Lesley, S.A., and Godzik, A. 2007. XtalPred: a web server for prediction of protein crystallizability. *Bioinformatics* 23:3403-3405.

Sleator, R.D., Gahan, C.G., Abee, T., and Hill, C. 1999. Identification and disruption of BetL, a secondary glycine betaine transport system linked to the salt tolerance of Listeria monocytogenes LO28. *Applied and environmental microbiology.* 65:2078-2083.

Sleator, R.D., and Hill, C. 2001. Bacterial osmoadaptation: the role of osmolytes in bacterial stress and virulence. *FEMS Microbiology Reviews.* 26:49-71.

Slepkov, E.R., Rainey, J.K., Sykes, B.D., and Fliegel, L. 2007. Structural and functional analysis of the Na+/H+ exchanger. *Biochem J.* 401:623-633.

Smirnova, I., Kasho, V., Choe, J.Y., Altenbach, C., Hubbell, W.L., and Kaback, H.R. 2007. Sugar binding induces an outward facing conformation of LacY. *Proc Natl Acad Sci U S A.* 104:16504-16509.

Son, M.S., Matthews, W.J., Jr., Kang, Y., Nguyen, D.T., and Hoang, T.T. 2007. In vivo evidence of Pseudomonas aeruginosa nutrient acquisition and pathogenesis in the lungs of cystic fibrosis patients. *Infection and immunity.* 75:5313-5324.

Spindler, P.E., Waclawska, I., Endeward, B., Plackmeyer, J., Ziegler, C., and Prisner, T. 2015. Carr-Purcell Pulsed Electron Double Resonance with shaped inversion pulses. *J Phys Chem Lett*. DOI:10.1021/acs.jpclett.5b01933

Spyropoulos, I.C., Liakopoulos, T.D., Bagos, P.G., and Hamodrakas, S.J. 2004. TMRPres2D: high quality visual representation of transmembrane protein models. *Bioinformatics.* 20:3258-3260.

Steger, R., Weinand, M., Krämer, R., and Morbach, S. 2004. LcoP, an osmoregulated betaine/ectoine uptake system from Corynebacterium glutamicum. *FEBS Lett.* 573:155-160.

Studier, F.W. 2005. Protein production by auto-induction in high-density shaking cultures. *Protein Expression and Purification.* 41:207-234.

Tang, L., Bai, L., Wang, W.H., and Jiang, T. 2010. Crystal structure of the carnitine transporter and insights into the antiport mechanism. *Nature structural & molecular biology.* 17:492-496.

Todd, J.D., Curson, A.R., Nikolaidou-Katsaraidou, N., Brearley, C.A., Watmough, N.J., Chan, Y., Page, P.C., Sun, L., and Johnston, A.W. 2010. Molecular dissection of bacterial acrylate catabolism--unexpected links with dimethylsulfoniopropionate catabolism and dimethyl sulfide production. *Environmental microbiology.* 12:327-343.

Tondervik, A., and Strom, A.R. 2007. Membrane topology and mutational analysis of the osmotically activated BetT choline transporter of Escherichia coli. *Microbiology.* 153:803-813.

Traiffort, E., O'Regan, S., and Ruat, M. 2013. The choline transporter-like family SLC44: properties and roles in human diseases. *Mol Aspects Med.* 34:646-654.

Truong, K., and Ikura, M. 2001. The use of FRET imaging microscopy to detect protein–protein interactions and protein conformational changes in vivo. *Curr Opin Struct Biol.* 11:573-578.

Tsai, C.J., Khafizov, K., Hakulinen, J., Forrest, L.R., Krämer, R., Kuhlbrandt, W., and Ziegler, C. 2011. Structural asymmetry in a trimeric Na+/betaine symporter, BetP, from Corynebacterium glutamicum. *J Mol Biol.* 407:368-381.

Tsai, C.J., and Ziegler, C. 2005. Structure determination of secondary transport proteins by electron crystallography: two-dimensional crystallization of the betaine uptake system BetP. *J Mol Microbiol Biotechnol.* 10:197-207.

Tsatskis, Y., Khambati, J., Dobson, M., Bogdanov, M., Dowhan, W., and Wood, J.M. 2005. The osmotic activation of transporter ProP is tuned by both its C-terminal coiled-coil and osmotically induced changes in phospholipid composition. *J Biol Chem.* 280:41387-41394.

Tsatskis, Y., Kwok, S.C., Becker, E., Gill, C., Smith, M.N., Keates, R.A.B., Hodges, R.S., and Wood, J.M. 2008. Core Residue Replacements Cause Coiled-Coil Orientation Switching in Vitro and in ViVo: Structure-Function Correlations for Osmosensory Transporter ProP. *Biochemistry.* 47:60-72.

Vallenet, D., Nordmann, P., Barbe, V., Poirel, L., Mangenot, S., Bataille, E., Dossat, C., Gas, S., Kreimeyer, A., Lenoble, P., Oztas, S., Poulain, J., Segurens, B., Robert, C., Abergel, C., Claverie, J.M., Raoult, D., Medigue, C., Weissenbach, J., and Cruveiller, S. 2008. Comparative Analysis of Acinetobacters: Three Genomes for Three Lifestyles. *Plos One.* 3:e1805

Van Dort, H.M., Knowles, D.W., Chasis, J.A., Lee, G., Mohandas, N., and Low, P.S. 2001. Analysis of integral membrane protein contributions to the deformability and stability of the human erythrocyte membrane. *J Biol Chem.* 276:46968-46974.

Verdon, G., and Boudker, O. 2012. Crystal structure of an asymmetric trimer of a bacterial glutamate transporter homolog. *Nature structural & molecular biology.* 19:355-357.

Vermeulen, V., and Kunte, H.J. 2004. Marinococcus halophilus DSM 20408T encodes two transporters for compatible solutes belonging to the betaine-carnitine-choline transporter family: identification and characterization of ectoine transporter EctM and glycine betaine transporter BetM. *Extremophiles: life under extreme conditions.* 8:175-184.

Von Hagens, T., Polyhach, Y., Sajid, M., Godt, A., and Jeschke, G. 2013. Suppression of ghost distances in multiple-spin double electron-electron resonance. *Phys Chem Chem Phys.* 15:5854-5866.

Waclawska, I., and Ziegler, C. 2015. Regulatory role of charged clusters in the N-terminal domain of BetP from *Corynebacterium glutamicum*. *Biol. Chem.* 396: 1117-1126

Warburg, O., and Christian, W. 1942. Insulation and crystalisation of the fermenting process of Enolase. *Biochem Z.* 310:384-421.

Weinand, M., Krämer, R., and Morbach, S. 2007. Characterization of compatible solute transporter multiplicity in Corynebacterium glutamicum. *Applied microbiology and biotechnology.* 76:701-708.

Weyand, S., Shimamura, T., Yajima, S., Suzuki, S., Mirza, O., Krusong, K., Carpenter, E.P., Rutherford, N.G., Hadden, J.M., O'Reilly, J., Ma, P., Saidijam, M., Patching, S.G., Hope, R.J., Norbertczak, H.T., Roach, P.C.J., Iwata, S., Henderson, P.J.F., and Cameron, A.D. 2008. Structure and Molecular Mechanism of a Nucleobase-Cation-Symport-1 Family Transporter. *Science.* 322:709-713.

Wolf, A., Krämer, R., and Morbach, S. 2003. Three pathways for trehalose metabolism in Corynebacterium glutamicum ATCC13032 and their significance in response to osmotic stress. *Molecular Microbiology.* 49:1119-1134.

Yamada, K., Yanagihara, K., Araki, N., Harada, Y., Morinaga, Y., Akamatsu, N., Matsuda, J., Izumikawa, K., Kakeya, H., Yamamoto, Y., Hasegawa, H., Kohno, S., and Kamihira, S. 2012. Clinical Characteristics of Tertiary Hospital Patients from Whom Acinetobacter calcoaceticus-Acinetobacter baumannii Complex Strains were Isolated. *Internal Medicine.* 51:51-57.

Yamashita, A., Singh, S.K., Kawate, T., Jin, Y., and Gouaux, E. 2005. Crystal structure of a bacterial homologue of Na+/Cl–dependent neurotransmitter transporters. *Nature.* 437:215-223.

Yernool, D., Boudker, O., Jin, Y., and Gouaux, E. 2004. Structure of a glutamate transporter homologue from Pyrococcus horikoshii. *Nature.* 431:811-818.

Zachowski, A. 1993. Phospholipids in animal eukaryotic membranes: transverse asymmetry and movement. *Biochem. J.* 294:1-14.

Ziegler, C., Bremer, E., and Krämer, R. 2010. The BCCT family of carriers: from physiology to crystal structure. *Mol Microbiol.* 78:13-34.

Ziegler, C., Morbach, S., Schiller, D., Krämer, R., Tziatzios, C., Schubert, D., and Kuhlbrandt, W. 2004. Projection structure and oligomeric state of the osmoregulated sodium/glycine betaine symporter BetP of Corynebacterium glutamicum. *J Mol Biol.* 337:1137-1147.

Zoetewey, D.L., Tripet, B.P., Kutateladze, T.G., Overduin, M.J., Wood, J.M., and Hodges, R.S. 2003. Solution Structure of the C-terminal Antiparallel Coiled-coil Domain from Escherichia coli Osmosensor ProP. *Journal of Molecular Biology.* 334:1063-1076.

Acknowledgement

Ich danke Prof. Dr. Christine Ziegler für die Betreuung während meiner Doktorarbeit sowie für die Bereitstellung der interessanten Forschungsprojekte. Zudem möchte ich mich für die hilfreiche Unterstützung und die anregenden Diskussionen bedanken.

Prof. Dr. Werner Kühlbrandt danke ich für die Möglichkeit meine Doktorarbeit in der Abteilung Strukturbiologie am Max-Planck-Institut für Biophysik durchführen zu können.

Weiterhin möchte ich mich bei Prof. Dr. Glaubitz für die Übernahme der Betreuung seitens der Goethe Universität sowie des SFB 807/TRAM und für die Erstellung des Gutachtens bedanken.

Prof. Dr. Thomas Meier danke ich ebenfalls für die Übernahme der Betreuung im SFB 807/TRAM.

Unter anderem danke ich auch Dr. Özkan Yildiz für die Unterstützung sowie Fahrbereitschaft bei den Synchrotrontrips.

Bei Prof. Dr. Thomas Prisner, Dr. Haleh Hashemi Haeri und Dr. Philipp Spindler möchte ich mich für die erfolgreiche PELDOR-Kollaboration bedanken. Dabei gilt besonderer Dank, Dr. Burkhard Endeward für seine kompetente Hilfsbereitschaft während des gesamten Projekts.

Prof. Dr. Beate Averhoff und Miriam Sand danke ich für die gelungene Zusammenarbeit im Projekt *Acinetobacter*.

Bei Jessica Devant bedanke ich mich für ihr Engagement während ihrer Bachelorarbeit.

Beim SFB 807 ''Transport and Communication across Biological Membranes'' und der Trainingsgruppe TRAM (Transport across Membranes) bedanke ich mich für die finanzielle Unterstützung dieser Arbeit.